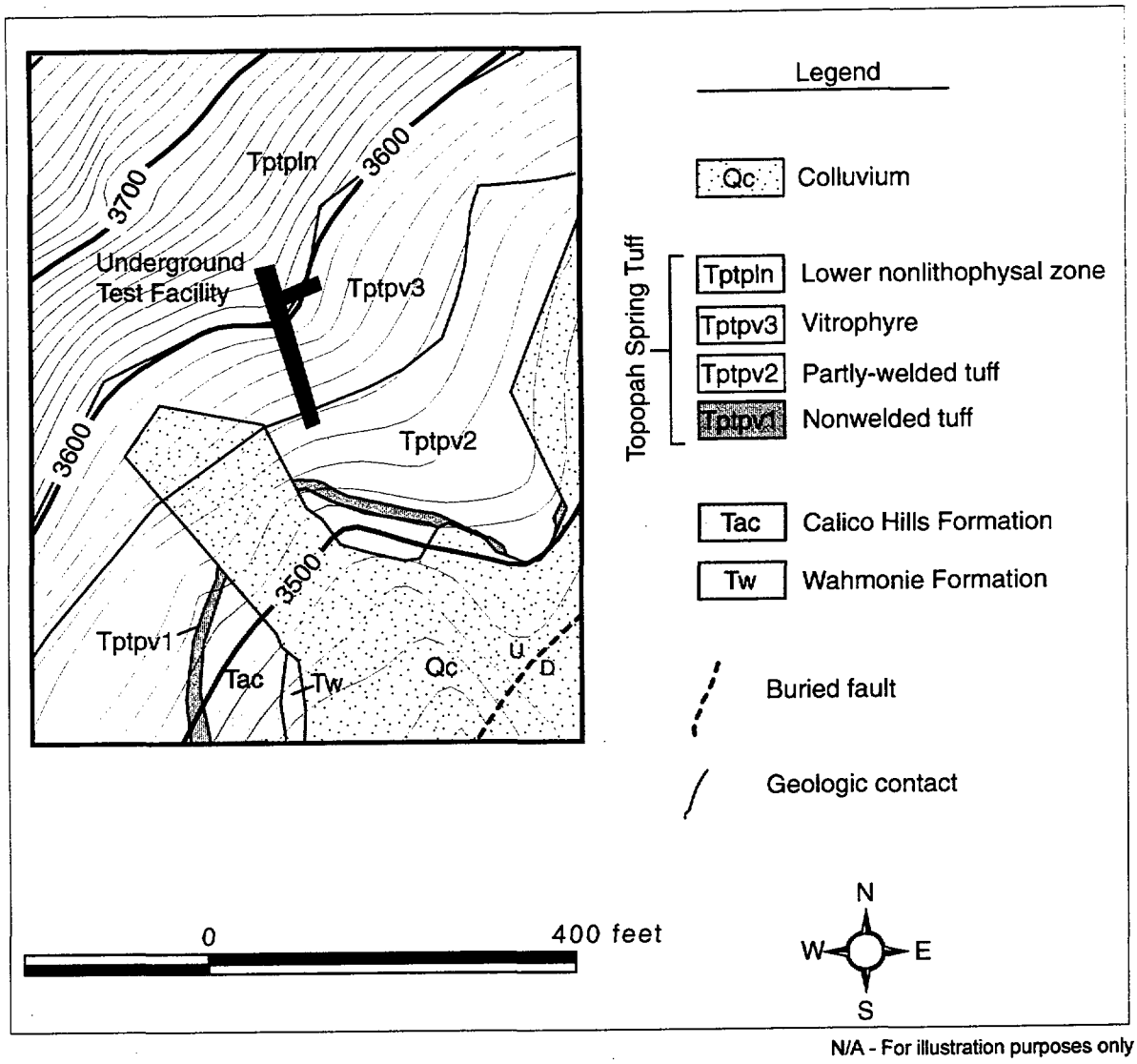

N/A - For illustration purposes only

NOTE: The plot is a geologic map of the area around the underground test facility in the southeastern part of Busted Butte. The contour interval is 10 feet. The tunnel entrance is at the southern end of the facility.

Figure 44. Busted Butte Geologic Map

6.8.3.1.1 Calico Hills Formation

Up to several meters of nonwelded Calico Hills Formation are exposed in the test area of the facility in the lower walls of both the Main Adit and the Test Alcove. The exposed Calico Hills Tuff consists of alternating beds of poorly cemented salmon-pink massive tuff and variably cemented, white ash beds.

The salmon-pink tuffs contain round to slightly elongated white vitric pumices that are generally less than a centimeter in diameter. The matrix is a mixture of fine ash, phenocrysts, and locally abundant fragments of black glass. The salmon-pink tuffs gradually become more deeply colored

upsection, suggesting that the upper parts of these units are more oxidized and may represent weakly developed paleosols. The clay content of these tuffs is low (see Table 22).

There are two variably cemented ash beds intercalated with the salmon-pink tuffs in the Main Adit and Test Alcove. These ash beds are about 130 cm apart on the right rib of the Main Adit. The ash beds are 15 to 20 cm thick and typically form resistant ledges in outcrops outside of the test facility and resistant layers inside the facility.

6.8.3.1.2 Topopah Spring Tuff

Tptpv1—The lowermost 1 to 1.5 m of the Topopah Spring Tuff is nonwelded ash-flow unit Tptpv1. The base of Tptpv1 is locally marked by a 3- to 4-cm coarsely bedded ashfall deposit. This deposit consists of 0.5- to 3-cm pumice fragments and 0.25-cm black perlitic lava clasts. This thin deposit pinches out laterally and is similar to thin discontinuous beds of ashfall deposits at the base of the Topopah Spring Tuff in outcrops outside of the test facility. A 4.5-cm-thick, crudely laminated shardy tuff overlies the ashfall deposit. The shardy tuff is also discontinous laterally.

Above the thin bedded deposits, Tptpv1 consists of light-gray nonwelded ignimbrites. The ignimbrite flow units contain medium-gray pumice clasts in a pink-gray matrix. Near the top of Tptpv1, the pumice clasts are tan. Glassy lava fragments and red-brown lithics are common. Pumice clasts increase in size and abundance upsection in individual ignimbrite flow units. The two lowermost ignimbrite flow units are separated by one or more bedded tuffs 0.2 to 8 cm thick. The lithology of the bedded tuffs is variable, consisting of laminated shardy tuff in some places and clast-supported pumiceous deposits in others. Because of relief differences on the surface on which these bedded tuffs were deposited, they fall within Tptpv1 in the Test Alcove and within Tptpv2 toward the back of the Main Adit.

In the Test Alcove, the upper part of Tptpv1 contains a distinctive zone of clay alteration typically about 70 cm thick. The clay occurs both as rinds around pumice clasts and as complete replacement of the pumice clasts. The clays are typically reddish brown but also include small round bodies of white clay within the reddish-brown clays (giving it a mottled appearance). In some replaced pumice clasts, white clay overlies layers of reddish-brown clay. Clay alteration also occurs in the tuff matrix and along subhorizontal fractures. One such fracture contains four different layers of clay up to 1.5 cm thick. The lower boundary of clay alteration is undulatory and has up to 0.5 m of relief.

Tptpv2—Tptpv2 is the highest stratigraphic unit exposed in the back of the Main Adit and in the Test Alcove area. It is characterized by tan, partly welded ignimbrite that has well-developed columnar joints. The matrix of the ignimbrite has a distinctive salt and pepper appearance due to the presence of black glass shards in a tan ashy matrix. Pumice clasts are typically 1 to 6 cm in their long dimension and exhibit flattening ratios from 6:1 to 8:1. Welding increases upsection through Tptpv2.

6.8.3.2 Mineralogy of the Busted Butte Locality

Samples from outcrops were collected at the Busted Butte site for mineralogic and petrologic analysis. Some of these samples were also used for determinations for hydrologic properties. Other samples were collected from the test block walls throughout the year for the study, and descriptions of the lithologies present in the test area were gathered.

The tables below summarize the mineralogic data for outcrop samples at the Busted Butted test locality. Tables 20 and 21 are for the Tpt samples. Table 20 provides stratigraphic descriptions for the samples in Table 21. The calcite and gypsum reported in the Tpt samples represent pedogenic calcrete contamination in the surface samples.

Table 20. Descriptions of Outcrop Samples Collected from Busted Butte

Sample	Lithology
SPC #517962	densely welded perlitic vitrophyre (upper Tptpv3)
SPC #517963	densely to moderately welded vitric tuff (mid Tptpv2)
SPC #517964	moderately welded to nonwelded vitric tuff (mid Tptpv1)
LANL #2814	densely welded perlitic vitrophyre (lower Tptpv3)
LANL #2815	densely to moderately welded vitric tuff (upper Tptpv2)
LANL #2816	densely to moderately welded vitric tuff (mid Tptpv2)
LANL #2817	densely to moderately welded vitric tuff (lower Tptpv2)
LANL #2818	moderately welded to nonwelded vitric tuff (upper Tptpv1)
LANL #2819	moderately welded to nonwelded vitric tuff (lower Tptpv1)
LANL #2820	vitric pumice swarm at base of the Topopah Spring Tuff (basal Tptpv1)

DTN: LA9909WS831372.005

The samples from the Tptpv2 and Tptpv1 intervals show that the poorly welded to nonwelded vitric portions of the lower Topopah Spring Tuff at this site are largely unaltered, without zeolites but with modest smectite occurrences. The Tptpv3 interval, although not part of the transport test section, is also largely unaltered.

Table 22 presents mineralogic data from the Calico Hills Formation and the Wahmonie Formation surface samples at the Busted Butte site. These samples are arranged in Table 22 by relative depth and show that the lowermost part of the Calico Hills Formation (Tac) contains appreciable amounts of clinoptilolite. The upper part of the Calico Hills Formation at this site, however, is characterized more by smectite than by zeolite alteration. Access to both types of alteration is, therefore, possible at this site. The three lowest samples from auger hole AUG-1 in the floor of the Busted Butte Alcove were analyzed (Table 23) for comparison with the vitric Calico Hills Formation samples from outcrop. Alteration in the alcove samples is generally similar, with smectite > clinoptilolite. The low biotite and feldspar contents of the AUG-1 samples are characteristic of the Calico Hills Tuff, indicating that Wahmonie deposits are at least 396 cm below the present alcove floor and are not expected to have any measurable influence on the test results.

Table 21. Quantitative X-ray Diffraction Results for Samples from Lower Tpt Section (weight %)

Sample	Smec-tite	Opal-CT/ Cristob.	Quartz	Feld-spar	Glass/ Amorph	Hema-tite	Mica/ Illite	Cal-cite	Gyp-sum	Kaoli-nite	Total
Tptpv3											
SPC #517962	1 ± 1	2 ± 1	tr	4 ± 1	93 ± 2	—	tr	tr	—	—	100 ± 2
LANL #2814p1	1 ± 1	4 ± 1	tr	3 ± 1	92 ± 2	—	tr	—	—	—	100 ± 2
Tptpv2											
LANL #2815p1	—	4 ± 1	1 ± 1	5 ± 1	90 ± 2	—	—	tr	—	—	100 ± 2
SPC #517963	1 ± 1	—	tr	3 ± 1	95 ± 2	tr	tr	1 ± 1	tr	—	100 ± 2
LANL #2816p1	2 ± 1	4 ± 1	tr	4 ± 1	90 ± 2	—	tr	—	—	—	100 ± 2
LANL #2817p1	3 ± 1	3 ± 1	tr	3 ± 1	91 ± 2	—	tr	—	—	—	100 ± 2
Tptpv1											
SPC #517964	tr	—	tr	2 ± 1	95 ± 1	—	tr	3 ± 1	—	—	100 ± 1
LANL #2818p1	tr	2 ± 1	tr	2 ± 1	96 ± 1	—	tr	tr	—	—	100 ± 1
LANL #2819p1	3 ± 1	1 ± 1	tr	3 ± 1	91 ± 2	—	tr	tr	—	2 ± 1	100 ± 2
LANL #2820p1	2 ± 1	1 ± 1	4 ± 1	8 ± 1	84 ± 2	1 ± 1	tr	tr	—	—	100 ± 2

DTN: LA9909WS831372.005

NOTE: — = not detected. tr = Trace abundance of < 0.5 wt %. Errors are conservative 2-sigma values. The "p1" appended to LANL samples is a designator for the X-ray diffraction split of the sample.

Table 22. Mineral Abundances (weight %) in Calico Hills Formation (Tac) Surface Samples from Busted Butte

Sample	Smec-tite	Clinop-tilolite	Crist./ OpalCT	Quartz	Feld-spar	Glass	Hema-tite	Bio-tite	Total
vitric Tac									
DEB 3/90-10	1(1)	—	—	2(1)	11(1)	86(2)	—	tr	100(2)
DEB 3/90-9	6(2)	—	—	4(1)	15(2)	74(3)	—	tr	100(3)
DTV-97-2	2(1)	—	1(1)	1(1)	2(1)	94(2)	—	tr	100(2)
DEB 3/90-8a	—	—	1(1)	1(1)	1(1)	97(2)	—	tr	100(2)
DEB 3/90-8b	1(1)	—	1(1)	4(1)	7(1)	86(2)	—	tr	100(2)
DEB 3/90-7	3(1)	1(1)	1(1)	7(1)	12(1)	76(2)	tr	tr	100(2)
zeolitic Tac									
DTV-97-3	—	9(1)	1(1)	7(1)	16(2)	64(3)	1(1)	2(1)	100(3)
DEB 3/90-6	1(1)	12(1)	1(1)	7(1)	16(2)	62(3)	—	1(1)	100(3)
Wahmonie									
DEB 3/90-5	5(2)	—	—	1(1)	26(3)	54(5)	1(1)	9(3)	100(5)
DEB 3/90-4	4(1)	—	—	2(1)	24(3)	46(6)	2(1)	17(5)	100(6)

DTN: LA9909WS831372.006

NOTE: — = not detected. tr = trace abundance. Numbers in parentheses are 2-sigma standard errors.

Table 23. Mineral Abundances (weight %) in Calico Hills Formation (Tac) Samples from Auger Hole AUG-1 in the Floor of the Busted Butte Test Alcove

Sample	Depth (cm)	Smec-tite	Clinop-tilolite	Crist./ OpalCT	Quartz	Feld-spar	Glass	Hema-tite	Bio-tite	Total
vitric Tac										
AUG-1-P	375–383	3(1)	1(1)	1(1)	8(1)	12(2)	74(3)	tr	1(1)	100(3)
AUG-1-Q	383–389	6(2)	1(1)	1(1)	8(1)	18(3)	65(4)	tr	1(1)	100(4)
AUG-1-R	389–396	3(1)	1(1)	1(1)	7(1)	11(2)	76(3)	tr	1(1)	100(3)

DTN: LA9909WS831372.010

NOTE: tr = trace abundance. Numbers in parentheses are 2-sigma standard errors.

6.8.3.2.1 Mineralogic Comparison with Yucca Mountain: Boreholes H-5 and SD-6

The excavated section at Busted Butte is in the lower Topopah Spring Tuff and the upper Calico Hills Formation (Tac). The vitric nature of this section and the relatively low abundances of smectite and clinoptilolite alteration are similar to that in drill holes near the crest of Yucca Mountain, such as USW H-5 (Table 24) and USW SD-6 (Table 25). The increase in zeolitization at the base of the Calico Hills Formation, particularly in the bedded tuff (Tacbt) unit, is comparable to the localized zeolitization in the lower part of the Calico Hills Formation at Busted Butte (Tables 22 and 23). The data indicate a distribution of alteration similar to that at Busted Butte. In considering the SD-6 and H-5 data, however, it is important to bear in mind that both drill holes had only partial core or cuttings recovery, potentially skewing the mineralogic information. A much more accurate picture of these poorly indurated vitric units is obtained by excavation, as was accomplished at Busted Butte.

6.8.3.3 Hydrologic Properties

Samples of the Calico Hills Formation and Topopah Spring Tuff exposed in Busted Butte outcrops were used to determine the hydrologic properties of the formations in the test block. These results are reported in DTNs: GS990308312242.007 and GS990708312242.008.

Table 24. Quantitative X-ray Diffraction Results (weight %) for USW H-5 Core and Drill Cuttings

Sample	Depth (m)	Smec-tite	Clinop-tilolite	Mor-denite	Tridy-mite	Cristo-balite	Opal-CT	Quartz	Feld-spar	Glass	Mica	Hema-tite	Calcite	Horn-blende	Total
Tptpv2	***505.7–509.6***														
Tptpv1	***509.6–517.9***														
Tpbt1	***517.9–519.7***														
Tac	***519.7–573.0***														
1710/1720	522.7	3 ± 2	—	—	—	5 ± 3	—	5 ± 3	20 ± 10	70 ± 10	—	—	—	—	103 ± 15
1750 (DC)	533.4	—	tr?	—	—	5 ± 5	—	2 ± 3	5 ± 5	85 ± 5	—	—	—	—	97 ± 9
1762 (SW)	537.1	—	—	—	—	1 ± 1	—	1 ± 1	5 ± 5	95 ± 5	—	—	—	—	102 ± 7
1760/1770	538.0	—	6 ± 1	—	—	—	4 ± 1	3 ± 1	6 ± 1	81 ± 2	—	—	—	—	100 ± 2
1800 (SW)	548.6	—	—	—	—	2 ± 3	—	2 ± 3	10 ± 5	85 ± 5	1 ± 1	—	—	—	100 ± 8
1820/1830	556.3	tr	4 ± 1	—	—	—	2 ± 1	4 ± 1	10 ± 1	80 ± 2	—	—	—	—	100 ± 2
1852 (SW)	564.5	—	—	—	—	—	—	2 ± 3	7 ± 3	90 ± 5	1 ± 1	—	—	—	100 ± 7
1875 (SW)	571.5	—	tr?	—	—	—	tr?	2 ± 3	5 ± 5	92 ± 3	—	—	—	—	99 ± 7
Tacbt	***573.0–592.0***														
1890/1900	577.6	1 ± 1	11 ± 1	—	—	—	3 ± 1	4 ± 1	6 ± 1	75 ± 2	—	—	—	—	100 ± 2
1900/1910	580.6	tr	10 ± 1	—	—	—	1 ± 1	3 ± 1	8 ± 1	78 ± 2	tr	—	—	—	100 ± 2
1910/1920	583.7	tr	18 ± 1	—	—	—	5 ± 1	5 ± 1	7 ± 1	65 ± 2	tr	—	—	—	100 ± 2
1917 (SW)	584.3	—	25 ± 5	—	—	—	10 ± 5	30 ± 5	35 ± 10	—	tr	—	—	—	100 ± 13
1920/1930	586.7	3 ± 1	52 ± 3	—	—	—	7 ± 2	14 ± 1	16 ± 3	6 ± 5	2 ± 1	—	—	—	100 ± 5
1930 (DC)	588.3	2 ± 3	50 ± 10	—	—	—	—	15 ± 5	30 ± 5	—	1 ± 1	—	—	—	98 ± 13

DTN: LA9909WS831372.007

NOTE: — = not detected. tr = trace abundance. DC = drill-bit cutting sample. SW = sidewall core sample.

Table 25. Quantitative X-ray Diffraction Results (weight %) for Samples from Drill Hole USW SD-6

Sample	Depth (m)	LANL number[a]	Smec-tite	Clinop-tilolite	Tridy-mite	Cristo-balite	Opal-CT	Quartz	Feld-spar	Glass	Hema-tite	Mica	Horn-blende	Cal-cite	Total
Tptpv2	***455.7–461.5***														
1496.5/1496.7	456.2	2984p1	—	—	—	—	17±4	1±1	11±2	71±4	—	tr	—	—	100±5
1500.1/1500.2	457.3	2985p1	2±1	—	—	—	17±4	1±1	12±2	68±4	—	tr	—	—	100±5
1503.3/1503.4	458.2	2986p1	2±1	—	—	—	20±6	2±1	16±2	60±6	tr	tr	—	—	100±6
1506.2/1506.3	459.1	2987p1	3±1	—	—	—	18±5	1±1	13±2	65±5	tr	tr	—	—	100±6
1509.2/1509.3	460.0	2988p1	3±1	—	—	—	15±4	1±1	11±2	70±4	tr	—	—	—	100±5
1512.1/1512.2	460.9	2989p1	4±1	—	—	—	14±4	1±1	12±2	69±4	—	tr	—	—	100±5
Tptpv1	***461.5–471.7***														
1516.9/1517.0	462.4	2990p1	4±1	—	—	—	9±2	1±1	10±1	76±2	tr	tr	—	—	100±3
1521.5/1521.6	463.8	2991p1	5±2	—	—	—	4±1	1±1	5±1	85±2	—	tr	—	—	100±3
1524.9/1525.0	464.8	2992p1	5±2	—	3±1	2±1	—	2±1	11±2	77±3	tr	tr	—	—	100±3
1527.8/1527.9	465.7	2993p1	3±1	—	2±1	4±1	—	5±1	21±3	65±3	tr	tr	—	—	100±4
1546.5/1546.6	471.4	2994p1	1±1	—	—	1±1	—	5±1	10±1	83±2	tr	tr	—	—	100±2
Tpbt1	***471.7–473.8***														
Tac	***473.8–526.5***														
1560.8/1560.9	475.8	2995p1[b]	tr	4±1	6±1	10±1	—	27±2	53±8	—	tr	tr	—	—	100±8
1563.3/1563.4	476.5	2996p2[b]	—	6±1	5±1	13±1	—	25±2	53±8	—	tr	tr	—	—	102±8
1563.3/1563.4	476.5	2996p1	4±1	4±1	—	2±1	—	2±1	7±1	81±2	—	tr	—	—	100±2
1566.7/1566.8	477.6	2997p1	—	2±1	1±1	2±1	—	4±1	10±1	81±2	tr	tr	—	—	100±2
1570.3/1570.5	478.7	2998p1	—	1±1	1±1	3±1	—	8±1	16±2	71±2	tr	tr	—	—	100±3

DTN: LASC831321AQ98.003

NOTES: — = not detected tr = Trace abundance
[a]The "p1" or "p2" appended to LANL numbers of samples denote specific X-ray diffraction splits.
[b]The analyses 2995p1 and 2996p2 are from large (> 5 cm) lithic clasts that occur at these depths.

6.8.4 Tomographic Studies: Geophysical Techniques at the Busted Butte Unsaturated Zone Test Facility—Overview

Real-time geophysical monitoring techniques may be used to provide real-time data on the advance of fluid fronts and tracer fronts through the block and enable us to optimize our collection-pad sampling schedule to collect data. Combining two techniques enables the collection of detailed, high-resolution, 3-D, calibrated, real-time monitoring of moisture and tracer movement through the unsaturated fractured medium. Specifically, electrical resistance tomography (ERT) provides 3-D global coverage and ground-penetrating radar tomography (GPR-T) provides high spatial resolution. The techniques are listed below, along with their characteristics and the advantages they bring to the test program at Busted Butte.

Electrical Resistance Tomography (ERT):

- 3-D snapshot of moisture content and tracer front
- Covers entire test block
- Half-meter spatial resolution
- Measurements on demand (probably weekly or monthly).

Ground Penetrating Radar Tomography (GPR-T):

- 2-D slices of moisture content
- Selected locations through available boreholes
- 1- to 10-cm spatial resolution
- Measurements at opportunistic intervals (tied to collection-borehole sampling frequency)
- Can determine matrix permeabilities.

Ongoing geophysical monitoring is presently helping us guide the timing of collection-pad retrieval for detailed tracer analysis. Independent physical measurement techniques (collection pads and block mineback) will ultimately provide field-scale evaluation of geophysical techniques, increasing their applicability and acceptability for other YMP activities. None of these techniques interfere physically with the test or with the testing schedule.

6.8.4.1 Ground-Penetrating Radar Tomography

6.8.4.1.1 Experimental Objective and Status

The objective of the ground penetrating radar (GPR) data acquisition is to monitor the tracer injection of the Busted Butte UZTT both spatially and temporally and to investigate the nature of fluid migration through the Calico Hills member of the Yucca Mountain lithologic sequence. The data collected, analyzed, and submitted to the Technical Data Management System (TDMS) thus far include the pre-injection baseline radar velocity measurements as well as the subsequent velocity measurements made after the start of tracer injection (seven data collection visits through September 1999). Additional measurements shall continue to be made on a regular schedule approximately every three to four months. All analyzed data are periodically compared to the other available geophysical data as well as to the tracer breakthrough data in order to better constrain the interpretation of fluid/tracer migration within the block.

6.8.4.1.2 Background and Experimental Approach

The borehole radar method is one in which modified surface radar antennae are emplaced into a rock formation and high-frequency electromagnetic signals are transmitted through the formation to a receiving antenna. The electrical properties of the subsurface material greatly influence the transmitted electromagnetic signal. In particular, the dielectric permittivity of the rock has a strong influence on the propagation of the signal and whether it travels at a high or low velocity. Moisture content has such an effect. The high dielectric permittivity (κ) of water ($\kappa \sim 80$) or wet rock ($\kappa \sim 20$–30) in contrast to drier rock ($\kappa \sim 3$–6) typically results in greatly reduced signal velocities. Changing chemical compositions (i.e., tracers) may also alter the bulk dielectric permittivity of the rock and, hence, the velocity of propagation of the radar wave. Because such changes in signal character are what are to be measured over the course of the Busted Butte UZTT, any increase (or decrease) in background moisture content or chemical composition resulting from the tracer injection (or rock dry-out) should result in changes in the received radar wave velocity.

The transmitted signals may be represented as multiple ray paths crossing through a zone of interest within the block. If sufficient ray paths are recorded, a tomographic image may be obtained through computer processing. The information extracted from such data consists of the transit time, which depends on the wave velocity. This information, in the form of a processed radar velocity tomogram, offers a high-resolution approach to monitoring the changes occurring in the rock over the duration of the tracer-injection experiment.

6.8.4.1.3 Equipment Description, Component Specifications, Operating Principles, and Survey Methodology

A description of the equipment used, the component specifications, the operating principles, and the GPR-T survey methodology can be found in the Technical Implementing Procedure governing all GPR-T data acquisition done in support of the Yucca Mountain site characterization effort (YMP-LBNL-TIP/GP 5.0, Rev. 0, Mod. 0).

6.8.4.1.4 Results of Busted Butte Unsaturated Zone Transport Test Radar Data Acquisition

The radar data were acquired in eight of the Phase-2 collection boreholes orthogonal to the direction of the Phase-2 injection boreholes. Additionally, two of the Phase-2 injection boreholes were used to acquire data only one time, after the boreholes were apparently affected by grout infiltration resulting from nearby electrical resistance tomography (ERT) borehole grouting. The 10 boreholes include the following: 9, 11, 13, 15, 16, 46, 47, and 48 (Phase-2 collection); 19 and 22 (Phase-2 injection). The configuration and layout of the boreholes used are illustrated in Figure 38.

The radar data are acquired in the two-dimensional planes defined by two boreholes, more commonly referred to as well pairs. The well pairs acquired in support of the Busted Butte UZTT are the following: 15-13, 48-46, 47-11, 46-9, 46-16, and 22-19 (one time only for the last pair listed). The decision to acquire data in these particular well pairs was made based on their

relative proximity to the injection boreholes. Data from both the upper horizontal well pair 15-13 and the vertical well pair 46-16 are acquired to monitor tracer injection associated with the upper injection boreholes 18, 20, 21, and 23. Data from the lower horizontal well pairs 46-9, 47-11, and 48-46 are acquired to monitor tracer injection associated with the lower injection boreholes 24, 25, 26, and 27. The vertical well pair 46-16 may also be used to image any tracer injection associated with the lower injection boreholes and the progress of the tracer beneath the horizontal well pair 15-13.

Thus far the data collected have been processed for travel times with the result being radar velocity tomograms (DTN: LB00032412213U.001). Differencing or subtraction of the velocity tomograms over time has also been completed for each of the well pairs. Such differencing or subtraction allows for the highlighting of the tracer or moisture front as it changes spatially and temporally. In essence, the background formation remains static in those areas not affected by the changing tracer or moisture front. By subtracting one velocity tomogram from another, we are able to discount those areas remaining static while emphasizing those areas where change is occurring.

Two of the well pairs differ slightly in the acquisition method used between the baseline and the post-injection surveys. These well pairs are 46-16 and 46-9. Data for well pair 46-16 was collected at a higher frequency (200 MHz) during the post-injection survey to better match the data collected in all of the other well pairs. Higher frequencies generally result in data of higher resolution (approximately 10.0 cm for 200 MHz), so the highest-frequency antennae should be used if at all possible. Data were not originally acquired in well pair 46-9 because it was believed that well pair 48-46 provided sufficient coverage in the area of the lower injection boreholes. A decision was subsequently made after tracer injection began to gather more spatial information below the lower injection boreholes and, hence, well pair 46-9 was added to the GPR acquisition list. Also, it should be noted that the pre-injection baseline data for several of the well pairs differs significantly from data acquired just one month after tracer injection began. The differences are likely the result of changes in the overall block assemblies (e.g. grouting of the ERT boreholes, addition of the injection apparatus, etc.) rather than the immediate consequence of the tracer injection. In order to enhance the subsequent differencing tomography, the "baseline" set of velocity tomograms chosen are those collected in August-September 1998 approximately one month after tracer injection began. Comparison with tracer breakthrough data on the collection pads indicates that tracer had not yet significantly entered those regions imaged by the GPR tomograms. Therefore, it was determined that the August–September 1998 data would provide an adequate starting point from which to evaluate the changes in the block over time.

Each of the well pairs have witnessed some degree of velocity change over the course of the experiment. For the purposes of this AMR, however, only three of the well pairs will be discussed in detail: 46-16, 46-9 and 15-13. This is done in an effort to be concise as the results for each well pair are essentially similar. Again, all of the data from each of the well pairs have been submitted to the TDMS and are available for review.

Well Pair 46-16

This well pair represents the only vertical slice through the block (approximately 9.5 m in length and 3.5 m in height). It images tracer and moisture contributions from both the upper and the lower injection boreholes. When evaluating changes in velocity over time, one would expect such changes to occur in the regions directly surrounding the injection boreholes with decreased velocities representing areas of increased moisture content. This is exactly what is seen in the differenced tomograms. Figures 45 to 47 represent several time steps throughout the course of the experiment (dates of data acquisition are noted above each tomogram). As can be seen, decreases in the velocity relative to the baseline (August–September 1998) data are immediately obvious surrounding the high and low injection boreholes (these locations are marked on the tomogram as small white dots). Furthermore, the zones of decreased velocity can be seen to expand away from the injection boreholes over time both in a vertical as well as a horizontal direction. Such vertical and horizontal spreading is to be expected as a result of matrix or capillary-driven flow and was, in fact, confirmed in the Phase-1A excavation. Precluding a similar excavation of the rock included by this well pair, the GPR data would seem to indicate a similar mechanism of flow for the Phase-2 block.

Also of note is the seemingly large extent of decreased velocity. It should be restated that low velocities are indicative of zones of higher dielectric permittivity; zones of higher dielectric permittivity are indicative of zones of elevated moisture content. That being the case, those zones of decreased velocity may represent regions of elevated moisture content and not simply the presence of tracer. This subtlety is born out when comparing the tracer breakthrough data with the tomography results. The zones of increased moisture content (i.e., decreased velocity) do not directly overlay the tracer breakthrough within boreholes 46 or 16. In fact, the locations of tracer breakthrough are contained within the zones of decreased velocity. This result implies that as the fluid front containing the tracer spreads away from the injection boreholes, some of the tracer may be retarded in relation to the spread of the moisture front. In effect, the tracer may be moving more slowly through the block than its associated fluid or water component. Conversely, the fluid front leaving the injection boreholes may be simply displacing existing pore fluids and mobilizing them within the block. The radar velocities are insensitive to this effect and are thus incapable of distinguishing between existing pore waters, introduced pore waters or tracers. Again, comparing the tomography results with those recorded in the tracer breakthrough logs, it appears that some form of fluid breakthrough is occurring in the collection boreholes which is not comprised of tracer. This is evidently what is being imaged by the differenced radar tomograms and it is not an inconsequential finding.

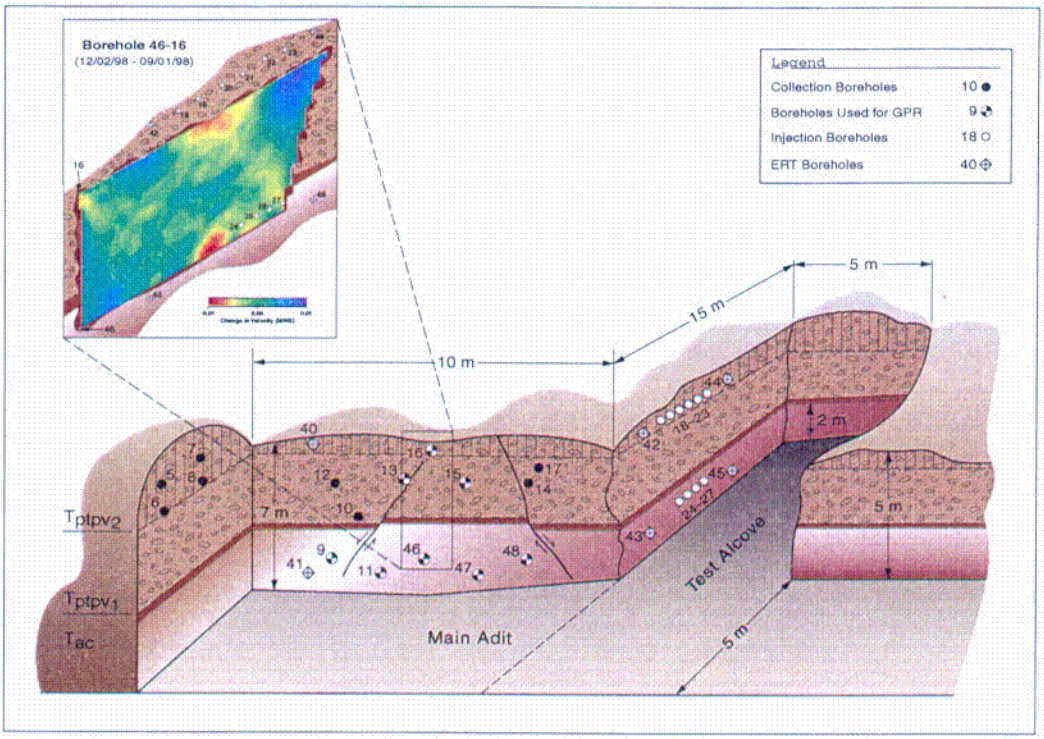

DTN: LB00032412213U.001; MO0004GSC00167.000 (for location)

Figure 45. Tomography (GPR-T) Results for Well Pair 46-16, December 1998

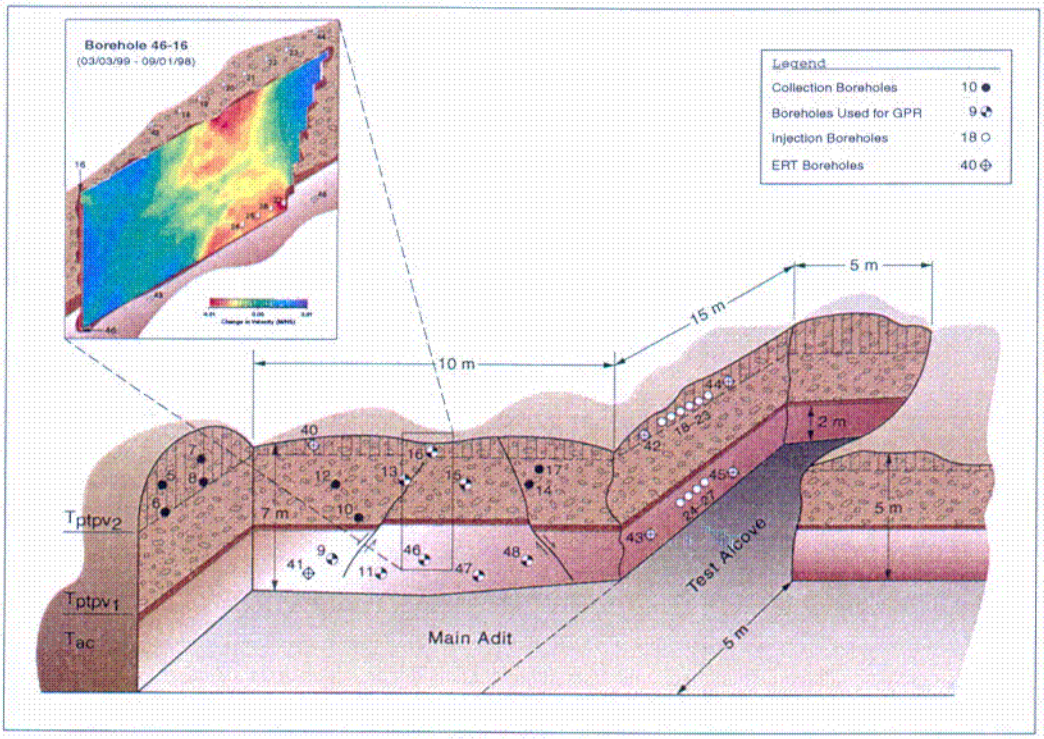

DTN: LB00032412213U.001; MO0004GSC00167.000 (for location)

Figure 46. Tomography (GPR-T) Results for Well Pair 46-16, March 1999

C1

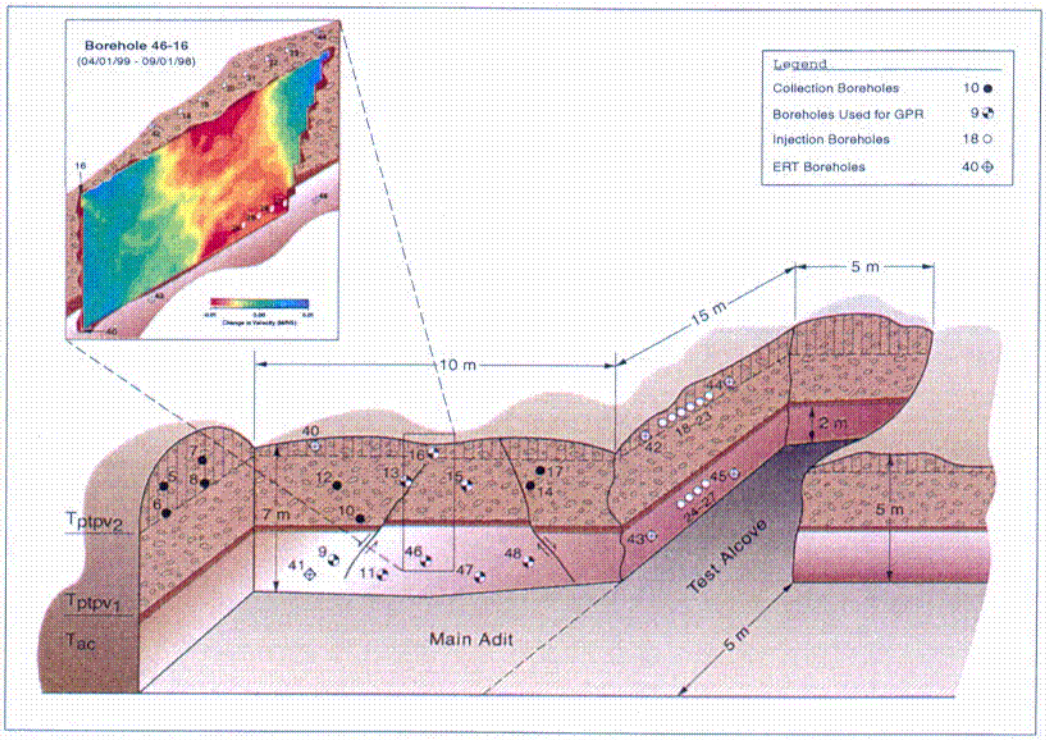

DTN: LB00032412213U.001; MO0004GSC00167.000 (for location)

Figure 47. Tomography (GPR-T) Results for Well Pair 46-16, April 1999.

Well Pair 46-9

This well pair represents a horizontal slice (approximately 8.0 m in length and 2.6 m in width) through the block and images the tracer/moisture front associated with the lower injection boreholes. Figures 48 and 49 represent two time steps throughout the course of the experiment (dates of data acquisition are noted above each tomogram). As can be seen, decreases in the velocity relative to the baseline (August-September 1998) data are immediately obvious surrounding the low injection boreholes (these locations are marked on the tomogram as orthogonal tubes). Furthermore, the zones of decreased velocity can be seen to expand away from the injection boreholes over time in a horizontal direction. Because a horizontal well pair cannot capture the vertical flow of moisture away from the boreholes, only the extent of the horizontal flow can be imaged. What is observed is that the decrease in velocity (i.e., the increase in moisture content), moves rapidly away from the injection boreholes early on in the experiment and then remains relatively constant aside from some localized changes. This would seem to imply that much of the moisture front moves away from the injection apparatus to its greatest possible horizontal extent at which time it can no longer spread in such a direction. Presumably, the majority of fluid flow from this time on continues in a direction other than horizontal.

C2

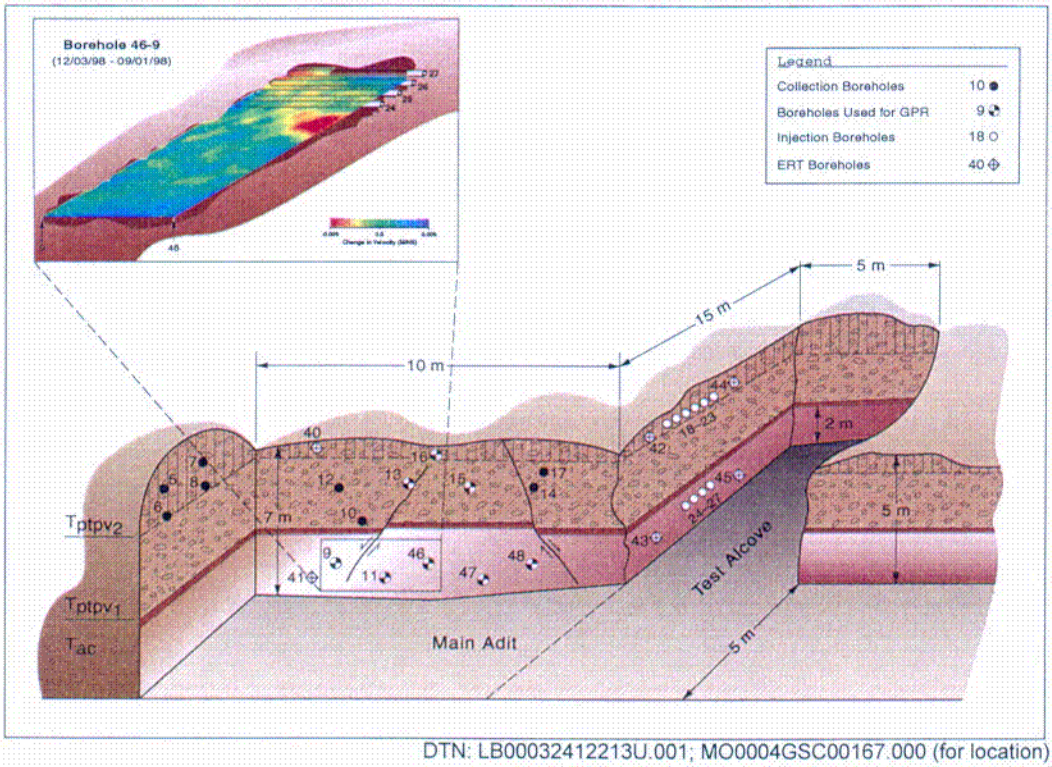

DTN: LB00032412213U.001; MO0004GSC00167.000 (for location)

Figure 48. Tomography (GPR-T) Results for Well Pair 46-9, December 1998.

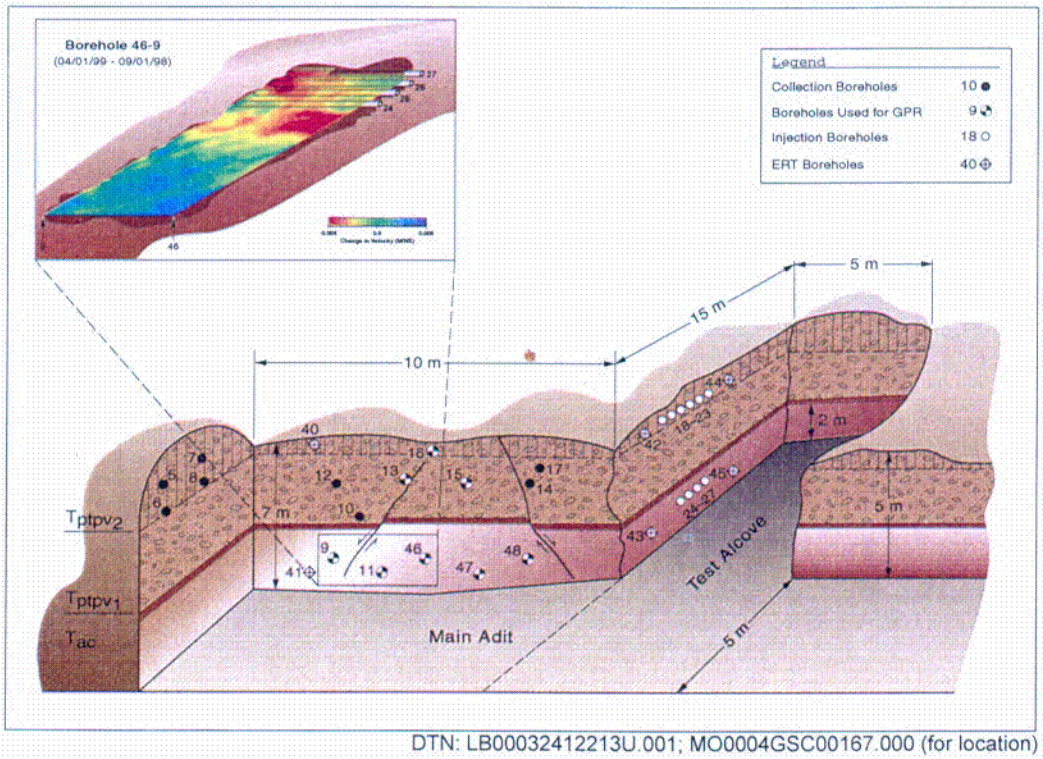

DTN: LB00032412213U.001; MO0004GSC00167.000 (for location)

Figure 49. Tomography (GPR-T) Results for Well Pair 46-9, April 1999.

C3

The results implied by the radar tomograms are in concurrence with the tracer breakthrough logs for boreholes 46 and 9. Again, those zones of decreased velocity overlay those locations in the boreholes where tracer has been seen to break through. The additional contribution of the moisture front relative to the tracer (as described above for well pair 46-16) does not appear to be as significant for this horizontal well pair. It is not yet clear whether this is because the region imaged is smaller or spatially closer to the injection boreholes.

Well Pair 15-13

This well pair represents a horizontal slice (approximately 9.5 m in length and 2.0 m in width) through the block and images the tracer/moisture front associated with the upper injection boreholes. Figure 50 represents one time step throughout the course of the experiment (dates of data acquisition are noted above each tomogram). As can be seen, decreases in the velocity relative to the baseline (August-September 1998) data are immediately obvious surrounding the upper injection boreholes (these locations are marked on the tomogram as orthogonal tubes). Furthermore, the zones of decreased velocity can be seen to expand away from the injection boreholes over time in a horizontal direction. What is observed is that the decrease in velocity (i.e., the increase in moisture content), moves steadily away from the injection boreholes throughout the course of the experiment. This varies a bit from the analogous well pair 46-9. Rather than reaching a maximum extent, the moisture front appears to be continually expanding away from the boreholes. This is probably the result of the well pair's increased distance beneath the injection boreholes and the much larger volume of fluid being introduced by the upper injection boreholes.

The results implied by the radar tomograms are in concurrence with the tracer breakthrough logs for boreholes 15 and 13. Again, those zones of decreased velocity overlay those locations in the boreholes where tracer has been seen to break through. The additional input of the moisture front relative to the tracer (as described above for well pair 46-16) does not appear to be as significant for this well pair. As for well pair 46-9, it is not yet clear whether this is because the region imaged is smaller or spatially closer to the injection boreholes. Also, the much larger volume of tracer injected into the region of this well pair may account for the lack of a discrepancy (i.e. there is simply more tracer in the area of the collection boreholes). Additionally, the neutron probe data collected in these two boreholes implies a very similar pattern of elevated moisture content. Those zones that appear to be wetting as well as those that remain dry agree nicely with the same regions on the tomograms. The ERT data in this region appear to indicate an area of changing resistivity with time. It remains to be seen if this anomalous zone of resistivity correlates with the zone of decreased velocity imaged by the radar tomograms. Further analysis is planned to resolve this issue.

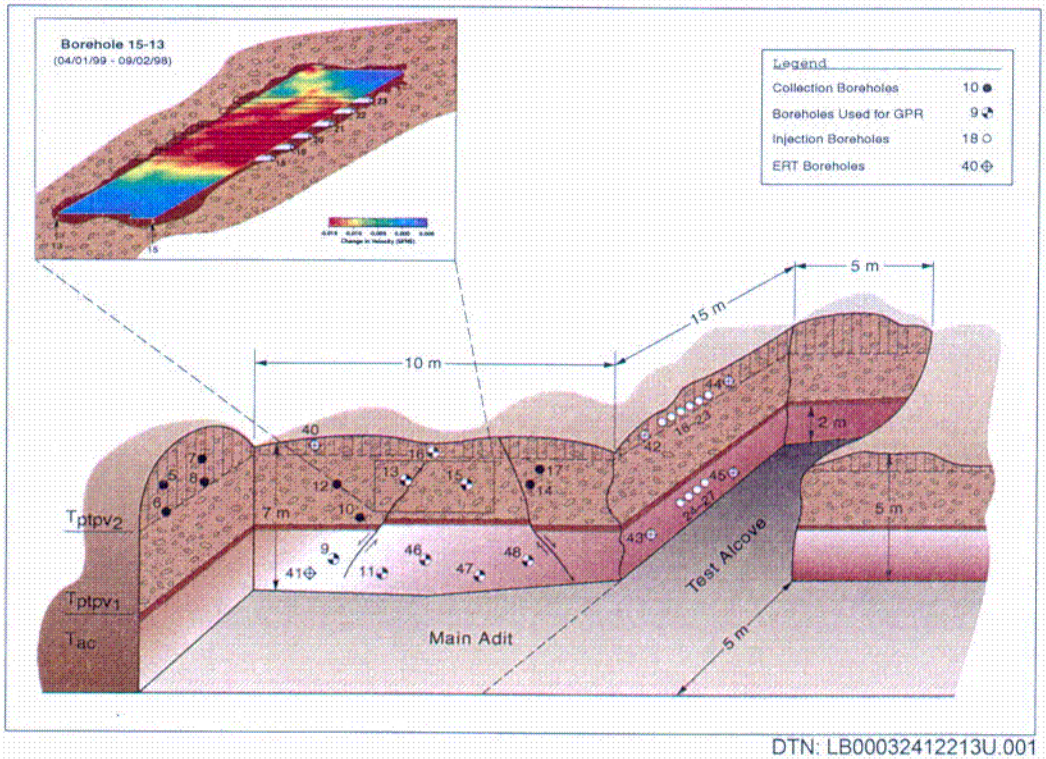

DTN: LB00032412213U.001

Figure 50. Tomography (GPR-T) Results for Well Pair 15-13, April 1999

6.8.4.1.5 Conclusions

The radar data collected thus far in support of the Busted Butte UZTT suggest that the method is an appropriate one for investigating subsurface velocity anomalies that may be related to tracer injection and moisture migration. Such anomalies are the result of changes in the dielectric permittivity of the rock mass. As noted above, such changes are most likely the result of some combination of the injected tracer and its associated fluid component. The regions of low velocity (i.e. elevated moisture content) appear to be in very close agreement with the other complementary evidence, including the tracer breakthrough logs and the neutron logging results. At this time, it appears very likely that the differenced radar tomograms are defining the total extent of elevated moisture content within those zones defined by the radar well pairs. By defining the extent of this front, the radar tomography should provide an excellent control mechanism for any planned excavation of the Phase-2 block or any hydrologic flow modeling done to date.

6.8.4.2 Electrical-Resistance Tomography

6.8.4.2.1 Experimental Objective

The objective of this work is to provide 3-D electrical-resistance tomography (ERT) images of the movement of a tracer through the test block at the UZTT at Busted Butte. ERT was chosen as an appropriate technology based on its success at many other locations, including the Drift Scale Test at Yucca Mountain. This report describes the results obtained during four separate data collections starting in July and ending in early September 1998.

C4

6.8.4.2.2 Description of the Electrical-Resistance Tomography Method

Electrical-resistance tomography (ERT) is a new geophysical imaging technique that can be used to map subsurface liquids as flow occurs during natural or man-induced processes and to map geologic structure. Man-induced processes, such as tank leaks and clean-up processes such as steam injection, can create changes in a rock's electrical properties that are readily measured. ERT is a technique for reconstruction of subsurface electrical resistivity. The result of such a reconstruction is a 2- or 3-D map of the electrical resistivity distribution underground made from a series of voltage and current measurements from buried electrodes. The ERT approach we follow here relies on detection and mapping of the changes in electrical resistivity associated with the movement of a tracer through the test block at the UZTT site.

ERT surveys are performed using a number of electrodes in boreholes and/or at the rock surface to image the resistivity distribution between two boreholes. Using an automatic data-collection and switching system, we collect a few hundred electrical-resistance measurements. The data are then processed to produce electrical-resistivity tomographs using state-of-the-art data-inversion algorithms. We use these measurements to calculate tomographs that show the spatial distribution of the subsurface resistivities.

6.8.4.2.3 Description of 2-D Algorithms

Finite-element Iterative Algorithm

This algorithm involves solving both the forward and inverse problems. The forward and inverse algorithms used in this work are described in detail by LaBrecque et al. (1996, pp. 538–548) and summarized below. The solution to the forward problem uses the finite-element method (FEM) to compute the potential electrical response of a 2-D earth to a 3-D source. To avoid the difficulty of numerically solving a 3-D problem, Poisson's equation is formulated in the wave-number domain using the Fourier transformation in the strike (y) direction. The governing equation is:

$$\frac{\partial}{\partial x}\left(\sigma\frac{\partial V}{\partial x}\right)+\frac{\partial}{\partial z}\left(\sigma\frac{\partial V}{\partial z}\right)-\lambda^2\sigma V=-I\delta(x)\delta(z), \qquad \text{(Eq. 25)}$$

where V is the potential in the Fourier transform domain, σ is the conductivity, λ is the Fourier-transform variable, I is the source current, and $\delta(x)$ is the delta function.

Using the FEM, we can calculate the potentials for a discrete number of transform variables at the nodes of a mesh of quadrilateral elements. We can then transform the potentials back into the Cartesian domain. The boundary conditions are assumed to be Neumann (zero potential gradient, no vertical current flow) at the ground-air interface and Dirichlet (potential set to zero) along the other three boundaries.

The inverse algorithm iteratively finds the maximum value of the stabilization parameter α to minimize the objective function for the stabilization parameter:

$$Y(\mathbf{P})=\chi^2(\mathbf{P})+\alpha W(\mathbf{P}) \qquad \text{(Eq. 26)}$$

where **P** is the vector of unknown parameters, $W(\mathbf{P})$ is the roughness operator, and χ^2 is the chi-squared statistic. Minimizing this function yields a value of $\chi^2(\mathbf{P})$ equal to an a-priori value, $\chi^2_{\text{a-priori}}$, which in our work, is assumed to equal the number of data points. The inverted parameters are the natural logarithms of the conductivities of pixels, where each pixel contains the elements of a rectangular region of a FEM mesh. The chi-squared statistic is given by:

$$\chi^2 = [\mathbf{D} - \mathbf{F}(\mathbf{P})]^{\mathrm{T}} \mathrm{W}^{-1} [\mathbf{D} - \mathbf{F}(\mathbf{P})] \qquad \text{(Eq. 27)}$$

where **D** is the vector of known data values, **F(P)** is the forward solution, T signifies transpose, and **W** is the data covariance matrix.

The roughness operator stabilizes and removes ambiguity in the resistivity inversion by minimizing the model roughness, which is referred to as "smoothest inversion." The roughness operator $W(\mathbf{P})$ is given by:

$$W(\mathbf{P}) = \mathbf{P}^{\mathrm{T}} \mathbf{R}(\mathbf{P}) \,, \qquad \text{(Eq. 28)}$$

where, here, **R** is the roughness matrix.

At the *ith* iteration, our algorithm begins by approximating the forward solution by a first-order Taylor's series of the form:

$$\mathbf{F}(\mathbf{P}) = \mathbf{F}(\mathbf{P}_i) + \mathbf{A}(\mathbf{P} - \mathbf{P}_i), \qquad \text{(Eq. 29)}$$

where **F(P)** is the forward solution, **A** is the sensitivity matrix, and $\mathbf{P}_i$ is the vector of estimated parameters at the *i*th iteration.

Using a root-finding algorithm, we estimate α for this linearized system. We then use a modified Marquardt method iteration to find the parameters that minimize the objective function (Equation 26) for the estimated value of α. Iteration is repeated until the changes in α and χ^2 from one iteration to the next are suitably small.

Single-pass Image Reconstruction

The computational demands and potential convergence failure of a formal inverse solution such as that above has prompted the development of a number of image-reconstruction algorithms that are purely qualitative. We use an algorithm that computes a "gray scale" associated with each element $j = 1, 2, \ldots m$ according to a simple matrix-vector product:

$$\mathrm{P}_j = \sum_{i=1}^{n} S_{i,j} \ln(\mathrm{T}'_i / \mathrm{T}_i) \qquad j = 1, 2, \ldots m \qquad \text{(Eq. 30)}$$

where n is the number of independent measurements, T_i and T'_i are the *i*th-measured boundary transfer resistances before and after a change in resistivity within the region, and $S_{i,j}$ is a sensitivity coefficient for element j and independent measurement i derived in the same manner as the smoothness algorithm in the previous section.

The sensitivity matrix is computed on a finite-element mesh with uniform resistivity. Because no inverse matrices are required, the algorithm is computationally efficient and very fast as only one matrix vector product is required for each image.

6.8.4.2.4 Description of the 3-D Imaging Algorithm

Our 3-D inversion algorithm requires a forward solution, which can numerically solve the potential equation:

$$\frac{\partial}{\partial x}\left(\sigma\frac{\partial}{\partial x}V\right)+\frac{\partial}{\partial y}\left(\sigma\frac{\partial}{\partial y}V\right)+\frac{\partial}{\partial z}\left(\sigma\frac{\partial}{\partial z}V\right)=I(x,y,z), \qquad \text{(Eq. 31)}$$

where V is the scalar electrical potential and $I(x,y,z)$ is the distribution of electrical current sources and sinks. We convert the differential equation (Equation 25) into a system of linear equations. This system of equations is then solved iteratively using the diagonally weighted preconditioned-conjugate-gradient method. The boundary conditions are assumed to be Neumann (zero potential gradient, no vertical current flow) at the ground-air interface and Dirichlet (potential set to zero) along the other five boundaries.

Three-dimensional inversion is by nature strongly underdetermined, and so, inverse solutions that consider only the fitting of the forward model to field data are nonunique. Therefore, we implemented a regularized solution that jointly minimizes the misfit of the forward model to the field data and stabilizes the inverted value of the parameters. To find the optimal value of the parameter vector **P**, our algorithm finds the maximum value of α, the stabilization parameter, for which minimizing:

$$Y(\mathbf{P}) = \chi^2(\mathbf{P}) + \alpha\ \mathbf{P}^{\mathsf{T}}\underline{\mathbf{R}}\mathbf{P} \qquad \text{(Eq. 32)}$$

gives

$$\chi^2(\mathbf{P}) = \chi^2_{\text{a-priori}} \qquad \text{(Eq. 33)}$$

In Equation 32, we have chosen to use, $\underline{\mathbf{R}}$, the solution roughness, as the stabilizing functional. This parameter is approximated by:

$$\underline{\mathbf{R}} = \underline{\mathbf{x}}^{\mathsf{T}}\underline{\mathbf{x}} + \underline{\mathbf{y}}^{\mathsf{T}}\underline{\mathbf{y}} + \underline{\mathbf{z}}^{\mathsf{T}}\underline{\mathbf{z}}\ , \qquad \text{(Eq. 34)}$$

where $\underline{\mathbf{x}}$, $\underline{\mathbf{y}}$, and $\underline{\mathbf{z}}$ are the first-order difference operators in the x, y, and z directions. Also in Equation 33, $\chi^2_{\text{a-priori}}$ is equal to the number of data points, and χ^2 is given by:

$$\chi^2 = (\mathbf{D} - \mathbf{F}(\mathbf{P}))^{\mathsf{T}}\underline{\mathbf{W}}(\mathbf{D} - \mathbf{F}(\mathbf{P}))\ , \qquad \text{(Eq. 35)}$$

where **D** is the vector of known data values, **F(P)** is the forward solution and $\underline{\mathbf{W}}$ is a data weight matrix. The diagonal elements of $\underline{\mathbf{W}}$ are the reciprocals of the data variances and the nondiagonal elements are zero. This assumes noncorrelated data errors.

The parameters, **P**, are the natural logarithms of the conductivity of the FEM elements. In the foreground (the part of the FEM mesh between the boreholes and near the boreholes), each parameter corresponds to a single finite element. In the background (the region away from the boreholes), we lump several finite elements together into a single parameter.

The nonlinear inversion is carried out iteratively as:

$$\mathbf{P}_{k+1} = \mathbf{P}_k + \Delta\mathbf{P}_k \ , \qquad \text{(Eq. 36)}$$

where $\mathbf{P}_k$ is the vector of parameters from the previous iteration and $\Delta\mathbf{P}_k$ is the parameter change vector. The $\Delta\mathbf{P}_k$ vector is found by solving the linear problem:

$$\Delta\mathbf{P}_k = \left(\underline{\mathbf{A}}_k^{\mathrm{T}}\ \mathbf{W}\ \underline{\mathbf{A}}_k + \alpha\underline{\mathbf{R}}\right)^{-1}\left(\underline{\mathbf{W}}\ \Delta\mathbf{D}_k - \alpha\mathbf{R}\ \mathbf{P}_k\right) \ , \qquad \text{(Eq. 37)}$$

where $\underline{\mathbf{A}}_k$ is the sensitivity matrix and $\Delta\mathbf{D}_k = \mathbf{F}(\mathbf{P}) - \mathbf{D}$. The elements of the sensitivity matrix, $a_{i,j}$, are:

$$a_{i,j} = \frac{\partial\, F_i(\mathbf{P}_k)}{\partial p_j} \ , \qquad \text{(Eq. 38)}$$

where p_j is the jth element of $\mathbf{P}_k$ and $F_i(\mathbf{P}_k)$ is the forward solution for the ith data point. Solving Equation 37 exactly is not practical because the system is very large (50,000 by 50,000), full, and ill-conditioned. Instead, we use the conjugate-gradient method described by Mackie and Madden (1993, pp. 215–219) to give a stable, approximate solution to this linear system. The details will not be repeated here, but note that the solution does not require the calculation of the full sensitivity matrix, only the calculation of the sensitivity matrix and its transpose multiplied by a vector.

Our routine differs from that of Mackie and Madden in three ways. First, we use a method similar to that described by Rodi (1976, pp. 483–506) to calculate $\underline{\mathbf{A}}^{\mathrm{T}}\mathbf{u}$ and $\underline{\mathbf{A}}\mathbf{v}$ where **u** and **v** are vectors. Since we calculate a forward model for every electrode, this method does not require any additional forward solutions during the conjugate gradient iterations. Second, we use more conjugate gradient iterations than Mackie and Madden (1993). For the magnetotelluric inverse problem, Mackie and Madden found that the nonlinear inversion routine converged well with three conjugate gradient iterations. We usually require between 10 and 40 conjugate gradient iterations to achieve adequate convergence. Third, we use smoothness instead of comparison with an a-priori model to stabilize the inverse solution.

We found that choosing the correct value of α is critical for both achieving rapid convergence of the nonlinear inversion and for finding a good final parameter estimate. With our method, a new value of α is estimated at the end of each nonlinear iteration. The estimate uses the assumption that the relation between χ^2 and α can be approximated by the rational function:

$$\chi^2 \cong \frac{b\,\alpha}{\alpha + a}\,. \qquad \text{(Eq. 39)}$$

The constant a is estimated from the values of α and χ^2 of the previous iteration. If the misfit is χ^2_k and the desired misfit is χ^2_{target}, then the new estimate of α, α_{k+1}, is:

$$\alpha_{k+1} = \frac{\dfrac{b}{\chi^2_k} - 1}{\dfrac{b}{\chi^2_{\text{target}}} - 1}\alpha_k. \qquad \text{(Eq. 40)}$$

The value of χ^2_{target} is chosen as the larger of $\chi^2_{\text{a-priori}}$ and $0.5\chi^2_k$.

Although the approach is simplistic, it usually converges to the correct value of χ^2 in 10 to 20 iterations.

6.8.4.2.5 Electrical-Resistance Tomography Data-Collection and Processing Codes

Computer codes are used for both data collection and processing/presentation. Figure 51 contains a block diagram flow chart summarizing these codes and a description of how they are used.

6.8.4.2.6 Electrical-Resistance Tomography Data-Collection System

As shown in the block diagram of Figure 52, the data-collection system is composed of three main parts: a transmitter, a receiver, and a laptop computer to control the system and archive the data. The action of the system can be described briefly, as follows. The computer sets the switches in the MX-30 multiplexer according to a predefined schedule so as to connect the transmitter to a particular electrode pair and the receiver channels in the GDP-32 receiver to other sets of electrode pairs. The GDP-32 tells the ZT-30 to apply current to the transmitter pair and measures the resulting potentials at the other pairs. The data are then sent back to the computer and stored. A new transmitter pair is selected according to the schedule, and the process begins again until all the combinations in the schedule have been used.

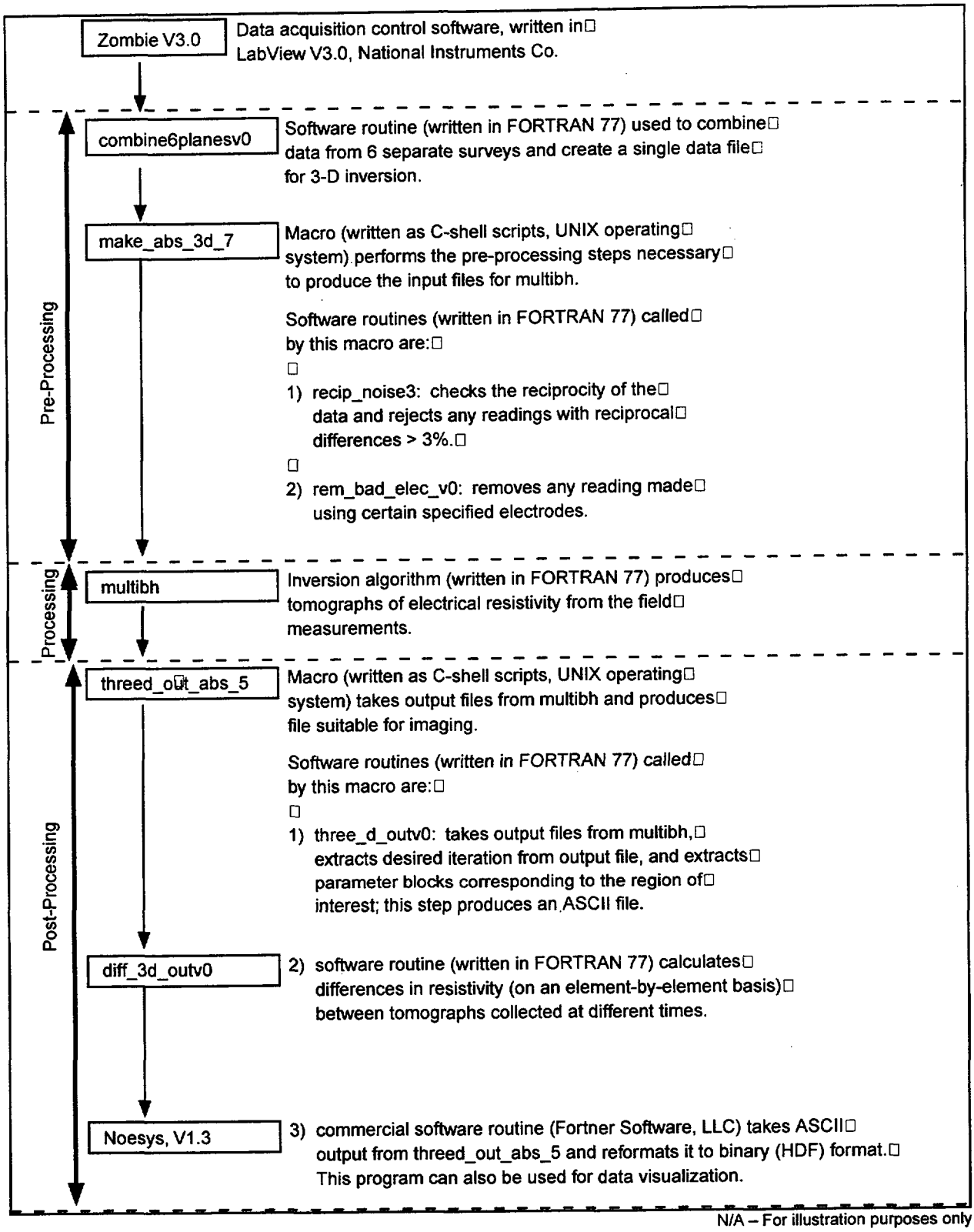

N/A – For illustration purposes only

Figure 51. Flow Chart of Computer Codes Used for Electrical-Resistance Tomography Data Collection and Processing at Busted Butte

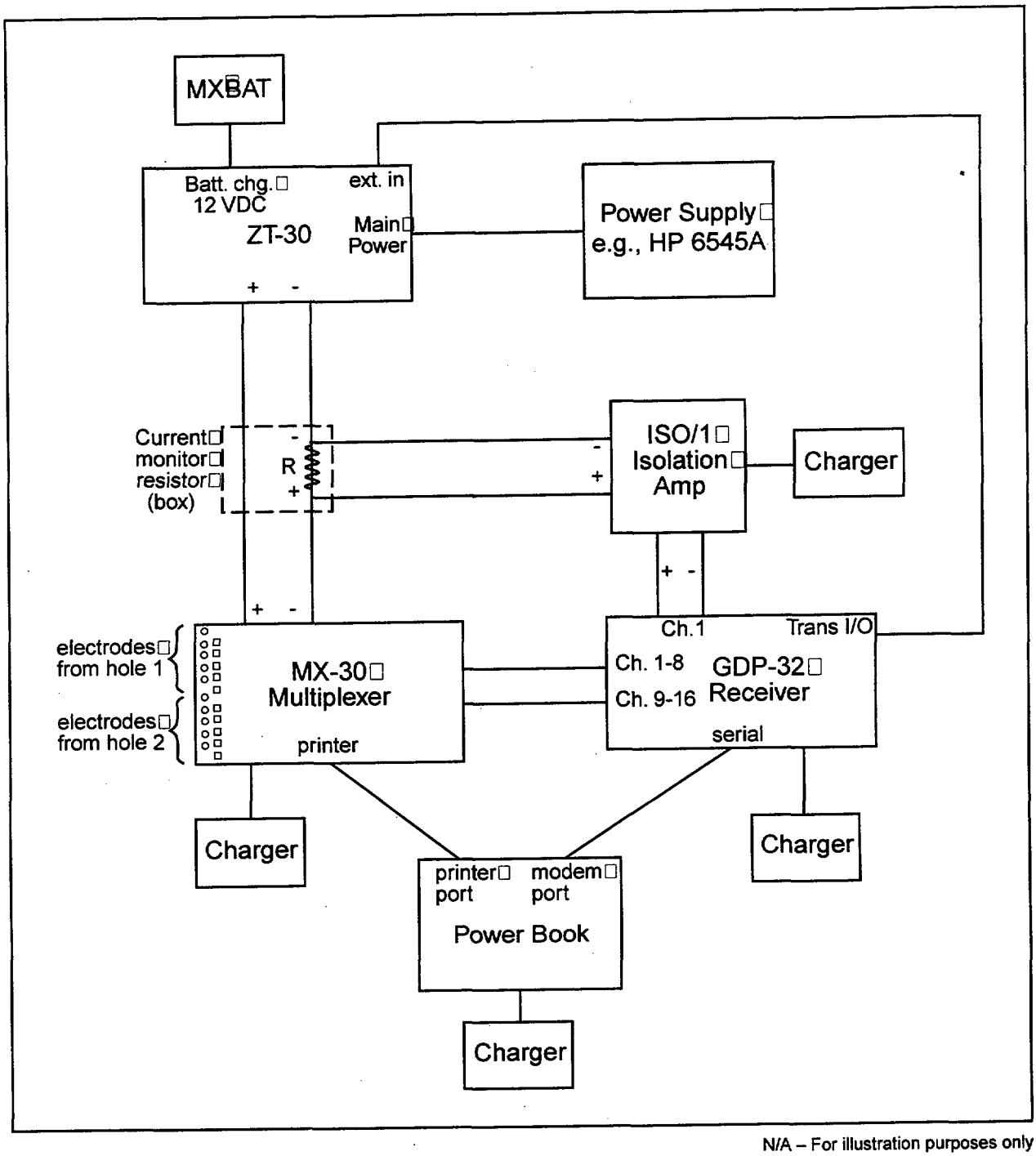

N/A – For illustration purposes only

NOTE: This block diagram illustrates the ERT data-collection system used at Busted Butte.

Figure 52. Electrical-Resistance Tomography Data-Collection System

6.8.4.2.7 Results of Data Collections—July to Early September

ERT data were collected four times: July 2, July 14, August 19, and September 9, 1998. The intent was to make comparisons between the baseline condition on July 2 and data collected at later times. Comparisons between July 2 and August 19 and between July 2 and September 9 are presented because the data from July 14 were of questionable quality. These data have been submitted to the YMP Technical Data Management System (DTN: LL990612704244.098).

Sixty ERT electrodes were installed in the test block as shown in Figure 53. The electrodes were placed in six drilled holes, ERT-1 though ERT-6, and two surface arrays (upper and lower). Holes ERT-3, 4, 5, and 6 and the surface arrays were drilled perpendicular to and from the instrumentation alcove. Holes ERT-1 and 2 were drilled from the main drift. The electrodes were grouped into boreholes 1 through 4 as shown in Figure 54. As is evident, each borehole is L-shaped and contains 15 electrodes. For example, borehole 1 is composed of the 8 electrodes in hole ERT-3 along with the 7 electrodes in the upper-surface array.

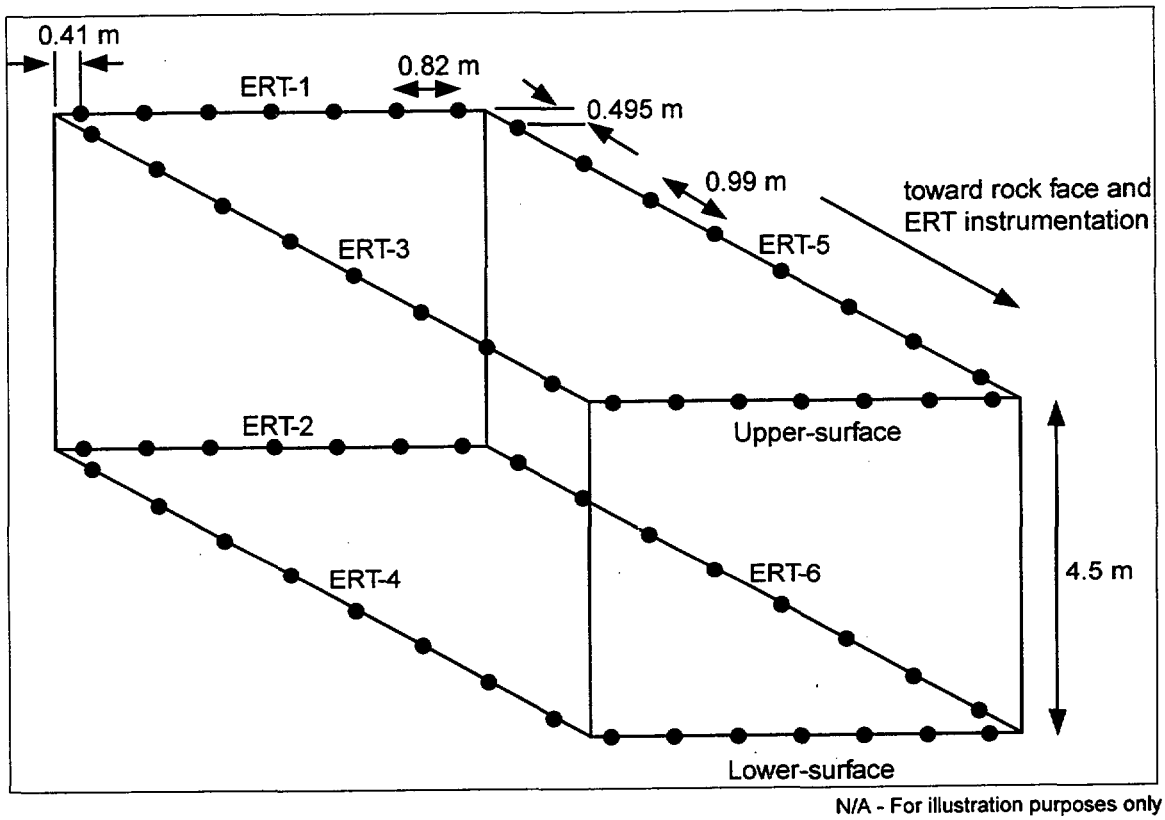

N/A - For illustration purposes only

NOTE: This diagram gives the layout of drilled holes, ERT electrode locations, and spacing in the UZTT test block at Busted Butte.

Figure 53. Electrical-Resistance Tomography Layout

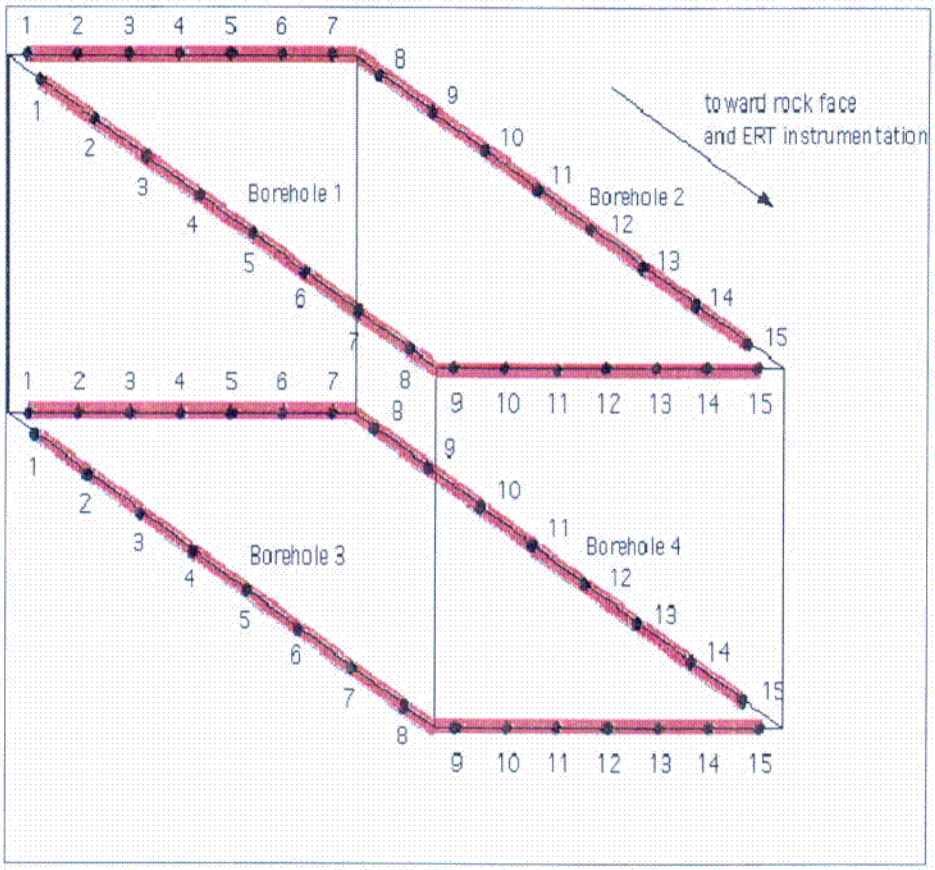

N/A – For illustration purposes only

NOTE: This diagram gives the layout of the ERT boreholes and electrode assignments in the UZTT test block at Busted Butte.

Figure 54. Electrical-Resistance Tomography Electrode Assignments

The ERT data are collected between borehole pairs. Thus, the data are collected between boreholes 1 and 2 (upper horizontal plane), 3 and 4 (lower horizontal plane), 1 and 3 (left vertical plane), 2 and 4 (right vertical plane), 1 and 4 (diagonal), and finally 2 and 3 (diagonal) for a total of six data sets. The total number of data values collected is 2430. These 2430 values provide the 3-D sampling of the test block resistivity, and the 3-D inversion algorithm operates on these data to produce a reconstruction of the 3-D resistivity distribution, a 3-D ERT image, of the block.

One could look at absolute ERT images or comparison images. It is most useful to look at comparison images when changes are taking place over time. The results presented here consider difference images that compare the resistivity of the block on August 19 and September 9 to July 2. Because the water injected during Phase 2 of the UZTT experiment was approximately eight times more conductive than the pore water, resistivity decreases in the images are of interest.

C5

6.8.4.2.8 Absolute Electrical-Resistance Tomography Images of the Block

Figure 55 shows an absolute image of the baseline condition of July 2 (top) and the difference between August 19 and July 2 (bottom). The baseline image shows a layered structure consistent with the lithology in the rear half of the block. That is, a high-resistivity layer over most of the middle of the block, Tptpv1, with a lower-resistivity region, Tptpv2, at the top, and a low-resistivity region, Tac, at the bottom. The image also shows an anomalously low resistivity region in the front half of the block, particularly near the bottom.

6.8.4.2.9 Difference Electrical-Resistance Tomography Images of the Block

The difference image of Figure 55 shows regions of resistivity decrease near injection holes 18, 20, and 21, as one would expect from the injection of conductive water. It is apparent that a pronounced resistivity decrease exists in the slice 2.66 m from the front of the block, which could be associated with water moving downward in the block. The region of the block between 1.33 and 4.0 m, which contains this slice, also appears to be a low-resistivity region in the absolute image.

The September 9 to July 2 difference (Figure 56) also shows regions of resistivity decrease near injection holes 18, 20, and 21. The effect is even stronger in the 5.33-m slice. Moreover, the effect of water moving down into the block seems to be more pronounced in the 4.0-m slice compared to August 19.

6.8.4.2.10 Conclusions

The ERT baseline images show a resistivity structure that is consistent with the known lithology in the rear part of the block. There appears to be a low-resistivity region in the front half of the block, particularly near the bottom. This is not well understood and should be confirmed, if possible, by other means.

The difference images from August 19 and September 9 show clear and consistent resistivity decreases in the region near holes 18, 20, and 21 that can be associated with the injection of conductive water. This effect appears to be stronger on September 9 in the 5.33-m slice. The images show very little effect in the region around the other injection holes, 23 and 24 through 27, where far less water was injected.

In addition, the difference images from August 19 and September 9 show resistivity decreases that could be interpreted as water moving down into the block between the 1.33-m and 4.0-m slices. This is the same region that has an anomalously low resistivity in the baseline image.

These results should be considered preliminary and subject to change based on new information, such as borehole radar data and, perhaps, neutron data.

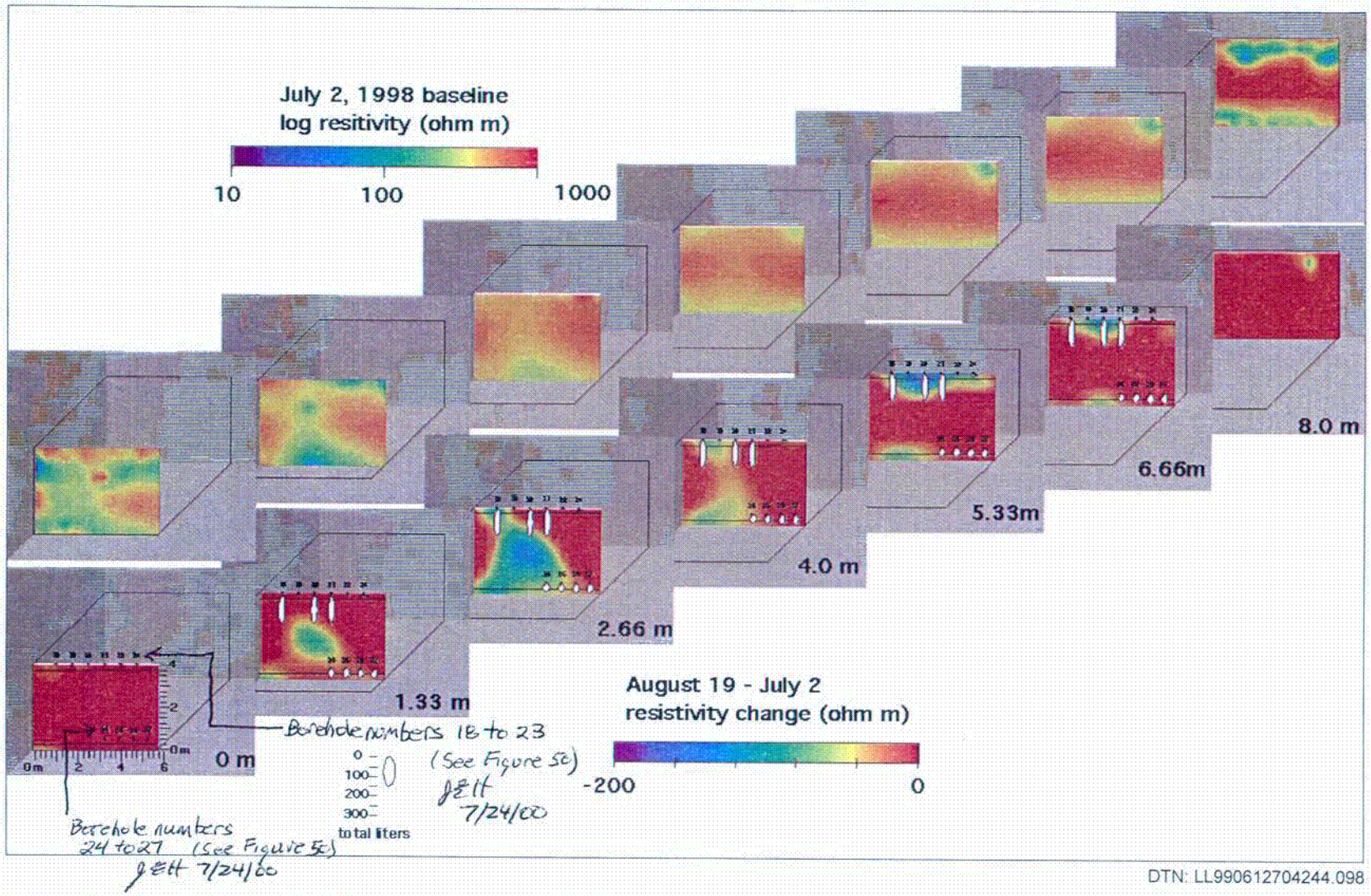

DTN: LL990612704244.098

NOTE: The diagram shows vertical slices through block at 0, 1.33 2.66, 4.0, 5.33,6.66, and 8.0 m. The top series is an absolute image (baseline, July 2), and the bottom series is the August 19–July 2 difference images.

Figure 55. Electrical-Resistance Tomography Images of Test Block Viewed from Test Alcove: Baseline and August Differences

C6

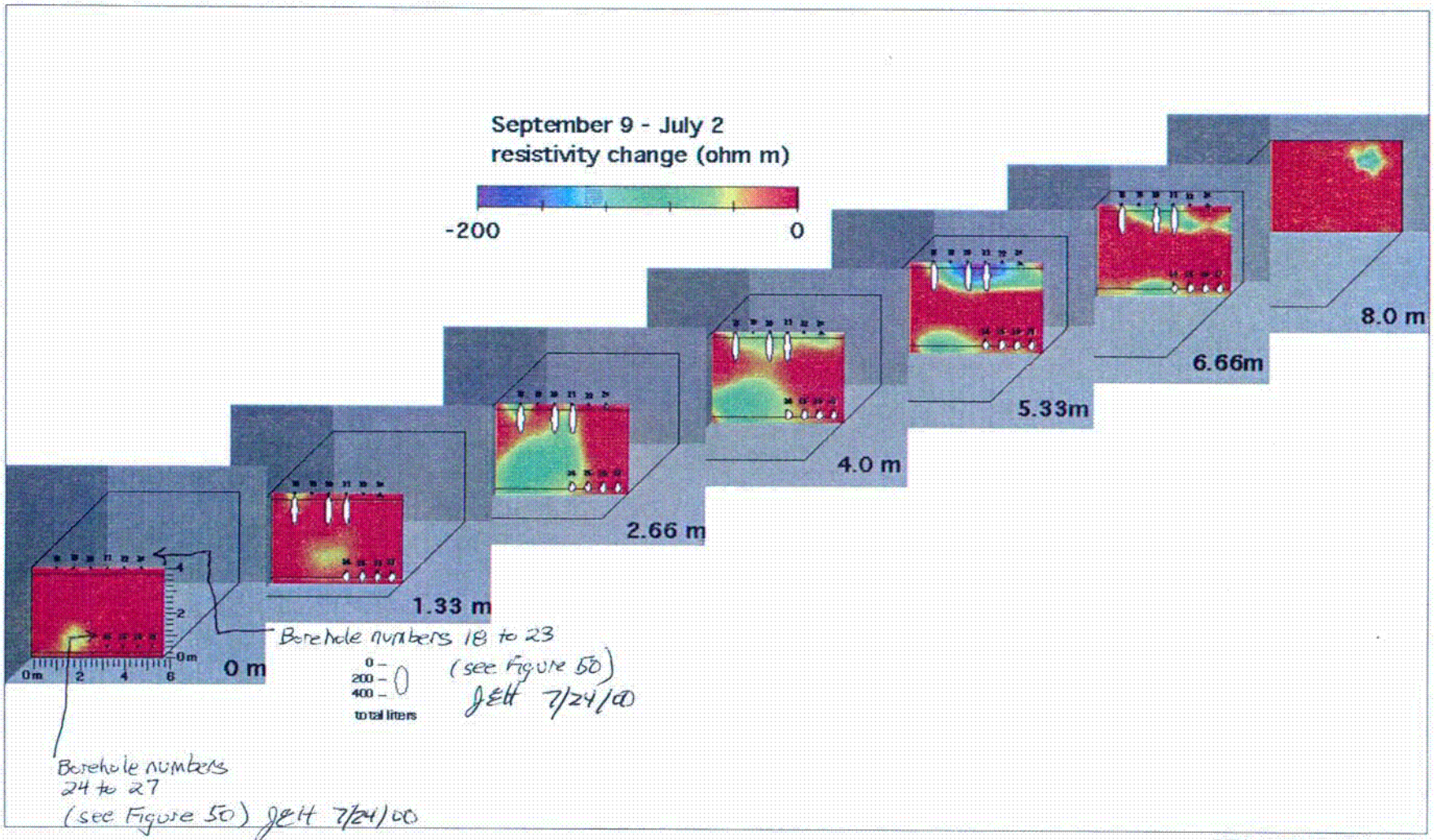

DTN: LL990612704244.098

NOTE: The diagram shows vertical slices through the block at 0, 1.33, 2.66, 4.0, 5.33, 6.66, and 8.0 m that represent September 9–July 2 difference images.

Figure 56. Electrical-Resistance Tomography Images of Test Block Viewed from Test Alcove: September Differences

C7

6.8.5 Geochemistry and Tracer Migration - Laboratory and Field Tests

This section discusses all aspects of chemical and geochemical measurements that have been conducted in association with the Busted Butte project. These include laboratory measurements of sorption of both radionuclides and tracers onto Busted Butte rock samples, measurements of in-situ pore-water chemistry used in formulating the field tracer mixture, and measurements of field-scale tracer transport.

6.8.5.1 Laboratory Sorption Studies

As discussed in Section 6.8.2.4, analog conservative and reactive tracers are used as surrogates for radionuclides. To validate the use of these tracers and the site-scale use of the minimum-K_d approach for sorption and the processes of matrix diffusion and colloid migration, a series of laboratory batch-sorption studies have been conducted. Preliminary tracer sorption studies used in tracer selection are complete, detailed radionuclide sorption studies are complete, and detailed tracer sorption studies are in progress. Each type of study will be discussed in turn.

6.8.5.1.1 Preliminary Studies

A large number of possible tracers were proposed in the Busted Butte work plan. Final determination of tracer selection and concentration was dependent on both rock and pore-water characteristics. Rock and pore-water samples became available in early 1998, and a set of fast-turnaround batch studies and geochemical modeling efforts were initiated.

Preliminary batch-sorption studies were conducted using proposed reactive tracers and two rock samples from the Main Adit at Busted Butte. Tracers tested included lithium, manganese, cobalt, nickel, molybdate, and perrhenate (this list differs from the final list of tracers used in the field and described in section 6.8.2.4.1 and 6.8.2.4.2); rocks were samples of the Calico Hills (Tac) and Topopah Spring (Tptpv2) from Phase-1 boreholes 4 and 7. The results of the preliminary sorption studies for lithium, manganese, cobalt, and nickel are presented in Table 26. The results indicate that the Tac sample sorbed the metals more strongly than the Tptpv2 sample and that, on both samples, the metals showed a consistent sequence of sorption: Li << Mn << Ni < Co. Based on these results, all four of these metals show significant sorption and may be useful reactive tracers in the field. Neither of the proposed pertechnetate analogues (molybdate and perrhenate) displayed any significant sorption and were, therefore, eliminated from further consideration in our testing.

Table 26. Preliminary Measured Sorption Coefficients

Rock sample	Measured K_d (mL g^{-1})			
	Li	Mn	Co	Ni
Tac (Phase 1, borehole 4)	≤ 1	16	38	34
Tptpv2 (Phase 1, borehole 7)	≤ 1	6	14	13

DTN: LA9909WS831372.011

6.8.5.1.2 Detailed Studies

6.8.5.1.2.1 Sample Description

Three core samples were selected for detailed sorption and mineralogic characterization. These samples are described in Table 27. These rock samples were uniformly ground, sieved, and homogenized, and subsamples were used for radionuclide sorption, tracer sorption, and quantitative x-ray diffraction studies (QXRD).

Table 27. Sorption Mineralogy Samples

Sample Source	Sample Name	Short Name	Geologic Unit
Phase 1A, borehole 3	UZTT-BB-PH1-3	PH1-3	Tptpv1
Phase 1A, borehole 4	UZTT-BB-PH1-4	PH1-4	Tac
Phase 1B, borehole 7	UZTT-BB-PH1-7	PH1-7	Tptpv2

NOTE: Borehole locations and lithology are from Figures 37 and 38.

6.8.5.1.2.2 Radionuclide Sorption

The sorption of Np, Pu, and Am to the three Busted Butte rock samples was measured at five different concentration levels; each measurement was conducted in duplicate. The radionuclide sorption studies were completed in fiscal year 1999, and the results are summarized in Table 28.

Table 28. Summary of Radionuclide Sorption Results

Sample	Approximate Average K_d (mL g^{-1})		
	Np	Am	Pu
PH1-3	0.3	380	19
PH1-4	1.4	470	2500
PH1-7	1.1	460	1100

DTN: LA0004WS831372.002

6.8.5.1.2.3 Tracer Sorption

Laboratory batch measurements of the sorption of the field tracers onto the same three rock samples were begun in fiscal year 1999. The laboratory procedures and the chemical analysis of the sorption supernatant are underway.

6.8.5.1.2.4 Quantitative X-ray Diffraction

QXRD analysis have been obtained for subsamples of the same three rock samples (DTN: LA9910WS831372.009).

6.8.5.2 In-Situ Pore-Water Chemistry

Field-scale transport behavior is primarily a function of the ambient flow field and the interactions between the geologic host and the material being transported. Secondary influences include details of the pore-water chemistry, including pH, Eh, ionic strength, and chemical composition. Changes in any of these variables may affect solute sorption behavior and colloid stability and may lead to dissolution or precipitation of minerals resulting in permeability changes. These considerations lead to a fundamental conflict in field-tracer studies. Alteration of the in-situ water chemistry should be limited to minimize the artificial perturbations introduced by chemistry variations. Introduction of any artificial tracer will inherently alter water chemistry. (One exception might be the use of miniscule amounts of isotopic tracers—not a practical alternative at this phase of the Busted Butte studies.)

The plan at Busted Butte was to introduce artificial tracers in a matrix designed to mimic natural pore-water chemistry as closely as practical, acknowledging that some alterations were inevitable. Accordingly, pore-water samples from rock cores collected in the Adit were analyzed, a recipe for "synthetic" Busted Butte water that closely resembled the in-situ chemistry was developed, and this synthetic water was used as our injection matrix. Results of the chemical analyses are presented here, and details of the synthetic water recipe are presented in Section 6.8.2.4.3.

A set of rock samples were collected in the Test Alcove on January 30, 1998. These samples were collected from the Tac horizon by hand augering and immediately sealed. A series of samples were collected in sequence, starting with sample 3A at the Adit wall, extending to Sample 3U, 1.93 m away from the tunnel into the wall.

Pore water was extracted from a subset of these samples by ultracentrifugation. Gravimetric moisture contents of the rock samples were determined by weight difference upon drying, and the chemical composition of the extracted pore water was determined using standard ion chromatography (IC) and inductively coupled-plasma/atomic-emission spectrometry (ICP/AES). Full results are presented in Table 29. Note that the IC analyses involve a bicarbonate buffer and, thus, no direct measurement of bicarbonate is possible. The bicarbonate concentrations listed in Table 29 are estimated by charge balance.

The results in Table 29 show that the pore water is a mixed-ion water (Ca-Na-HCO_3-SO_4) with an average total dissolved solids (TDS) of approximately 200 mg L^{-1}. Compared to more typical groundwater compositions, the pore water shows high nitrate (probably due to soil biological activity) and high silica (due to relatively rapid equilibration with amorphous silica in the tuff). Sample 3B, from near the Adit wall, differs somewhat from the other samples, perhaps due to the influence of construction water and atmospheric CO_2 levels. The compositions of the other three pore-water samples were averaged (as shown in the table), and these average values were used to develop the synthetic pore-water recipe presented in Section 6.8.2.4.3.

Also listed in Table 29 are pH values measured on extracted pore water. Despite obvious opportunities for pH alteration due to CO_2 exchange during sample collection, extraction, and analysis, these pH values were the best available at the time of Phase-1 planning. Thus, Phase-1

tracer mixtures were pH-adjusted to a value of 8.4 ± 0.1. During Phase-2 installation, attempts were made to measure pH in situ by inserting pH paper into boreholes for a few days. Results were mixed but seemed to indicate lower in-situ pH values than those measured in the laboratory (consistent with degassing of excess soil CO_2 before lab analysis). Accordingly, Phase-2 tracer mixtures were pH adjusted to a value of 7.0 ± 0.1.

Table 29. Chemical Composition of Busted Butte Pore Water with J-13 Groundwater for Comparison

Constituent	Concentrations (mg L^{-1})					
	Sample 3B	Sample 3N	Sample 3Q	Sample 3U	Average 3N – 3U	J-13 water
Br	0.06	0.07	0.06	0.06	0.06	—
Ca	17.73	24.35	21.16	19.81	21.77	12.5
Ce	< 0.5	< 0.5	< 0.5	< 0.5	< 0.6	—
Cl	16.13	19.06	17.71	16.74	17.84	6.5
Co	< 1.0	< 1.0	< 1.0	< 1.0	< 1.1	—
F	2.36	1.82	1.85	1.41	1.69	0.53
Fe	< 0.1	< 0.1	< 0.1	< 0.1	< 0.2	< 0.05
HCO_3 (est.)	*33.0*	*52.7*	*45.6*	*40.6*	*46.3*	*137.2*
K	4.14	3.35	3.37	3.44	3.39	4.5
Li	0.11	0.11	0.10	< 0.1	0.10	< 0.1
Mg	3.20	4.13	3.64	3.19	3.66	2.1
Mn	< 0.5	< 0.5	< 0.5	< 0.5	< 0.6	< 0.01
Mo	< 1.0	< 1.0	< 1.0	< 1.0	< 1.1	—
Na	17.67	21.36	19.63	17.89	19.63	44.6
Ni	< 1.0	< 1.0	< 1.0	1.34	1.34	—
NO_3	22.76	26.48	22.62	20.99	23.36	1.3
PO_4	< 0.1	< 0.1	< 0.1	< 0.1	< 0.2	—
Re	< 1.0	< 1.0	< 1.0	< 1.0	< 1.1	—
Si	29.69	31.85	34.10	31.00	32.32	29.6
Sm	< 0.5	< 0.5	< 0.5	< 0.5	< 0.6	—
SO_4	31.29	33.63	31.36	30.08	31.69	18.6
Sr	0.37	0.49	0.42	0.38	0.43	—
TDS	178.5	219.4	201.6	186.9	203.6	257.4
pH	8.20	8.48	8.45	8.28	8.40	7.3–8.4
Gravimetric moisture content:	0.123	0.134	0.158	0.109	0.133	n/a

DTN: LA9909WS831372.015, LA9909WS831372.016, LA9909WS831372.017, LA9909WS831372.018

6.8.5.3 Field-Scale Tracer Transport

6.8.5.3.1 Phase 1A

6.8.5.3.1.1 Description

Phase 1A consisted of four 2-m injection boreholes (boreholes 1–4). The Phase-1A tracer mixture was described in Section 6.8.2.4.1. The tracer mixture was injected at 10 mL hr^{-1} in boreholes 1 and 3, and at 1 mL hr^{-1} in boreholes 2 and 4. Phase-1A injection ran continuously from April 2, 1998, until January 12, 1999. Mineback of the Phase-1A test block began on January 15, 1999, and ended on March 3, 1999. During mineback, as successive layers of the Adit wall were removed, digital photographs under visible and UV illumination were taken, rock samples were collected by augering, and the exposed face was accurately surveyed.

6.8.5.3.1.2 Results

The visualization of the tracer plume using UV illumination of the fluorescein tracer was very successful, and the digital imagery resulting from this effort serves as the primary result of Phase 1A. Detailed comparison of the digital plume imagery and numerical modeling results is underway and will be completed this year.

A small number of augered rock samples have been analyzed for bromide and moisture content (DTN: LA9910WS831372.008). Values from these analyses will be used for re-calibrating the Phase 1A model (Section 6.8.6 discusses the blind modeling results).

6.8.5.3.2 Phase 1B

6.8.5.3.2.1 Description

Phase 1B consisted of two 2-m injection boreholes (5 and 7) and two 2-m collection boreholes (6 and 8). The Phase-1B tracer mixture was described in Section 6.8.2.4.1. The tracer mixture was injected at 10 mL hr^{-1} in borehole 5 and at 1 mL hr^{-1} in borehole 7. Phase-1B injection began on May 12, 1998. Borehole 7 injection was terminated on November 9, 1998, and borehole 5 injection was terminated on November 18, 1998. Throughout the experiment, rock pore-water samples were collected at regular intervals using collection pads installed in boreholes 6 and 8. A total of 558 pad samples were collected and shipped to the laboratory for analysis.

At the conclusion of the experiment, overcoring of the Phase-1B boreholes was conducted as follows: moisture pad collection was conducted on collection hole 8 directly below injection hole 7 until injection shut down of hole 7 on November 9, 1998. Tracer injection and moisture pad collection was continued in holes 5 and 6 while two 10-inch-diameter overcores were drilled approximately tangential to one another with their centerlines in a vertical plane and contained in the area between the top of injection borehole 7 and the bottom of collection borehole 8. When injection hole 5 was shut down, three 10-inch-diameter overcores were drilled approximately tangential to one another with their centerlines in a vertical plane and contained in the area between the top of injection borehole 5 and 10 inches below the bottom of collection borehole 6.

As soon as each of the injection holes was turned off, the injection and collection holes were surveyed as well as video and neutron logged.

6.8.5.3.2.2 Results

There were 176 selected pads extracted for tracers, and the extracts were analyzed by IC, ICP/MS, HPLC, spectrofluorimetry, and epifluorescent microscopy. The extraction/analysis procedure is shown schematically in Figure 57. Also, 883 individual analyses were conducted, and full results were submitted (DTNs: LA9909WS831372.001 and LA9909WS831372.002). Breakthrough of all 5 solute tracers was detected in borehole 6, directly below the 10 mL hr^{-1} injection site in borehole 5. No breakthrough was detected in borehole 8 below the 1 mL hr^{-1} injection site in borehole 7. No clear evidence of microsphere breakthrough was detected in either borehole, but this may be due to analytical difficulties, discussed below in Section 6.8.5.3.5. The borehole-6 breakthrough results are summarized in Figure 58 (a through e), which shows tracer concentration in pad moisture (C) normalized by the theoretical input tracer concentration (C_0) listed in Table 30.

Table 30. Tracer C_0 Values for Phase 1B Injection

Tracer	C_0 (mg/kg)
Lithium	40
Bromide	460
2,6-DFBA (Borehole #5 only)	100
Pyridone	100
Sodium fluorescein	500

Note: Initial chemical concentration calculated from information presented in Section 6.8.2.4.1.

All five tracers shown in Figure 58 give clear evidence of breakthrough by the end of the experiment. All of the figures show peak concentrations at a (horizontal) depth of approximately 130 cm, directly below the injection port in borehole 5; but maximum recovery varies greatly. Bromide and 2,6-DFBA, both anionic supposedly nonreactive tracers, show similar and reasonable breakthrough patterns, with initial breakthrough detected in mid-late June 1998, after approximately 1 month of injection. Both bromide and 2,6-DFBA reached 50% injection concentrations in mid-July, after 2 months of injection. The fluorescein breakthrough pattern is more erratic. In particular, the peak concentration measured is over twice the injected concentration, which is clearly not reasonable. These anomalies probably reflect analytical difficulties associated with the extremely high concentration of fluorescein injected. The high concentration succeeded in improving field visualization of the plumes during mineback and overcore, even though it hurt the laboratory quantification. This analytical problem will be less severe for Phase 2, in which injected fluorescein concentrations are just 1/50 of that used in Phase 1. The later breakthrough and lower detected concentrations of pyridone may also reflect analytical difficulties; if real, they may indicate either sorption or degradation of this supposedly conservative tracer. Ongoing laboratory sorption and degradation studies will provide more information. Finally, although detected lithium concentrations are quite low, their contrast with background levels and their consistent location both in time and space indicate that true lithium

breakthrough was observed in the field. The low and late breakthrough indicate that lithium was sorbed quite significantly. Ongoing numerical analyses will provide quantitative field retardation estimates, which can be compared with lab sorption estimates.

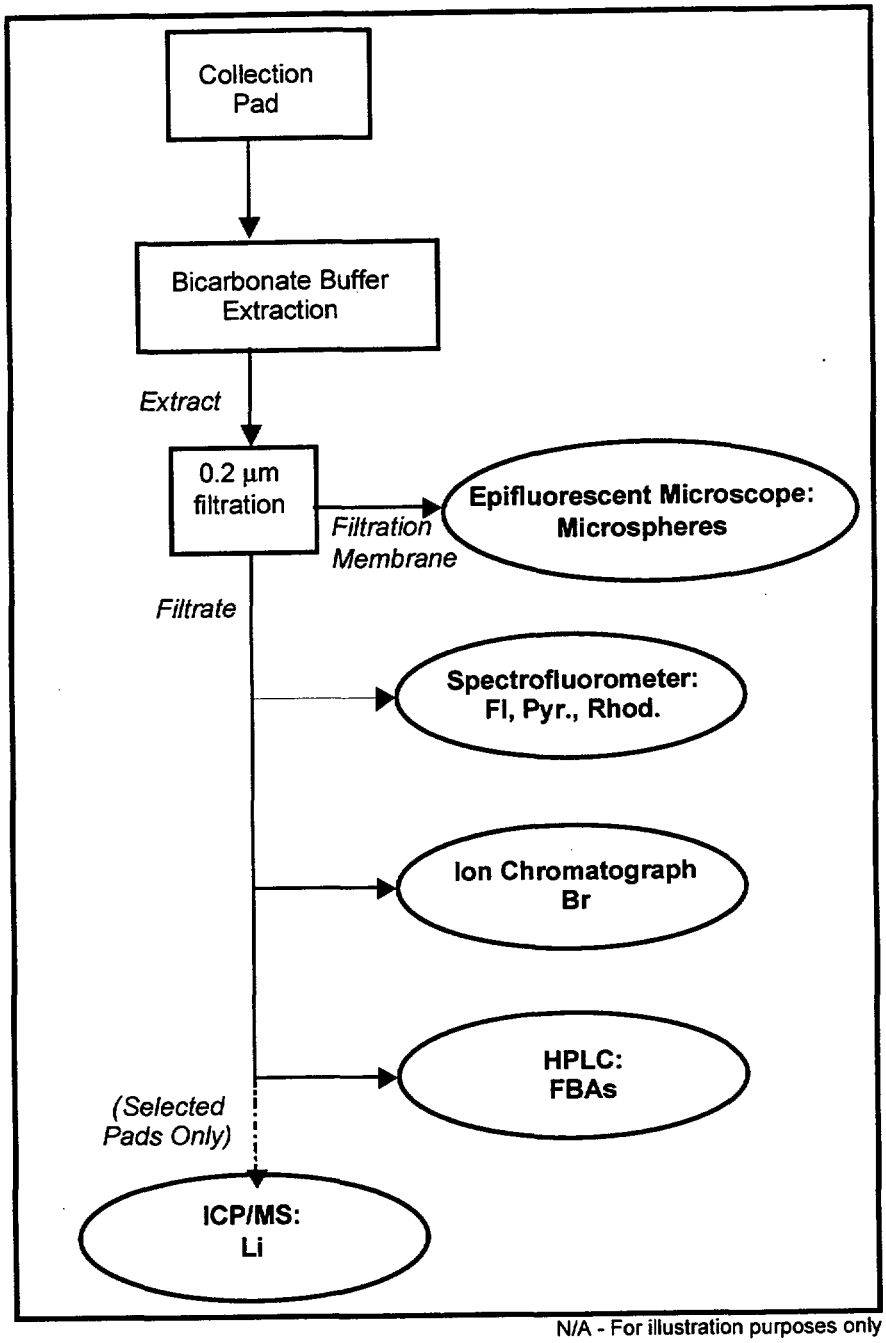

Figure 57. Phase-1B Pad Extraction/Analysis Scheme

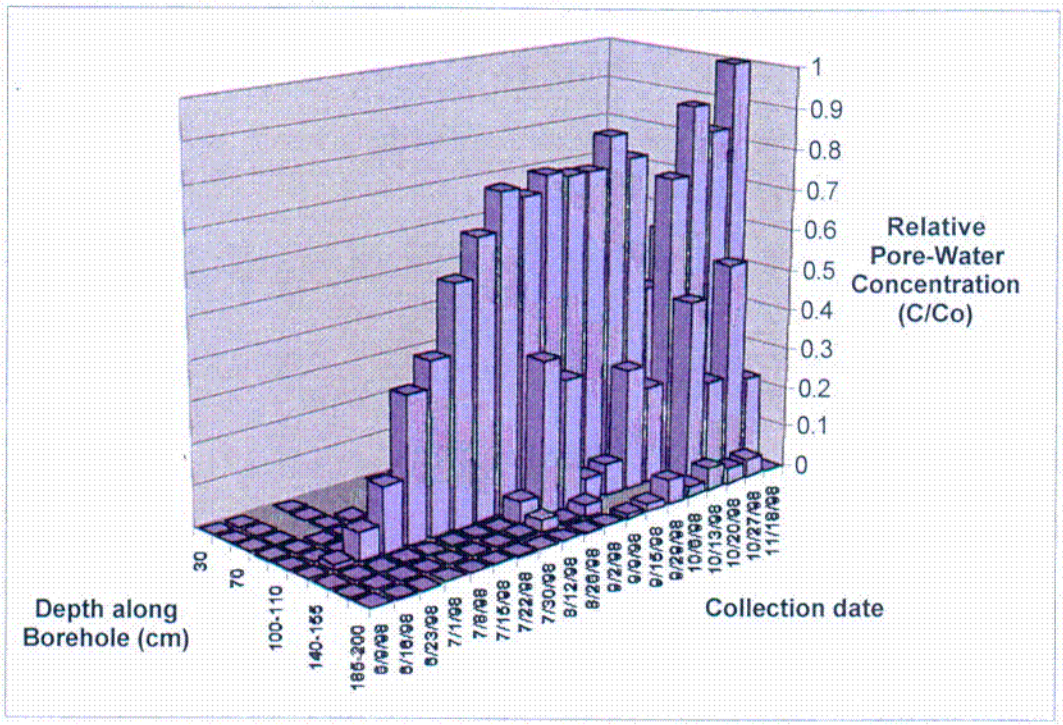

DTN: LA9909WS831372.001; LA9909WS831372.002

Figure 58a. Bromide Concentrations in Borehole 6 for Phase 1B

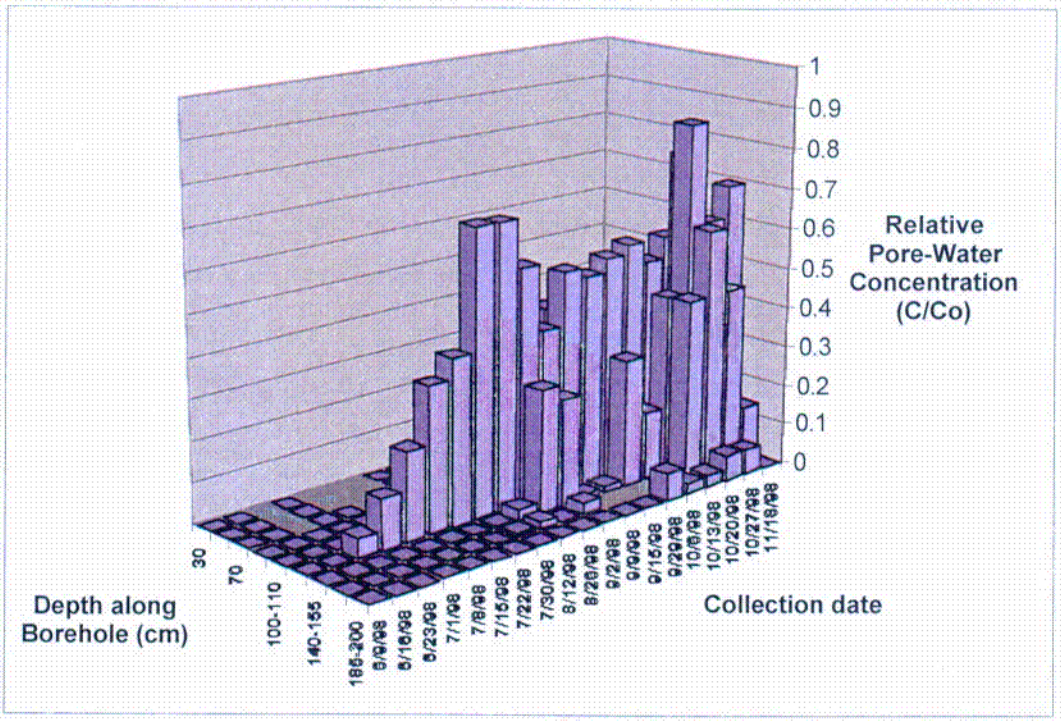

DTN: LA9909WS831372.001; LA9909WS831372.002

Figure 58b. 2,6-DFBA Concentrations in Borehole 6 for Phase 1B

C8

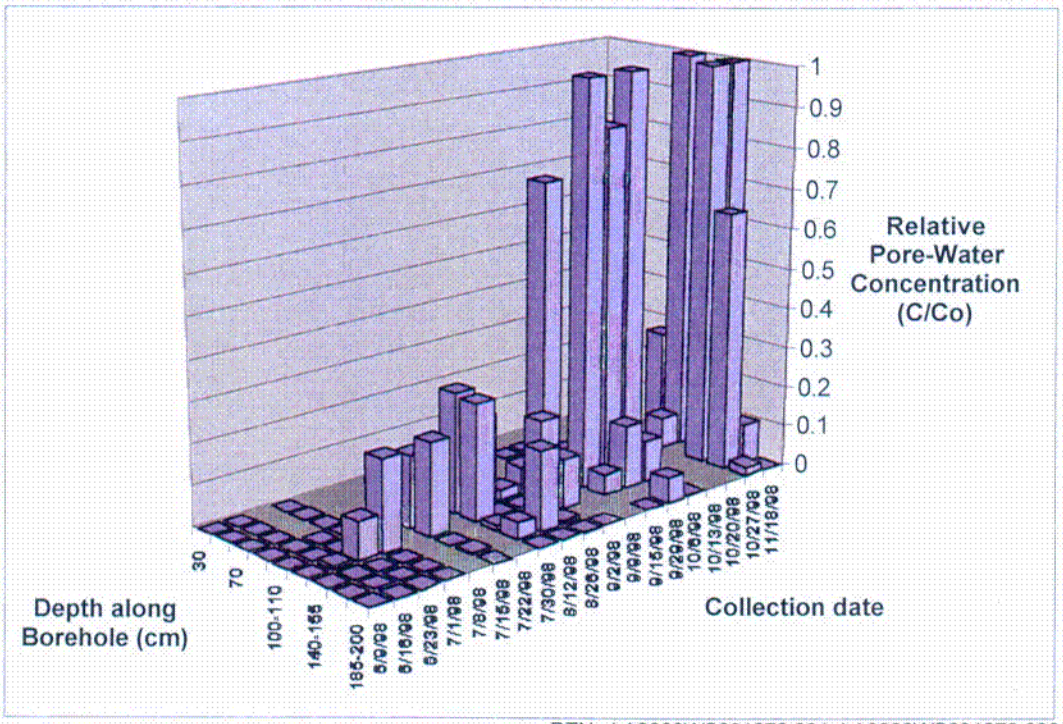

DTN: LA9909WS831372.001; LA9909WS831372.002

Figure 58c. Fluorescein Concentrations in Borehole 6 for Phase 1B

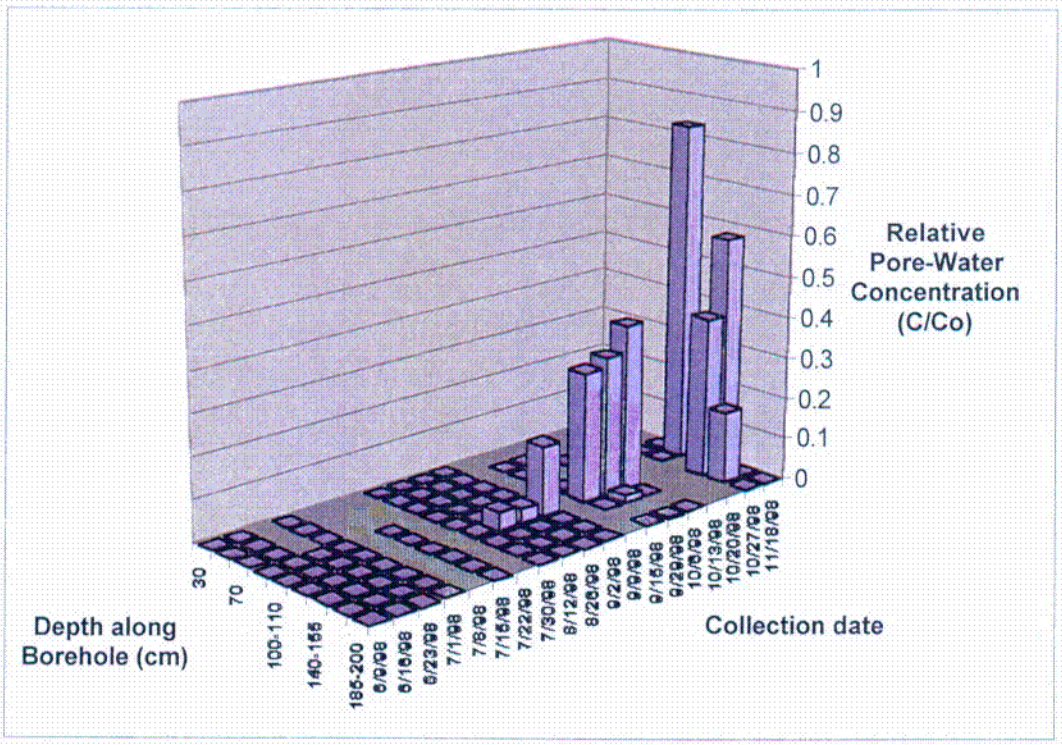

DTN: LA9909WS831372.001; LA9909WS831372.002

Figure 58d. Pyridone Concentrations in Borehole 6 for Phase 1B

C9

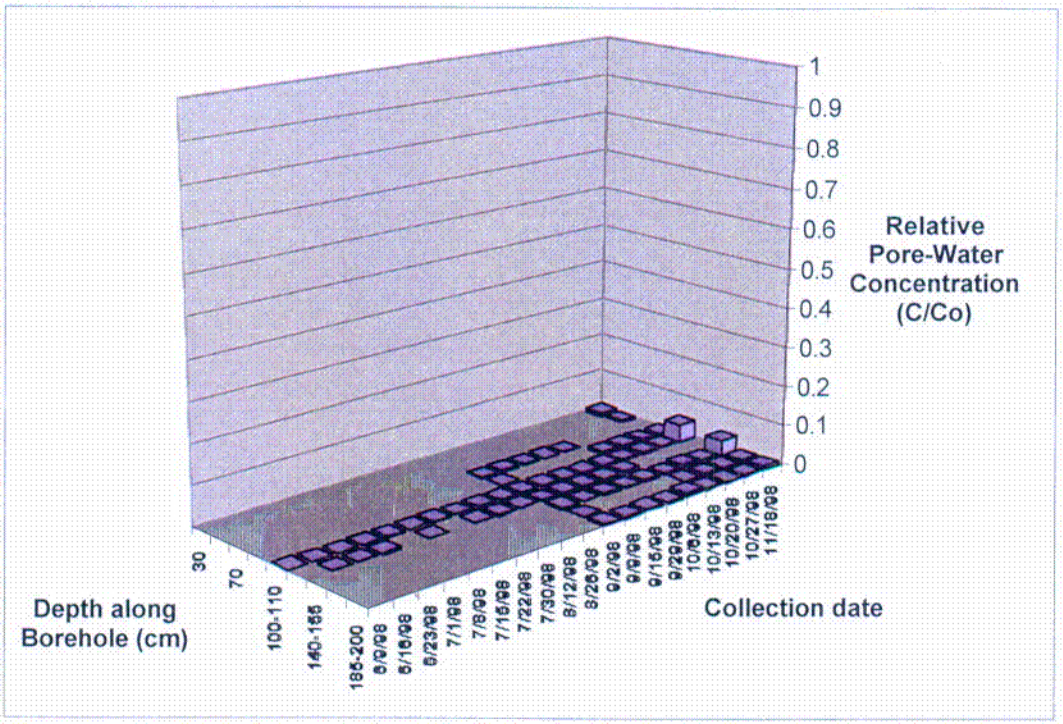

DTN: LA9909WS831372.001; LA9909WS831372.002

Figure 58e. Lithium Concentrations in Borehole 6 for Phase 1B

6.8.5.3.3 Phase 2

6.8.5.3.3.1 Description

Phase 2 involves eight injection boreholes and 12 collection boreholes drilled into the Phase-2 test block from the Test Alcove. The injection boreholes are subdivided into three subphases. Phase 2A consists of a single horizontal borehole (23) in the Tptpv2 horizon. The borehole has 10 injection points, each injecting tracer at 1 mL hr^{-1}. Phase-2A injection began on July 23, 1998, and is ongoing. Phase 2B consists of four parallel horizontal injection boreholes (24, 25, 26, and 27) in the Tac horizon. Each borehole is fitted with 10 injection points flowing at 10 mL hr^{-1}. Phase-2B injection began on July 30, 1998, and is ongoing. Phase 2C consists of three parallel horizontal injection boreholes (18, 20, and 21) coplanar with the Phase-2A borehole in the Tptpv2 horizon. Each borehole is equipped with 9 injection points flowing at 50 mL hr^{-1}. Phase-2C injection was initiated on August 5, 1998, and is ongoing. Details on the tracer mixtures for each borehole are presented in Section 6.8.2.4.2.

The 12 collection boreholes were drilled into the Phase-2 test block from the Main Adit and are, thus, perpendicular to the injection boreholes. Ten of the collection boreholes are horizontal, whereas the two deepest boreholes (11 and 47) are dipping downward beneath the block. The collection boreholes are arranged to allow interception of the tracer plumes after varying travel distances. Figure 59 is a schematic layout of the collection boreholes.

C10

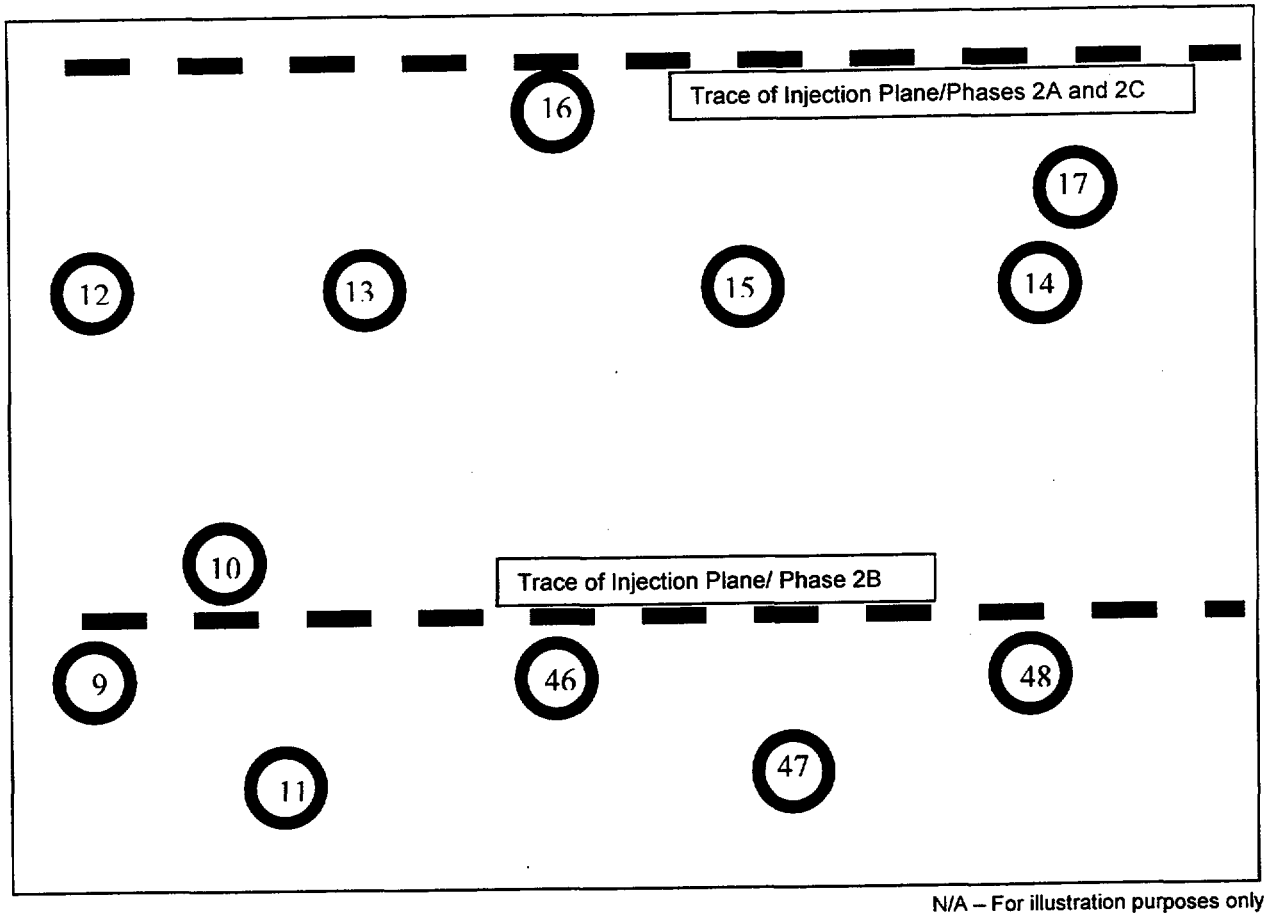

N/A – For illustration purposes only

Figure 59. Schematic Layout of Phase-2 Collection Boreholes (not to scale)

6.8.5.3.3.2 Status

Between the initiation of Phase-2 activities and September 21, 1999, a total of 9,188 sampling pads have been collected. Of these, over 2,200 have been extracted for the Phase-2 extraction/ analysis scheme, shown in Figure 60. Over 10,000 individual analyses have been conducted by the various instrument laboratories shown in Figure 59, and more are being received on a day-to-day basis. The results will help guide decisions on the future course of the field test and will be reported in future revisions of YMP documents.

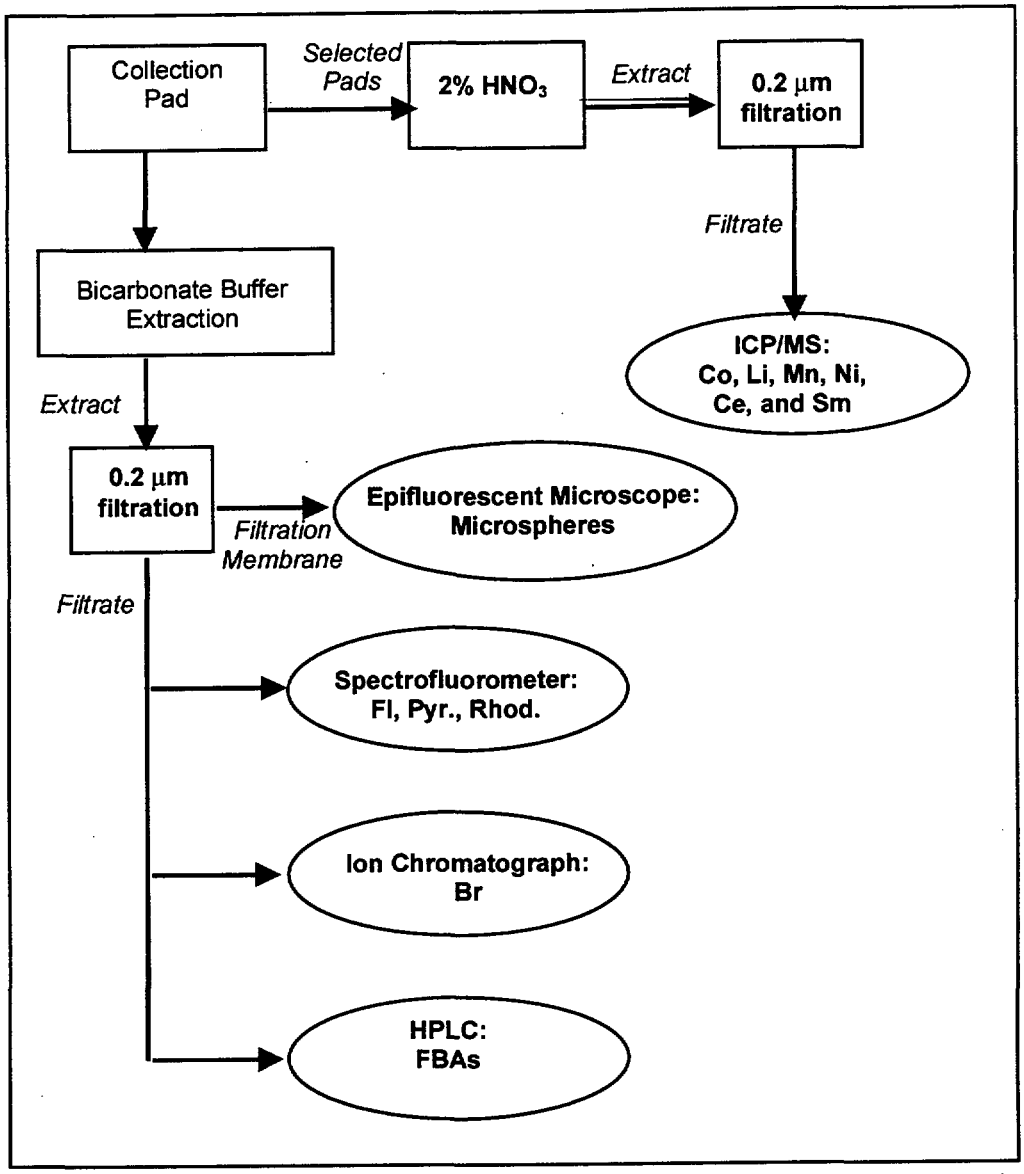

N/A – For illustration purposes only

Figure 60. Phase-2 Pad Extraction/Analysis Scheme

6.8.5.4 Special Topic—Microsphere Measurements

Fluorescent polystyrene microspheres were injected in both Phase-1 and Phase-2 tracer solutions. Two sizes of microspheres have been used at Busted Butte: 0.3-µm-diameter nile red spheres, and 1.0-µm-diameter blue spheres (these are nominal diameters; actual measurements are detailed in DTN: LA9909WS831372.014). Stock microsphere suspensions were prepared by taking aliquots of commercially produced microsphere latex (colloidal suspension) and diluting them with deionized water to give approximately 10^9 to 10^{10} nile red particles per mL and 10^8 to 10^9 blue particles per mL (the higher concentration of particles was used for Phase 1; the lower concentration for Phase 2).

Stock microsphere suspensions are then added in sufficient amounts to tracer solutions to further reduce the number of microspheres to ~10^6-nile-red particles mL^{-1} for Phase 2 and 10^7-nile-red particles per mL for Phase 1. Concentrations of blue particles for Phase 1 and Phase 2 were ~10^6 and ~10^5 particles per mL, respectively.

Initial microscopic examination of a few collection pads from both Phase 1 and Phase 2 produced no evidence for microsphere transport; however, subsequent verification studies cast serious doubt on the ability of our simple extraction method to extract microspheres from the pads efficiently and reproducibly. Progress on resolution of this issue will be reported in future YMP documents.

6.8.5.5 Special Topic—Tracer Degradation

One concern that has been raised is the possible biodegradation of some of the tracers on the collection pads during transportation and storage. This concern only applies to the organic tracers (dyes and FBAs); the metals, inorganic anions (bromide and iodide), and polystyrene microspheres are not subject to degradation. Among the organic tracers, FBAs are unlikely to degrade rapidly due to their strong fluorine-carbon bonds; the dyes' primary purpose is field-screening, so degradation, if it occurs, is not particularly damaging to the overall goals of the test. Nevertheless, to address this concern, a long-term tracer biodegradation study was initiated in 1999 and will be concluded in 2000, at which time data and discussion of the potential impacts of tracer degradation will be reported.

6.8.5.6 Forward Efforts

Current plans (as of February 2000) call for continued operation of the Phase-2 field study through at least September 2000. Collection pads from the collection boreholes shown in Figure 59 will continue on a regular basis and the pads will be analyzed for both nonreactive and reactive tracers. Three new collection boreholes will be drilled in the February/March 2000 timeframe; selected rock samples collected during drilling will be analyzed for tracers, collection pad membranes will be installed in the holes, and these new collection boreholes will be added to the ongoing pad collection schedule.

6.8.6 Phase-1A Predictions

6.8.6.1 Deterministic Model

This section reports predictions of the behavior of Phase 1A of the UZTT. The numerical experiments presented here were set up to determine the ability of numerical models to predict actual field response of flow and transport in porous media. These predictions were done previous to any actual experiment data being available. The simulations are intended to provide insight into the quality and extent of the information needed to accurately represent a physical system and to identify physical processes that are not currently adequately represented in numerical models.

Here, parameters from the available Yucca Mountain hydrologic database, as well as initial laboratory values on samples taken from the Busted Butte site are used. At the time of this document, additional data from Phase 1A were just becoming available but not early enough to be incorporated into the modeling work for Rev 00 of this AMR.

The computer code FEHM V2.00 (STN: 10031-2.00-00) is used in the development of the predictions presented here. FEHM is a multidimensional, multiphase, unsaturated and saturated, transient, finite-element code and is used by YMP for radionuclide migration predictions.

6.8.6.1.1 Model Configuration and Parameter Set

In these simulations of Phase 1A, the focus is on the injection of a conservative tracer into the vitric Calico Hills Formation via a single injection point in a borehole. The simulations of the Phase-1A field experiment were run in a model system that approximates the field configuration as closely as possible. The model system was a single borehole with a diameter of 0.10 m embedded in a matrix of tuff in the Tac unit. The domain size for the simulations is 6 m by 6 m by 1.5 m. The borehole extends the full 1.5-m length of the z direction, and gravity acts in the $-x$ direction. The system configuration is shown in Figure 61. Both 2-D and 3-D simulations of the system were run. The 2-D system was a vertical plane, an x-y slice through the injection point at 0.75 m.

The model accurately captured the configuration of the injection pad, as well. The tracer solution is injected through a polypropylene pad located 0.75 m down the length of the borehole. The injection pad resided inside the borehole, centered at $x = 0.0$, $y = 0.05$, $z = 0.75$ (Figure 61). The pad was 0.05-m by 0.05-m polypropylene material, with material parameters shown at the bottom of Table 30. Injection occurred at a single point in the center of the pad, consistent with the actual physical injection system. For Phase 1A, the pad and injection point are located on the side of the borehole, 90° off vertical, as shown in Figure 61.

Simulations were done before having detailed geologic and hydrologic property distributions in three dimensions for the UZTT. The simulation domain used a homogeneous, isotropic, unfractured description of the porous media. However, 3-D effects are likely to become important in representing the test. Therefore, the model is fully three dimensional from the outset to make it possible to capture any of these effects.

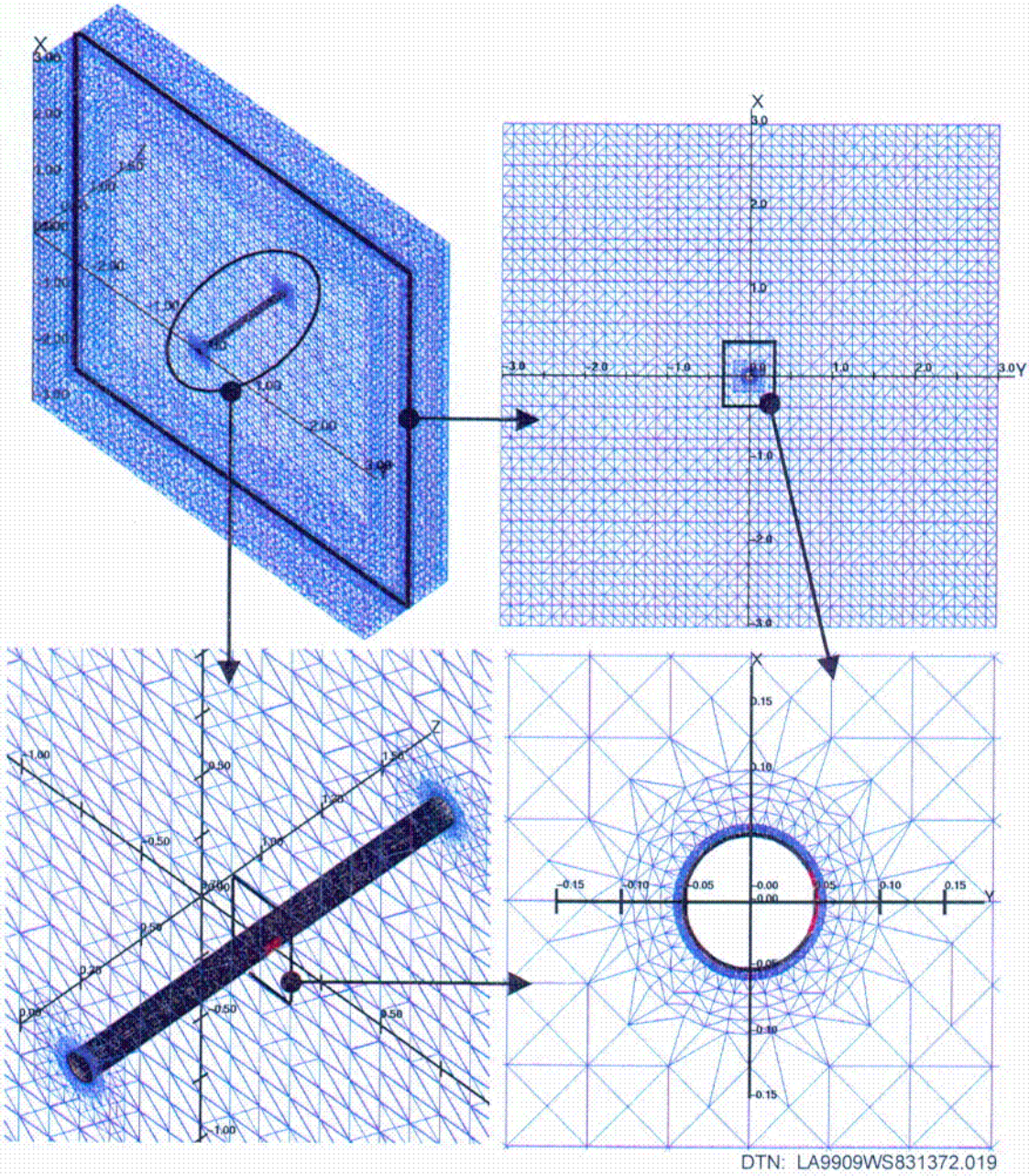

NOTE: LAGRIT-generated computational grid for single-borehole simulations. The grid has 82,000 nodes. The domain is 6 m x 6 m x 1.5 m and includes the porous rock matrix (blue) and the injection pad (red).

Figure 61. Computational Grid for UZTT Single-Borehole Simulations

C11

An 82,000-node, 3-D, unstructured grid represents the single borehole configuration. This grid was generated using the LAGRIT V1.0 (STN: 10212-1.0-00) computer code. It contains the full representation of the injection borehole, the 25-cm^2 injection pad, and 54 m^3 of the surrounding rock mass (Figure 61).

The boundary conditions for the simulation were no flow for the lateral sides ($y = \pm 3$ m) and the front face of the borehole ($z = 0$ m). The exposed face of the rock in the field ($z = 0$ m) has been sealed to minimize evaporative losses resulting from the experimental tunnel. The top and bottom faces ($x = \pm 3$ m) of the model, as well as the back side ($z = 1.5$ m), were held at a fixed capillary pressure. Capillary pressures were chosen to match measured in-situ saturation and capillary-pressure conditions. The use of capillary-pressure boundary conditions provide the most accurate means of capturing the real saturation distribution of the system. Although for a homogeneous rock matrix, capillary pressure can readily be converted to a constant saturation boundary, in a heterogeneous system, the saturation may vary drastically around the boundary, though the capillary pressure is relatively constant. In the vadose zone, the capillary pressure provides a much better representation of the steady-state condition of the system, and measured in-situ saturations can be much better captured by a model.

In the simulations, the influence of a number of model parameters were assessed that can, at best, be only approximately known. These parameters include rock permeability, relative permeability, porosity, and in-situ conditions (saturation). For these simulations, the constitutive relationships (relative permeability versus saturation and capillary pressure versus saturation) are characterized using the van Genuchten curve fit (van Genuchten 1980, pp. 892–898). The van Genuchten method fits the data points of permeability versus saturation measured in the laboratory to a two-parameter function. The two parameters are typically denoted as α and n. The α parameter represents the air entry pressure and is given here in units of m^{-1}. The n parameter controls the slope of the capillary-pressure saturation curve, and is nondimensional.

Tables 31 and 32, respectively, list the different parameter combinations that were run in 2-D and 3-D representations of Phase 1A. The "base case" represents our current best knowledge of the properties and conditions of the system. Using available data from Flint (1998, Figure 3, p. 22-23; Figure 9, p. 30; Figure 10, p. 31; Table 7, p. 44; and Table 8, p. 45) and DTN: LB970601233129.001, a range for each parameter was simulated. Calculations were initiated in January 1998. Since these calculations are only scoping calculations and since a range of values was being used, the exactness of the data is not critical to the results presented here. Note that this situation also applies to data used for Phase-1A Monte Carlo simulations, Section 6.8.6.3, and Phase-2 modeling, Section 6.8.7.

The response of the system to various rates of injection of the tracer fluid was also assessed. Injection rates simulated were 1, 10, and 50 mL hr^{-1}. These injection rates were chosen to span the range of rates being applied in the various UZTT phases.

Table 31. Hydrologic Parameters Used for the 2-D Simulations

Parameter List for 2-D Simulations						
Simulation variable	**Porosity**	**Permeability (m^2)**	**α (m^{-1})**	***n***	**Saturation, *S* (in situ)**	**Inj. rate (mL hr^{-1})**
1. Base Case	0.30	1.3×10^{-12}	0.82	1.31	0.30	10
2. Matrix perm.=0.1x base case perm.	0.30	1.3×10^{-12}	0.82	1.31	0.30	10
3.Matrix perm.=10x base case perm.	0.30	1.3×10^{-12}	0.82	1.31	0.30	10
4. Porosity = 0.20	0.20	1.3×10^{-12}	0.82	1.31	0.30	10
5. Porosity = 0.40	0.40	1.3×10^{-12}	0.82	1.31	0.30	10
6. α low, *n* low	0.30	1.3×10^{-12}	0.60	1.20	0.30	10
7. α high, *n* low	0.30	1.3×10^{-12}	1.20	1.20	0.30	10
8. α low, *n* high	0.30	1.3×10^{-12}	0.60	1.80	0.30	10
9. α high, *n* high	0.30	1.3×10^{-12}	1.20	1.80	0.30	10
10. *In situ S* = 0.2	0.30	1.3×10^{-12}	0.82	1.31	0.20	10
11. *In situ S* = 0.4	0.30	1.3×10^{-12}	0.82	1.31	0.40	10
12. *In situ S* = 0.5	0.30	1.3×10^{-12}	0.82	1.31	0.50	10
13. *In situ S* = 0.6	0.30	1.3×10^{-12}	0.82	1.31	0.60	10
14. *In situ S* = 0.7	0.30	1.3×10^{-12}	0.82	1.31	0.70	10
15. *In situ S* = 0.8	0.30	1.3×10^{-12}	0.82	1.31	0.80	10
16. *In situ S* = 0.9	0.30	1.3×10^{-12}	0.82	1.31	0.90	10
17. *In situ S* = 0.2, Inj = 1	0.30	1.3×10^{-12}	0.82	1.31	0.20	1
18. *In situ S* = 0.3, Inj = 1	0.30	1.3×10^{-12}	0.82	1.31	0.30	1
19. *In situ S* = 0.4, Inj = 1	0.30	1.3×10^{-12}	0.82	1.31	0.40	1
20. *In situ S* = 0.5, Inj = 1	0.30	1.3×10^{-12}	0.82	1.31	0.50	1
21. *In situ S* = 0.6, Inj = 1	0.30	1.3×10^{-12}	0.82	1.31	0.60	1
22. *In situ S* = 0.7, Inj = 1	0.30	1.3×10^{-12}	0.82	1.31	0.70	1
23. *In situ S* = 0.8, Inj = 1	0.30	1.3×10^{-12}	0.82	1.31	0.80	1
24. *In situ S* = 0.9, Inj = 1	0.30	1.3×10^{-12}	0.82	1.31	0.90	1
25. *In situ S* = 0.3, Inj = 50	0.30	1.3×10^{-12}	0.82	1.31	0.30	50
26. *In situ S* = 0.9, Inj = 50	0.30	1.3×10^{-12}	0.82	1.31	0.90	50
Polypropylene pad	0.85	2.2×10^{-11}	17.0	1.12	N/A	N/A

DTN: LA9909WS831372.019

NOTE: [a]The simulation-variable column shows the parameter being varied (tested) in the simulation. Permeability is the intrinsic value (value under saturated conditions). The variables α and *n* are the van Genuchten function parameters taken from laboratory measurements; Inj. stands for injection rate in mL hr^{-1}.

Table 32. Hydrologic Parameters Used for the 3-D Simulations

Parameter List for 3-D Simulations						
Simulation variable	**Porosity**	**Permeability (m^2)**	**α (m^{-1})**	***n***	**Saturation, *S* (in situ)**	**Inj. rate (mL hr^{-1})**
1. Base Case	0.35	1.3×10^{-12}	0.82	1.31	0.35	10
2. Matrix perm.=0.1x base case perm	0.35	1.3×10^{-12}	0.82	1.31	0.35	10
3. Porosity = 0.20	0.20	1.3×10^{-12}	0.82	1.31	0.35	10
4. α high, *n* low	0.35	1.3×10^{-12}	1.20	1.20	0.35	10
5. α high, *n* high	0.35	1.3×10^{-12}	1.20	1.80	0.35	10
6. *In situ S* = 0.2	0.35	1.3×10^{-12}	0.82	1.31	0.20	10
7. *In situ S* = 0.6	0.35	1.3×10^{-12}	0.82	1.31	0.60	10
8. *In situ S* = 0.9	0.35	1.3×10^{-12}	0.82	1.31	0.90	10
9. *In situ S* = 0.2, Inj = 1	0.35	1.3×10^{-12}	0.82	1.31	0.20	1
10. *In situ S* = 0.35, Inj = 1	0.35	1.3×10^{-12}	0.82	1.31	0.35	1
11. *In situ S* = 0.6, Inj = 1	0.35	1.3×10^{-12}	0.82	1.31	0.60	1
12. *In situ S* = 0.9, Inj = 1	0.35	1.3×10^{-12}	0.82	1.31	0.90	1
13. *In situ S* = 0.2, Inj = 50	0.35	1.3×10^{-12}	0.82	1.31	0.20	50
14. *In situ S* = 0.35, Inj = 50	0.35	1.3×10^{-12}	0.82	1.31	0.35	50

DTN: LA9909WS831372.019

NOTE: The simulation-variable column shows the parameter being varied (tested) in the simulation. Permeability is the intrinsic value (value under saturated conditions). The variables α and *n* are the van Genuchten function parameters taken from laboratory measurements; Inj. stands for injection rate in mL hr^{-1}.

6.8.6.1.2 Modeling Results

All simulated concentrations presented in Section 6.8.6 are normalized (C/C_0) concentrations and, as such, are dimensionless.

6.8.6.1.2.1 Overview of Simulations

The large 3-D system size required relatively long simulation times. In an effort to minimize computer time and use the time most effectively, 2-D simulations were run first. These simulations were used as scoping calculations to identify important simulations to run in three dimensions. As shown in the numerical results, the 2-D simulations showed shorter travel distances for the tracer than did the same simulation in 3-D. The differences in tracer movement between 2-D and 3-D simulations at the same effective injection rate are primarily due to the effective volume of injection. The 2-D system is implicitly 1 m in depth, resulting in a lower effective point-injection rate. Therefore, all quantitative predictions are made using values from the 3-D simulations; however, the 2-D simulations can be used to identify the relative response of one set of conditions versus another. The results indicate that trends in the 2-D simulations mirror those in the 3-D simulations.

A series of 2-D simulations (Table 31) were run to identify the relative importance of different parameters and injection scenarios. Figure 62, a graph of concentration versus distance from the borehole center, indicates that this system is relatively insensitive to many of the parameters but is quite sensitive to some. Three-dimensional simulations were then chosen from the parameter sets to which the system was most sensitive; the parameter combinations are listed in Table 32.

The most influential parameter, based on Figure 62, is the value of the van Genuchten power n. Figure 62 shows the two simulations with a high n value dramatically increase concentration at a given distance over the other simulations. The values of both van Genuchten parameters, α and n, for the base case were taken from laboratory measurements made on cores from the Busted Butte site. Available data for the Tac unit were also collected from other sources (GS000408312231.003, GS951108312231.009, GS960808312231.003, GS960808312231.005, GS950408312231.004, GS990408312231.001, GS940508312231.006, GS960808312231.001, GS950608312231.008, LB970601233129.001) to try to capture the uncertainty in these parameters. From these data, high and low reported values of α and n were selected, testing the range of responses for the combinations of those values. The value of n strongly controls the relative influence of capillary forces and gravity forces. Increasing n decreases the capillary forces, resulting in more gravity-driven flow.

Another parameter that clearly influenced the tracer transport was the porosity. Although flow is only slightly affected by even relatively large changes in porosity, transport is more strongly affected. Porosity affects transport because the bulk velocity of the fluid is divided by the porosity to get the pore velocity. Two-dimensional and 3-D simulations were run with porosity increased and decreased by 10% to 15%. The higher porosity did not substantially change the transport, but the lower porosity made an observable difference.

A third factor affecting tracer transport was the injection rate. Prior to starting Phase 1A, simulations were run using different injection rates to help select a rate for Phase 1A that would allow the tracer to move sufficiently far to produce readily measurable distributions but not so far that the tracer could not be fully recovered. Testing multiple injection rates was also intended to help select injection rates for Phase 2. An injection rate of 10 mL hr^{-1} was chosen for Phase 1A. Therefore, the discussion below focuses on simulation results using 10 mL hr^{-1}. Results with other injection rates are presented later, for completeness. These other injection scenarios are also useful for making predictions for Phase 2.

Simulation results are presented as both spatial and time-history concentration profiles. For Phase 1A, however, the concentration distribution between 180 days and 365 days after injection is of most interest. Temporal snapshots are presented for 180 days, as this is the time corresponding to the original mineback and auger schedule for Phase 1A. The mineback was actually delayed until 284 days.

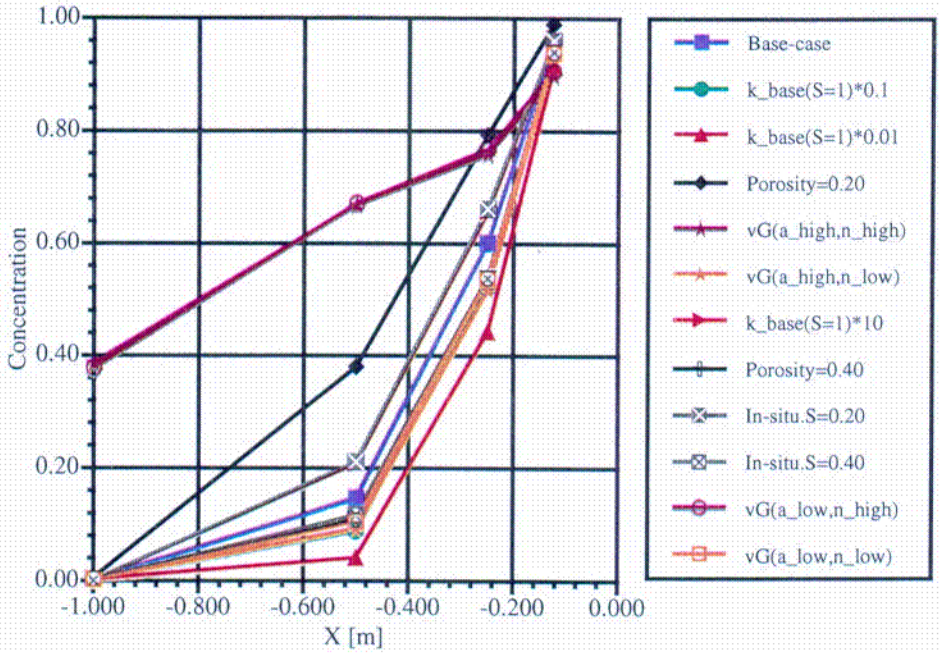

DTN: LA9909WS831372.019

NOTE: Normalized concentration as a function of vertical distance from the injection point for different 2-D sensitivity runs. Parameter values for each case shown in the legend are listed in Table 31.

Figure 62. 2-D Sensitivity Runs

6.8.6.1.2.2 Discussion of Simulations: Base Case

Tables 33 and 34 present the results from the 3-D base-case simulation, against which all other runs were compared. Using the experimental injection rate of 10 mL hr^{-1}, after 180 days, the model predicts tracer transport distances as shown in the Table 32. (In all the simulations discussed in this section, the tracer was injected at a concentration of "1," and cited concentration values are relative to this initial value.)

Measurements from core samples suggested in-situ saturations in the range of 20 to 40%. In the simulations, an initial capillary pressure of 5.6 MPa corresponds to a saturation of 20%, 0.55 MPa corresponds to 35%, and 0.07 MPa corresponds to 60%. Comparing locally measured values and values reported for the Tac unit, the in-situ saturation of approximately 35% most closely represented "reality."

Table 33. Predicted Transport Distances for a Given Concentration

Normalized concentration (C/C_0)	Distance traveled
0.01	0.85 m
0.1	0.67 m
0.25	0.56 m
0.50	0.45 m

DTN: LA9909WS831372.019

C12

The predicted distribution of the tracer is generally uniform in all directions, that is, a spherical distribution (see Figure 62). Changes in saturation from the background (in-situ) level are generally small. Table 34 shows the saturation at different distances from the injection point at 180 days for the base-case simulation. Note that the initial background saturation for this simulation is 35%, based on measured moisture contents of 14.0 ± 2.5% and a porosity of approximately 0.5.

Table 34. Simulation Results at 180 Days

Distance from injection point (m)	Saturation at 180 days
0.125	0.402
0.25	0.381
0.50	0.366
1.00	0.357

DTN: LA9909WS831372.019

The saturation of the system changed only slightly over the 180-day period for the base case. After 180 days, at a distance of 0.125 m below the injection point, the saturation had increased by only 5%, whereas at a distance of 1 m it had increased by only a fraction of a percent (0.7%). The tracer distributes relatively evenly in all directions, centered at the injection point. Some asymmetry is introduced, however, by the presence of the borehole and by injecting 90 degrees off vertical. Water and tracer must move around the borehole to flow in the negative horizontal direction where there is no impedance in the positive horizontal direction. Thus, flow and transport are somewhat asymmetric.

The relatively even distribution of tracer and the lack of increase in saturation near the borehole indicate that this system is dominated by capillary forces over gravitational forces. Gravitationally dominated flows have a much more asymmetric character. These simulations show that a 10-mL hr^{-1} injection rate should not introduce enough water to change the overall flow and transport processes that occur in the undisturbed system.

At 180 days, for the 2-D run, the approximate radius of the tracer at a normalized concentration of 0.01 is 0.75 m and at a concentration of 0.5 is 0.30 m. Normalized concentrations of 0.01 and 0.5 for the 3-D simulation occur, respectively, at 0.85 m and 0.45 m. Figure 63 plots the concentration as a function of distance from the borehole center at 180 days for the 2-D and 3-D systems. In the 3-D simulation, at a distance of 0.125 m, the normalized concentration is almost 1 (0.96), whereas at 1 m the concentration has fallen to 2×10^{-4}.

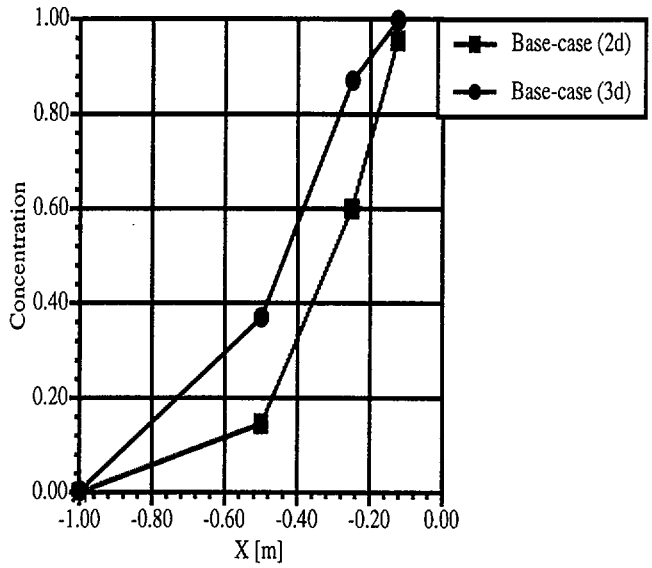

DTN: LA9909WS831372.019

NOTE: The graph shows tracer concentration as a function of vertical distance from the injection point. Although the shapes of the curves are similar, the 2-D system lags the 3-D system by a concentration of approximately 0.20. Parameter values used in these simulations are listed in row 1 of Tables 31 and 32.

Figure 63. Tracer Concentration versus Distance for 2-D and 3-D Simulations

Figure 64 plots the time history of concentration at a vertical distance of 0.125 m, 0.25 m, 0.5 m, and 1m below the center of the borehole for the 3-D simulation. Figure 64 shows that, at 180 days and a distance of 0.125 m, the tracer concentration has almost reached a value of 1.0, whereas at 0.5 m, the concentration is still increasing rapidly.

6.8.6.1.2.3 Discussion of Simulations: Sensitivity Analyses

Knowledge of the actual hydrologic and material properties will always contain some uncertainty. Furthermore, these properties vary somewhat within the hydrogeologic units, as reflected in variations in measured values from different cores. Using stochastic methods, these uncertainties can be incorporated directly into the calculations. Such predictions will be presented in later sections. Within this deterministic modeling approach, an attempt has been made to account for and understand the influence of such uncertainty by assessing the sensitivity of the simulation to various system parameters (Table 32). Figures 65 to 68 compare the results of these simulations. Figure 65 shows the effect of water injection on matrix saturation with time for the different sensitivity runs. Figure 66 plots concentration against distance from the borehole for the 3-D simulations 1 through 6 in Table 32. Figure 67 shows the same information plotted as concentration versus time with each graph plotting a different distance from the borehole. Figure 68 compares the 3-D concentration-versus-time values against those for 2-D.

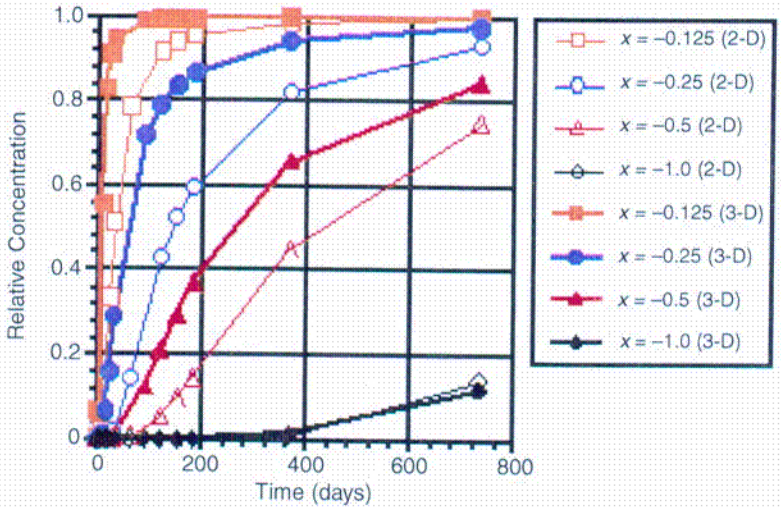

DTN: LA9909WS831372.019

NOTE: The graph shows plots of normalized tracer concentration as a function of time for different vertical distances (x in meters) from the injection point. Curves for both 2-D and 3-D simulations (2d and 3d in legend, respectively) are shown.

Figure 64. Time Profiles of Tracer Concentrations

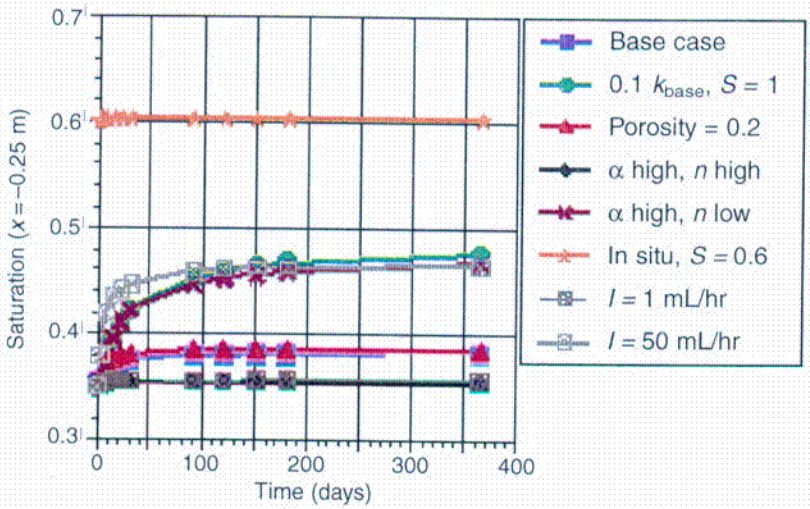

DTN: LA9909WS831372.019

NOTE: The graph shows changes in saturation through time at a distance of 0.25 m from the injection point. Note that in most cases there is little change in saturation over a year. Parameter values for the cases shown in the legend are listed in Table 32 (rows 1, 2, 3, 5, 4, 7, 10, and 14, respectively).

Figure 65. Effect of Water Injection on Matrix Saturation

Figure 65 shows that saturation for the Phase-1A model system is not greatly affected by any of the simulation scenarios. Further, the saturation is not particularly sensitive to many of the parameters. The biggest changes are observed for conditions that increase the relative influence of gravity forces over the otherwise prevailing capillary forces. Both a higher α and the much

C13

higher injection rate produce relatively rapid and readily apparent increases in saturation. Otherwise little change in saturation is observed.

At 180 days, Figure 66 demonstrates that, based on simulated measurements at a distance of 0.25 m from the borehole, it is not likely that actual field measurements at such a distance would be useful for evaluating how well the system characteristics have been captured by the model for a 10 mL hr^{-1} injection rate. At 0.25 m, there is negligible difference in concentrations among the different simulations. At a distance of 0.5 m, however, variations in system characteristics result in a 60% range of concentrations. Figure 66 shows that a system with an order-of-magnitude lower intrinsic permeability k is indistinguishable from one with a value of van Genuchten power n that is at the low end of reported values. Both of these cases are very similar to the base case as well. This fact indicates that transport in this system is not particularly sensitive to the values of k or α; errors in these values are not expected to demonstrably influence the accuracy of predictions in this system.

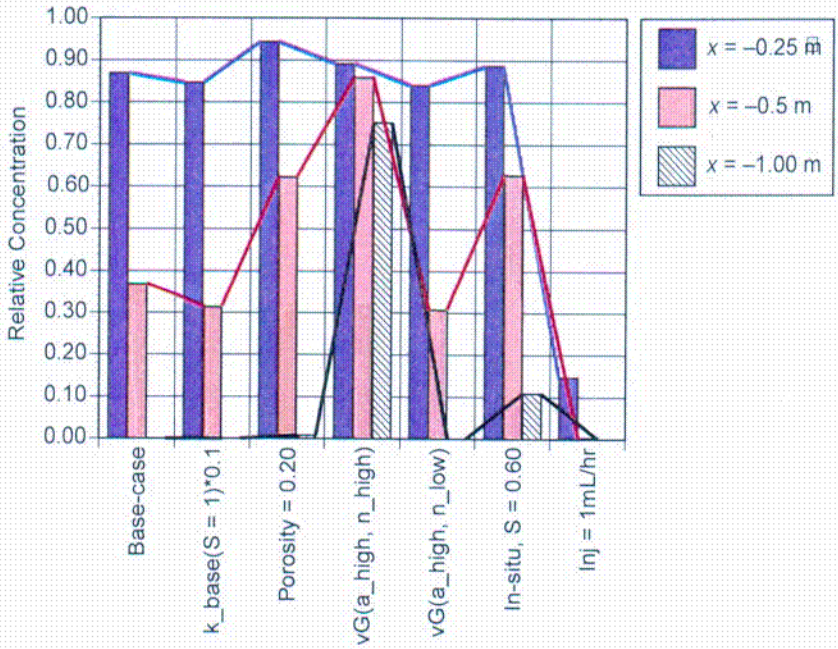

DTN: LA9909WS831372.019

NOTE: The graph shows differences in normalized concentration for different sensitivity runs at three distances (x in meters) from the injection point. The sensitivity to the system parameters is not captured at the smallest distances but is apparent at a distance of 0.5 m. Parameter values for the cases shown along the horizontal axis are listed in Table 32 (rows 1, 2, 3, 5, 4, 7, and 10, respectively).

Figure 66. Tracer Concentration for Different Sensitivity Runs

If the reported porosity is in error by as much as 15% (0.20 instead of 0.35), tracer concentration at 0.5 m and 180 days is expected to be 0.58, which is a difference of 25% from the base value. By 365 days, as seen in Figure 67, the difference in concentration has decreased somewhat but is still a substantial 10%. At shorter distances from the injection point, the low-porosity system is very close to the fastest transport system—one with high van Genuchten n—and leads the base prediction by 10% concentration.

C14

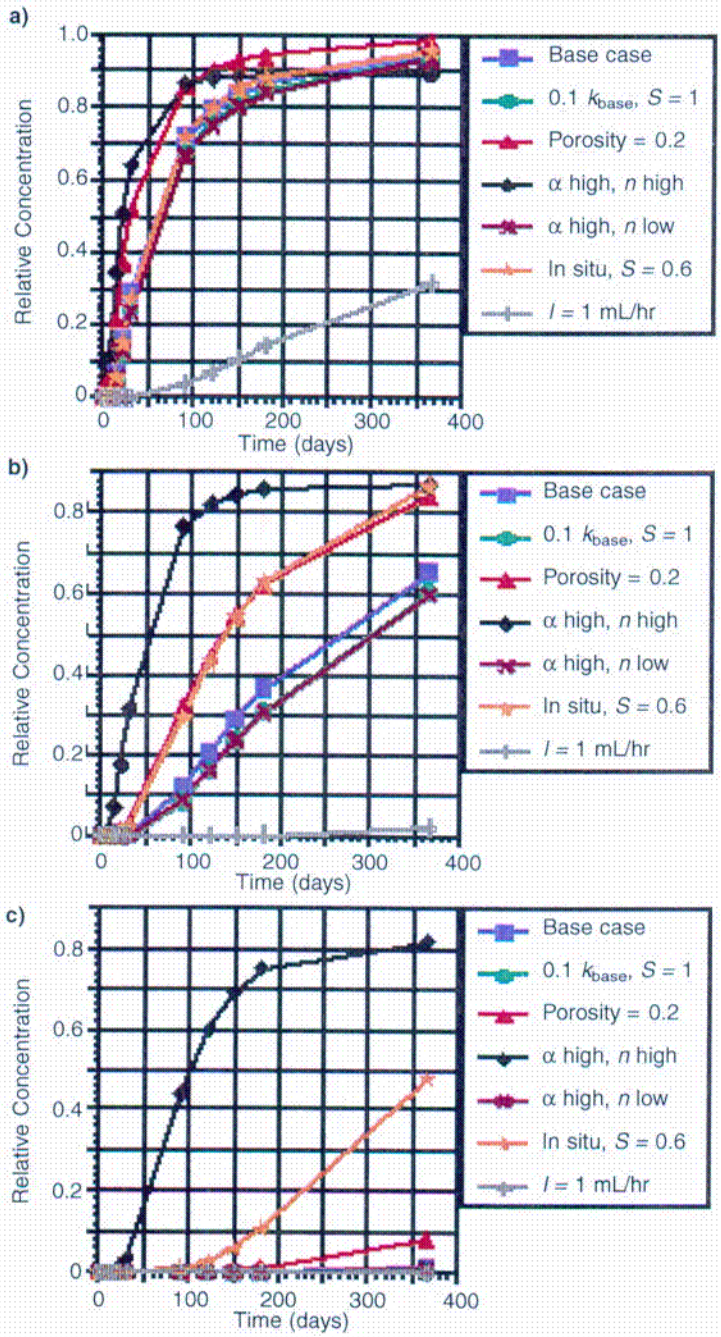

DTN: LA9909WS831372.019

NOTE: These plots show concentration changes as a function of time for a distances from the injection point of (a) 0.25 m, (b) 0.5 m, and (c) 1.0 m. Note that at a 1-m distance, there is, in most cases, little change in concentration after injecting tracer for 1 year. Parameter values for the cases shown in the legend are listed in Table 32 (rows 1, 2, 3, 5, 4, 7, and 10, respectively).

Figure 67. Concentration versus Time at Various Distances from Injection

C15

Flow in the simulation that starts with an in-situ saturation of 60%, instead of the estimated 35%, is dominated by gravity rather than capillarity. For this simulation, tracer is carried much farther down than in any of the lateral directions. At 180 days and a vertical distance of 0.5 m below the borehole, the concentration is 0.57 versus 0.11 laterally. The transport rate is substantially faster than the base case, as demonstrated by much higher concentrations at greater distances (Figure 66). At a distance of 0.5 m below the borehole, decreased porosity and increased saturation runs are virtually indistinguishable but differ significantly in 3-D distribution. The lower-porosity transport is capillary-driven, producing a relatively uniform tracer cloud, whereas the high-saturation system produces a highly elongated tracer profile. Note that saturation as high as 60% is not indicated by the reported capillary pressures measured in this system. The measured pressures indicate an in-situ saturation in the vicinity of 25 to 35%.

The simulation results were most sensitive to the value of the van Genuchten parameter n. Reported values for this parameter ranged from 1.2 to 1.8, with the value from Busted Butte samples being 1.31. At a value of $n = 1.8$, transport was strongly gravity-dominated. The resulting concentration profiles were long vertically and thin laterally. This effect was much stronger than that observed for the high-saturation simulation. Concentration at a vertical distance of 0.5 m was 0.88 versus 0.04 at the same lateral distance. At a distance of 0.5 m, tracer concentration was 60% higher than the base case and 30% higher than the high-saturation case. Furthermore, by 180 days, this system had just about reached its steady-state distribution, whereas even at 365 days (Figure 67), the other systems were continuing to change. If the actual value of n at Busted Butte is significantly different from the value used here, it should be recognizable by the distinct, long and thin, tracer distribution and by the high vertical concentrations.

The 2-D simulations (Figure 62) indicated that the value of α appears to have little influence on the system as compared to n. As a result, 3-D simulations were only done for the two different variations in van Genuchten parameters presented.

6.8.6.1.2.4 Discussion of Simulations: 2-D versus 3-D

The 2-D and 3-D simulations followed very much the same trends in tracer distribution and concentrations in space and time. Figure 68 shows concentration as a function of time, measured at a distance of 0.5 m vertically below the borehole center for both 2-D and 3-D simulations. The numerical difference in concentration between equivalent 2-D and 3-D systems remained relatively constant, approximately 10 to 15% after 90 simulation days. Concentration values between the 2-D runs and the 3-D runs were much closer at early times and began to converge at later times, as all concentrations approached unity.

6.8.6.1.3 Implications for Unsaturated Zone Transport Test Phase-2 Design and Analysis

Using different tracers at various injection rates and injection separation distances can provide an opportunity to differentiate controlling processes and material features. These simulations provide us with a tool to select injection rates for the Phase-2 experiment, as well as to help understand how the injection rates used influence what is observed at different monitoring locations. For example, after 180 days at an injection rate of 10 mL hr^{-1}, normalized

concentrations had increased to greater than 0.20 within a radius of 0.4 m from the injection point but fell off rapidly beyond that and were below 1% beyond 0.9 m. Thus, a 2-m spacing between boreholes and injection points within boreholes would probably produce a system in which each injection location was distinct from every other.

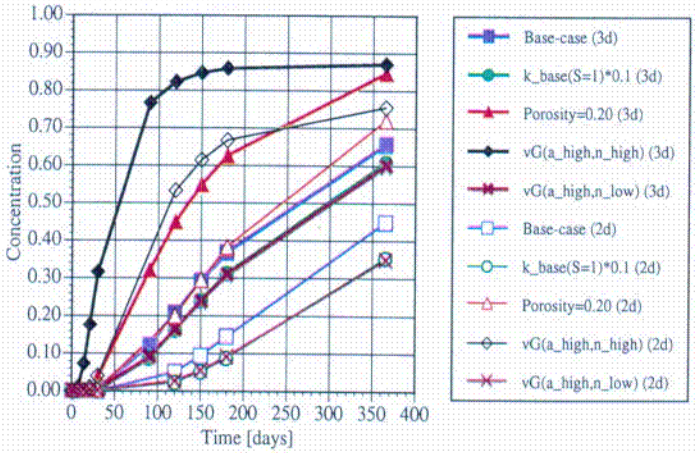

DTN: LA9909WS831372.019

NOTE: These plots of normalized concentration versus time show that differences between 2-D and 3-D values are fairly consistent between different runs. The concentration is measured at a distance of 0.5 m vertically below the borehole center. Parameter values for the cases shown in the legend are listed in Table 32 for 3-D cases and in Table 31 for 2-D cases.

Figure 68. Differences in 2-D and 3-D Predicted Concentrations

Faster injection rates, such as 50 mL hr^{-1}, can be expected to strongly modify natural flow patterns, producing gravity-dominated flow. At this injection rate, concentrations 0.5 m from the injection point are predicted to rise to 0.80 in only 3 months. Thus, boreholes or injection points spaced 1 m apart are expected to start influencing each other very early in the experiment.

On the other hand, an injection rate of 1 mL hr^{-1} is seen to hardly influence the system at all. Even after 1 yr, normalized concentrations do not rise even to 0.05 at the 0.5-m distance. At such a low injection rate, it would take an extremely long time to characterize the behavior of the system or identify important physical and chemical processes that are occurring. Further, at such slow rates of movement, it is very difficult to distinguish differences in tracer movement that might arise due to geochemical effects.

6.8.6.2 Stochastic Model

6.8.6.2.1 Introduction

The purpose of this section is to document the use of stochastic predictions made for Phase 1A of the Busted Butte testing program. At this time, there is a paucity of physical-properties information on the lithologies of that site, and the spatial variability of rock properties cannot be accurately depicted. Although this lack of information results in uncertainties for any flow and

C16

transport prediction, this section attempts to use stochastic predictions for the site using current YMP databases. The input uncertainties from these databases are directly incorporated into flow predictions through a recently developed stochastic model. The predictions represent the first two moments (expected value and standard deviation) of flow quantities, and these two moments are used to construct confidence intervals for the flow quantities.

It is expected that the field-test results will fall within the predicted confidence intervals with a 68% probability. However, because the statistical and other input parameters are taken or estimated from the YMP databases, these parameters may or may not represent the rock properties at the test site, thereby introducing another level of uncertainty in the analyses. Some sensitivity analyses were performed on these parameters and found that the flow predictions are sensitive to the background saturation, the mean and variance of pore-size-distribution parameter α, the mean and variance of the logarithm of the saturated hydraulic conductivity, and the injection rate. This indicates that the refinement of these parameters is important.

6.8.6.2.2 Stochastic Modeling

Although geologic media exhibit a high degree of spatial variability, rock properties, including fundamental parameters such as permeability and porosity, are usually observed only at a few locations due to the high cost associated with subsurface measurements. This combination of significant spatial heterogeneity with a relatively small number of observations leads to uncertainty about the values of material properties and, thus, to uncertainties in predicting flow and solute transport in such media. It has been recognized that the theory of stochastic processes provides a natural method for evaluating flow and transport uncertainties. In the last two decades, many stochastic theories have been developed to study the effects of spatial variability on flow and transport in both saturated (e.g., Gelhar and Axness 1983, pp. 161–180; Dagan 1984, pp. 151–177; Neuman et al. 1987, pp. 453–466; Graham and McLaughlin 1989, pp. 2331–2355; Zhang and Neuman 1995, pp. 39–51) and unsaturated zones (e.g., Yeh et al. 1985, pp. 457–464; Mantoglou and Gelhar 1987, pp. 37–46; Russo 1995, pp. 1647–1658; Harter and Yeh 1996, pp. 1585–1595; Zhang and Winter 1998, pp. 1091–1100). In the unsaturated zone, the problem is complicated by the fact that the flow equations are nonlinear because unsaturated hydraulic conductivity depends on pressure head.

In many of these previous theories, there are a number of simplifying assumptions such as gravity-dominated flow (for steady-state cases) and slow-varying gradient (for transient flow). These assumptions restrict the applicability of existing theories to modeling the UZTT results. For example, the assumption of gravity-dominated flow excludes the presence of domain boundaries and the existence of a water table. In addition, a slow-varying gradient does not permit local injection or fast-varying recharge. Recently, a stochastic model for transient unsaturated flow in bounded domains free of the above mentioned assumptions (STO-UNSAT, V1.0, STN: 10292-1.0LV-00) was developed. The model results are the first two moments of the flow quantities, which may be used to construct confidence intervals for these quantities. The confidence intervals are a measure of the uncertainty caused by incomplete knowledge of material heterogeneities.

6.8.6.2.3 Phase-1A Modeling

For Phase-1A simulations, the input uncertainties from YMP databases are directly incorporated into flow predictions using STO-UNSAT, V1.0 (STN: 10292-1.0LV-00). This model requires that the first two statistical moments for rock properties, such as saturated hydraulic conductivity and pore-size-distribution parameter α, be specified. Because the variabilities of porosity and residual water content are likely to be small compared to that of hydraulic conductivity, both of them are assumed to be known with certainty. To model unsaturated flow, the constitutive relationships between capillary pressure and unsaturated hydraulic conductivity and between capillary pressure and saturation must also be specified. Although the parameters characterizing these relationships are reported in the YMP databases (Schenker et al. 1995; Flint 1998), these are based on the van Genuchten model (van Genuchten 1980, pp. 892–808). Conversely, STO-UNSAT, V1.0 assumes the constitutive relationships to obey the Gardner-Russo model (Gardner 1958, pp. 228–232; Russo 1988, pp. 453–459). In this study, the Gardner-Russo parameter α is estimated from the reported van Genuchten parameters by matching the main features of the retention curves for these two models. The first row of Table 35 summarizes the relevant parameters that are taken or estimated from the YMP databases (Schenker et al. 1995). No information is found with respect to the correlation lengths of the logarithm of the hydraulic conductivity and pore size distribution. The value of 20 cm is assumed for both of these correlation lengths.

Baseline Case

In the baseline case, the size domain is 200 cm by 200 cm with material properties specified in Table 35. The steady-state simulations are run with the following boundary conditions: specified flux at the top, a constant head of –488 cm at the bottom, and no-flow boundaries at the sides. The specified flux is consistent with the constant head at the bottom such that at steady-state (t = 0), the flow is gravity-dominated with a constant mean pressure head (h = –488 cm) and a constant saturation (S = 30%) through the whole domain. Specifically, the initial mean saturation is assumed to be 30% and then the initial mean head is computed to be –488 cm using the gravity-dominated condition and the specified characteristic curves. However, the head standard deviation is not uniform in such a bounded domain. The head standard deviation is zero at the bottom boundary, increases with distance from there, and reaches its maximum at the top. Figure 69 shows the confidence intervals for the pressure head h and the saturation S along horizontal (y) and vertical (z) lines passing through the injection point. The profiles are obtained by adding one standard deviation to the result and subtracting it from the mean quantity. This result corresponds to the 68% confidence intervals for the flow quantities. By comparing the vertical profiles for pressure head and saturation (Figure 69), it is seen that unlike the head standard deviation, the saturation standard deviation is not zero at the bottom boundary of constant head. This result happens because the uncertainty in saturation comes from the uncertainty in the soil parameter α, even though the head is specified with certainty there.

An injection of rate Q = 1 mL hr^{-1} starts at time t = 0, and lasts for 150 days. The actual injection at the field test site is a point in 3-D, whereas the model is in 2-D. In the model, the injection is approximated by a line source of length L_3 perpendicular to the 2-D domain. Therefore, the injection rate is Q/L_3 in 2-D. In this baseline case, L_3 = 50 cm. It should be realized that the 2-D representation is an approximation and the accuracy of this approximation

depends strongly on the choice of L_3, which is, in turn, a strong function of injection rate. The 2-D predictions should have the same general trend as the 3-D predictions.

Table 35. Case Description

Case	Description
1	$\langle f \rangle = -6.258$, $\sigma^2_f = 2.459$, $\lambda_f = 20$ cm, $\langle \alpha \rangle = 0.01$ cm^{-1}, $\sigma^2_\alpha = 9 \times 10^{-6}$ (cm^{-1})^2, $\lambda_\alpha = 20$ cm, $\phi = 0.5$, $L_1 = L_2 = 200$ cm, $L_3 = 50$ cm, $Q = 1$ mL hr^{-1}, $S_o = 30\%$
2	Same as in Case 1, except $\lambda_f = \lambda_\alpha = 30$ cm
3	Same as in Case 1, except $L_1 = L_2 = 400$ cm
4	Same as in Case 1, except $S_o = 20\%$
5	Same as in Case 1, except $S_o = 40\%$
6	Same as in Case 1, except $S_o = 60\%$
7	Same as in Case 1, except $\phi = 0.3$
8	Same as in Case 1, except $\langle f \rangle = -4.258$ and $L_1 = L_2 = 400$ cm
9	Same as in Case 1, except $\langle \alpha \rangle = 0.02$ cm^{-1}
10	Same as in Case 1, except $\sigma^2_\alpha = 0$
11	Same as in Case 1, except $Q = 10$ mL hr^{-1}
12	Same as in Case 8, except $Q = 50$ mL hr^{-1}, $L_3 = 100$ cm
13	Same as in Case 1, except $\langle f \rangle = -4.258$ and $L_1 = L_2 = 400$ cm, and $Q = 10$ mL hr^{-1}
14	Same as in Case 13, except $Q = 50$ mL hr^{-1} and $L_3 = 100$ cm

Data Source: Schenker et al. 1995; DTN: LA9909WS831372.020

NOTE: $f = \ln K_s$ is the log-transformed saturated hydraulic conductivity (for Case 1, the mean $\langle f \rangle$ and variance σ^2_f are obtained with $\langle K_s \rangle = 6.552 \times 10^{-3}$ cm hr^{-1} and $\sigma_{Ks} = 2.143 \times 10^{-2}$ cm hr^{-1}), α is a parameter related to pore-size distribution, λ_f and λ_α are the respective correlation lengths of f and α, ϕ is porosity, L_1 and L_2 are the vertical and horizontal dimensions of the domain, L_3 is the length of the third dimension used to calculate the injection rate for 2-D simulation, S_o is the background saturation, and Q is the actual injection rate.

Figure 70 shows the vertical and horizontal profiles of pressure head and saturation at 150 days. It is seen that the impact of injection is the increase of pressure head and saturation in the vicinity of injection. The effects seem to be even in all directions near the injection. This result is caused by the fact that the injection rate is overwhelmingly large compared to the background unsaturated hydraulic conductivity. The approximate radius of noticeable pressure head and saturation changes is 40 cm.

Other flow quantities (e.g., flux and velocity) and their associated uncertainties can be given similarly. In principle, the concentration field and its associated uncertainty may be predicted based on this information. However, at this stage, there is no existing model for solute transport in a nonstationary, unsaturated flow field. Our ongoing related research may provide us with a model during Phase-2 prediction.

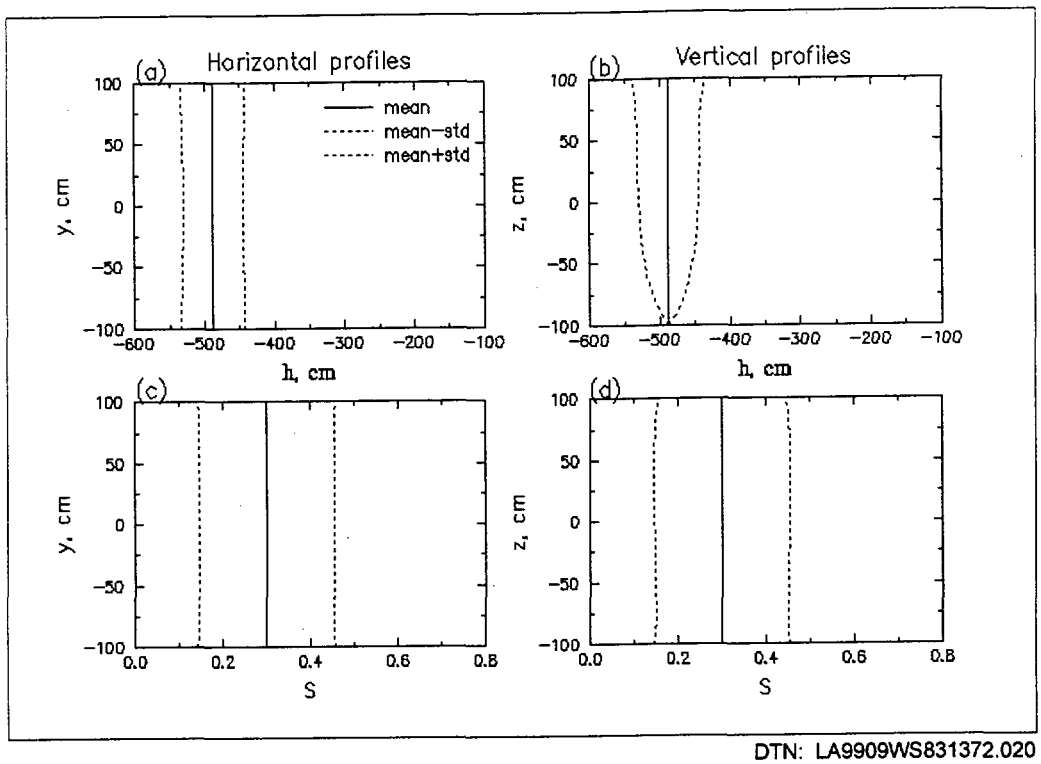

DTN: LA9909WS831372.020

NOTE: Horizontal and vertical profiles of pressure head *h* and saturation *S* under steady-state conditions.

Figure 69. Steady-State Profiles

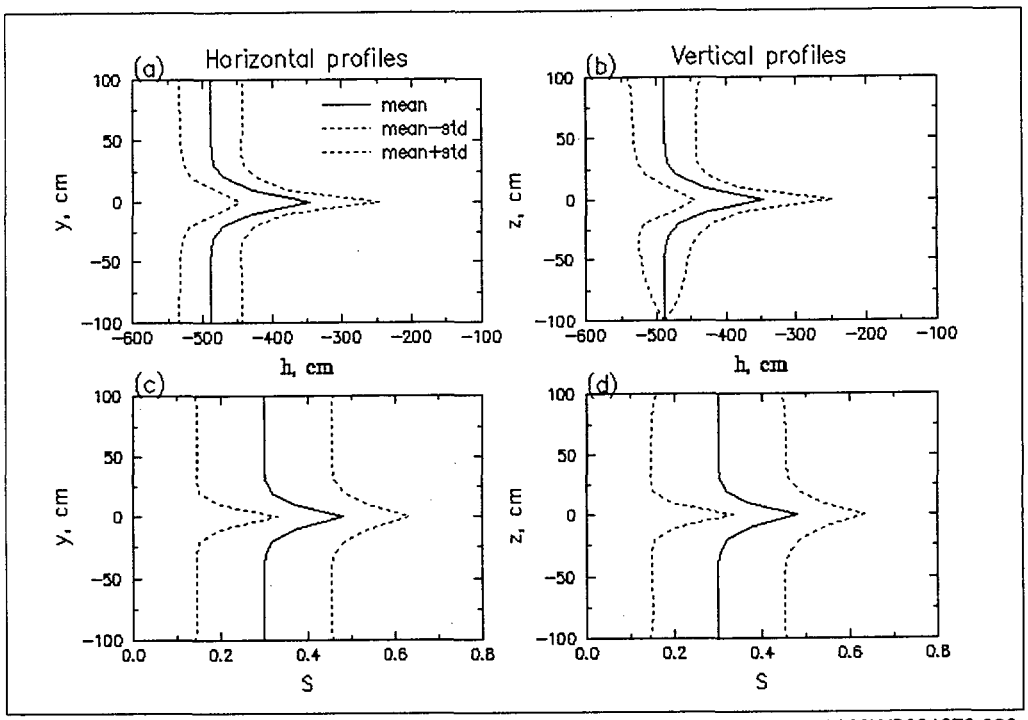

DTN: LA9909WS831372.020

Figure 70. Case 1. Horizontal and Vertical Profiles of Pressure Head *h* and Saturation *S* at 150 Days after Injection Started

Sensitivity Cases

Because the number of actual measurements at the site is too few to perform any statistical analysis, the statistical parameters are either taken or estimated from the relevant YMP databases. There is another level of uncertainty associated with inaccurate statistical and other parameters. Sensitivity studies, presented below, are performed using the stochastic model.

As mentioned before, there is no information regarding the correlation lengths of the log of the saturated hydraulic conductivity and the rock pore-size distribution parameter α. Case 2 investigates the effect of the correlation lengths by changing it from 20 cm to 30 cm. Figure 71 shows the corresponding profiles of pressure head and saturation. Comparison of Figures 70 and 71 reveals that the prediction is insensitive to the correlation lengths.

In the base case, the domain size is taken to be L_1 = 200 cm by L_2 = 200 cm. However, the real domain is much larger than this. The size of the domain is expected to affect the standard deviations of flow quantities to some extent. In Case 3, L_1 = 400 cm and L_2 = 400 cm. It is seen from Figure 72 that, in areas away from the boundaries, the confidence intervals are quite insensitive to the domain size.

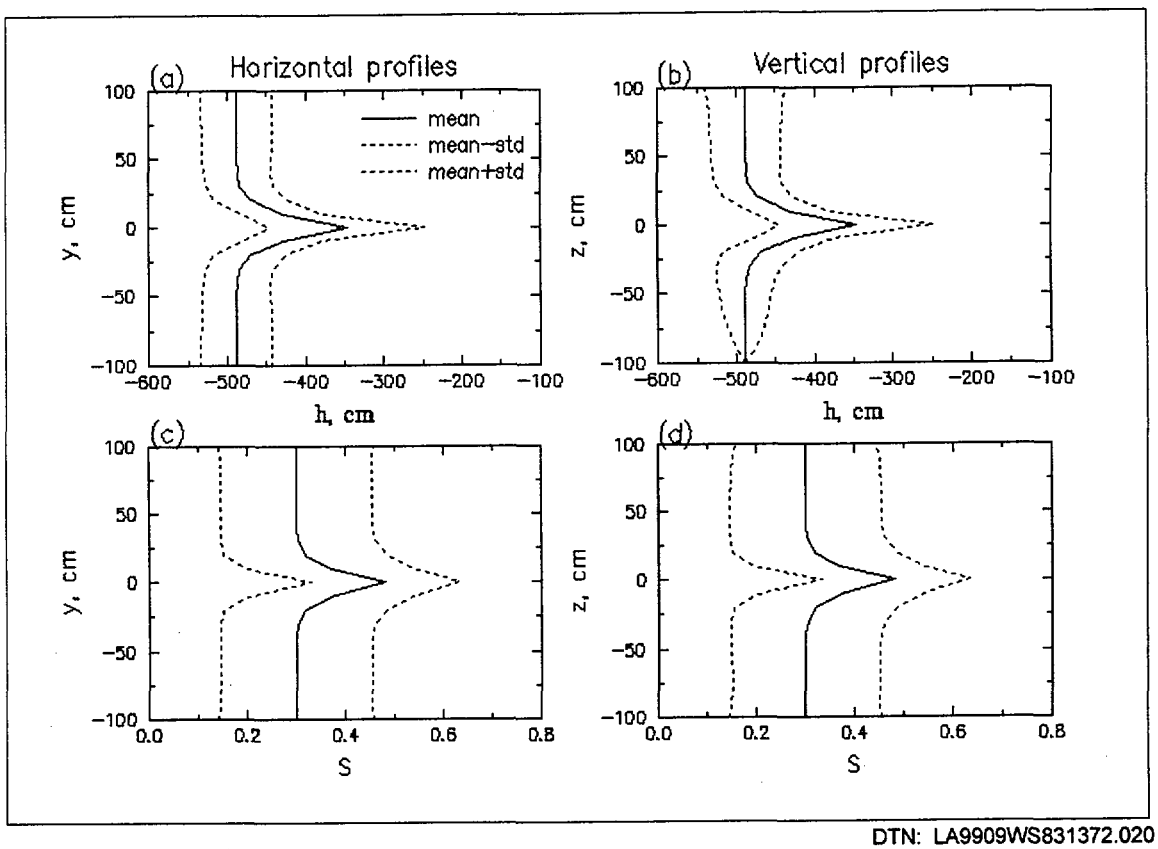

DTN: LA9909WS831372.020

Figure 71. Case 2. The Same as Case 1 in Figure 70 but with $\lambda_f = \lambda_\alpha$ = 30 cm

Cases 4 through 6 from Table 35 investigate the effect of background saturation by changing the specified flux at the top and the constant head at the bottom. Figures 73 to 74 show the cases for

S_o = 20%, 40%, and 60%, respectively. It is seen that the peak pressure head and saturation at the injection location decrease with the increase of the background saturation, but the impact radius increases with it. The width of confidence intervals for pressure head decreases with the increase of background saturation, whereas that for saturation profiles is quite insensitive to the background saturation.

In Case 7, the porosity is varied from $\phi = 0.5$ to 0.3 (Figure 76). Comparison of Figure 76 and Figure 77 reveals that a lower porosity results in a slight increase in both the peak saturation and the radius of influence. However, the effect of porosity on solute transport is expected to be greater.

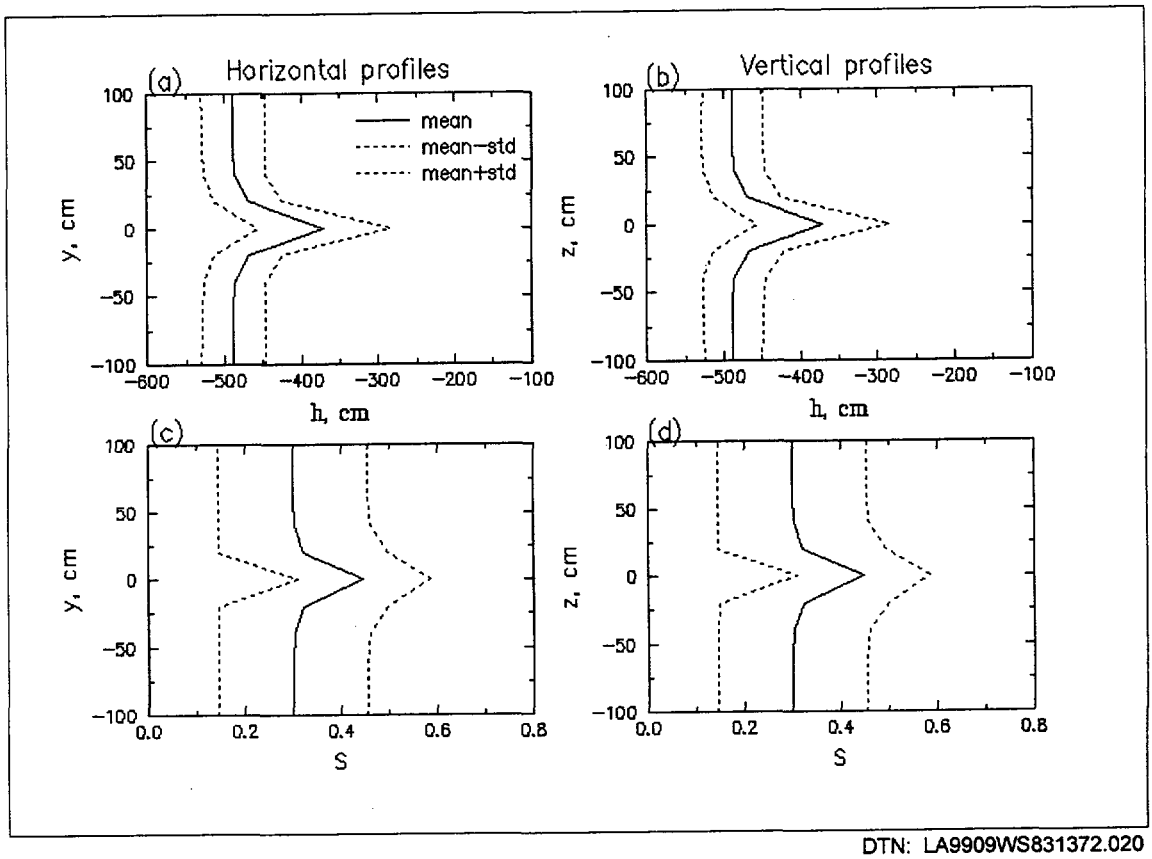

DTN: LA9909WS831372.020

Figure 72. Case 3. The Same as Case 1 in Figure 70 but with $L_1 = L_2 = 400$ cm

In Case 8, the mean of the log of the saturated hydraulic conductivity K is increased from $\langle f \rangle$ = –6.258 to –4.258 (where $f = \ln K$). As one should expect, a larger hydraulic conductivity renders a lower peak saturation and a larger radius of influence (Figure 77). In this case, the size of the domain was changed to 400 cm by 400 cm to accommodate the increase of saturation at large distance. In Case 9, the mean of α is varied from 0.01 to 0.02 cm^{-1} while the variance of α is kept the same. It is seen that the mean head has increased significantly with a larger α for a given saturation (Figure 78). The confidence intervals are qualitatively similar to those in Figure 70, but the intervals are tighter in Figure 79. This difference occurs because the variability in α is actually reduced by keeping the same variance but with an increased mean value. As expected, the prediction—in particular, the width of confidence intervals—is sensitive to the

variabilities in saturated hydraulic conductivity and pore size distribution α. Case 10 shows the case in which the variability of α is zero. It is seen from Figure 79 that the width of the confidence intervals is significantly reduced in the absence of variability in α. In this case, the uncertainties in the prediction are entirely caused by the variability in saturated hydraulic conductivity K_s. In the baseline case, the coefficient of variation $CV_\alpha = \sigma_\alpha/\langle\alpha\rangle = 0.3$, while $CV_{Ks} = 3.27$. That is to say, the variability in saturated hydraulic conductivity K_s is much larger than that in pore size distribution α. Therefore, it may be concluded that the results are much more sensitive to the variability in α than to that in K_s.

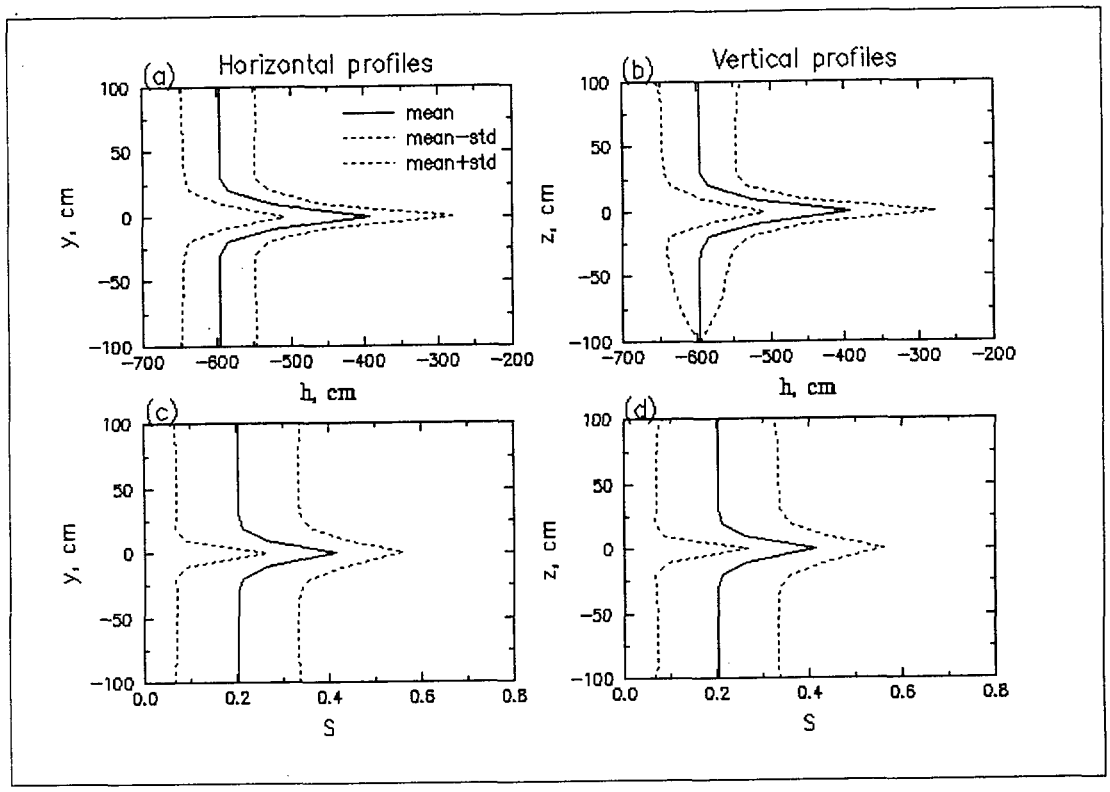

DTN: LA9909WS831372.020

Figure 73. Case 4. The Same as Case 1 in Figure 70 but with S_o = 20%

As one should expect, the behaviors of pressure head and saturation profiles are very sensitive to the injection rate. In Case 11, the injection rate is Q = 10 mL hr^{-1} (Figure 80). The peak saturation is much higher than that in Case 1 (Figure 70) and the radius of influence is also larger. This difference is even clearer from Case 12 (Figure 81), for which Q = 50 mL hr^{-1}.

In the last two cases, the mean saturated hydraulic conductivity $\langle K_s \rangle$ is taken to be 4.68 cm hr^{-1}. This value is based on some site-specific measurements and is three orders of magnitude larger than the value found in the YMP databases mentioned earlier. As for sensitivity runs, this value is taken as the mean and $CV_{Ks} = \sigma_{Ks}/\langle K_s\rangle = 3.27$, as in the baseline case. Equivalently, $\langle f\rangle = 0.314$ and $\sigma^2_f = 2.459$. In Case 13, Q = 10 mL/hr and L_3 = 50 cm (Figure 82); in Case 14, Q = 50 mL hr^{-1} and L_3 = 100 cm (Figure 83). As found in Case 8 (Figure 77), a larger hydraulic

conductivity renders a lower peak saturation and a larger radius of influence. It is expected that the tracer travels significantly faster in these cases.

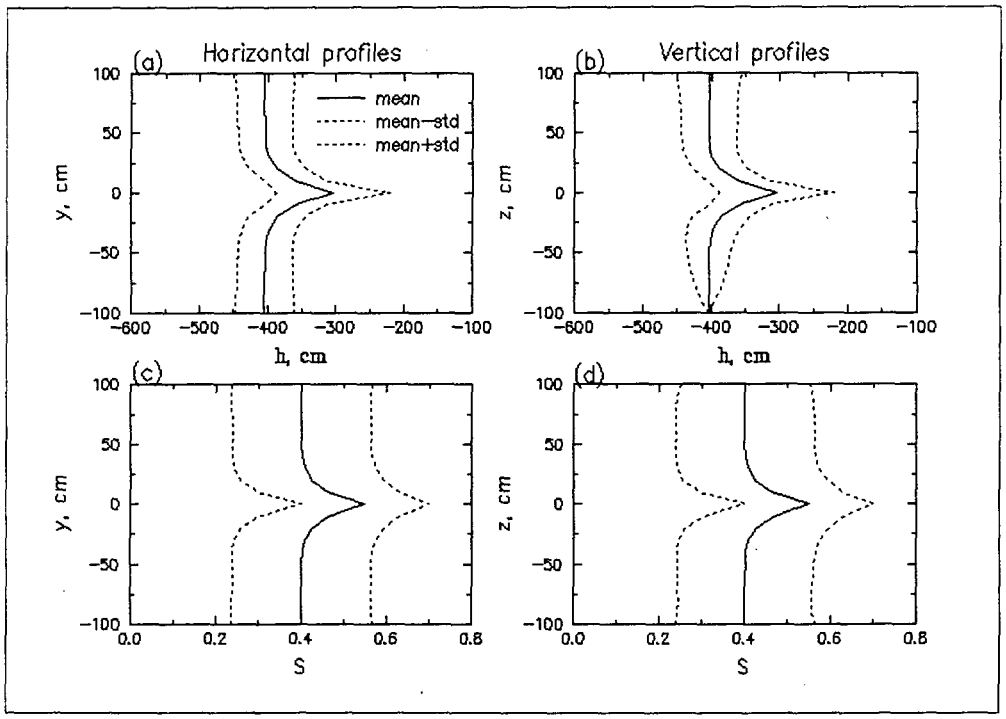

DTN: LA9909WS831372.020

Figure 74. Case 5. The Same as Case 1 in Figure 70 but with S_o = 40%

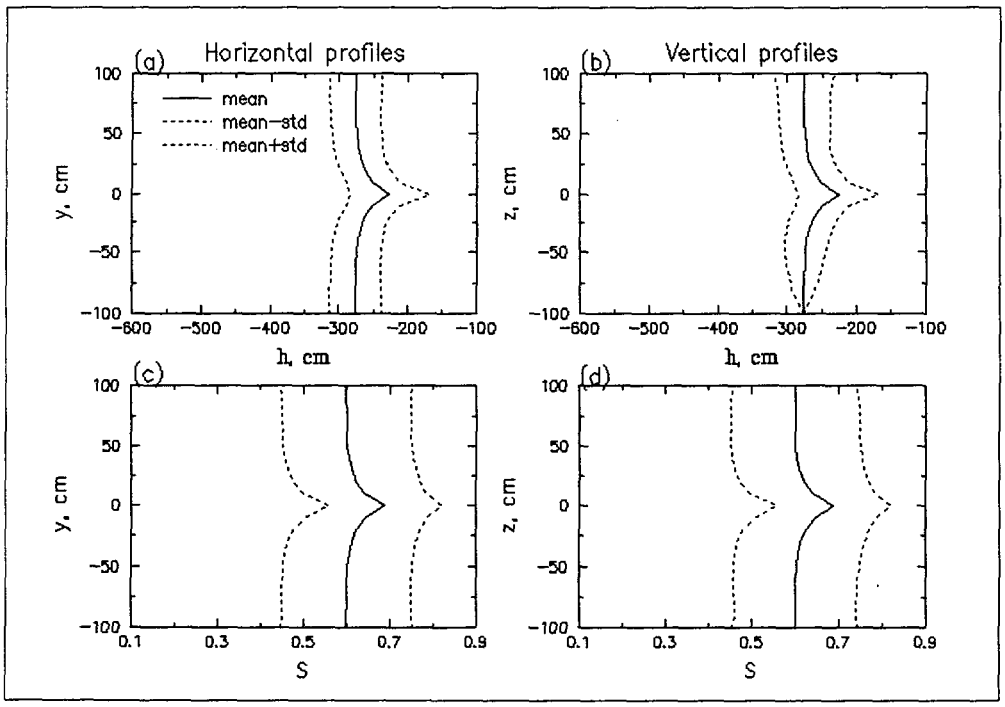

DTN: LA9909WS831372.020

Figure 75. Case 6. The Same as Case 1 in Figure 70 but with S_o = 60%

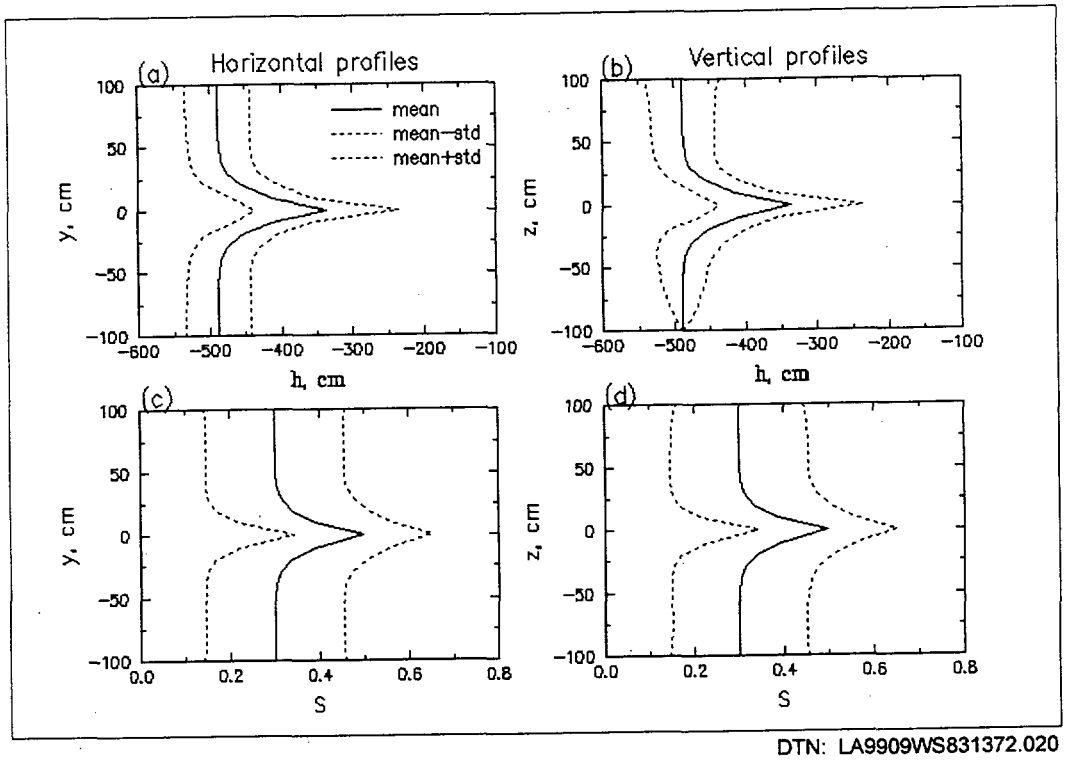

DTN: LA9909WS831372.020

Figure 76. Case 7. The Same as Case 1 in Figure 70 but with $\phi = 0.3$

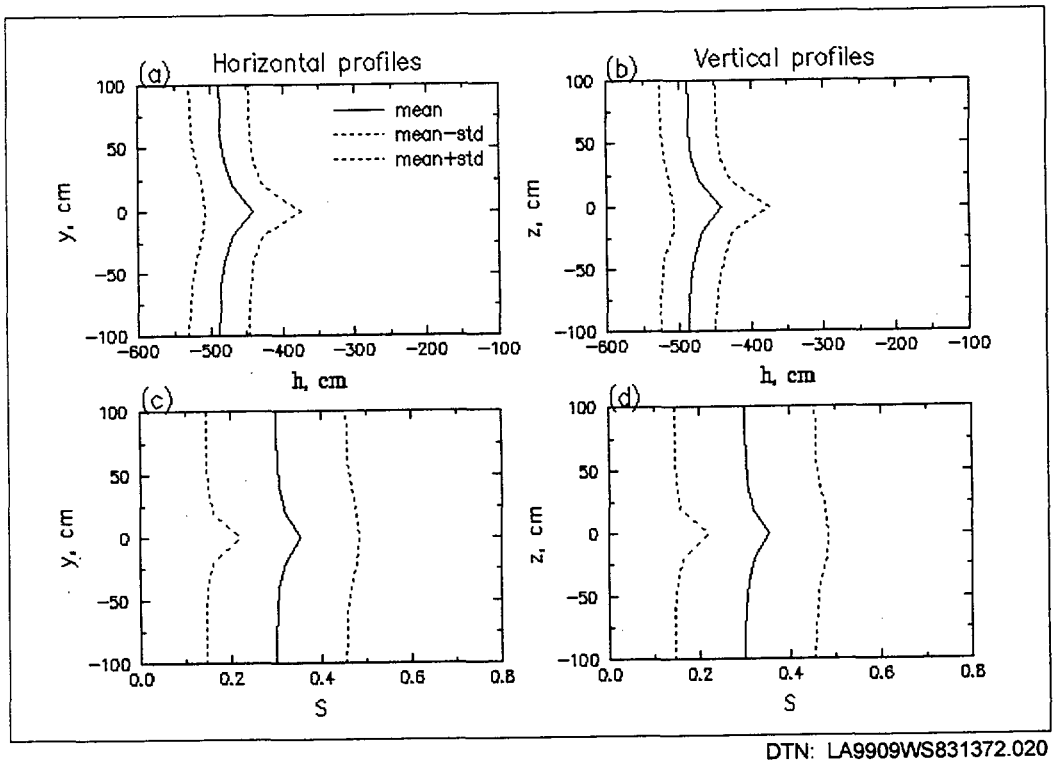

DTN: LA9909WS831372.020

Figure 77. Case 8. The Same as Case 1 in Figure 70 but with $\langle f \rangle = -4.258$ and $L_1 = L_2 = 400$ cm

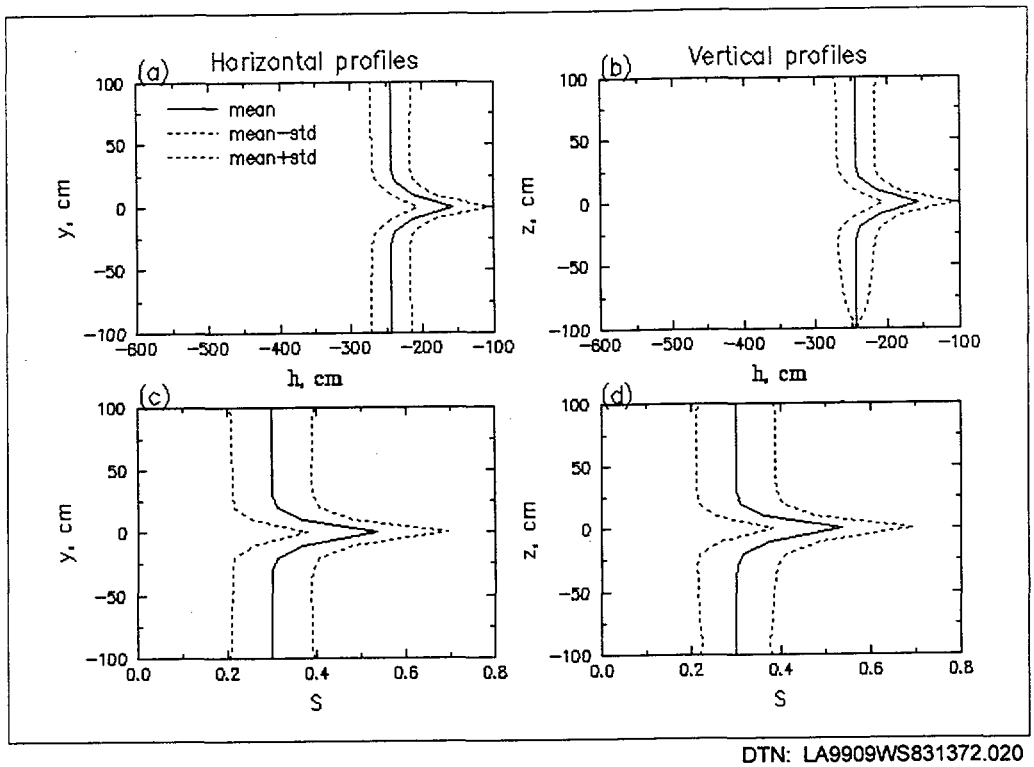

DTN: LA9909WS831372.020

Figure 78. Case 9. The Same as Case 1 in Figure 70 but with $\langle \alpha \rangle = 0.02\ \mathrm{cm}^{-1}$

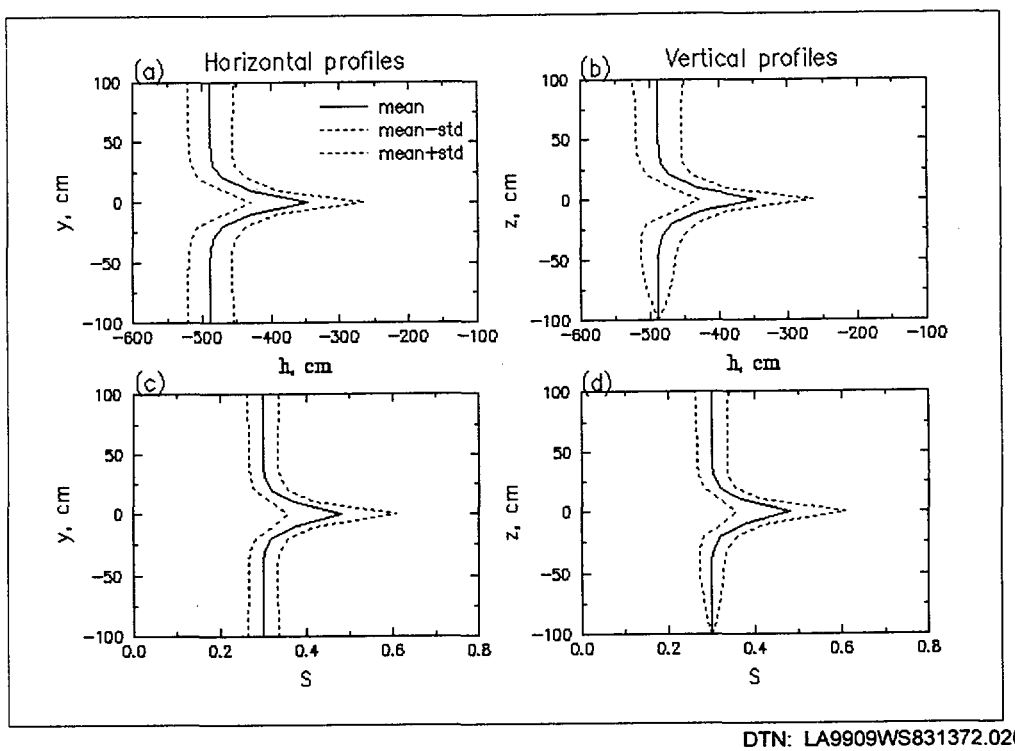

DTN: LA9909WS831372.020

Figure 79. Case 10. The Same as Case 1 in Figure 70 but with $\sigma_\alpha = 0$

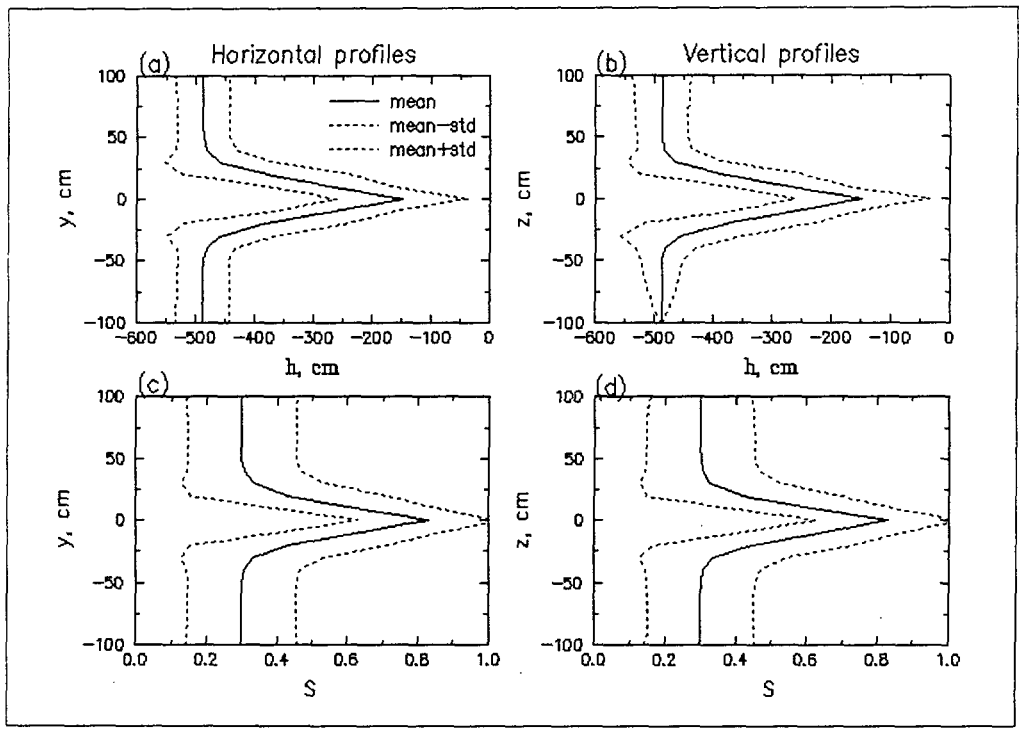

DTN: LA9909WS831372.020

Figure 80. Case 11. The Same as Case 1 in Figure 70 but with Q = 10 mL hr^{-1}

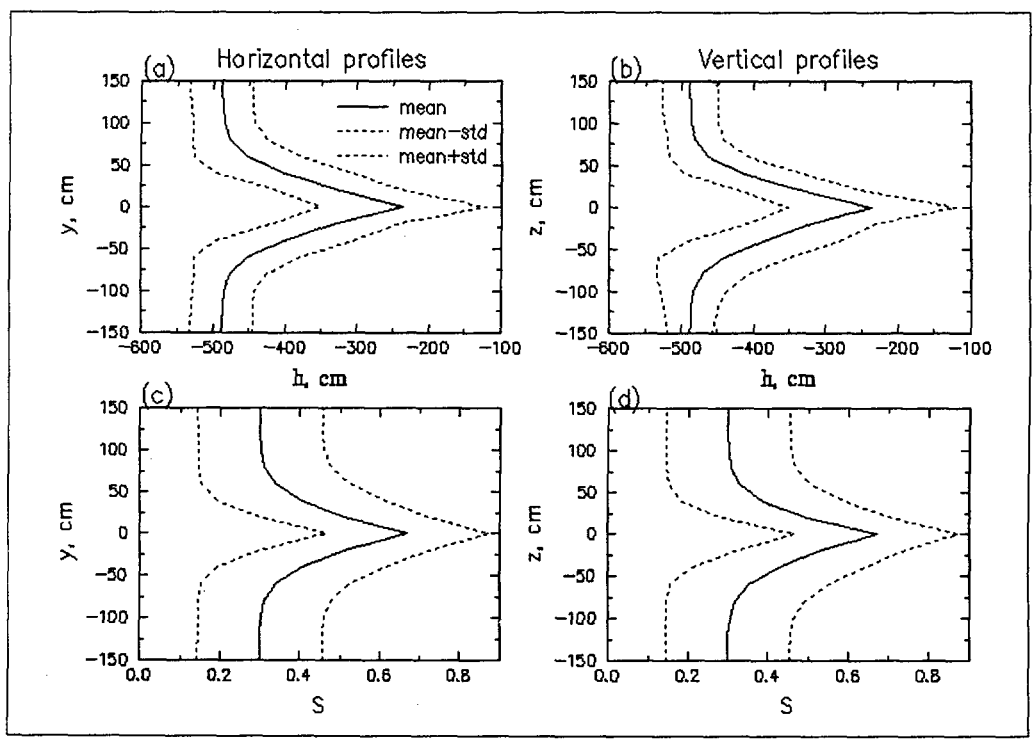

DTN: LA9909WS831372.020

Figure 81. Case 12. The Same as Case 8 in Figure 77 but with Q = 50 mL hr^{-1} and L_3 = 100 cm

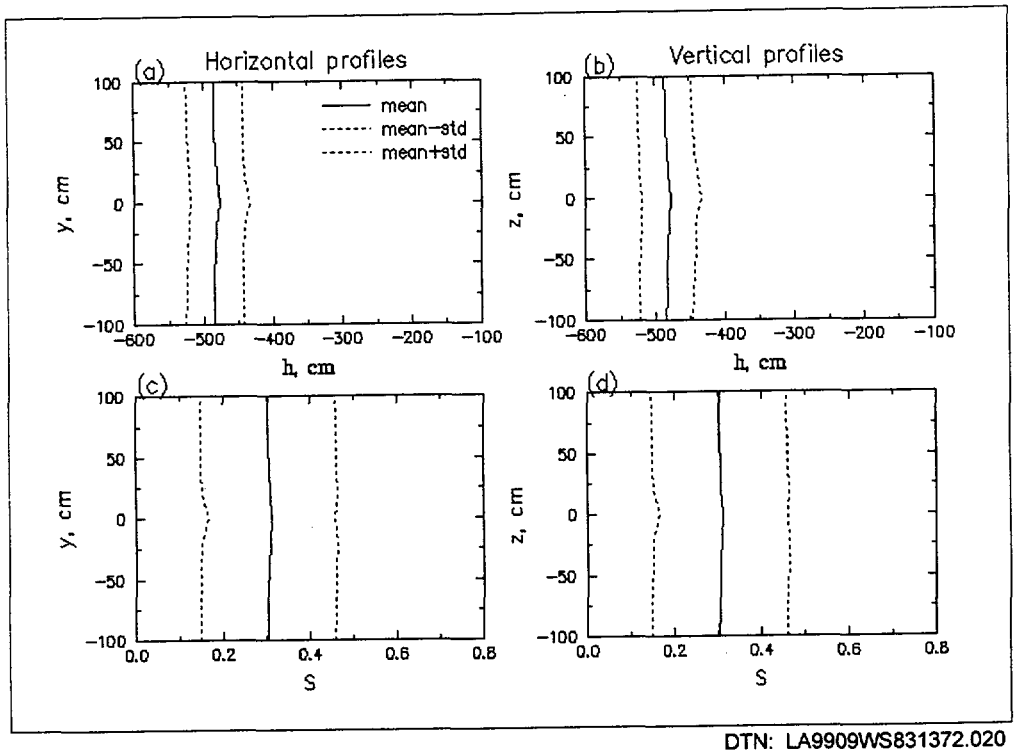

DTN: LA9909WS831372.020

Figure 82. Case 13. The Same as Case 1 in Figure 70 but with $\langle f \rangle = 0.314$, $L_1 = L_2 = 400$ cm, and $Q = 10$ mL hr^{-1}

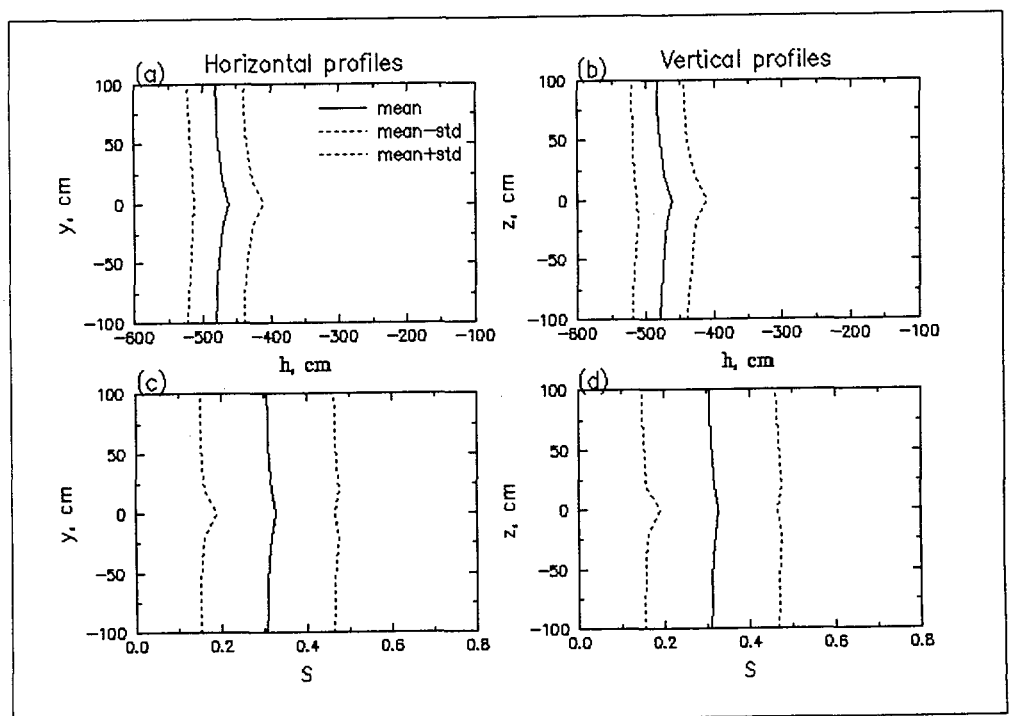

DTN: LA9909WS831372.020

Figure 83. Case 14. The Same as Case 13 in Figure 82 but with $Q = 50$ mL hr^{-1} and $L_3 = 100$ cm

6.8.6.2.4 Nonstationarity

The stochastic model of transient fluid flow in unsaturated, stationary (statistically homogeneous) media was modified to account for nonstationary features such as distinct layers in the rock properties. This extension was then implemented into the stochastic model and tested with some two-dimensional examples. In these examples, some special cases of medium nonstationarity are considered: trending in the statistical moments of the log of saturated hydraulic conductivity and pore size distribution parameter; zones of different rock properties existing in the domain; and different layers present in the domain. The effect of an embedded thin layer on fluid flow for the Phase-1A test was investigated with this modified stochastic model. It was found that this thin layer acts like a barrier to fluid flow and induces lateral fluid spreading. Only after accounting for this thin layer did the stochastic model produce fluid redistribution behaviors that are qualitatively similar to those observed by the mineback. A quantitative comparison will be made after the site-specific statistical parameters are obtained from the on-going geostatistical analysis of the rock property measurements at the site. In addition, it was found that the flow nonstationarity under unsaturated conditions significantly affects the behaviors of solute migration in such flow fields. The effect of the thin layer in the Phase-1A area on the migration of injected tracers can be assessed with site-specific statistical parameters.

6.8.6.3 Monte Carlo Flow and Transport Simulations

6.8.6.3.1 Introduction

To augment the results of the sensitivity analyses for the homogeneous-model calculations and the stochastic-model results, a series of Monte Carlo analyses were carried out in two dimensions. The goal of these simulations is to bracket the range of possible transport behaviors that could arise due to variability in the hydrologic parameters. To accomplish this goal, a refined 2-D grid was generated (Figure 84) for performing flow and transport calculations. As in the homogeneous simulations using FEHM (V2.00, STN: 10031-2.00-00), the top and bottom boundaries of the model are held at constant capillary pressure. A single realization of the model consists of two simulations: a background simulation (without fluid injection at the borehole) to establish a steady-state flow condition followed by a simulation in which fluid of unit concentration (arbitrary concentration units) is injected for 180 days, the planned duration of the Phase-1A experiments. To simulate a heterogeneous system, the model is populated with a distribution of permeability values with a given mean value and an assumed correlation length. Figure 85 shows a permeability distribution chosen at random from the Case-1 simulations (see Table 36 for a summary of the different cases treated in the Monte Carlo simulations; detailed discussion of the individual cases considered is described below). Contrasting permeability values within the region of rock in which fluid is injected is expected to affect the flow and transport behavior by providing preferential pathways for fluid migration through the rock.

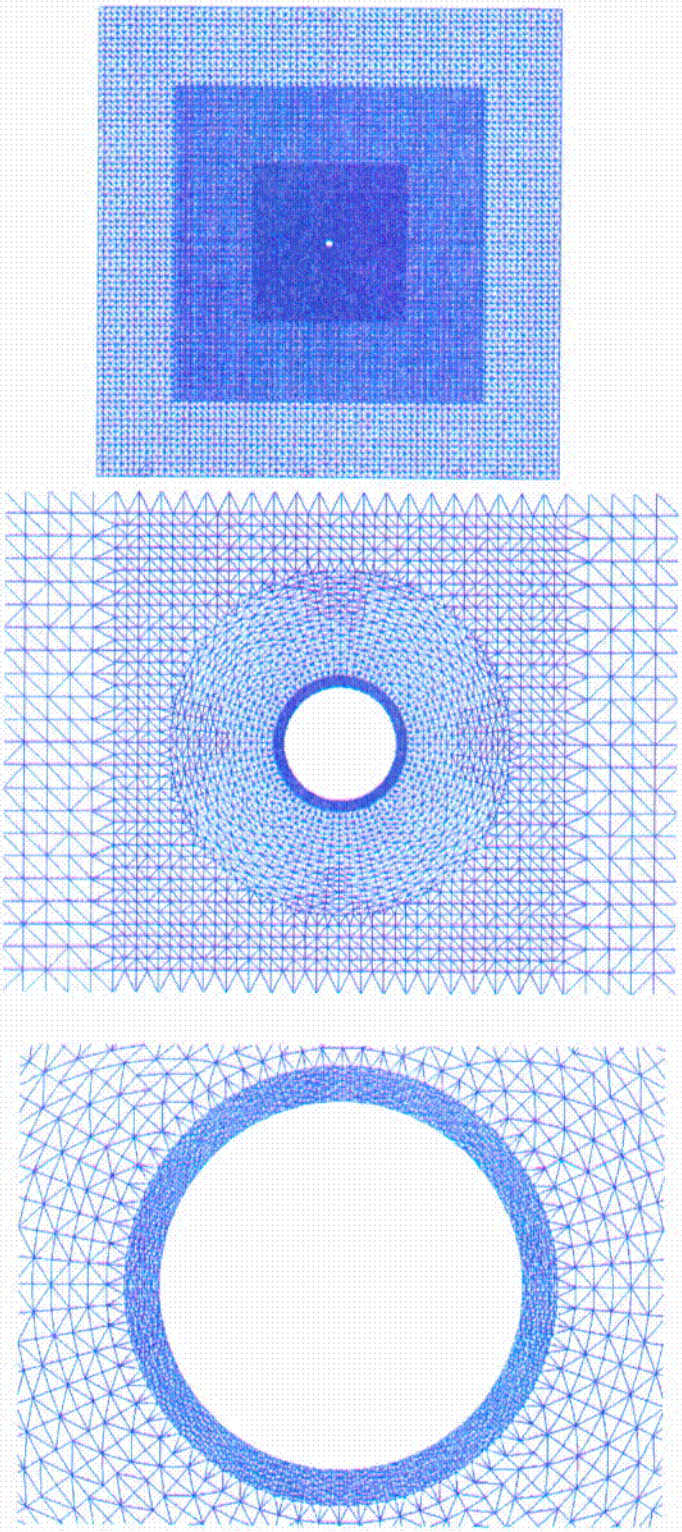

DTN: LA9909WS831372.021

NOTE: Top: full view (6 m x 6 m); Middle: intermediate close-up view (0.4 m x 0.5 m); Bottom: close-up of borehole.

Figure 84. Finite-Element Grid Used in the Monte Carlo Simulation

C17

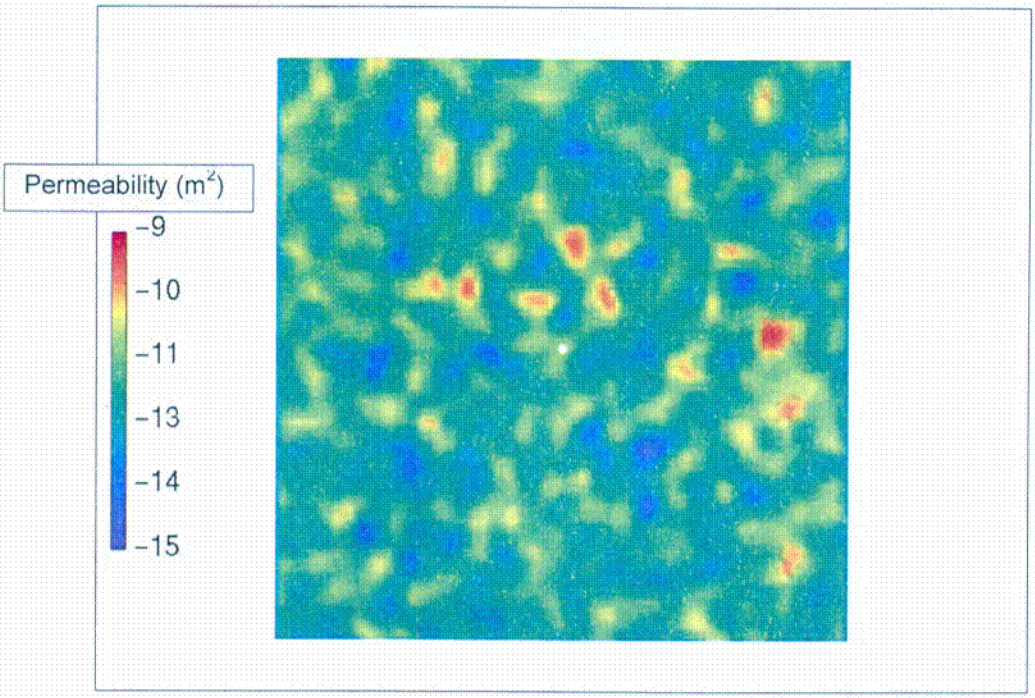

DTN: LA9909WS831372.021

NOTE: This plot shows the permeability distribution for the Monte Carlo realization selected for discussion.

Figure 85. Permeability Distribution

Table 36. Summary of Monte Carlo Cases*

Case number	Correlation of α and permeability	Correlation length of heterogeneities
1	None	0.2 m
2	Altman et al. (1996, Eq. on p. 34)	0.2 m
3	Altman et al. (1996, Eq. on p. 34)	0.1 m
4	Altman et al. (1996, Eq. on p. 34)	0.5 m

DTN: LA9909WS831372.021

NOTE: *All cases assume $\ln(k_s) = 1.54$, where k_s is in cm hr^{-1}.

6.8.6.3.2 Methodology

The Monte Carlo approach considers the results of all individual realizations to be equally likely outcomes of the behavior of the system. Therefore, once a metric is chosen for quantifying the behavior of the system, statistical properties of the behavior of the system can be established. In the present study, the movement of a conservative solute injected with the fluid is used. The maximum penetration distances in all four directions away from the injection point are recorded for several different concentrations to establish the direction of movement of tracer. Then, for all 50 realizations in a given case, the mean values for these distances are recorded along with the standard deviation. The mean values establish the general location of the concentration front,

C18

whereas the standard deviation is a measure of the uncertainty in the predictions of concentration-front movement due to the heterogeneities of the rock mass.

6.8.6.3.3 Statistical Results

One advantage of the Monte Carlo approach is that an individual realization can be examined in detail to understand the behavior of the system, after which, the multiple realizations can be used to quantify the uncertainty. The behavior of the flow and transport system is now examined (Figure 86) for the permeability distribution shown in Figure 85. The background saturation distribution shows little or no variability. This result is in contrast to the variability in predicted fluid saturation for the cases in which permeability and van Genuchten α are correlated.

For that type of heterogeneous field, the fluid saturation is a strong function of α. The left-hand panels of Figure 86 show the movement of the saturation front into the rock mass for various times during the injection phase, and the right-hand panels are the concentrations of the conservative tracer for those same times. For this rock at this injection rate, there appears to be a relatively uniform migration of fluid and tracer away from the injection point in all directions, even upward. Under these conditions, the capillary-pressure driving forces are strong enough to pull water against the force of gravity. The presence of the borehole produces a "shadow effect" in which fluid must migrate around the borehole to reach the rock on the opposite side of the injection pad. Regarding the influence of heterogeneities, there is some tendency for fluid to be drawn preferentially into portions of the rock with higher capillary suction. The resulting saturation and concentration fronts exhibit an irregular pattern that tracks the heterogeneities. Nevertheless, the general patterns of movement of fluid and solute match fairly closely those of the homogeneous simulations.

Now the results of the statistical analyses of the Monte Carlo simulations are examined. Table 37 shows the mean and standard-deviation values for the four cases summarized in Table 36. The y coordinate in the table represents the vertical direction, with negative values below the borehole injection point. The x coordinate is laterally away from the borehole, with positive values located on the side at which the injection pad is located. First consider the results of Case 1, in which the permeability field is assumed to vary but the van Genuchten α value is constant. The mean values for the minimum and maximum y values illustrate the degree to which the transport occurs uniformly in upward and downward directions. The Case-1 results show that capillary forces tend to pull water (and tracer) uniformly upward and downward with little or no tendency for downward migration due to gravity. The $C = 0.01$ isoconcentration value is meant to represent the migration of the front edge of the concentration plume; it travels approximately 40 to 45 cm in the upward, downward, and outward (positive x) directions, on average. The injection point is located at approximately $x = 5$ cm and $y = 0$. The travel distance for the $C = 0.5$ isoconcentration value is more indicative of bulk plume movement, rather than the leading edge. This front travels approximately 30 cm in the three directions. The x_{min} values suggest a slight asymmetry in plume migration. This asymmetry is caused by the "shadow effect" due to the presence of the borehole, as described above.

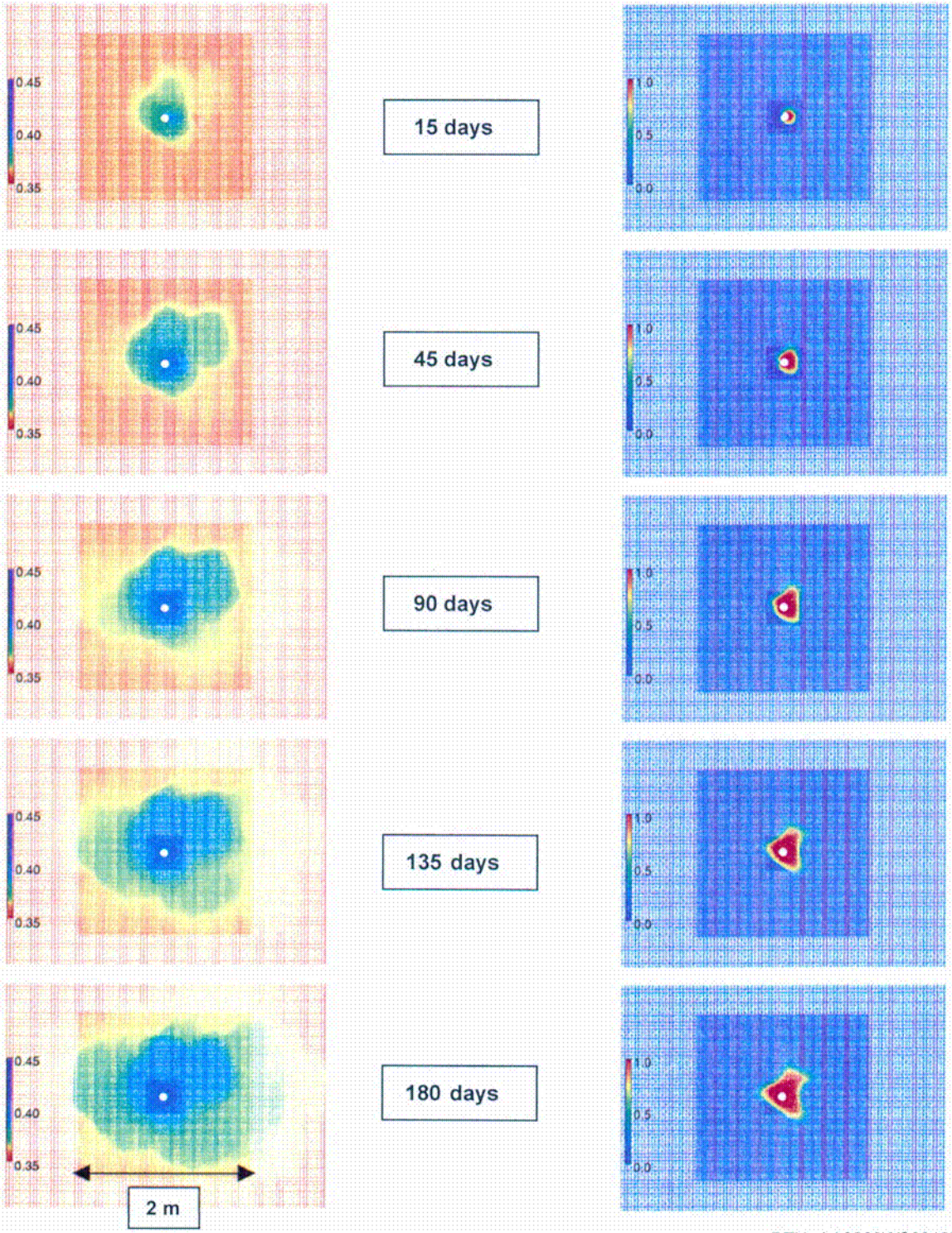

DTN: LA9909WS831372.021

NOTE: These plots show fluid saturations (left panels) and tracer concentrations (right panels) at various times during a Monte Carlo simulation. Note the restricted range of saturation values used.

Figure 86. Fluid Saturations and Tracer Concentrations

C19

Table 37. Statistical Results of Monte Carlo Simulations

	C = 0.01				C = 0.1				C = 0.5			
	x_{min}	x_{max}	y_{min}	y_{max}	x_{min}	x_{max}	y_{min}	y_{max}	x_{min}	x_{max}	y_{min}	y_{max}
Case 1												
Mean	–0.35	0.53	–0.45	0.42	–0.28	0.46	–0.37	0.35	–0.20	0.37	–0.29	0.27
Std. dev.	0.11	0.12	0.082	0.093	0.098	0.11	0.077	0.085	0.08	0.098	0.070	0.068
Case 2												
Mean	–0.30	0.47	–0.42	0.41	–0.23	0.41	–0.35	0.35	–0.16	0.33	–0.27	0.27
Std. dev.	0.019	0.014	0.015	0.012	0.016	0.013	0.013	0.013	0.010	0.012	0.011	0.013
Case 3												
Mean	–0.29	0.48	–0.41	0.41	–0.22	0.41	–0.35	0.35	–0.15	0.33	–0.27	0.27
Std. dev.	0.014	0.012	0.011	0.011	0.011	0.012	0.011	0.011	0.007	0.013	0.011	0.010
Case 4												
Mean	–0.28	0.49	–0.41	0.42	–0.22	0.42	–0.35	0.35	–0.15	0.34	–0.27	0.27
Std. dev.	0.027	0.024	0.022	0.024	0.022	0.020	0.019	0.018	0.015	0.017	0.018	0.017

DTN: LA9909WS831372.021

NOTE: Results based on 50 realizations for each case listed in Table 36.

The borehole causes the plume to have more difficulty migrating in the negative x direction. The standard deviation values reflect the uncertainty in the predicted migration of the plume caused by the heterogeneous permeability distribution. For Case 1, the uncertainty in the $C = 0.01$ isoconcentration value is about 8 to 12 cm (depending on direction), whereas for the $C = 0.5$ value, the uncertainty ranges from about 7 to 10 cm. Therefore, for Case 1, the heterogeneous permeability field (with no variability in α) adds considerable uncertainty to the predictions.

A comparison of Cases 1 and 2 illustrates the influence of imposing a correlation of permeability and α on the uncertainty of the predictions. The mean values for the spreading of the plume in all directions are very similar for the two cases, but the uncertainty due to heterogeneity is much smaller when α is assumed to be correlated with permeability (Case 2). The correlation imposes a larger α for lower permeability, resulting in a larger capillary suction for regions of the rock with lower permeability. This result counteracts the tendency for fluid to travel preferentially through higher permeability rock, as in Case 1. Therefore, the spreading of tracer in Case 2 is more uniform, and the standard deviation values are consequently smaller.

Finally, the influence of correlation length on plume spreading can be examined by comparing Cases 2, 3, and 4, which assumed correlation lengths of 0.2 m, 0.1 m, and 0.5 m, respectively. The mean behavior of the plumes is very insensitive to the correlation length. Regarding the uncertainty in plume prediction (as measured by the standard deviation), there is a trend toward larger uncertainty as the correlation length increases, as expected. Nevertheless, the uncertainty for these cases is much smaller than the correlation length itself. This result is caused by the assumed correlation of permeability and α for each of these cases, which, as just discussed, largely negates the distribution of permeability values. Therefore, the largest uncertainty in these simulations appears to be the nature of the correlation (or lack thereof) of different hydrologic

properties. Permeability and the van Genuchten α parameter were correlated in these simulations. Altman et al. (1996, p. 34) also propose correlations between permeability and porosity for Yucca Mountain tuffs. Therefore, the most important data that could be collected to further constrain these predictions are hydrologic property measurements on a much larger set of samples from the test block. A full suite of property measurements (porosity, permeability, and unsaturated hydrologic parameters) on samples collected from known locations in the block would be useful to set correlations between parameters and assign correlation lengths for future simulations.

6.8.6.3.4 Interpretations of the Monte Carlo Phase-1A Study

The modeling analyses for Phase 1A indicate that strong capillary forces in the rock matrix of the Tac unit are likely to modulate fracture flow from overlying units, thereby dampening pulses of infiltrating water and providing a large degree of contact between radionuclides and the rock matrix. Several modeling approaches, from deterministic to Monte Carlo to stochastic models, were used to simulate the Phase-1A experiments. All yielded similar qualitative results. From these results, the tentative conclusion is that the deterministic modeling approach taken at the site scale may be adequate. As the data from the UZTT become available, parameterizations used in these calculations will be updated.

A particularly interesting observation from the Phase-1B experiment is that, even when injection occurs immediately adjacent to a fracture, water appears to be imbibed quickly into the surrounding matrix. The transport times observed immediately below the injection point were on the order of 30 days, whereas pure fracture flow would have resulted in travel times of minutes to hours at this flow rate. Site-scale models must be evaluated in light of this observation. Models that predict significant fracture flow at percolation rates low enough for the matrix to transmit the flow may be inconsistent with the Phase-1B experiment.

6.8.6.3.5 Forward Efforts

In Phase 1A, the fluorescein image information is being incorporated into the modeling effort. Also, a small number of moisture and bromide samples from the Phase-1A rock are being analyzed. The strengths and weaknesses of the three conceptual approaches presented in this section are being assessed based on their relative accuracy in predicting flow and concentration. Predictions will be compared with flow and transport experimental data.

Measurements of the tracer concentrations from collected samples are to be conducted after that date. After auger samples are collected and analyzed and mineback completed, the numerical predictions will be compared against the measured values, and the accuracy of the model configuration will be addressed.

6.8.7 Initial Phase-2 Model Predictions

6.8.7.1 Introduction

In this section, conservative and reactive tracer breakthrough times are predicted for each of the sampling boreholes for up to one year from the start of Phase-2 injection. This work constitutes the first "blind" prediction on the behavior of the Phase-2 block of the Busted Butte transport test prior to injection. These predictions were made and presented prior to starting Phase-2 injection. These predictions are intended to test the current modeling concepts and tools available to the integrated site-scale model and the validity of the abstractions of that model for performance assessment. The predictions use parameters from currently available Yucca Mountain hydrologic and geochemical databases. At this stage, no model calibration to the UZTT has been performed. As data become available from the various phases of the UZTT, they will be incorporated into refined versions of the model. The new information will be used to make improved predictions.

The computer code FEHM (V2.00, STN: 10031-2.00-00), which was used in the site-scale UZ flow and transport model and its abstractions for performance assessment, is also used in the development of the 3-D model presented in this report. Specifically, this code is used for radionuclide migration predictions using "calibrated" site-scale flow solutions. Although detailed geologic and hydrologic property distributions in three dimensions are not available at present for the UZTT, it is anticipated that during the course of the testing, these data will become available. Three-dimensional effects will probably become important as data specific to the test block become available for the Phase-2 block. The model is, therefore, being developed in three dimensions at the outset to capture these effects and to anticipate the 3-D property database that will be collected for the test block.

6.8.7.2 Model Description

The Phase-2 test block at Busted Butte encompasses, from top to bottom, the lower section of the Topopah Spring Tuff vitrophyre (Tptpv2) and the hydrologic Calico Hills unit (CHn, comprised of Tptpv1 and Tac). The first step in constructing a 3-D finite-element model of the Phase-2 test is to build a finite-element mesh using the coordinates of the injection and collection boreholes. The file used in this work contains the surveyed local coordinates of the boreholes and the layered stratigraphy at the site.

Figure 87 gives a representation of the Phase-2 block with the boreholes represented as colored lines. The simulation block is approximately 7-m high by 12-m deep by 12-m wide and contains 28 boreholes ranging from 7.5 m to 10.0 m in length. The 8 injection boreholes (shown in red) all originate in the left rib of the Test Alcove (located in front of the figure). These boreholes are subparallel, distributed along two horizontal planes, and are perpendicular to the 12 collection boreholes (dark blue) coming from the right rib of the Main Adit (to the left of the vertical *yz* plane). The other boreholes (light blue) are dedicated to ERT and GPR-T measurements.

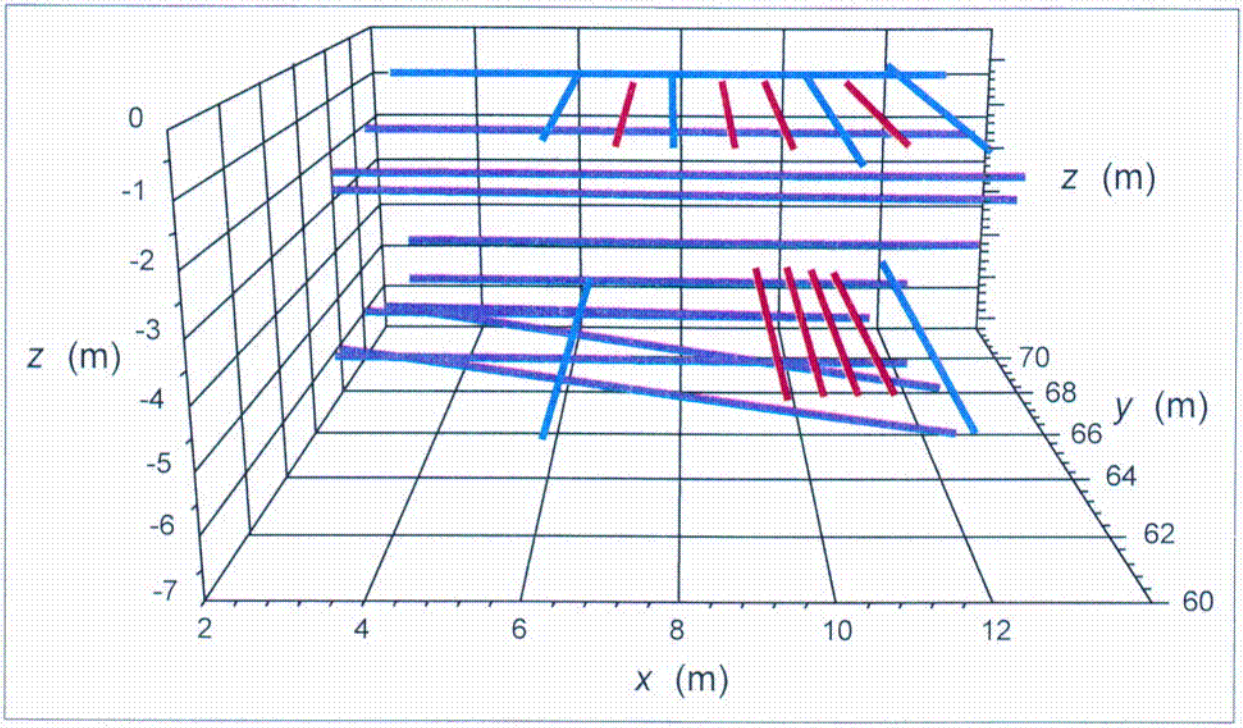

DTN: MO0004GSC00167.000 (for location); LA9909WS831372.022

NOTE: The red lines represent injection boreholes; the dark blue lines collection boreholes; and the light blue lines are devoted to tomography. In this view, the Test Alcove is located in front of the figure, and the Main Adit is to the left of the figure (beyond the $x = 2$ plane). Dimensions are in meters.

Figure 87. Three-Dimensional View of the Injection and Collection Boreholes

The model domain extends from +2 to +14 m in the x-direction, +60 to +72 m in the y-direction, and –8.2845 to +2.5015 m in the z-direction. These coordinates are consistent with the surveyed local coordinates and the stratigraphy of the block. Figure 88 shows a top view of the finite-element grid with the borehole locations.

In general, the mesh was refined at locations between the injection and collection boreholes to accurately capture the migration of the tracers and heterogeneities at scales smaller than the layer thickness. In the x-direction, a grid spacing of 0.25 m at locations close to the boreholes was chosen. In both the x- and y-directions, a coarse mesh spacing at the block boundaries was chosen because no transport is expected at these locations. In the y-direction, a mesh spacing of 0.125 m at locations close to boreholes was chosen. A slightly finer grid spacing was used in the y-direction than the x-direction to capture accurately the location of the injection points, which are spaced 0.61 m apart in the y-direction (10 injection points per injection borehole). In the z-direction, the stratigraphy is represented with 6 distinct layers: 5 layers to represent the Calico Hills hydrogeologic unit (Tac: 3 layers; Tptpv1: 2 layers), and 1 layer to represent Tptpv2. The discretization in the z-direction is dependent on the particular layer because some layers are thicker than others. The discretization ranged from 0.15 to 0.25 m. The entire model is

C20

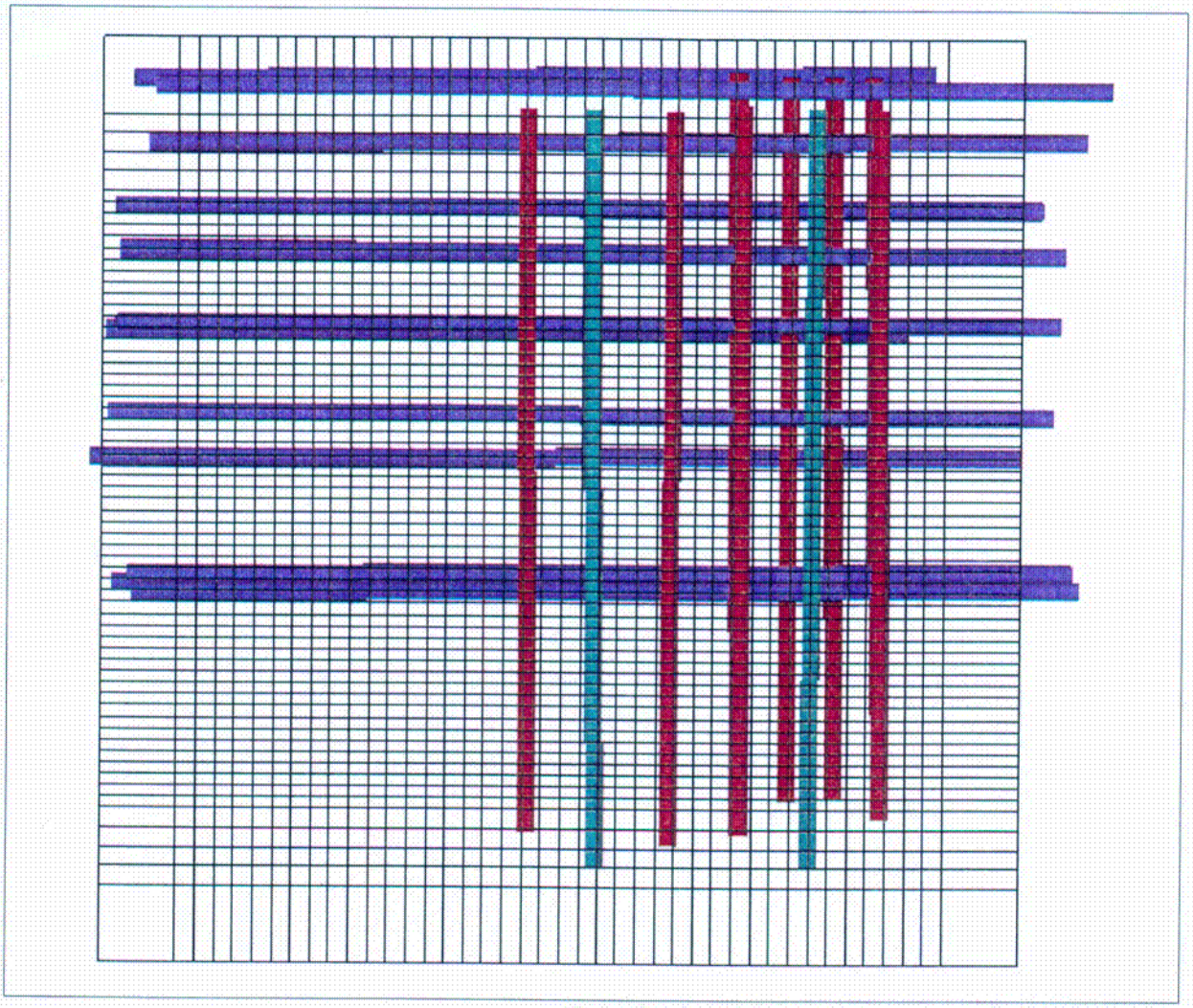

DTN: MO0004GSC00167.000 (for location); LA9909WS831372.022

NOTE: As in Figure 87, injection boreholes are depicted as red lines, collection boreholes as blue, and ERT boreholes as green. The horizontal axis represents the *x*-direction, increasing to the right. The vertical axis represents the *y*-direction, increasing bottom to top.

Figure 88. Top View of Finite-Element Grid and the Injection and Collection Boreholes

comprised of 128,570 nodes. Figures 89 and 90 show views of the grid from the Test Alcove and the Main Adit, respectively. Once the mesh was constructed, the next step was to assign properties to the model. Table 38 contains the property sets used in the different layers. These properties are based upon measurements collected from the same units in the Yucca Mountain area but not actually from Busted Butte.

C21

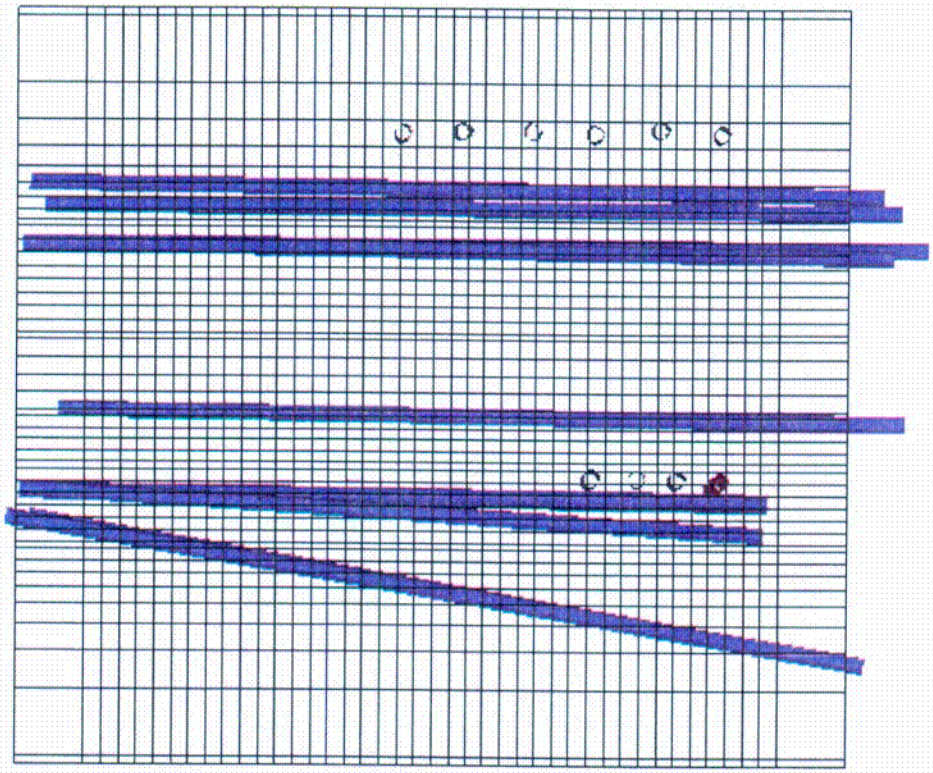

DTN: MO0004GSC00167.000 (for location); LA9909WS831372.022

NOTE: The blue colored lines represent collection boreholes. Because the injection boreholes originate in the Test Alcove, they are perpendicular to the plane of the figure and are depicted as circles. The horizontal axis represents the *x*-direction. The vertical axis represents the *y*-direction.

Figure 89. Finite-Element Grid as seen from the Test Alcove

Table 38. Property Sets for the Phase-2 Test

Busted Butte Layer	Matrix Material (Flint 1998)				Fracture Material					
	Layer	α_m (m^{-1})	n_m	K_m (m^2)	Layer	α_f (m^{-1})	n_f	K_f (m^2)	ϕ_f	θ
Tac1	CHv	3.5	1.19	5×10^{-12}	CH1v	11.52	3.0	2.43×10^{-9}	7.14×10^{-5}	0.5
Tac2	CHv	3.5	1.19	5×10^{-12}	CH1v	11.52	3.0	2.43×10^{-9}	7.14×10^{-5}	0.5
Tac3	CHv	3.5	1.19	5×10^{-12}	CH1v	11.52	3.0	2.43×10^{-9}	7.14×10^{-5}	0.5
Tptpv1	BT1	0.56	1.31	1×10^{-13}	CH1v	11.52	3.0	2.43×10^{-9}	7.14×10^{-5}	0.5
Tptpv1	BT1	0.56	1.31	1×10^{-13}	CH1v	11.52	3.0	2.43×10^{-9}	7.14×10^{-5}	0.5
Tptpv2	PV2	2.2	1.25	1×10^{-16}	TSW2	0.91	2.92	6.6×10^{-9}	1.29×10^{-4}	0.25

DTN: LA9909WS831372.022, LB970601233129.001

NOTE: Here, α and n are the van Genuchten parameters, K is permeability, ϕ is volume fraction, and θ is porosity. The subscript m signifies matrix material and the subscript f signifies fracture material.

C22

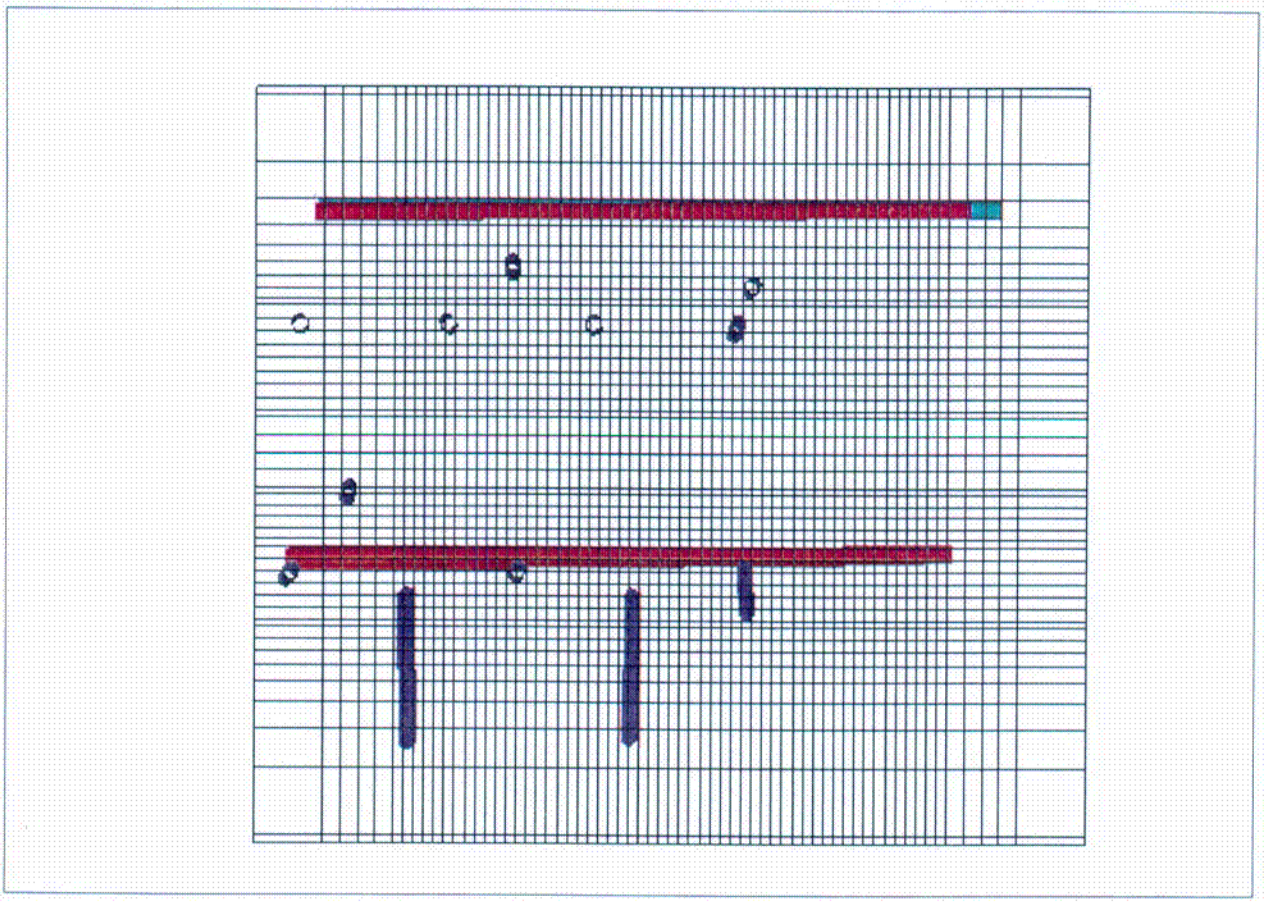

DTN: LA9909WS831372.022

NOTE: The horizontal red lines represent the location of injection boreholes, which are perpendicular to the collection boreholes (blue). The collection boreholes originate in the Main Adit, but several are plunging down and, thus, appear as blue lines rather than circles. The green line represents one of the tomography boreholes. The horizontal axis represents the *y*-direction, and the vertical axis represents the *z*-direction.

Figure 90. Finite-Element Grid as seen from the Main Adit

For this preliminary investigation, layers 1 through 3 were combined into a single Calico Hills unit (Tac), layers 4 to 5 were assigned Tptpv1 properties, and layer 6 was assigned Tptpv2 properties. As additional data become available, layers 1 through 3 and 4 through 5 will all be treated as distinct layers. Porosity values were obtained from a few samples from the Busted Butte site. Permeabilities and van Genuchten relative-permeability parameters for the matrix were obtained from Flint (1998). This study (Flint 1998) was chosen because it represents the existing YMP database for the unsaturated zone and contains sufficient samples to generate statistics on the variability of key parameters, such as matrix permeability and matrix van Genuchten parameters. Fracture van Genuchten parameters were taken from the "calibrated" flow model in DTN: LB970601233129.001. These data were obtained by fitting field data at the site scale. Although there is a great amount of uncertainty in fracture properties, this data set is considered to be a reasonable representation of YMP material properties applicable to Busted Butte.

For this "blind" investigation, and in view of the absence of data on fracture-matrix interactions in the Calico Hills, the equivalent-continuum model (ECM) was used to model Phase 2. The

C23

ECM was also used in scoping calculations done during design of the test and is currently being used to understand both Phases 1A and 1B.

Tracer breakthrough has occurred in the 10 mL hr^{-1} injection system of Phase 1B (borehole 6). Specifically, tracer was detected at the pad 35 days after injection. This result means the time of breakthrough occurred between 28 and 35 days in relation to the collection-pad schedule. To compare model predictions with test breakthrough times as defined by the appearance of fluorescein tracer on a collection pad, the concentration of the tracer must be known. For example, if the time of breakthrough is defined to be when the normalized concentration reaches 0.5, then for Tptpv2, the ECM predicts a breakthrough at 47 days for a distance traveled by the tracer of 28 cm (Figure 91). At a normalized concentration of 0.3, the model predicts breakthrough at 31 days for the same distance, which is close to the observed breakthrough time for borehole 6.

For the first phase of predictive modeling and in the absence of appropriate data, the property sets listed in Table 38 were used with no attempt at calibration. The background flow conditions were obtained by setting a capillary pressure at the top and bottom boundaries and allowing the block to equilibrate to a steady-state saturation profile. A capillary pressure of 200 m of water was chosen, which is within the range of capillary-pressure measurements at Yucca Mountain (Altman et al. 1996, p. 34). The capillary pressure was set so that a saturation of about 0.35 to 0.45 was obtained in the block. Moisture measurements and preliminary porosity data from test-block lithologies indicate that these saturation values are reasonable. Once the background conditions are set, the next step is to begin pumping and injecting tracer.

Three different pumping rates were used for injection boreholes in the Phase 2 experiment: (a) 1 mL hr^{-1} (1 upper borehole), (b) 10 mL hr^{-1} (4 lower boreholes), and (c) 50 mL hr^{-1} (3 upper boreholes). The 1 mL hr^{-1} rate is equivalent to an infiltration rate of approximately 30 mm yr^{-1}, which is well within the range of infiltration rates at Yucca Mountain. The predictions made (given below) show that during a 1-yr test, the 1 mL-hr^{-1} pumping rate is not expected to transport any tracer to the sampling boreholes. Injection borehole 23 will be the only one that pumps at 1 mL hr^{-1}. The 10-mL-hr^{-1} injection rate is equivalent to an infiltration rate of approximately 380 mm yr^{-1}, which is slightly higher than the highest anticipated infiltration that could occur at Yucca Mountain. The lower injection boreholes 24, 25, 26, and 27 will operate at 10 mL hr^{-1}. Finally, 50 mL hr^{-1} is equivalent to an approximate infiltration rate of 1550 mm yr^{-1}. This infiltration rate is far higher than what is expected at Yucca Mountain even under wetter, future climate scenarios. The purpose of the 50 mL hr^{-1} rate is to obtain enough separation in travel times between the conservative and reactive tracers so as to be visible and distinct in the field test. Injection boreholes 18, 20, and 21 will pump continuously at 50 mL hr^{-1}.

6.8.7.3 Predictions

The predictions below are borehole specific and can, therefore, be used to compare directly to test-block results. Phase-2 borehole numbers and relative locations were presented in Figure 38 (Section 6.8.2.4.1). Table 39 shows the distance between the closest sampling point and the

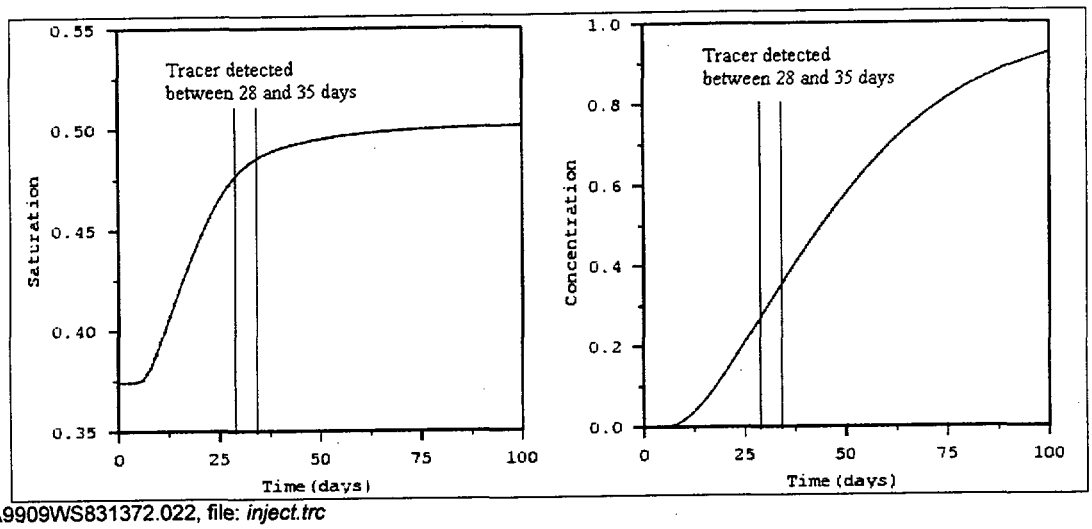

DTN: LA9909WS831372.022, file: *inject.trc*

NOTES: The plots show the conservative breakthrough of tracer 28 cm from the injection pad: (a) saturation breakthrough, (b) concentration breakthrough

Figure 91. Phase-1B Breakthrough Predictions Using Equivalent-Continuum Model and Tptpv2 Properties

Table 39. Closest Sampling Point to the Injection Planes Within Each Collection Borehole

Collection borehole	Distance from top injection plane (m)	Collection borehole	Distance from bottom injection plane (m)
16	0.61	46	0.175
17	0.80	48	0.175
14	1.17	9	0.175
15	1.17	10	0.59 (above plane)
13	1.17		
12	1.17		

DTN: LA9909WS831372.022

injection planes. Tables 40 through 48 predict the tracer breakthroughs at each of these locations.

For all predictions, three criteria were used for tracer-breakthrough times: (a) a 5% concentration limit, (b) a 50% concentration limit, and (c) the concentration after 1 year from the time of injection (the time of submittal of results for TSPA-LA). Note that it was assumed that the concentration of tracer in the injection fluid is unity. Also, note that tracers are continuously injected for the duration of the test.

A diffusion coefficient of 1×10^{-11} m^2 s^{-1} was used for all tracers. Longitudinal and transverse dispersivities were zeroed out for this preliminary set of calculations. However, as with any finite-element model, some numerical dispersion is present. Due to the fine mesh spacing and small time steps taken in these simulations, numerical dispersion is not expected to play a significant role in these simulations. A bulk-rock density of 2,580 kg m^{-3} was used for all layers. This parameter only affects the reactive-tracer breakthrough times. As more data become available, all of these parameters will be adjusted. However, the values chosen are reasonable representations of Yucca Mountain properties, given the existing database.

Conservative Tracers

Travel times were first predicted for fluorescein, a conservative tracer. Uniform properties were assumed for porosity, permeability, and van Genuchten model parameters within each of the six layers of the test block. The effect of heterogeneous property distributions is discussed at the end of this subsection. Figure 92 depicts a concentration plume for fluorescein after 1 year.

Table 40. Fluorescein from Upper Injection Boreholes

Borehole number	5% Breakthrough concentration	50% Breakthrough concentration	Normalized concentration at 1 yr
16	27 days	68 days	1.0
17	48 days	118 days	1.0
14	118 days	238 days	0.87
15	103 days	218 days	0.90
13	103 days	218 days	0.90
12	212 days	> 1 yr	0.46
Remaining collection boreholes	> 1 yr	> 1 yr	0.0

DTN: LA9909WS831372.022, file: *cons.trc*

Table 41. Fluorescein from Lower Injection Boreholes

Borehole number	5% Breakthrough concentration	50% Breakthrough concentration	Normalized concentration at 1 yr
46	4 days	30 days	1.0
48	20 days	91 days	0.98
9	53 days	166 days	0.91
10	171 days	> 1 yr	0.37

DTN: LA9909WS831372.022, file: *cons.trc*

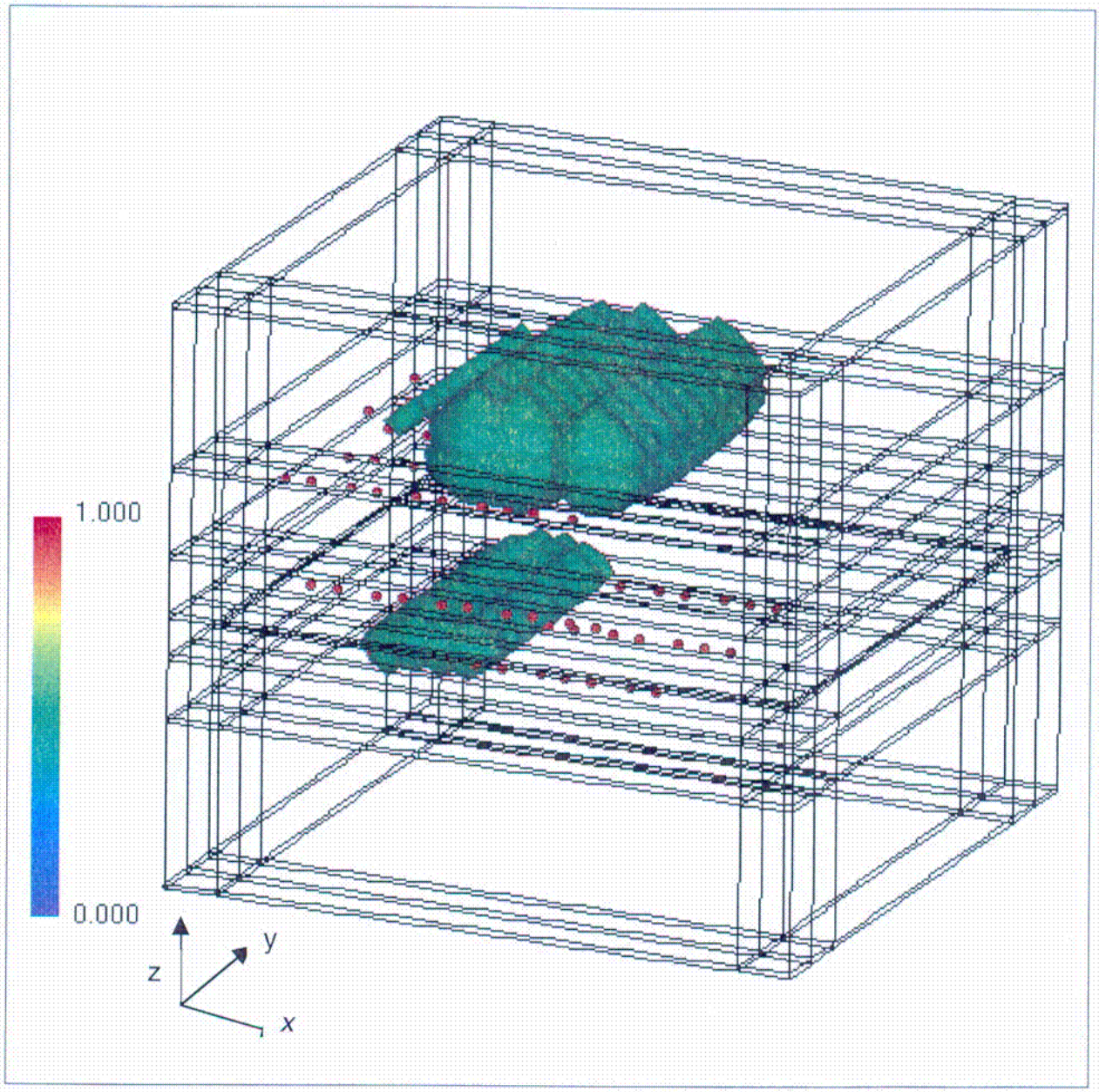

DTN: LA9909WS831372.022, file: *inject.10004_con_node*

NOTES: The figure depicts the concentration plume after 1 year of conservative-tracer injection. The green isosurface represents a normalized concentration of 0.5; the red dots represent the sampling points along the collection boreholes.

Figure 92. A Conservative Tracer Concentration Plume

C24

Tables 40 and 41 show the predicted breakthrough times of tracer for the upper and lower collection sampling points, respectively. As expected, sampling locations closer to the injection planes exhibit tracer breakthrough times that are earlier than those from more distant locations. As discussed in the next section, for simulations involving heterogeneous property distributions, this result may be modified due to preferential flow paths. The results indicate that tracer breakthrough is expected at several sampling locations within the first year, and some are expected within the first month. Conservative tracer breakthroughs could occur at earlier times than predicted by the ECM model if the model assumptions are erroneous. Fracture flow through Tptpv2, for example, could result in faster travel times. Even so, an additional year of operation may be required to achieve transport distances on the order of the entire length of the block.

Nonconservative Tracers

Table 42 shows the distribution coefficients, K_d, for the reactive, nonconservative tracers determined by parallel laboratory studies and used in Phase 2 for the various units. The measurements are preliminary but provide a starting point for the modeling effort. Travel times for reactive tracers are extremely sensitive to these distribution coefficients, and errors in these parameters strongly bias the results. One major deficiency in the preliminary measurements is that these results do not include reversible sorption, and equilibrium may not have been achieved when obtaining the distribution coefficients.

Table 42. Retardation of Reactive Tracers

Tracer	Tptpv1, Tac K_d (mL g^{-1})	Tptpv2 K_d (mL g^{-1})
Lithium	1.0	0.0
Manganese	15.6	6.5
Nickel/cobalt	34.0	13.0

DTN: LA9909WS831372.022

The next set of tables shows the predicted breakthroughs for the three reactive tracers: lithium Tables 43 and 44), manganese (Tables 45 and 46), and nickel or cobalt (Tables 47 and 48).

The data indicate that lithium does not sorb in Tptpv2 but mildly sorbs in Tac and Tptpv1. Although lithium sorption in Tac is mild when compared to manganese and nickel or cobalt, the sorption has a large effect on travel times over the time scale of interest. The lithium only breaks through at locations that are extremely close to the injection boreholes (i.e., boreholes 16, 17, 46, 48 and 9).

Manganese is predicted to sorb much more strongly than lithium. For this reason, manganese is only expected to break through at boreholes 46 and 48 within a one-year time span. Cobalt or nickel sorbs even more strongly than manganese and is not expected to break through at any of the boreholes during the time of the test.

Table 43. Lithium from Upper Injection Boreholes

Borehole number	5% Breakthrough concentration	50% Breakthrough concentration	Normalized concentration at 1 yr
16	52 days	193 days	0.79
17	257 days	> 1 yr	0.12
14	> 1 yr	> 1 yr	0.0
15	> 1 yr	> 1 yr	0.02
13	> 1 yr	> 1 yr	0.0
12	> 1 yr	> 1 yr	0.0
Remaining collection boreholes	> 1 yr	> 1 yr	0.0

DTN: LA9909WS831372.022, file: *chem.trc*

Table 44. Lithium from Lower Injection Boreholes

Borehole number	5% Breakthrough concentration	50% Breakthrough concentration	Normalized concentration at 1 yr
46	28 days	267 days	0.62
48	63 days	327 days	0.55
9	242 days	> 1 yr	0.12
10	> 1 yr	> 1 yr	0.0

DTN: LA9909WS831372.022, file: *chem.trc*

There are many caveats that could strongly affect the predicted travel times of the reactive tracers. First, the model is extremely sensitive to the values of K_d, and the current K_d measurements are uncertain at this time. A simple K_d may not be sufficient to model sorption of these tracers due to chemical heterogeneities and nonlinear reactions. Finally, these immobile reactive tracers may sorb onto colloids, thereby enhancing their mobility.

Heterogeneous System

A major assumption of the above modeling results is that properties are homogeneous within a layer. In this section, the effects of the heterogeneity of properties within the layers are explored. In these simulations, permeability values are distributed within each layer. The means of the permeability values for each layer are assumed to be the same as the permeability values used in the homogeneous simulations. In each layer, a log-normal distribution of permeability with a ln (k) variance of 2.0 and a correlation length of 1 m in the x, y and z directions is assumed. In the Tac and Tptpv1 units, an equation has been proposed to represent the correlation between the van Genuchten parameter α_m and matrix permeability (Altman et al. 1996, unnumbered equation on p. 34). To explore the sensitivity of the model results to this type of correlation, this relation is used to distribute α_m throughout these units.

Table 45. Manganese from Upper Injection Boreholes

Borehole number	5% Breakthrough concentration	50% Breakthrough concentration	Normalized concentration at 1 yr
16	> 1 yr	> 1 yr	0.0
17	> 1 yr	> 1 yr	0.0
14	> 1 yr	> 1 yr	0.0
15	> 1 yr	> 1 yr	0.0
13	> 1 yr	> 1 yr	0.0
12	> 1 yr	> 1 yr	0.0
Remaining collection boreholes	> 1 yr	> 1 yr	0.0

DTN: LA9909WS831372.022, file: *chem.trc*

Table 46. Manganese from Lower Injection Boreholes

Borehole number	5% Breakthrough concentration	50% Breakthrough concentration	Normalized concentration at 1 yr
46	277 days	> 1 yr	0.06
48	328 days	> 1 yr	0.06
9	> 1 yr	> 1 yr	0.0
10	> 1 yr	> 1 yr	0.0

DTN: LA9909WS831372.022, file: *chem.trc*

Figure 93 shows the background saturation profile and the saturation profile after one year of continuous injection. The saturation profile shows that the 50 mL hr^{-1} boreholes have a strong effect on the saturation profile. This effect is for two reasons, including the obvious reason that 50 mL hr^{-1} is the high injection rate. The second reason is that the 50 mL hr^{-1} boreholes inject into the Tptpv2 layer, which has a much lower matrix permeability than the Calico Hills hydrogeologic unit (Tac and Tptpv1). The 10-mL hr^{-1} injections in the Tac unit do not have a large effect on the saturation profile. The simulations indicate that capillary action is an important process around the 10 mL hr^{-1} injections, which is mostly due to the high matrix permeabilities in this unit.

Table 47. Nickel or Cobalt from Upper Injection Boreholes

Borehole number	5% Breakthrough concentration	50% Breakthrough concentration	Normalized concentration at 1 yr
16	> 1 yr	> 1 yr	0.0
17	> 1 yr	> 1 yr	0.0
14	> 1 yr	> 1 yr	0.0
15	> 1 yr	> 1 yr	0.0
13	> 1 yr	> 1 yr	0.0
12	> 1 yr	> 1 yr	0.0
Remaining collection boreholes	> 1 yr	> 1 yr	0.0

DTN: LA9909WS831372.022, file: *chem.trc*

Table 48. Nickel or Cobalt from Lower Injection Boreholes

Borehole number	5% Breakthrough concentration	50% Breakthrough concentration	Normalized concentration at 1 yr
46	> 1 yr	> 1 yr	0.0
48	> 1 yr	> 1 yr	0.0
9	> 1 yr	> 1 yr	0.0
10	> 1 yr	> 1 yr	0.0

DTN: LA9909WS831372.022, file: *chem.trc*

Tables 49 and 50 show the breakthrough times for two realizations. As expected, heterogeneities do add some fluctuations in the trends observed previously; however, many of the trends still hold.

6.8.7.4 Summary and Interpretation

This section constitutes a preliminary "blind" prediction of the behavior of the Phase-2 block of the UZTT at Busted Butte. The prediction is intended to test the current modeling concepts and tools available to the integrated site-scale model and their abstractions for performance assessment. This prediction uses parameters from the available Yucca Mountain hydrologic and geochemical databases and is considered to be preliminary because calibrations have not been performed using information from Busted Butte.

Modeling results for fluorescein, a conservative tracer, indicate that tracer breakthrough is expected at several sampling locations within the first year of testing. For some sampling locations, tracer breakthrough is predicted for travel times of less than a month. Tracer breakthroughs could be even quicker than predicted if the ECM assumption does not hold.

Table 49. Fluorescein from Upper Injection Boreholes with Physical Heterogeneities

Borehole number	5% Breakthrough concentration		50% Breakthrough concentration		Normalized concentration at 1 yr	
	Real.* 1	Real. 2	Real. 1	Real. 2	Real. 1	Real. 2
16	28 days	36 days	70 days	106 days	1.0	0.96
17	70 days	60 days	238 days	161 days	0.7	0.91
14	173 days	170 days	> 1 yr	> 1 yr	0.35	0.38
15	126 days	126 days	278 days	267 days	0.72	0.76
13	118 days	142 days	247 days	347 days	0.80	0.54
12	222 days	247 days	> 1 yr	> 1 yr	0.42	0.29
Remaining collection boreholes	> 1 yr		> 1 yr	> 1 yr	0.0	0.0

DTN: LA9909WS831372.022, files: *real1.trc* and *real2.trc*

NOTE: *Real. = realization

Table 50. Fluorescein from Lower Injection Boreholes with Physical Heterogeneities

Borehole number	5% Breakthrough concentration		50% Breakthrough concentration		Normalized concentration at 1 yr	
	Real.* 1	Real. 2	Real. 1	Real. 2	Real. 1	Real. 2
46	4 days	4 days	37 days	32 days	1.0	1.0
48	24 days	22 days	106 days	96 days	0.97	0.98
9	52 days	47 days	156 days	> 1 yr	0.94	0.94
10	197 days	202 days	> 1 yr	> 1 yr	0.28	0.26

DTN: LA9909WS831372.022, files: *real1.trc* and *real2.trc*

NOTE: *Real. = realization

Fracture flow through the Topopah Spring (Tptpv2) could result in faster travel times. The fracture parameters for the van Genuchten model are not known to a high degree of accuracy. Another caveat in these modeling results is the effect of physical heterogeneities within each layer. Small-scale heterogeneities could result in preferential flow paths, which results in faster flow paths in some parts of the block and slower flow paths in other parts of the block. Monte Carlo simulations and more elegant stochastic techniques could be employed to capture the uncertainty in the travel times.

More uncertainty exists in the predicted travel times of the reactive tracers when compared with the conservative-tracer predictions. The strongly sorbing tracers manganese and cobalt (or nickel) are not expected to break through within the first year of testing. Even weakly sorbing

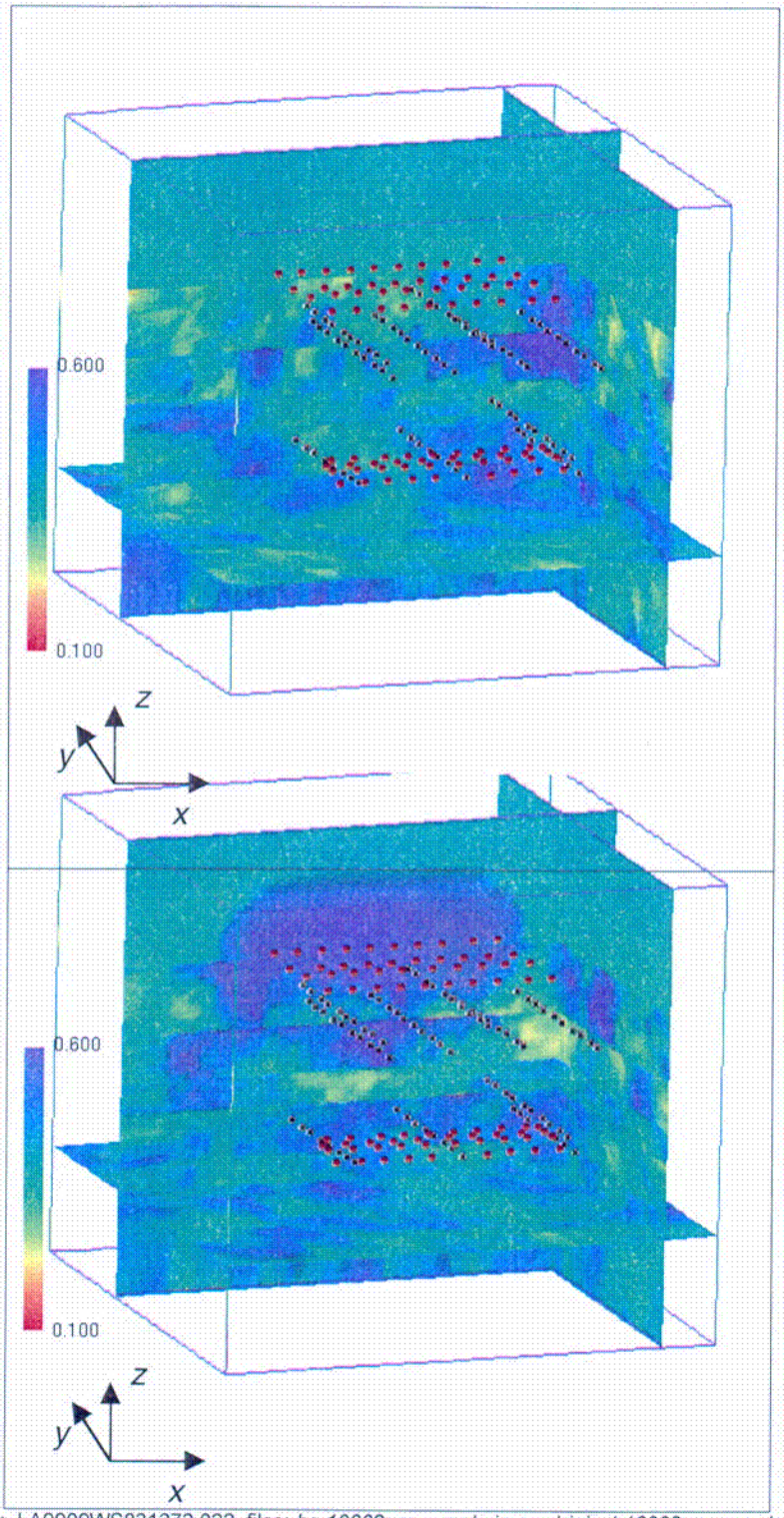

DTN: LA9909WS831372.022, files: *bg.10002_sca_node.inp* and *inject.10002_sca_node.inp*

NOTES: These saturation profiles are from 10 to 60% of the heterogeneous Realization 1: (a) background saturation, (b) saturation profile after 1 yr of injection. In the figure, injection points are red dots and collection points are blue dots.

Figure 93. Predicted Saturation Profiles for Phase 2

C25

lithium only reaches a few collection boreholes. Therefore, an additional year of operation may be required to achieve transport distances that reach more sampling points. At this stage, it is important to note that the model is extremely sensitive to the values of K_d used, which are preliminary. In addition, a linear K_d model may not be sufficient to model sorption of these tracers due to chemical heterogeneities and nonlinear reactions. More rigorous reactive transport models could be used to check the linear K_d assumption. Finally, these immobile reactive tracers may sorb onto colloids, thereby enhancing their mobility.

6.8.8 Model Validation

Model validation is a process to demonstrate and document that a model is appropriate and adequate for its intended use. Models used in this AMR express a conceptual model of unsaturated flow as mathematical equations, which are solved by computer codes that execute numerical methods. Input to the problem includes rock properties and, in the case of FEHM V2.00 (STN: 10031-2.00-00), a mesh or grid that expresses the geometry. Validation includes developing confidence in the grid, the input values, and the conceptual and numerical models embedded in the code.

The conceptual model underlying the models used in this AMR is the standard model of unsaturated Darcy flow with constitutive relationships defined by either van Genuchten or Gardner-Russo equations (van Genuchten 1980; Gardner 1958; Russo 1988), which are generally accepted by the scientific community. For this work, all rock property values were measured on samples either from the Busted Butte site or from the same geologic units at Yucca Mountain (Table 1e). Mesh validation was done by plotting the location of features such as boreholes and geologic contacts and comparing them visually with the known geometry, such as shown in Figures 34, 45, and 87. The codes were validated by comparing outputs for simple problems against analytical solutions where such exist. Close correspondence between the analytical and numerical methods was judged visually by inspection of plotted output. Output was also inspected visually to ensure that the behavior of the system conformed to what is expected for this conceptual model.

The UZTT is an integration of field experiment, laboratory analysis, and conceptual and numerical simulation. The UZTT is designed to verify and validate the project's ability to capture transport, dispersion, fracture flow, and other features significant to the Yucca Mountain site in a computational model.

The UZTT applies a variety of computer codes for the computational analyses. The primary flow and transport modeling code being used is FEHM. Computational grids for FEHM were generated using LAGRIT V1.0 (STN: 10212-1.0-00). The software code STO-UNSAT V1.0 (STN: 10292-1.0LV-00) is used for stochastic flow modeling. STO-UNSAT numerically solves the moment differential equations that describe transient unsaturated flow in randomly heterogeneous porous media (Zhang 1999). Verification of this code included running solutions to steady state and then comparing with published one- and two-dimensional steady-state solutions (Zhang et al. 1998; Zhang and Winter 1998). All other computational tools used are standard commercial software as listed in Section 3.0 of this AMR.

Computational grids were generated using site data from the TDMS (Table 1e). Domain size, stratigraphy, and borehole configuration were taken from site survey data and measurements. These configurations generated by LAGRIT were visually compared against the input data and judged to be accurate representations of these data. The correctness of the computational grids themselves was tested by running simple steady-state flow- and heat-conduction simulations with homogeneous material properties. Phase-1A deterministic and Monte Carlo simulations and Phase-2 simulations were run using FEHM V2.00, which is the primary code used to simulate the flow and transport of the field experiment. FEHM was chosen because it is the code that will be used to simulate flow and transport at the proposed repository for PA. FEHM has been used extensively within the YMP, and no modifications of FEHM were made for the UZTT modeling. In addition to extensive verification and validation of FEHM reported in Dash et al. (1997), these FEHM simulations were initially validated for simple homogeneous flow under uniform saturation. Plots of model results at a range of saturations showed the expected transition from capillary-dominated to gravity-dominated between 60% and 90% initial saturation. This agreement with expected behavior and the previously documented agreement with analytical solutions (Dash et al. 1997) indicates that the computational code was running correctly for this configuration (Soll 1997, pp. 18 to 26).

Material properties used in the model were either site-specific when available or otherwise were derived from field and laboratory measurements made at or near Yucca Mountain. The ultimate validation of the UZTT models will be with data collected from the UZTT itself. The model results presented in this AMR are predictions that will be compared against actual field results. Full validation of these models at this time is, thus, premature. The only data currently available to validate the Phase-2 FEHM model qualitatively are those depicting the first detection of fluorescein (Figure 91). The Phase-2 model reported here adequately met the criterion that the tracer concentration predicted in the time interval when breakthrough actually occurred must be between 25% and 75%.

STO-UNSAT, a stochastic differential equation code for modeling flow and transport, was used to develop a 2-D model for Phase-1A predictions. The STO-UNSAT model was validated by first running a simple homogeneous case (Zhang and Winter 1998, Figures 1 and 2) and comparing against the analytical results derived in Zhang et al. 1998 (Equations 63 and 46, respectively). Good agreement was also found between Phase-1A stochastic simulations using STO-UNSAT and Phase-1A deterministic predictions using the FEHM model. Further examples are contained in Zhang 1998 (pp. 12 to 21, 76).

Note that the UZTT is itself a model validation process. As additional data become available, they will be incorporated into the UZTT computational models to improve their representativeness. Validation of the UZTT models to date has shown that they adequately reproduce input data and provide similar results in comparison tests. Because of the limited comparisons of UZTT model predictions and test data that are available to date, a final conclusion regarding the validity of these models for simulating the test conditions and environments of the UZTT cannot be made at this stage of the testing and modeling program. However, the results obtained thus far, as described in this AMR, support the conclusion that these models are adequate for their intended use.

6.8.9 Summary: Implications for Performance Assessment

The UZ transport test is designed to provide information suitable for assessing the validity of flow and transport models used in the site characterization and performance assessment programs for Yucca Mountain. Observations of the available data collected to date for Phase 1 and Phase 2, and the modeling of these data, lead to several key conclusions of relevance to performance assessment. These conclusions are summarized below, categorizing them with respect to the particular field or modeling activity in this report.

1. *Laboratory measurements*: The collection of unsaturated hydrologic property data using the UFA provides data of particular relevance to flow and transport models because they are direct measurements under unsaturated conditions rather than indirect, model-derived parameters. The Monte Carlo analyses (Section 6.8.6) indicate that the nature of the correlations between parameters such as permeability and the van Genuchten α parameter have a strong impact on the predictability of the flow and transport system. Therefore, additional measurements of hydrologic and transport parameters under unsaturated conditions could be used to constrain models and develop correlations.

2. *Phase-1A and -1B model results*: In addition to the point just made, the modeling analyses for Phase 1A indicate that strong capillary forces in the rock matrix of the Tac unit are likely to modulate fracture flow from overlying units, thereby damping pulses of infiltrating water and providing a large degree of contact between radionuclides and the rock matrix. Several modeling approaches, from deterministic to Monte Carlo and stochastic models, were used to simulate the Phase-1A experiments (Sections 6.8.6 and 6.8.7). All yielded similar qualitative results. From this we conclude tentatively that the deterministic modeling approach taken at the site scale may be adequate. The parameterizations used in performing these calculations must be evaluated after data from the UZTT are available.

   A particularly interesting observation from the Phase-1B experiment is that, even when injection occurs immediately adjacent to a fracture, water appears to be imbibed quickly into the surrounding matrix. The transport times observed immediately below the injection point were on the order of 30 days, whereas pure fracture flow would have resulted in travel times of minutes to hours at this flow rate. Site-scale models must be evaluated in light of this observation. Models that predict significant fracture flow at percolation rates low enough for the matrix to transmit the flow may be inconsistent with the Phase-1B experiment.

3. *Phase-2 modeling*: Significant uncertainties uncovered by the modeling include the adequacy of continuum models in nonwelded units of high matrix permeability and the nature of the transition from fracture flow to matrix flow at contacts between hydrogeologic units. These are exactly the issues being studied within the UZTT.

Primary focus over the past year has been on flow and transport field data collection. Data collection/analysis for Phase 2 will be continuing through September 2000, with continuing compilation, analysis, and interpretation of the field data.

6.9 C-WELLS FIELD AND LABORATORY TRANSPORT TESTING

6.9.1 Introduction

To test conceptual SZ transport models for YMP, two major cross-hole, forced-gradient tracer tests were conducted at the C-wells (UE-25c#1, c#2, and c#3), which are located approximately 2 km southeast of the potential repository footprint (Figure 94), and completed in fractured volcanic tuffs. Groundwater flow at this location is thought to be toward the southeast, which puts the C-wells directly downgradient of the southern end of the potential repository. The tracer tests were conducted in two different saturated intervals that differed in horizontal hydraulic conductivity by about 2 orders of magnitude: the lower Bullfrog Tuff, with a conductivity of 27 to 52 m d^{-1} (Geldon et al. 1997, p. 34 in Hydraulic Tests section), and the lower Prow Pass Tuff, with a conductivity of 0.8 to 1.0 m d^{-1} (Reimus et al. 1999, p. A.7). Figure 95 depicts the hydrogeology of the C-wells and shows the packer locations in the tracer tests. Note from Figure 95 that the vast majority of the water produced at the C-wells comes from a small number of relatively discrete zones, most of which are located in the lower half of the Bullfrog Tuff. Both tracer tests were conducted between wells c#2 and c#3 (a linear distance of approximately 30 m), with c#3 being the production well in the Bullfrog Tuff test and c#2 the production well in the Prow Pass Tuff test.

The two tracer tests featured the simultaneous injection of several different tracers having different physical and chemical characteristics: (1) nonsorbing solutes with different diffusion coefficients (Br^- and pentafluorobenzoate), (2) a weakly-sorbing solute (Li^+), and (3) carboxylate-modified latex (CML) polystyrene microspheres, which served as colloidal tracers (Reimus et al. 1999, pp. 5.1-5.2 and C.1-C.2). Two additional tracer tests in the Bullfrog Tuff were conducted, each of which involved the injection of only a single nonsorbing solute (Reimus et al. 1999, Appendix C, Section C.2). These additional tests were conducted primarily to determine the optimal injection well for the test involving multiple tracers, and they will not be discussed further here except in the context of how they supported the interpretation of the multiple tracer test in the Bullfrog Tuff. The simultaneous injection of multiple tracers offers significant advantages over single tracer injections because it allows transport processes to be better distinguished and quantified by comparing the responses of the different tracers.

A series of laboratory studies were conducted in parallel with the field testing efforts to help support and constrain the interpretations of the field tests. These studies included (1) batch-sorption tests to characterize Li^+ sorption to C-wells tuffs, (2) diffusion-cell tests to determine matrix diffusion coefficients of tracers used in the field, and (3) dynamic-transport tests to study tracer transport in fractured and crushed tuffs under more controlled conditions than in the field. The batch-sorption tests and dynamic-transport tests have provided estimates of lithium sorption parameters for comparison with sorption parameters derived from the field tests. Such comparisons are important because they offer an indication of whether laboratory-derived radionuclide sorption parameters can be used defensibly in field-scale predictive calculations.

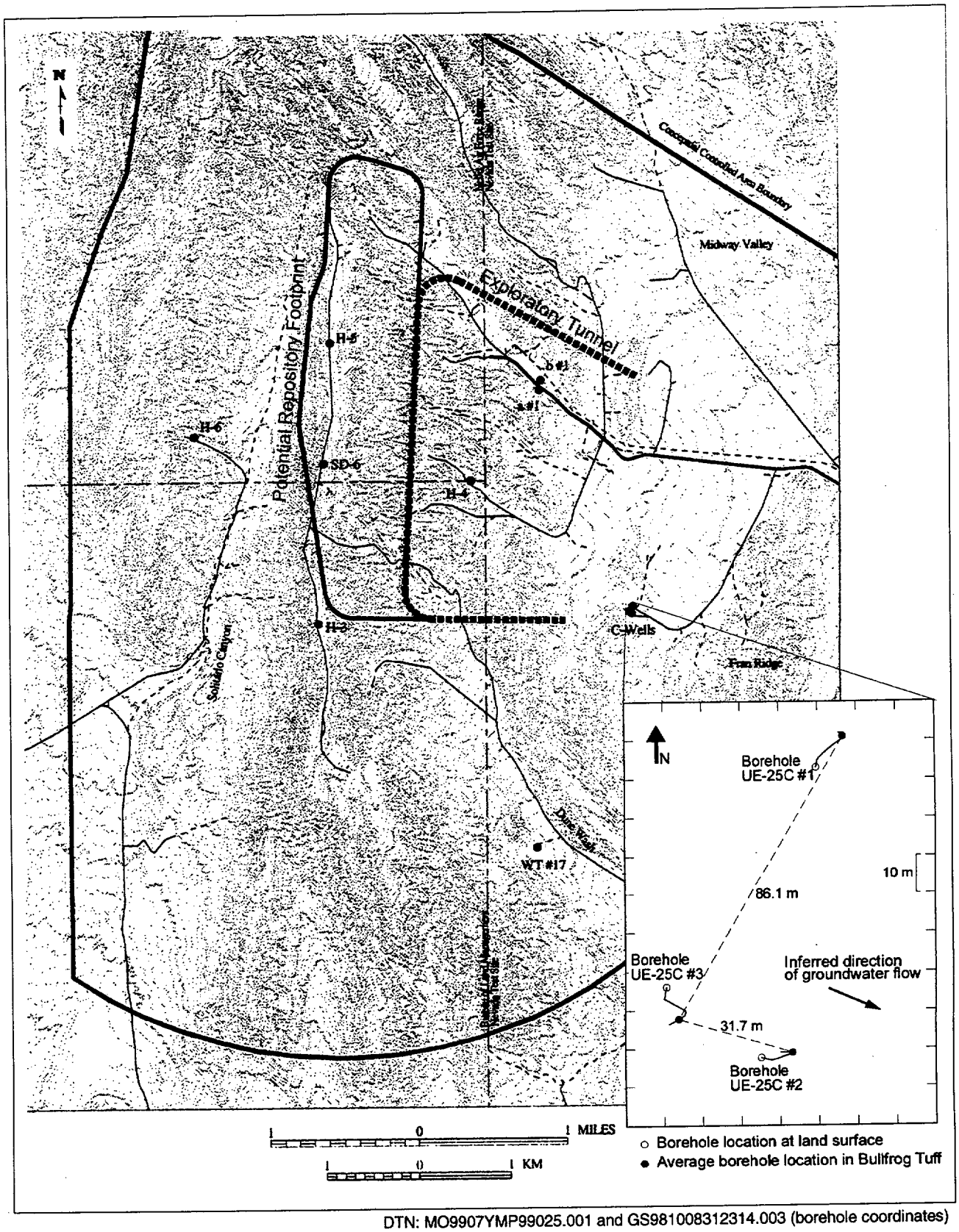

DTN: MO9907YMP99025.001 and GS981008312314.003 (borehole coordinates)

Figure 94. Location and Layout of the C-Wells Complex

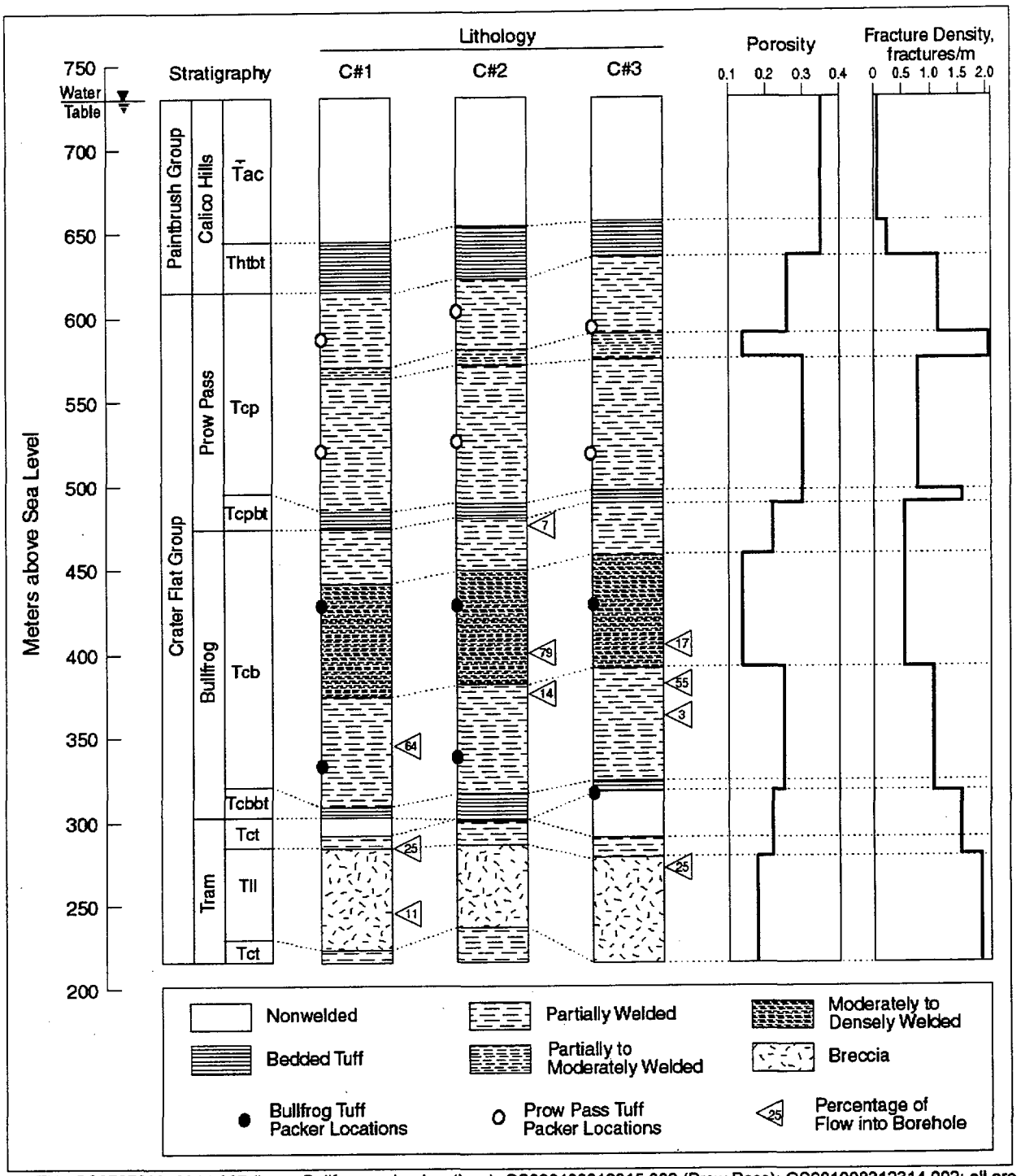

DTN: GS970708312314.007 (lower Bullfrog packer locations); GS990408312315.002 (Prow Pass); GS981008312314.002; all are reference only

NOTE: Packer locations indicate intervals in which hydraulic and tracer tests were conducted (the two tracer tests involving multiple tracers were conducted between c#2 and c#3). Packer locations for lower Bullfrog tests were derived from Geldon et al. (1997, Table 2). Porosity data are from Geldon (1993, Table 13), and fracture density data are from Geldon (1993, Tables 6 and 7); these data sets are shown only for reference purposes and have not been used in any of the analyses discussed in this report.

Figure 95. Stratigraphy, Lithology, Matrix Porosity, Fracture Density, and Inflow from Open-Hole Flow Surveys at the C-Wells

6.9.2 Summary of Field Test Results and Interpretations

Figure 96 shows the normalized tracer responses (concentrations divided by injection masses) in the multiple tracer test in the Bullfrog Tuff. Figure 97 shows the normalized tracer responses in the Prow Pass multiple tracer test. Note that the concentrations and times for the Bullfrog Tuff test in Figure 96 are shown on log-log axes. The test conditions and tracer injection masses in the two tests are described in detail in Reimus et al. (1999), Chapter 5 (Prow Pass Tuff) and Appendix C (Bullfrog Tuff). Both tests featured partial recirculation of the water produced from the pumped well: ~3.5% recirculation in the Bullfrog Tuff and ~30% recirculation in the Prow Pass Tuff.

The most striking feature of the tracer breakthrough curves in the Bullfrog Tuff test (Figure 96) is their bimodal (double-peaked) behavior. This behavior is attributed to a relatively small fraction (~13%) of the tracer solution exiting the injection borehole in short-residence-time pathways in the upper half of the injection interval, whereas the remaining tracer mass exited the borehole primarily in pathways of longer travel time deeper in the interval. The greater density of the tracer solution (injected just below the top packer) relative to the groundwater would have caused it to preferentially sink to the bottom of the relatively long (and unmixed) injection interval. Figure 98 shows that there was only one pentafluorobenzoate (PFBA) peak in a tracer test conducted earlier in the Bullfrog Tuff (same interval, same flow rates). The only difference between the two tests was that ~1,000 L of tracer solution was injected in the first test, and ~12,000 L was injected in the second test. The packed-off injection interval volume was ~4300 L, so in the first test, only about one-fourth of an interval volume was injected. Therefore, it is likely that only flow pathways in the lower part of the injection interval conducted tracers out of the borehole because of the tendency of the tracers to sink. In contrast, in the second test, approximately three interval volumes of tracer solution were injected, so the volume between the packers should have eventually filled with tracer solution, and tracers would have, thus, accessed flow pathways throughout the entire length of the interval. The flow survey information depicted in Figure 95 suggests that the zone of highest flow in the injection well (c#2) occurred in the upper half of the injection interval.

The PFBA and bromide responses in both the Bullfrog Tuff tracer test and the Prow Pass Tuff test show clear qualitative evidence of matrix diffusion. The peak-normalized PFBA concentrations are higher than the peak-normalized bromide concentrations in both tests, and the second bromide peak in the Bullfrog Tuff test is somewhat delayed relative to the PFBA with a tail that appears to cross over the PFBA at long times. These features are all consistent with greater matrix diffusion of the more diffusive tracer (bromide) relative to the less diffusive tracer (PFBA). Another qualitative indication of matrix diffusion in the Prow Pass Tuff test is the "jump(s)" in solute tracer concentrations after each of the three major flow interruptions during the tailing portion of the test, which indicate diffusion of tracers out of the matrix and into fractures during the interruptions. Thus, the two tests support the concept of dual-porosity behavior (where flow occurs primarily in fractures, but there is a large amount of stagnant water available for tracer/contaminant storage in the near-stagnant water of the rock matrix) in the saturated, fractured system at the C-wells.

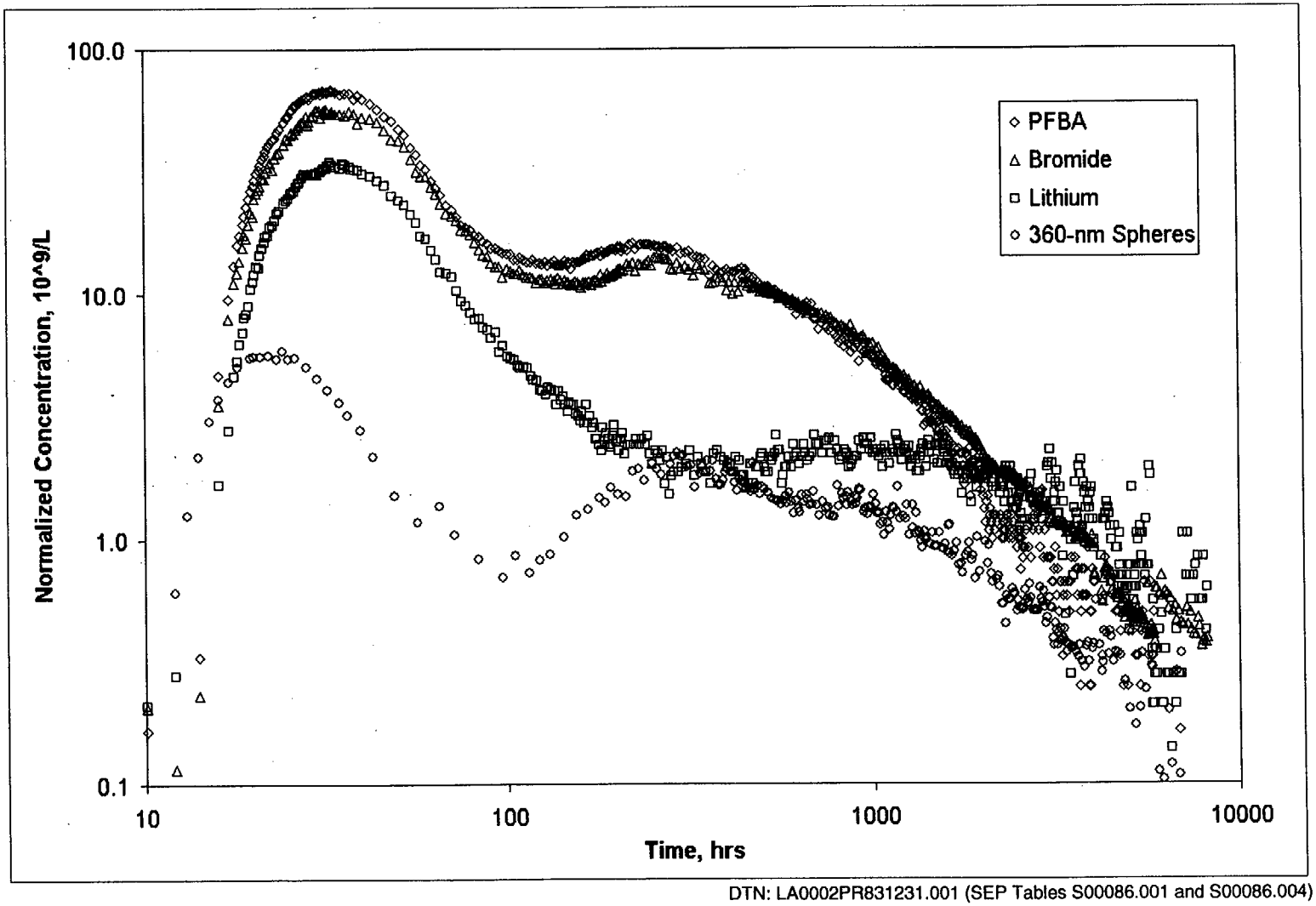

DTN: LA0002PR831231.001 (SEP Tables S00086.001 and S00086.004)

NOTE: Normalized tracer responses in the Bullfrog Tuff multiple tracer test (note both axes are log scale). Tracer recoveries were ~69% for PFBA, ~69% for bromide, ~39% for lithium, and ~15% for microspheres. Concentrations are normalized to mass injected.

Figure 96. Normalized Tracer Responses in the Bullfrog Tuff Multiple Tracer Test

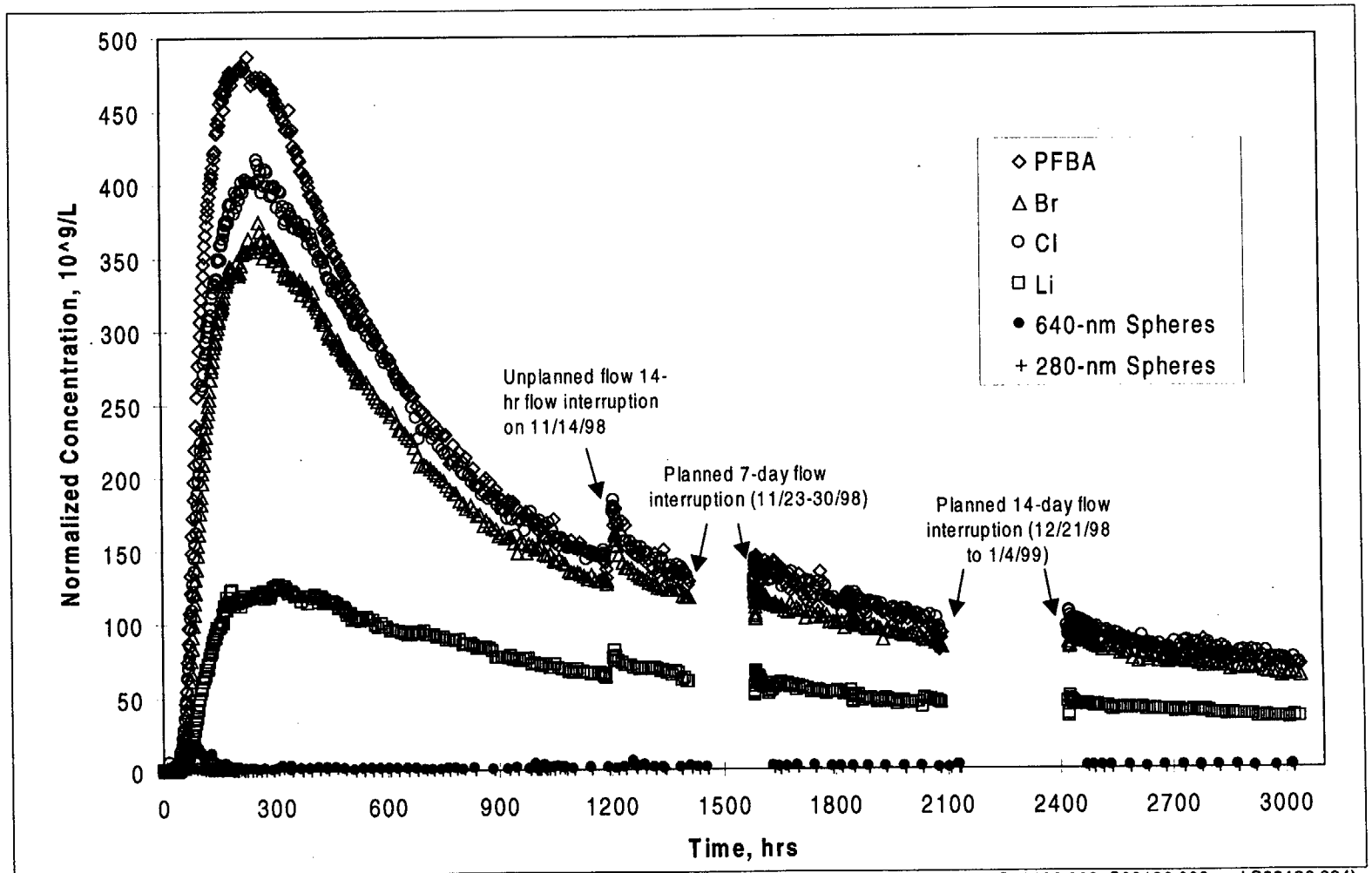

DTN: LAPR831231AQ99.001 (SEP Tables S99126.001, S99126.002, S99126.003 and S99126.004)

NOTE: Normalized tracer responses in the Prow Pass Tuff multiple tracer test. Microsphere responses are shown more clearly in Figure 99. Tracer recoveries were 52% for PFBA, 49% for Cl, 43% for Br, 19% for Li, 0.3% for 640-nm spheres, and 0.1% for 280-nm spheres.

Figure 97. Normalized Tracer Responses in the Prow Pass Tuff Multiple Tracer Test

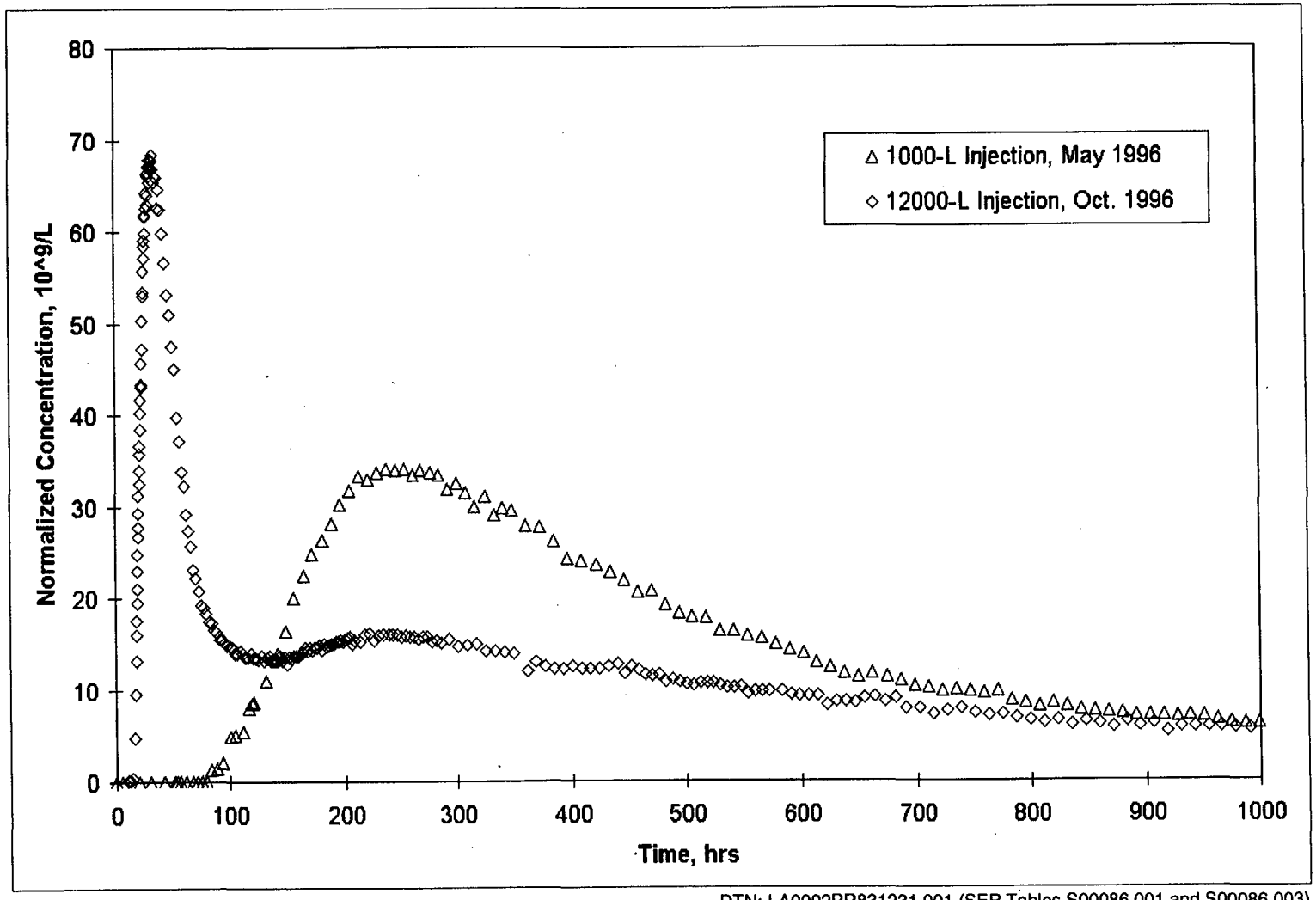

DTN: LA0002PR831231.001 (SEP Tables S00086.001 and S00086.003)

NOTE: The axes are both linear. These tests differed only in the amount of tracer solution injected.

Figure 98. Normalized PFBA Responses in Two Different Tracer Tests in the Bullfrog Tuff

The lithium responses in the two tests show obvious attenuation relative to the nonsorbing tracers, which is indicative of lithium sorption. The attenuation in the Prow Pass test and in the first peak of the Bullfrog Tuff test is almost exclusively a lowering of the peak concentration with little or no delay in arrival time. This behavior is consistent with lithium sorption in the matrix (after diffusion into the matrix). The attenuation in the second peak of the Bullfrog Tuff test involves a clear time delay along with a dramatic lowering of concentration. This behavior is consistent with sorption in both the fracture flow pathways and the matrix.

The CML microsphere responses in the two tests indicate that the microspheres were significantly attenuated relative to the solute tracers in both tests with the attenuation relative to solutes being greater in the Prow Pass Tuff test. The microsphere responses in the Prow Pass test are shown more clearly on a plot of log-normalized concentration versus time in Figure 99. The responses in both tests (including both sizes of spheres in the Prow Pass test) are characterized by truncated tails relative to the solutes but with measurable concentrations that persist throughout the tests. This behavior is consistent with filtration followed by some sort of nonlinear or stochastic resuspension of the microspheres.

The tracer responses in both tests were interpreted by simultaneously fitting the breakthrough curves using a semianalytical, dual-porosity transport model, RELAP, which is described in detail in Reimus et al. (1999, Appendix D). RELAP is part of the Reactive Transport Application (RTA) V1.1 (STN: 10032-1.1-00) software package. It solves Laplace domain "transfer functions" that describe tracer injection, well-bore mixing, recirculation, and tracer transport in a dual-porosity system. The equations used for transport in the flow system can take various forms depending on whether: (1) flow is assumed to be linear or radial, (2) the matrix is assumed to be finite or semi-infinite, or (3) sorption is assumed to be equilibrium or rate limited (Reimus et al. 1999, Appendix D).

The interpretation strategy in the Bullfrog Tuff test was to (1) fit the first tracer peaks, (2) subtract the fitted responses from the complete breakthrough curve(s), and (3) fit the resulting residual second peak(s) with a second set of transport parameters. In the Prow Pass test, a single set of transport parameters was sufficient to fit the single modal tracer responses. The sequence of fitting the different tracer responses in each test was as follows.

1. The Br^- and PFBA responses were fit simultaneously using RELAP. It was assumed that both tracers experienced the same mean residence time and the same longitudinal dispersivity (because they were injected simultaneously), but they had diffusion coefficients that differed by a factor of 3. Both tracers were assumed to be conservative (nonsorbing). (Assumptions 22, 23, and 24 in Section 5).

2. The lithium response was fit by assuming that the lithium experienced the same mean residence time and dispersivity as the bromide and PFBA, but it had a diffusion coefficient two-thirds that of bromide and twice that of PFBA. (Assumptions 22 and 24 in Section 5). The only parameters adjusted to obtain a fit to the lithium data were sorption parameters.

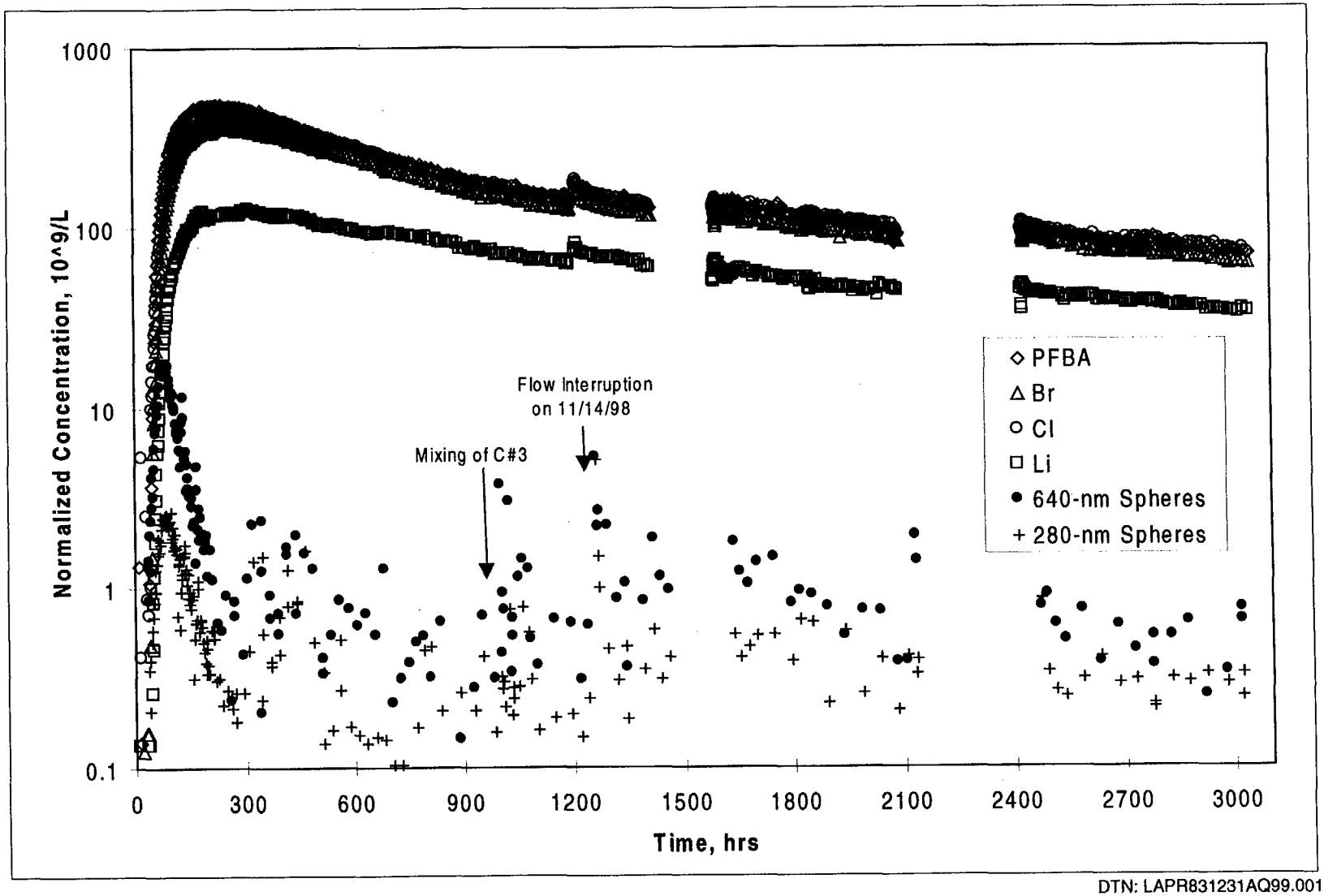

DTN: LAPR831231AQ99.001

NOTE: The time scale (*x* axis) is linear. The microspheres appeared to respond after pressure transients associated with mixing the injection well bore (c#3) and an unplanned flow interruption.

Figure 99. Log Normalized Tracer Responses in the Prow Pass Tuff Multiple Tracer Test

3. The microsphere responses were fitted assuming the same mean residence times and dispersion coefficients as the solute tracers but without any diffusion into the matrix (diffusion coefficient of zero) (Assumptions 22 and 25 in Section 5). The rate-limited sorption features of RELAP were used to adjust filtration and resuspension rate constants until a fit to the data was obtained.

4. To simulate the flow interruptions in the Prow Pass Tuff tracer test, a numerical code called RETRAN, also part of the RTA software package, was used. Unlike RELAP, RETRAN is capable of simulating nonlinear behavior and flow transients (Laplace transforms are limited to linear functions and steady-state flow behavior). RELAP fits were extended beyond the flow interruptions by using the transport parameters obtained from RELAP (up until the time of the flow interruptions) as inputs to RETRAN. RETRAN was also used to simulate nonlinear sorption behavior of lithium.

The model RETRAN solves the concentration of tracer only at the breakthrough point, using a semi-analytical method. No mesh is required. The breakthrough curve is obtained by numerical inversion of the solution in Laplace space. Complete model documentation is reported in Reimus and Dash (1999), including discussion on stability and accuracy of solutions. RETRAN was validated for this application by fitting the observed breakthrough curves and visually judging the goodness of fit as shown in Appendix C of Reimus et al. (1999). RETRAN was chosen for this application because no data other than breakthrough data are available to fit. Therefore, there is no advantage to using a model that predicts concentrations everywhere. The model fits to the tracer breakthrough curves are not shown here graphically; the reader is referred to Reimus et al. (1999, Chapter 5 and Appendix C) for graphical representations of the fits. All transport parameters obtained from the fits, with the exception of lithium sorption parameters, are listed in Tables 51 and 52 for the Bullfrog and Prow Pass Tuff tests, respectively. Note that there are separate estimates of mean residence times and dispersivities depending on whether "radial" or "linear" flow is assumed (the two possible extremes for flow to a pumped well in a confined aquifer). These values reflect the parameter uncertainty associated with not knowing the true nature of the flow field. Figure 100 shows the range of longitudinal dispersivities deduced from the C-wells tracer tests on a plot of dispersivity versus length scale taken from Neuman (1990, Figure 3). It is apparent that the C-wells longitudinal dispersivities (the darkened box) are in relatively good agreement with Neuman's published relationship of dispersivity versus length scale. Note that the lower end of the range of length scales associated with the darkened box corresponds to the interwell separation in the tracer tests and the upper end corresponds to the test interval thickness (used as an upper bound for the transport distance). The effective flow porosities listed in Tables 51 and 52 were calculated from the deduced mean tracer residence times using the following expression (Reimus et al. 1999, Section 5.6), which assumes radial convergent flow in a homogeneous, isotropic medium:

$$\eta = \frac{Q\,\tau}{\pi R^2 L} \qquad \text{(Eq. 41)}$$

where

η = flow porosity
Q = production rate (m^3/hr)
τ = mean tracer residence time (hr)
R = distance between boreholes (m)
L = formation thickness (m).

Table 51. Transport Parameters Deduced from Fits of the Bullfrog Tuff Tracer Responses [d]

Parameter	Pathway 1 [e]	Pathway 2
mass fraction in pathway	0.12	0.59
residence time, linear flow (hr)	37	995
longitudinal dispersivity, linear flow (m)	5.3	18.8
residence time, radial flow (hr)	31	640
longitudinal dispersivity, radial flow (m)	3.6	10.7
effective flow porosity, linear (radial) [a]	0.0029 (0.0025)	0.026 (0.017)
$\frac{\phi}{b}\sqrt{D_m}$ for bromide ($sec^{-1/2}$) [b]	0.00158	0.000458
microsphere filtration rate constant (hr^{-1}) [c]	0.2	0.04

DTN: LA9909PR831231.003

NOTES: [a] Based on flow log information (see Figure 95), it was assumed that 75% of the production flow contributed to the pathway 1 responses and 25% of the flow contributed to the pathway 2 responses. Equation 41 was used to estimate the flow porosity.
[b] This parameter is an effective matrix diffusion mass transfer coefficient (Reimus et al. 1999, Section 5.6). The value of the parameter for PFBA was assumed to be 0.577 times that for bromide.
[c] Multiple resuspension/detachment rate constants were assumed in each pathway to obtain a fit to the microsphere responses (see Reimus et al. 1999, Section C.5). Filtration coefficients (m^{-1}) can be calculated from the filtration rate constants (k_{filt}) using k_{filt}/V, where V = average linear velocity determined from mean fluid residence times.
[d] See Table 53 for lithium sorption parameters.
[e] Note that "Pathway 1" refers to pathways that resulted in the first tracer peak, and "Pathway 2" refers to pathways that resulted in the second peak.

Table 52. Transport Parameters Deduced from Fits of the Prow Pass Tuff Tracer Responses

Parameter	Value
mass fraction participating in test	0.75
residence time, linear flow (hr)	1230
longitudinal dispersivity, linear flow (m) [a]	23.1
residence time, radial flow (hr)	620
longitudinal dispersivity, radial flow (m) [a]	6.3
effective flow porosity, linear (radial)	0.0068 (0.0034)
$\frac{\phi}{b}\sqrt{D_m}$ for bromide ($sec^{-1/2}$) [b]	0.000968
640-nm sphere filtration rate constant (hr^{-1}) [c]	0.043
280-nm sphere filtration rate constant (hr^{-1}) [c]	0.07

DTN: LA9909PR831231.005

NOTES: [a] Longitudinal dispersivities calculated after subtracting out apparent dispersion due to the recirculating flow field (see Reimus et al. 1999, p. 5.14).
[b] See Table 51 for footnotes.
[c] See Table 53 for lithium sorption parameters.

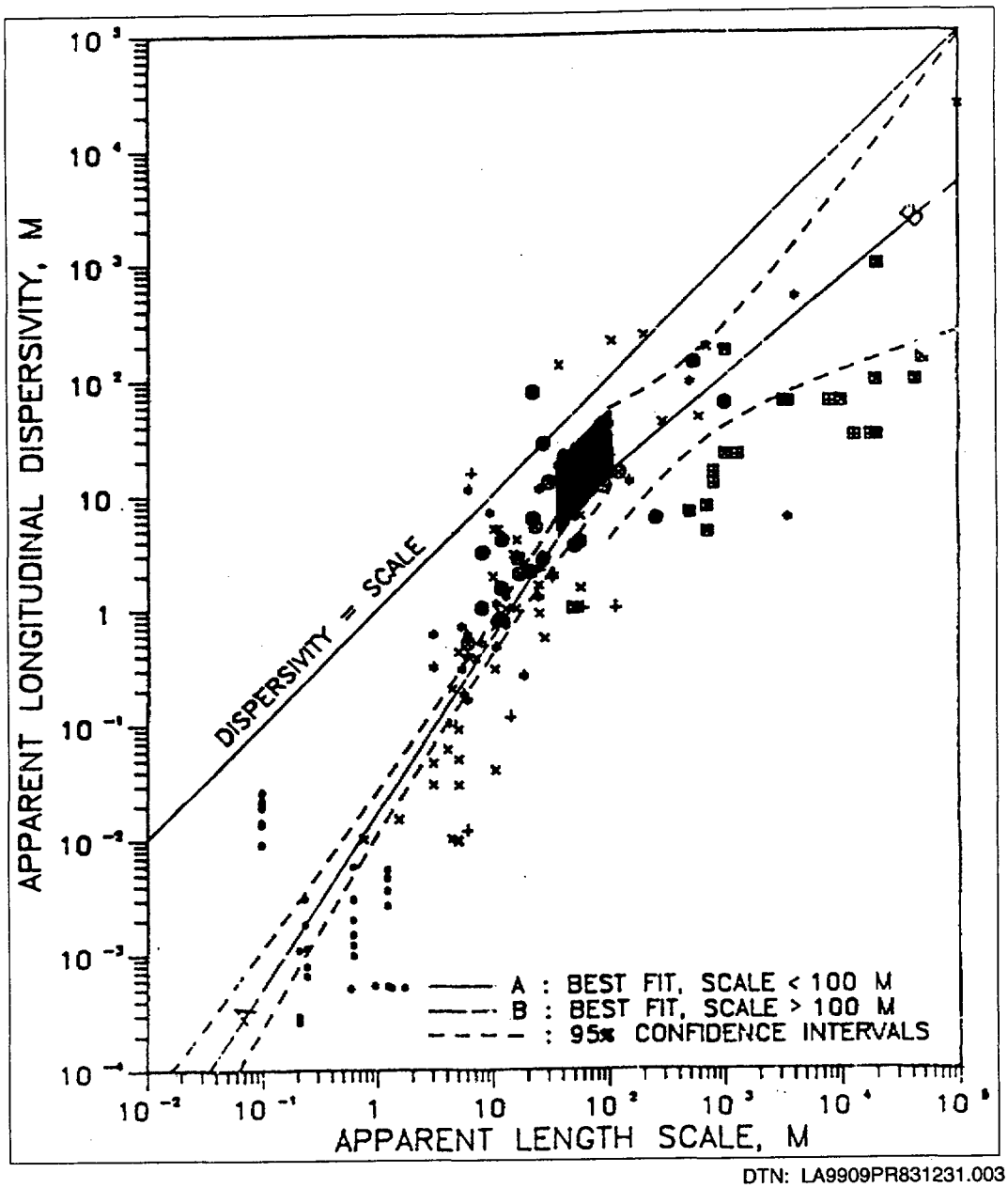

DTN: LA9909PR831231.003

NOTES: This figure shows the range of C-wells values derived from interpretations of the Prow Pass and Bullfrog reactive tracer tests (darkened box). Plot taken from Neuman (1990, Figure 3). Note that the right edge of the box corresponds to the interwell separation distance and the left edge of the box corresponds to the test interval thickness (taken to be the upper limit of transport distance).

Figure 100. Longitudinal Dispersivity versus Length Scale of C-Wells Values from Interpretations of the Prow Pass and Bullfrog Reactive Tracer Tests

The "mass tracer solution (which may have resulted in tracers "sinking" out of the zone of influence of the pump). Finite but slow flow through the matrix may also have resulted in some tracer being pushed out of the injection well into the matrix (rather than fractures) where it would have been effectively "lost" from the fracture flow system.

The parameter describing matrix diffusion in Tables 51 and 52 is actually a "lumped" parameter (Reimus et al. 1999 pp. C.7 and 5.15) which could be called the "mass transfer coefficient,"

$$\frac{\phi}{b}\sqrt{D_{\mathrm{m}}}$$

consisting of the matrix porosity, ϕ ,the fracture half-aperture, b, and the matrix diffusion coefficient, D_{m}. These parameters cannot be easily separated because it is not possible to obtain independent estimates of their in-situ values. It should be noted that the simultaneous fits to the nonsorbing tracer responses were *not* significantly improved by assuming a finite matrix (versus an infinite matrix) or by assuming multiple pathways with different matrix diffusion mass transfer coefficients (versus a single mass transfer coefficient).

Lithium sorption parameters deduced from the field tracer tests are listed in Table 53. Laboratory-derived lithium sorption parameters (see below) are also listed in Table 53 to allow a comparison between field- and laboratory-derived sorption data. Table 53 indicates that lithium sorption in the field was always approximately equal to or greater than the sorption measured in the laboratory. It should be noted that although Table 53 lists only linear equilibrium sorption parameters (K_{d} values), the first lithium peak in the Bullfrog Tuff tracer test was actually a better fit assuming either rate-limited sorption or nonlinear sorption. A discussion of these and other alternative approaches to fitting the early lithium peak in the Bullfrog Tuff test is provided by Reimus et al. (1999, Section C.4.2). For the second lithium peak in the Bullfrog Tuff test and the only peak in the Prow Pass test, the assumption of linear equilibrium sorption provided very good fits to the data.

The microsphere fitting procedure in the Bullfrog Tuff test is described in detail in Reimus et al. (1999, Section C.5). Two sets of pathways were assumed, each having a unique linear filtration rate constant. However, to fit the long tailing behavior, it was necessary to assume that there were multiple resuspension rate constants for different mass fractions of the spheres within each pathway. To match the low recovery of the spheres, a relatively large fraction of mass in each pathway was assumed to be irreversibly filtered (a resuspension rate constant of zero). The filtration rate constants resulting in a good fit to the complete microsphere response are given in Table 51. In the Prow Pass Tuff test, the microsphere responses were fit assuming only linear forward filtration with no resuspension (Reimus et al. 1999, p. 5.10). The resulting filtration rate constants are provided in Table 52. The fits provided a good match to the data up until the tails of the breakthrough curves began to flatten out. The long flat tails could probably be explained by multiple resuspension rate constants, but this was not attempted.

Table 53. Comparison of Field- and Laboratory-Derived Sorption Parameters for Lithium Ion [a]

Parameter	Field K_d	Laboratory K_d [b]
Prow Pass matrix K_d assuming Central Prow Pass Tuff	0.66	0.13 (0.26 at infinite dilution)
Prow Pass matrix K_d assuming Lower Prow Pass Tuff	1.68	0.084 (0.44 at infinite dilution)
Bullfrog matrix K_d in Pathway 1 assuming Central Bullfrog Tuff [c]	0.24	0.19 (0.44 at infinite dilution)
Bullfrog matrix K_d in Pathway 1 assuming Lower Bullfrog Tuff [c]	0.97	0.32 (1.64 at infinite dilution)
Bullfrog matrix K_d in Pathway 2 assuming Central Bullfrog Tuff [c]	0.67	0.19 (0.44 at infinite dilution)
Bullfrog matrix K_d in Pathway 2 assuming Lower Bullfrog Tuff [c]	2.75	0.32 (1.64 at infinite dilution)

DTN: LA9909PR831231.003 (field K_d for Bullfrog); LA9909PR831231.004 (SEP Table S99488.006, laboratory K_d); LA9909PR831231.005 (field K_d for Prow Pass)

NOTES: [a] This comparison assumes linear sorption isotherms.
[b] Values at "infinite dilution" obtained from slopes of Langmuir isotherm fits to the data (asymptotic slope at very low concentrations). Other values obtained from a simple linear fit to the entire range of data.
[c] Pathway 1 refers to pathways that resulted in the first tracer peak in the Bullfrog reactive tracer test, and Pathway 2 refers to pathways that resulted in the second peak in this test. K_d values were calculated from the smallest matrix retardation factors obtained from alternative interpretations of the test (see Reimus et al. 1999, Section C.4.2, Table C-8).

Only one other C-wells tracer test involved the simultaneous injection of more than one tracer (the combined iodide and 2,4,5-trifluorobenzoate (TFBA) injection in the Prow Pass Tuff in June 1998). This test exhibited the same qualitative behavior as the multiple tracer tests described above, that is, the iodide was more attenuated than the TFBA due to greater matrix diffusion. The comparisons of tracer responses resulting from injections into well c#1 and into either well c#2 while pumping well c#3 provided some insights into flow heterogeneity/ anisotropy in the lower Bullfrog Tuff at the C-wells. Table 54 lists the ratios of peak response times or first arrival times for conservative tracers between c#1 and c#3 and between c#2 and c#3 for the two tests in which a comparison was possible. For a homogeneous, isotropic medium, the response times under radial flow conditions are expected to vary as R^2, which is the distance between injection and production well squared. The ratios of R^2 values corresponding to both cases are also listed in Table 54. Note that the ratios of tracer response times and R^2 values are in reasonably good agreement in both cases, suggesting that anisotropy in the lower Bullfrog Tuff at the C-holes may be relatively small despite the apparent orientation of the fracture network in the general direction of c#1 to c#2 (Geldon 1993, pp. 44-46).

Table 54. Ratios of Observed Tracer Arrival Times and Distances Squared for C-Wells Tracer Tests

Tests	Time c#1/Time c#2–c#3	R^2 c#1/R^2 c#2–c#3
Bullfrog, PFBA (c#2) and Iodide (c#1) [a]	6	7.4
Bullfrog, 2,6-DFBA (c#2) and Pyridone (c#1) [b]	10	7.4

DTN: GS970708312315.001, LA0002PR831231.001.

NOTES: [a] Both tests conducted with 2.5 to 3.5% recirculation into injection well. Peak tracer arrivals compared.
[b] Both tests conducted with no recirculation. First tracer arrivals compared.

6.9.3 Summary of Laboratory Test Results and Interpretations

6.9.3.1 Batch-Sorption Testing of Lithium Ion

Batch-sorption tests were conducted to determine equilibrium sorption isotherms of lithium ion to seven different C-wells tuff lithologies over a three order-of-magnitude range of lithium solution concentrations that effectively spanned the range of concentrations in field tests (~1 to 1000 mg L^{-1}). The resulting best-fitting Langmuir isotherms for each lithology are shown in Figure 102 (without the fitted data, which would excessively clutter the plot) (Reimus et al. 1999, Section 6.2, Figures 6-3 to 6-9). In most cases, a Langmuir isotherm offered a better fit to the data than either a linear or Freundlich isotherm because of the tendency of the isotherm to plateau at higher concentrations, suggesting a "saturation" of the surface with lithium. These tests and their results are described in more detail in Reimus et al. (1999, Section 6.2).

In conjunction with the batch-sorption tests, all tuffs tested were analyzed quantitatively for major mineral phases by x-ray diffraction (XRD) (DTN: LA9909PR831231.004, SEP Table S99488.003). Cation exchange capacity experiments were also conducted on each rock (DTN: LA9909PR831231.004, SEP Table S99488.004). Not surprisingly, the tuffs that had the highest lithium sorption capacity (Bedded Prow Pass and Lower Bullfrog) also had the highest percentages of smectite clays and/or zeolites and the highest cation exchange capacities (Reimus et al. 1999, Table 6-4, Figure 6-2). The primary cations exchanging with the lithium in the cation exchange capacity tests were sodium and calcium.

6.9.3.2. Diffusion Cell Testing

Laboratory "diffusion cell" tests involved measuring the diffusion coefficients of the nonsorbing tracers used in field tests in intact blocks of saturated matrix material. The experimental apparatus and details of the test interpretations are presented in Reimus et al. (1999, Chapter 8). The diffusion coefficients of PFBA and bromide were measured in five different tuff lithologies, as listed in Table 55. Each of these lithologies could have been involved in the field tests. Table 55 also gives the measured matrix porosities and permeabilities of the tuffs. It is evident that the diffusion coefficients are positively correlated with both of these rock properties, although the correlation is better with permeability. The two diffusion cell tests conducted in the lower Prow Pass Tuff indicate very good experimental reproducibility using two different pieces of core from this lithological unit.

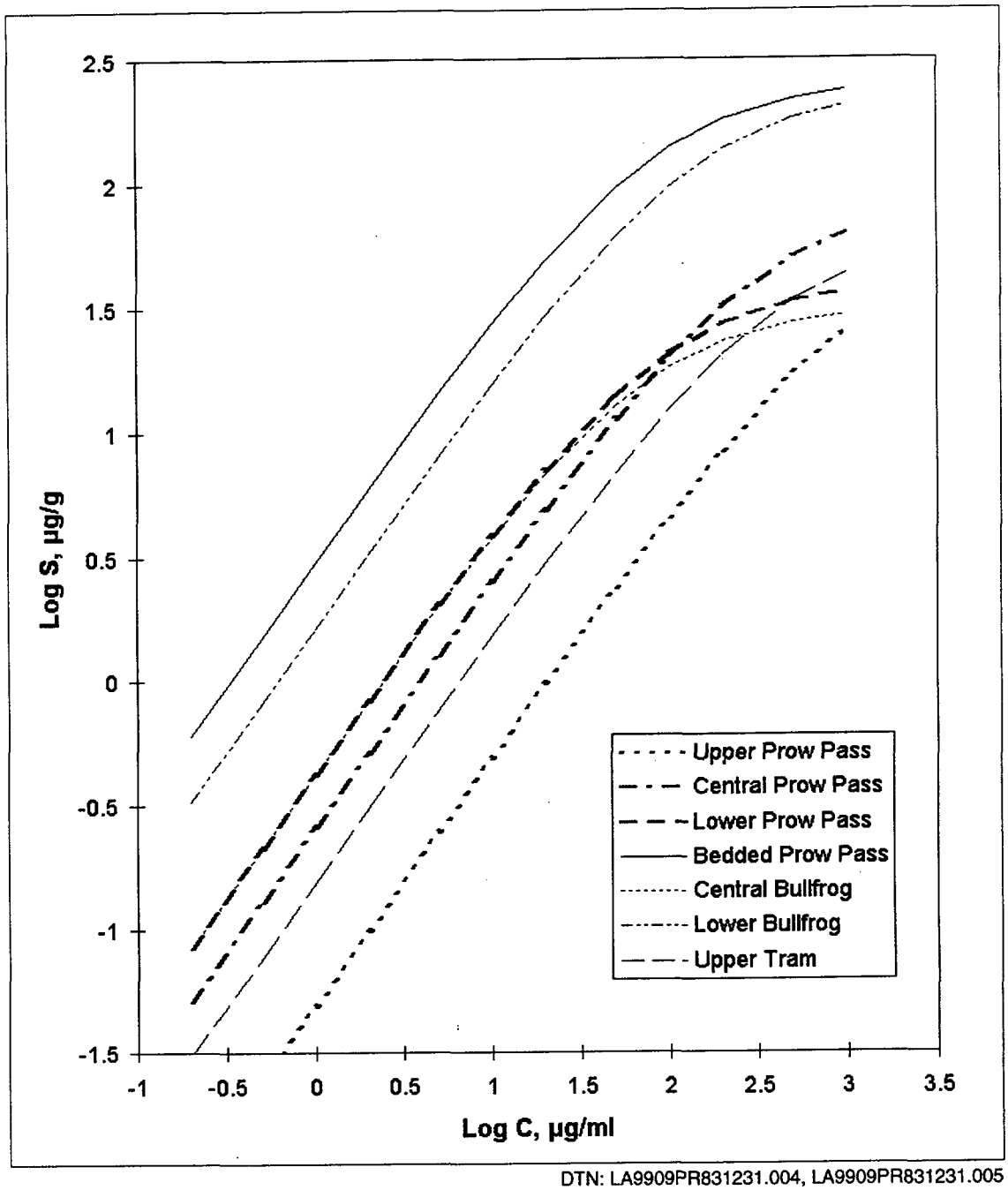

DTN: LA9909PR831231.004, LA9909PR831231.005

NOTES: See Figure 95.
The units are ordered in the legend from shallowest to deepest. Lithium concentrations in the field tests ranged from less than 0.1 mg L^{-1} to 2600 mg L^{-1}.
These isotherms are based on log amount sorbed versus log solution concentration.

Figure 101. Fitted Langmuir Sorption Isotherms for Lithium Sorption onto C-Wells Tuffs from Different Units/Lithologies

The ratio of bromide to PFBA diffusion coefficients in the diffusion cell tests was consistently about 3:1, regardless of the absolute values of the diffusion coefficients. This ratio was used as a constraint when simultaneously fitting the responses of these tracers in the field tests.

Table 55. Laboratory-Measured Matrix Diffusion Coefficients of Bromide and PFBA in Various C-Wells Tuffs [a]

Tuff	Porosity	Permeability (mDarcy)	L (cm) [b]	Matrix diff. coeff. ($cm^2 s^{-1} \times 10^6$)		
				Br	PFBA	Br/PFBA
Central Bullfrog	0.094	0.00107	1.16	0.45	0.13	3.46
Lower Bullfrog	0.298	0.0949	0.84	1.0	0.35	2.86
Upper Prow Pass	0.272	4.72	0.91	6.0	1.9	3.16
Central Prow Pass	0.138	0.000786	1.23	0.4	0.13	3.08
Lower Prow Pass-1 [c]	0.288	0.455	2.27	3.0	1.1	2.73
Lower Prow Pass-2 [c]	0.288	0.455	1.82	3.0	1.0	3.0

DTN: LA9909PR831231.003, LA9909PR831231.004 (SEP Tables S99488.001 and S99488.002), LA9909PR831231.005

NOTES: [a] The porosities and permeabilities of the tuffs are also listed in this table.
[b] L = thickness of tuff "wafer" used in diffusion cell experiment.
[c] Duplicate experiments were conducted in the lower Prow Pass Tuff.

6.9.3.3 Flowing Transport Experiments in Crushed and Fractured Tuffs

Two types of flowing transport experiments were conducted to support the field testing efforts: (1) crushed-tuff column experiments, and (2) fractured-core column experiments. In the former, lithium bromide solutions were eluted through columns of the same crushed Central Bullfrog Tuff at different concentrations and different flow rates. These tests showed that lithium sorption under flowing conditions was in very good agreement with batch-sorption measurements and demonstrated that lithium sorption kinetics were rapid enough that lithium sorption in the field should be well approximated by assuming local equilibrium between the solution and solid phases. More details of the crushed-tuff column experiments and their results are given in Reimus et al. (1999, Section 7.1). The tests were interpreted using the RELAP and RETRAN components of the RTA (STN: 10032-1.1-00) software package.

The fractured-core experiments offered more realistic laboratory simulations of the field tracer tests. These tests were conducted in induced (unnatural) fractures in both the Upper and Central Prow Pass Tuff lithologies (16–17 cm long). Experimental methods are described in Reimus et al. (1999, Section 7.2). Two different sets of tests were conducted in each fracture: (1) multiple tests at different flow rates using only iodide as a tracer and (2) tests involving the simultaneous injection of lithium, bromide, and PFBA (analogous to the field experiments). The first set of tests consistently exhibited higher peak concentrations of iodide at higher flow rates, consistent with matrix diffusion (more iodide would be expected to diffuse into the matrix as residence times increase). Simultaneous RELAP fits of these data sets allowed estimates of matrix diffusion parameters in the columns. The second set of tests exhibited behavior that was very consistent with the field observations, that is, peak normalized PFBA concentrations that were greater than peak Br concentrations and lithium concentrations that were lower yet but not significantly attenuated in time (Reimus et al. 1999, pp. 7.8 to 7.9, Figures 7-8 to 7-9, 7-11). All

of these features are consistent with dual-porosity transport behavior in the columns. These tests were interpreted using the same techniques (RTA) as the field tests involving multiple tracers. For brevity, the test results and interpretations are not presented here (see Reimus et al. 1999, Section 7.2). In general, apparent matrix-diffusion-mass-transfer coefficients were greater in the laboratory than in the field, and lithium sorption parameters in the laboratory were smaller than in the field.

6.9.4 Conclusions from C-Wells Field and Laboratory Testing

The C-wells field and laboratory tests have resulted in the following conclusions relevant to performance assessments of the potential Yucca Mountain repository.

- The responses of nonsorbing tracers in all field and laboratory tracer tests in fractured rocks have been consistent with matrix diffusion behavior. This result supports the use of a dual-porosity conceptual model to describe radionuclide transport through the saturated, fractured volcanic rocks near Yucca Mountain.

- Sorption of lithium ion in the field was greater than or equal to its measured sorption in the laboratory (see Table 53 for a comparison of lab- and field-derived sorption parameters). Although lithium does not behave identically to any radionuclide, this result suggests that the use of laboratory-derived radionuclide sorption parameters in field-scale transport predictions is defensible and may even be conservative.

- The effective flow porosities deduced from the field tests were less than 1% for all tracer responses except for the second tracer peak(s) in the Bullfrog Tuff test, for which the deduced flow porosity was several percent (even after apportioning 75% of the production flow to the first tracer peak). However, if the second peak was really the result of only 10% of the production flow, then the effective flow porosity would be only ~1%, and if it were only 5% of the production flow, then the flow porosity would be less than 1%. Such small percentages of production flow resulting in the second tracer response(s) are entirely possible in a heterogeneous fracture flow system such as that at the C-wells.

- The longitudinal dispersivities deduced from the field-scale experiments are consistent with published relationships of dispersivity versus length scale (see, for example, Figure 100).

- Matrix-diffusion-mass-transfer coefficients in the field experiments were less than in the laboratory experiments, and they generally decreased as tracer residence times increased. There are several possible explanations for this behavior including (1) larger average fracture apertures as length (and time) scales increase, (2) an increasingly greater influence of true matrix diffusion, as opposed to diffusion into stagnant free water as test durations increase, and/or (3) a greater tendency to encounter diffusion barriers in longer duration tests for which characteristic diffusion distances are greater. It should be noted that all tracer responses could be adequately fitted assuming a single matrix-diffusion-mass-transfer rate for each tracer peak.

7. CONCLUSIONS

Sorption is a function of water chemistry and the type of tuff at Yucca Mountain. It is assumed for the performance-assessment recommendations that the waters from wells J-13 and p#1 bound the major-ion chemistry of the groundwaters at Yucca Mountain, and that the number of sorption-coefficient distributions elicited to four per radionuclide: iron oxides, devitrified tuff, vitric tuff, and zeolitic tuff. The basis for this grouping is the fact that sorption of radionuclides is the result of a chemical reaction between the radionuclide in the groundwater and the minerals in the tuff. The mineralogy of the different strata of the same rock group is very similar, and the sorption coefficients can be grouped in terms of these rock types. Iron oxides were added to the list of "rock" types to reflect the containers to be used in the repository and the possibility that the corrosion by-products of a massive multipurpose container could become a substrate for sorption. Measured sorption coefficients onto tuffs were higher at elevated temperatures for all elements studied: americium, barium, cerium, cesium, europium, plutonium, strontium, and uranium. Therefore, sorption coefficients measured at ambient temperatures should be applicable and generally conservative when applied to describing aqueous transport from a hot repository. Table 2a gives recommended parameters for the sorption-coefficient probability models for performance assessment for unsaturated-zone units, and Table 2b shows the same parameters for the saturated zone.

The alluvium exhibited significant sorptive properties with respect to Np, Tc, and I. Distribution coefficients (K_ds) varied as a function of depth and borehole. K_d values for Np ranged from about 5 to 77 mL g^{-1}; K_d values for Tc ranged from about 0.35 to 0.8 mL g^{-1}; and preliminary K_d values for ^{129}I ranged from about 0.41 to 0.75 mL g^{-1}. Sorption was much faster for Np than for Tc or ^{129}I. The differences in sorptive properties among samples probably result from differences in the amount of the sorptive phase—smectite, clinoptilolite, calcite, and hematite—and perhaps from the presence of organic carbon and trace amounts of sulfides, which may explain the slow sorption response for Tc and ^{129}I. Biological activity, or simply sorption onto organics, could also be important and account for the slow sorption responses for Tc and ^{129}I. During these tests, significant amounts of colloids were also found, but their transport properties could not be investigated. These values are incorporated into Table 2a and b.

Conclusions drawn from available data regarding radionuclide transport through fractured-rock columns show that, contrary to previous views about the role of fractures in radionuclide retardation, fracture flow does not necessarily result in a fast pathway for actinide migration through fractures. The migration of actinides through fractures can be significantly retarded by sorption onto minerals coating the fractures and by diffusion into the tuff matrix, a result consistent with the results of the Busted Butte tests.

The results obtained from rock-beaker experiments agree with previous results and found that rate constants for uptake onto tuff of the sorbing cations from solution were consistent with a diffusion-limited model in which diffusion occurs in two stages. In the first stage, the cations diffuse into rock through water-filled pores; in the second stage, they diffuse into narrower intracrystalline channels. This diffusion model yielded sorption coefficients for cesium, strontium, and barium that agree well with the sorption coefficients determined by batch techniques.

The UZTT at Busted Butte was designed to provide information suitable for assessing the validity of flow and transport models used in the site characterization and performance assessment programs for Yucca Mountain. Critical evaluation and iterative improvement of the flow and transport conceptual and numerical models await the collection of further data, which is currently in progress. The first step in this process was reported in this AMR, namely the predictions of flow and transport behavior for both the Phase-1 and Phase-2 experiments and the preliminary results of those experiments. As discussed in Sections 6.8.6 and 6.8.7, the models are doing a reasonable job of capturing the flow phenomenon at this site. The major prediction is that fracture flow is not dominant at this site.

Although flow and transport field data collected to date are limited, observations of the available data collected so far, and the modeling of these data, lead to several key conclusions of relevance to performance assessment. These conclusions are summarized below, categorized with respect to the particular field or modeling activity in this report.

- *Laboratory measurements:* The collection of unsaturated hydrologic property data using the Unsaturated Flow Apparatus (UFA) provides data of particular relevance to flow and transport models because they are direct measurements under unsaturated conditions rather than indirect, model-derived parameters. The Monte Carlo analyses (Section 6.8.6) indicate that the nature of the correlations between parameters such as permeability and the van Genuchten α parameter have a strong impact on the predictability of the flow and transport system. This impact could be better defined by conducting a full suite of measurements of hydrologic and transport parameters on rock samples to constrain models and develop correlations.

- *Phase-1A and -1B model results for UZTT:* The modeling analyses for Phase 1A indicate that strong capillary forces in the rock matrix of the Tac unit are likely to modulate fracture flow from overlying units, thereby damping pulses of infiltrating water and providing a large degree of contact between radionuclides and the rock matrix. Several modeling approaches, from deterministic to Monte Carlo and stochastic models, were used to simulate the Phase-1A experiments (Sections 6.8.6 and 6.8.7). All yielded similar qualitative results. From this we conclude tentatively that the deterministic modeling approach taken at the site scale may be adequate. The parameterizations used in performing these calculations will be confirmed as data from the UZTT are available.

  A particularly interesting observation from the Phase-1B experiment is that, even when injection occurs immediately adjacent to a fracture, water appears to be imbibed quickly into the surrounding matrix. The transport times observed immediately below the injection point were on the order of 30 days, whereas pure fracture flow would have resulted in travel times of minutes to hours at this flow rate. Site-scale models must be evaluated in light of this observation. Models that predict significant fracture flow at percolation rates low enough for the matrix to transmit the flow are inconsistent with the Phase-1B experimental data results. This behavior was demonstrated in the Phase 1B experiments that occurred in the lower section of the TS (tptpv2), but the same general behavior should occur in the Calico Hills unit because the matrix capillarity is even stronger than the TS unit, and the in situ saturation is low.

- *Phase-2 modeling:* Because there were not field-test results at the time of preparation of this AMR, it is difficult to draw conclusions relevant to the evaluation of models. Significant uncertainties uncovered by the modeling include the adequacy of continuum models in nonwelded units of high matrix permeability, and the nature of the transition from fracture flow to matrix flow at contacts between hydrogeologic units. These are the issues being studied within the UZTT. Therefore, preliminary answers to these important questions are anticipated after test data have been collected and analyzed.

The UZTT has demonstrated that in the vitric Calico Hills unit, fluid movement is dominated by capillary forces and, thus, is predominantly matrix flow with little influence of fractures. Even with an overlying fractured unit (Topopah Spring welded tuff), the Calico Hills Formation below it strongly damps any fracture-dominated influence. These results suggest that commonly held views regarding the Calico Hills as a fast path for contaminants may be overstated. However, the UZTT is still in progress, and additional data regarding the influence of sorption and movement of radionuclides, as well as non-reactive contaminants, are still being collected for evaluation.

Some conclusions from the C-wells field and laboratory tests are relevant to performance assessment of the potential repository. The responses of nonsorbing tracers in all field and laboratory tracer tests in fractured rocks have been consistent with matrix diffusion behavior. This result supports the use of a dual-porosity conceptual model to describe radionuclide transport through saturated, fractured volcanic rock near Yucca Mountain. Results also suggest that the use of laboratory-derived radionuclide sorption parameters in field-scale transport predictions is defensible and conservative. The effective flow porosities deduced from the field tests were less than 1% for all tracer responses except for the second tracer peak in the Bullfrog Tuff test, for which the deduced flow porosity was several percent. Such small percentages of production are entirely possible in a heterogeneous fracture flow system such as that at the C-wells. The longitudinal dispersivities deduced from the field-scale experiments are consistent with published relationships of dispersivity versus length scale. Matrix diffusion mass transfer coefficients in the field experiments were less than in the laboratory experiments, and they generally decreased as tracer residence times increased. There are several possible explanations for this behavior, including (1) larger average fracture apertures as length (and time) scales increase, (2) an increasingly greater influence of true matrix diffusion, as opposed to diffusion into stagnant free water, as test durations increase, and/or (3) a greater tendency to encounter diffusion barriers in longer duration tests in which characteristic diffusion distances are greater. It should be noted that all tracer responses could be adequately fitted assuming a single matrix diffusion mass transfer rate for each tracer peak.

7.1 RECOMMENDATIONS

Sorption

The sorption data suggest that there are definite upper and lower bounds for the K_d values recommended to PA. Unfortunately, the ranges can be large, and large uncertainties in K_d values between 0 and 5 can result in very large uncertainties in predicted travel times. Further experiments under a wide variety of conditions relevant to the repository situation could reduce uncertainty in K_d values.

Because sorption is sensitive to the mineralogy, it is critical to either have an adequate understanding of the mineralogy and distributions along the flow pathway to the accessible environment or to accommodate this uncertainty in the PA evaluations. As an example, sorption of Np by hematite is thousands of times greater than sorption by the vitric tuff, and fracture coatings of hematite will influence transport well beyond what is indicated by its mass fraction in the system.

Sorption of Tc and I by the alluvium may be an important mechanism to be considered in PA evaluations. The preliminary data show non-zero K_d values of these radioisotopes in the 75-to-500-μm fraction of the alluvium (the standard size range for YMP sorption experiments). However, although this size range is appropriate for crushed whole-rock tuff samples, it omits the most sorptive components of the alluvium. Therefore, the alluvium may have higher K_d values than those measured to date.

Colloid-facilitated transport

The degree to which colloid-facilitated radionuclide migration will be a problem at Yucca Mountain depends very strongly on water chemistry, the specific radionuclide, type and size of the colloid, and ambient conditions, including degree of saturation. Unfortunately, the few colloid transport studies that have been documented have been conducted on systems and under conditions not relevant to the YMP. The data collected for this AMR are also of limited usefulness because they lack accompanying physical colloid transport data, such as colloid transport through fractured rock columns or invert/backfill materials in the laboratory or through tuff units in the field. In addition, a few well-designed studies on YMP-specific problems could resolve most of the colloid issues with respect to the repository environment.

1. The chemistry and type of colloids present in groundwaters should be determined.

2. Column experiments should be performed to determine the transport properties of colloids in Yucca Mountain materials.

3. The stability of colloids under various repository conditions should be determined.

4. The radionuclide and colloid attachment/detachment properties should be determined for all colloids anticipated in the repository environment.

5. The flux and water chemistry through the drift should be determined or more accurately bounded.

Busted Butte UZTT and C-Wells

The Busted Butte UZTT shows that there is no significant fracture flow through unsaturated nonwelded units and that the travel speed through these units are presently overestimated by orders of magnitude. This observation, together with the likely retardation properties of the alluvium units for Tc, I, and Np, and the corroboration of a dual-porosity conceptual model to describe radionuclide transport through the saturated, fractured volcanic rocks near Yucca Mountain determined from the C-wells field and laboratory tests, provides the greatest technical support for a successful LA, and it is recommended that their completion be a major focus of efforts leading to the LA.

7.2 IMPACTS

K_d values and diffusion coefficients enter into the Principal Factor of Dilution of Radionuclide Concentrations in the Geologic Setting and perhaps some of the Other Factors For the Post-Closure Safety Case. Consequently, PA calculations using these data will better illustrate the sensitivity of radionuclide release rates to the data, and an exact impact will be determinable; similarly, for Busted Butte and C-wells results.

If TBV data are not verified, the impact would be to invalidate the conclusions and recommendations, and this could significantly impact PA evaluations.

This document may be affected by technical product input information that requires confirmation. Any changes to the document that may occur as a result of completing the confirmation activities will be reflected in a subsequent revision. The status of the input information quality may be confirmed by review of the DIRS database.

7.3 OUTPUT DATA

Data developed by this analysis are included in the following.

- Sorption parameter values for both the unsaturated and the saturated zones can be found in DTN: LA0003AM831341.001.

- The matrix diffusion coefficients recommended for use in PA can be found in DTN: LA0003JC831362.001.

- Output data for the Busted Butte simulations are found in DTN: LA9909WS831372.019, LA9909WS831372.020, and LA9909WS831372.021.

INTENTIONALLY LEFT BLANK

8. INPUTS AND REFERENCES

8.1 DOCUMENTS CITED

Aagaard, P. 1974. "Rare Earth Elements Adsorption on Clay Minerals." *Bulletin du Groupe Francais des Argiles, 26*, (2), 193–199. Paris, France: Centre National de la Recherche Scientifique. Copyright Requested Library Tracking Number: 236921.

Allard, B. 1982. *Sorption of Actinides in Granitic Rock.* KBSTR 82-21. Goteborg, Sweden: Chalmers University of Technology. TIC: 205892.

Allard, B. and Beall, G.W. 1979. "Sorption of Americium on Geologic Media." *Journal of Environmental Health, A14*, (6), 507–518. New York, New York: Marcel Dekker. TIC: 224102.

Altman, S.J.; Arnold, B.W.; Barnard, R.W.; Barr, G.E.; Ho, C.K.; McKenna, S.A.; and Eaton, R.R. 1996. *Flow Calculations for Yucca Mountain Groundwater Travel Time (GWTT-95).* SAND96-0819. Albuquerque, New Mexico: Sandia National Laboratories. ACC: MOL.19961209.0152.

Ames, L.L., Jr.; McGarrah, J.E.; and Walker, B.A. 1983. "Sorption of Trace Constituents from Aqueous Solutions onto Secondary Minerals: 1. Uranium." *Clays and Clay Minerals, 31,* (5), 321–334. Long Island City, New York: Pergamon Press. TIC: 238914.

Andersson, K. 1988. *SKI Project-90: Chemical Data.* SKI Technical Report 91:21. Stockholm, Sweden: Swedish Nuclear Power Inspectorate. TIC: 242643.

Baes, C.F., Jr. and Mesmer, R.E. 1986. *The Hydrolysis of Cations.* Malabar, Florida: Krieger Publishing Company. TIC: 223481.

Balistrieri, L.S. and Chao, T.T. 1987. "Selenium Adsorption by Goethite." *Soil Science Society of America Journal, 51*, (5), 1145–1151. Madison, Wisconsin: Soil Science Society of America. TIC: 223172.

Balistrieri, L.S. and Murray, J.W. 1982. "The Adsorption of Cu, Pb, Zn, and Cd on Goethite from Major Ion Seawater." *Geochimica et Cosmochimica Acta, 46*, 1253–1265. New York, New York: Pergamon Press. TIC: 238913.

Banfield, J.F. and Eggleton, R.A. 1989. "Apatite Replacement and Rare Earth Mobilization, Fractionation, and Fixation during Weathering. *Clays Minerals Society, 37*, (2), 113–127. Long Island, New York: Pergamon Press. TIC: 236948.

Bar-Yosef, B. and Meek, D. 1987. "Selenium Sorption by Kaolinite and Montmorillonite." *Soil Science, 144*, (1), 11–19. Philadelphia, Pennsylvania: Lippincott, Williams & Wilkins. TIC: 237321.

Barrer, R.M. and Townsend, R.P. 1976. "Transition Metal Ion Exchange in Zeolites: Part 1.–Thermodynamics of Exchange of Hydrated Mn^{2+}, Co^{2+}, Ni^{2+}, Cu^{2+}, and Zn^{2+} Ions in Ammonium Mordenite." *Journal of the Chemical Society, Faraday Transactions I, 72*, 661–673. London, England: Royal Society of Chemistry. TIC: 239144.

Beckman, R.; Thomas, K.; and Crowe, B. 1988. *Preliminary Report on the Statistical Evaluation of Sorption Data: Sorption as a Function of Mineralogy, Temperature, Time, and Particle Size.* LA-11246-MS. Los Alamos, New Mexico: Los Alamos National Laboratory. ACC: NNA.19890918.0500.

Benjamin, M.M. 1983. "Adsorption and Surface Precipitation of Metals on Amorphous Iron Oxyhydroxide." *Environmental Science and Technology, 17*, 686–692. Easton, Pennsylvania: American Chemical Society. TIC: 239143.

Bird, R.B.; Stewart, W.E.; and Lightfoot, E.N. 1960. *Transport Phenomena.* New York, New York: John Wiley and Sons. TIC: 208957.

Bish, D.L. and Chipera, S.J. 1989. *Revised Mineralogic Summary of Yucca Mountain, Nevada.* LA-11497-MS. Los Alamos, New Mexico: Los Alamos National Laboratory. ACC: NNA.19891019.0029.

Blanchard, G.; Maunaye, M.; and Martin, G. 1984. "Removal of Heavy Metals from Waters by Means of Natural Zeolites." *Water Research, 18*, (12), 1501–1507. Oxford, Great Britain: Pergamon Press. TIC: 239004.

Bolt, G.H. and Bruggenwert, M.G.M., eds. 1978. *Soil Chemistry: A. Basic Elements.* Developments in Soil Science 5A. 2nd Revised Edition. New York, New York: Elsevier Scientific Publishing Company. TIC: 243742.

Bonnot-Courtois, C. and Jaffezic-Renault, N. 1982. "Etude des Echanges Entre Terres Rares et Cations Interfoliares de Deux Argiles." *Clays Minerals, 17*, 409–420. London, England: Mineralogical Society. TIC: 237359.

Borovec, Z. 1981. "The Adsorption of Uranyl Species by Fine Clay." *Chemical Geology, 32*, 45–58. Amsterdam, The Netherlands: Elsevier Science Publishing Company. TIC: 237323.

Bouwer, H. 1991. "Simple Derivation of the Retardation Equation and Application to Preferential Flow and Macrodispersion." *Ground Water, 29*, (1), 41–46. Dublin, Ohio: Water Well Publishing Company. TIC: 224079.

Bowman, R.S. and O'Connor, G.A. 1982. "Control of Nickel and Strontium Sorption by Free Metal Ion Activity." *Soil Science Society of America Journal, 46*, 933–936. Madison, Wisconsin: Soil Science Society of America. TIC: 236910.

Bradbury, M.H.; Green, A.; Lever, D.; and Stephen, I.G. 1986. *Diffusion and Permeability-Based Sorption Measurements in Sandstone, Anhydrite, and Upper Magnesian Limestone Samples*. AERE-R 11995. Oxfordshire, United Kingdom: Harwell Laboratory. TIC: 237243.

Brookins, D.G. 1983. "Migration and Retention of Elements at the Oklo Natural Reactor." *Environmental Geology, 4*, 201–208. New York, New York: Springer-Verlag. TIC: 239003.

Brookins, D.G. 1988. *Eh-pH Diagrams for Geochemistry*. New York, New York: Springer-Verlag. TIC: 237943.

Brown, R.E.; Parker, H.M.; and Smith, J.M. 1955. "Disposal of Liquid Wastes to the Ground." *Proceeding of the International Conference on the Peaceful Uses of Atomic Energy, August 8–20, 1955, Geneva, Switzerland, 9*, 669–675. New York, New York: United Nations Publications. TIC: 236932.

Broxton, D.E.; Warren, R.G.; Hagan, R.C.; and Luedemann, G. 1986. *Chemistry of Diagenetically Altered Tuffs at a Potential Nuclear Waste Repository, Yucca Mountain, Nye County, Nevada*. LA-10802-MS. Los Alamos, New Mexico: Los Alamos National Laboratory. ACC: 19980527.0202.

Bruque, S.; Mozas, T.; and Rodriguez, A. et al. 1980. "Factors Influencing Retention of Lanthanide Ions by Montmorillonite." *Clays Minerals, 15*, 413–420. London, England: Mineralogical Society. TIC: 237358.

Buesch, D.C.; Spengler, R.W.; Moyer, T.C.; and Geslin, J.K. 1996. *Proposed Stratigraphic Nomenclature and Macroscopic Identification of Lithostratigraphic Units of the Paintbrush Group Exposed at Yucca Mountain, Nevada*. Open File Report 94-469. Denver, Colorado: U. S. Geological Survey. ACC: MOL.19970205.0061.

Bussod, G.Y. 1998. Busted Butte On-Site Log Book #1/UZ Transport Field Test (LA-EES-5-NBK-98-010). SN-LANL-SCI-040-V1. ACC: MOL.20000321.0288.

Bussod, G.Y.; Robinson, B.A.; Vaniman, D.T.; Broxton, D.E.; and Viswanathan, H.S. 1997. *UZ Field Transport Test Plan*. SP341SM4. Los Alamos, New Mexico: Los Alamos National Laboratory. ACC: MOL.19980806.0715.

Byrne, R.H. and Kim, K.-H. 1993. "Rare-Earth Precipitation and Coprecipitation Behavior: The Limiting Role of PO_4^{3-} on Dissolved Rare-Earth Concentrations in Seawater." *Geochimica et Cosmochimica Acta, 57*, 519–526. New York, New York: Pergamon Press. TIC: 239120.

Cann, J.R. 1970. "Rb, Sr, Y, Zr, and Nb in Some Ocean Floor Basaltic Rocks." *Earth and Planetary Science Letters, 10*, 7–11. Amsterdam, The Netherlands: North Holland. TIC: 236899.

Carlos, B.A. 1985. *Minerals in Fractures of the Unsaturated Zone from Drill Core USW G-4, Yucca Mountain, Nye County, Nevada*. LA-10415-MS. Los Alamos, New Mexico: Los Alamos National Laboratory. ACC: NNA.19920506.0037.

Carlos, B.A. 1987. *Minerals in Fractures of the Saturated Zone from Drill Core USW G-4, Yucca Mountain, Nye County, Nevada*. LA-10927-MS. Los Alamos, New Mexico: Los Alamos National Laboratory. ACC: NNA.19900222.0149.

Carlos, B.A. 1989. *Fracture-Coating Minerals in the Topopah Spring Member and Upper Tuff of Calico Hills from Drill Hole J-13*. LA-11504-MS. Los Alamos, New Mexico: Los Alamos National Laboratory. TIC: 202383.

Carlos, B.A. 1994. *Field Guide to Fracture-Lining Minerals at Yucca Mountain, Nevada*. LA-12803-MS. Los Alamos, New Mexico: Los Alamos National Laboratory. ACC: MOL.19950717.0113.

Carlos, B.A.; Bish, D.L.; and Chipera, S.J. 1990. *Manganese-Oxide Minerals in Fractures of the Crater Flat Tuff in Drill Core USW G-4, Yucca Mountain, Nevada*. LA-11787-MS. Los Alamos, New Mexico: Los Alamos National Laboratory. ACC: NNA.19900206.0163.

Carlos, B.A.; Chipera, S.J.; Bish, D.L.; and Craven, S.J. 1993. "Fracture-Lining Manganese Oxide Minerals in Silicic Tuff, Yucca Mountain, Nevada, USA." *Chemical Geology, 107*, 47–69. Amsterdam, the Netherlands: Elsevier Science Publishers B.V. TIC: 208629.

Carpenter, R.; Beasley, T.M.; Zahnle, D.; and Somayajulu, B.L.K. 1987. "Cycling of Fallout (Pu, ^{241}Am, ^{137}Cs) and Natural (U, Th, ^{210}Pb) Radionuclides in Washington Continental Slope Sediments." *Geochimica et Cosmochimica Acta, 51*, 1897–1921. New York, New York: Pergamon Press. TIC: 239140.

Carsel, R.F. and Parrish, R.S. 1988. "Developing Joint Probability Distributions of Soil Water Retention Characteristics." *Water Resources Research, 24*, (5), 755–769. Washington, D.C.: American Geophysical Union. TIC: 247697.

Choppin, G.R. 1992. "The Role of Natural Organics in Radionuclide Migration in Natural Aquifer Systems." *Radiochimica Acta, 58/59*, 113–120. New York, New York: Academic Press. TIC: 222387.

Conca, J.L. and Wright, J. 1992. "Diffusion and Flow in Unsaturated Gravel, Soil, and Whole Rock." *Applied Hydrogeology, 1*, 5–24. Hanover, Germany: Verlag Heinz Heise GmbH. TIC: 224081.

Cotton, F.A. and Wilkinson, G. 1988. *Advanced Inorganic Chemistry*, Fifth Edition. New York, New York: John Wiley and Sons. TIC: 236867.

Cramer, J.J. and Sargent, F.P. 1994. "The Cigar Lake Analog Study: An International R&D Project." *High Level Radioactive Waste Management, Proceedings of the Fifth Annual*

International Conference, Las Vegas, Nevada, May 22–26, 1994, 4, 2237–2242. LaGrange Park, Illinois: American Nuclear Society. TIC: 210984.

CRWMS M&O (Civilian Radioactive Waste Management System Management and Operating Contractor) 1999a. *Work Package Planning Summary for Saturated Zone Flow and Transport PMR, 8191213SU1, Revision 00.* WPP-NBS-MD-000009. Las Vegas, Nevada: CRWMS M&O. ACC: MOL.19991008.0221.

CRWMS M&O 1999b. *UZ/SZ Transport Properties Data.* Development Plan TDP-NBS-HS-000041, Revision 00. Las Vegas, Nevada: CRWMS M&O. ACC: MOL.19990819.0270.

CRWMS M&O 1999c. *Work Package Planning Summary for Unsaturated Zone Transport Test, FY00 WP #1401213UM6 and 891213UU6, Revision 00A.* WPP-NBS-MD-000013. Las Vegas, Nevada: CRWMS M&O. ACC: MOL.19991021.0079.

CRWMS M&O 1999d. *M&O Site Investigations–(Q).* Activity Evaluation, September 28, 1999. Las Vegas, Nevada: CRWMS M&O. ACC: MOL.19990928.0224.

CRWMS M&O 2000a. *Pure Phase Solubility Limits—LANL.* ANL-EBS-MD-000017, Rev 00. Las Vegas, Nevada: CRWMS M&O. ACC: MOL.20000504.0311.

CRWMS M&O 2000b. *Unsaturated Zone Colloid Transport Model.* ANL-NBS-HS-000028, Rev 00. Las Vegas, Nevada: CRWMS M&O. Submit to RPC. URN-0031.

Dagan, G. 1984. "Solute Transport in Heterogeneous Porous Formations." *Journal of Fluid Mechanics, 145,* 151–177. Cambridge, United Kingdom: Cambridge University Press. TIC: 247700.

Daniels, W.R.; Erdal, B.R.; and Vaniman, D.T., eds. 1983. *Research and Development Related to the Nevada Nuclear Waste Storage Investigations, July 1–September 30, 1982.* LA-9577-PR. Los Alamos, New Mexico: Los Alamos National Laboratory. ACC: NNA.19870406.0180.

Daniels, W.R.; Wolfsberg, K.; Rundberg, R.S.; Ogard, A.E.; Kerrisk, J.F.; Duffy, C.J.; Newton, T.W.; Thompson, J.L.; Bayhurst, B.P.; Bish, D.L.; Blacic, J.D.; Crowe, B.M.; Erdal, B.R.; Griffith, J.F.; Knight, S.D.; Lawrence, F.O.; Rundberg, V.L.; Skyes, M.L.; Thompson, G.M.; Travis, B.J.; Treher, E.N.; Vidale, R.J.; Walter, G.R.; Aguilar, R.D.; Cisneros, M.R.; Maestas, S.; Mitchell, A.J.; Oliver, P.Q.; Raybold, N.A.; and Wanek, P.L. 1982. *Summary Report on the Geochemistry of Yucca Mountain and Environs.* LA-9328-MS. Los Alamos, New Mexico: Los Alamos National Laboratory. ACC: NNA.19870406.0243.

Dash, Z.V.; Robinson, B.A.; and Zyvoloski, G.A. 1997. *Software Requirements, Design, and Verification and Validation for the FEHM Application—A Finite-Element Heat- and Mass-*

Transfer Code. LA-13305-MS. Los Alamos, New Mexico: Los Alamos National Laboratory. TIC: 235234.

De Laeter, J.R.; Rosman, J.K.R.; and Smith, C.L. 1980. "The Oklo Natural Reactor: Cumulative Fission Yields and Retentivity of the Symmetric Mass Region Fission Products." *Earth and Planetary Science Letters, 50*, 238–246. Amsterdam, The Netherlands: Elsevier Scientific Publishing Company. TIC: 237501.

de Marsily, G. 1986. *Quantitative Hydrogeology: Groundwater Hydrology for Engineers*. San Diego, California: Academic Press. TIC: 208450.

Decarreau, A. 1985. "Partitioning of Divalent Transition Elements between Octahedral Sheets of Trioctahedral Smectites and Water." *Geochimica et Cosmochimica Acta, 49*, 1537–1544. New York, New York: Pergamon Press. TIC: 237522.

Degueldre, C.; Grauer, R.; Laube, A.; Oess, A.; and Silby, H. 1996. "Colloid Properties in Granitic Groundwater Systems: II. Stability and Transport Study." *Applied Geochemistry, 11*, 697–710. Oxford, England: Elsevier Science. TIC: 236569.

Degueldre, C.; Pfeiffer, H.-R.; Alexander, W.; Wernli, B.; and Bruetsch, R. 1996. "Colloid Properties in Granitic Groundwater Systems: I. Sampling and Characterization." *Applied Geochemistry, 11*, 677–694. Oxford, England: Elsevier Science. TIC: 236886.

DOE (U.S. Department of Energy). 2000. *Quality Assurance and Requirements Description*. DOE/RW-0333P, Rev. 10. Washington, DC.: DOE OCRWM. ACC: MOL.20000427.0422.

Doi, K.; Hirono, S.; and Sakamaki, Y. 1975. "Uranium Mineralization by Groundwater in Sedimentary Rocks, Japan." *Economic Geology, 70*, 628–646. El Paso, Texas: Economic Geology Publishing Company. TIC: 236987.

Drever, J.I. 1988. *The Geochemistry of Natural Waters*. 2nd Edition. Englewood Cliffs, New Jersey: Prentice Hall. TIC: 242836.

Duddy, I.R. 1980. "Redistribution and Fractionation of Rare-Earth and Other Elements in a Weathering Profile." *Chemical Geology,* (30), 363–381. Amsterdam, The Netherlands: Elsevier Scientific Publishing. TIC: 237498.

Dyer, J.R. 1999. "Revised Interim Guidance Pending Issuance of New U.S. Nuclear Regulatory Commission (NRC) Regulations (Revision 01, July 22, 1999), for Yucca Mountain, Nevada." Letter from J.R. Dyer (DOE/YMSCO) to D.R. Wilkins (CRWMS M&O), September 3, 1999, OL&RC:SB-1714, with enclosure, "Interim Guidance Pending Issuance of New U.S. Nuclear Regulatory Commission (NRC) Regulations for Yucca Mountain (Revision 01)." ACC: MOL.19990910.0079.

Eisenbud, M.; Krauskopf, K.; Franca, E.P.; Lei, W.; Ballad, R.; and Linsalata, P. 1984. "Natural Analogues for the Transuranic Actinide Elements: An Investigation in Minas Gerais, Brazil."

Environmental Geology and Water Science, 6, (1), 1–9. New York, New York: Springer-Verlag. TIC: 219069.

Flexser, S. and Wollenberg, H.A. 1992. "Radioelements and their Occurrence with Secondary Minerals in Heated and Unheated Tuff at the Nevada Test Site." *High Level Radioactive Waste Management, Proceedings of the Third International Conference, Las Vegas, Nevada, April 12–16, 1992*, 1593–1598. LaGrange Park, Illinois: American Nuclear Society. TIC: 239302.

Flint, A.L.; Hevesi, J.A.; and Flint, L.E. 1996. *Conceptual and Numerical Model of Infiltration for the Yucca Mountain Area, Nevada.* Milestone 3GUI623M. Denver, Colorado: U.S. Geological Survey. ACC: MOL.19970409.0087.

Flint, L.E. 1998. *Characterization of Hydrogeologic Units Using Matrix Properties, Yucca Mountain, Nevada.* Water-Resources Investigations Report 97-4243. Denver, Colorado: U.S. Geological Survey. ACC: MOL.19980429.0512.

Frysinger, G.R. and Thomas, H.C. 1960. "Adsorption Studies on Clay Minerals: VII. Yttrium-Cesium and Cerium(III)-Cesium on Montmorillonite." *Journal of Physical Chemistry,* (64), 224–228. Easton, Pennsylvania: American Chemical Society. TIC: 237120.

Gardner, W.R. 1958. "Some Steady-State Solutions of Unsaturated Moisture Flow Equations with Application to Evaporation from a Water Table." *Soil Science, 85*, 228–232. Baltimore, Maryland: Williams and Wilkins. TIC: 240150.

Geldon, A.L. 1993. *Preliminary Hydrogeologic Assessment of Boreholes UE-25 c#1, UE-25 c#2, and UE-25 c#3, Yucca Mountain, Nye County, Nevada.* Water Resources Investigations Report 92-4016. Denver, Colorado: U.S. Geological Survey. ACC: MOL.19960808.0136.

Geldon, A.L.; Umari, A.M.A.; Fahy, M.F.; Earle, J.D.; Gemmell, J.M.; and Darnell, J. 1997. *Results of Hydraulic and Conservative Tracer Tests in Miocene Tuffaceous Rocks at the C-Hole Complex, 1995 to 1997, Yucca Mountain, Nye County, NV.* Milestone SP23PM3. Denver, Colorado: U. S. Geological Survey. ACC: MOL.19980122.0412.

Gelhar, L.W. and Axness, C.L. 1983. "Three-Dimensional Stochastic Analysis of Macrodispersion in Aquifers." *Water Resources Research, 19,* (1), 161–180. Washington, D.C.: American Geophysical Union. TIC: 222815.

George-Aniel, B.; Leroy, J.L.; and Poty, B. 1991. "Volcanogenic Uranium Mineralizations in the Sierra Peña Blanca District, Chihuahua, Mexico: Three Genetic Models." *Economic Geology, 86*, (2), 233–248. El Paso, Texas: Economic Geology Publishing Company. TIC: 237050.

Giblin, A.M. and Snelling, A.A. 1983. "Application of Hydrogeochemistry to Uranium Exploration in the Pine Creek Geosyncline, Northern Territory, Australia." *Journal of Geochemical Exploration, 19*, 33–55. Amsterdam, The Netherlands: Elsevier Science Publishers B.V. TIC: 237423.

Goldschmidt, V.M. 1954. *Geochemistry.* London, United Kingdom: Oxford University Press. TIC: 243052.

Goodwin, B.W.; Cramer, J.J.; and McConnell, D.B. 1989. "The Cigar Lake Uranium Deposit: An Analogue for Nuclear Fuel Waste Disposal." Appendix B of *Natural Analogues in Performance Assessments for the Disposal of Long Lived Radioactive Wastes.* Technical Reports Series 304. Vienna, Austria: International Atomic Energy Agency. TIC: 7851.

Graham, W. and McLaughlin, D. 1989. "Stochastic Analysis of Nonstationary Subsurface Solute Transport: 2. Conditional Moments." *Water Resources Research, 25,* (11), 2331–2355. Washington, D.C.: American Geophysical Union. TIC: 239451.

Grimaldi, F.S. and Berger, I.A. 1961. "Niobium Content of Soils from West Africa." *Geochimica et Cosmochimica Acta, 25*, 71–80. Washington, D.C.: American Geophysical Union. TIC: 237436.

Harter, T. and Yeh, T.-C.J. 1996. "Stochastic Analysis of Solute Transport in Heterogeneous, Variably Saturated Soils." *Water Resources Research, 32*, (6), 1585–1595. Washington, D.C.: American Geophysical Union. TIC: 247170.

Hayes, K.F.; Roe, A.L.; Brown, G.E., Jr.; Hodgson, K.O.; Leckie, J.O.; and Parks, G.A. 1987. "In-Situ X-Ray Absorption Study of Surface Complexes: Selenium Oxyanions on α-FeOOH." *Science, 238*, 783–786. Washington, D.C.: American Association for the Advancement of Science. TIC: 237033.

Hiester, N.K. and Vermeulen, T. 1952. "Saturation Performance of Ion-Exchange and Adsorption Columns." *Chemical Engineering Progress, 48*, (10), 505–516. New York, New York: American Institute of Chemical Engineers. TIC: 224052.

Hingston, F.J.; Posner, A.M.; and Quirk, J.P. 1971. "Competitive Adsorption of Negatively Charged Ligands on Oxide Surfaces." *Surface Chemistry of Oxides, Discussions of the Faraday Society, 52*, 334–351. London, England: Royal Society of Chemistry. TIC: 237679.

Ho, C.H. and Miller, N.H. 1986. "Adsorption of Uranyl Species from Bicarbonate Solution onto Hematite Particles." *Journal of Colloid and Interface Science, 110*, (1) 165–171. New York, New York: Academic Press. TIC: 226326.

Hobart, D.E. 1990. "Actinides in the Environment." Chapter XIII of *Fifty Years with Transuranium Elements, Proceedings of the Robert A. Welch Foundation Conference on Chemical Research, XXXIV, Houston, Texas, October 22-23, 1990.* Houston, Texas: Robert A. Welch Foundation. TIC: 237030.

Howard, J. H., III. 1977. "Geochemistry of Selenium: Formation of Ferroselenite and Selenium Behavior in the Vicinity of Oxidizing Sulfide and Uranium Deposits." *Geochimica et Cosmochimica Acta, 41*, 1665–1678. New York, New York: Pergamon Press. TIC: 239142.

Hsi, C-K.D. and Langmuir, D. 1985. "Adsorption of Uranyl onto Ferric Oxyhydroxides: Application of the Surface Complexation Site-Binding Model." *Geochimica et Cosmochimica Acta, 49*, 1931–1941. New York, New York: Pergamon Press. TIC: 224090.

Hunter, K.A.; Hawke, D.J.; and Choo, L.K. 1988. "Equilibrium Adsorption of Thorium by Metal Oxides in Marine Electrolytes." *Geochimica et Cosmochimica Acta, 52*, 627–636. New York, New York: Pergamon Press. TIC: 237440.

Jonasson, R.G.; Bancroft, G.M.; and Nesbitt, H.W. 1985. "Solubilities of Some Hydrous REE Phosphates with Implications for Diagenesis and Seawater Concentrations." *Geochimica et Cosmochimica Acta, 49*, 2133–2139. New York, New York: Pergamon Press. TIC: 236998.

Keeney-Kennicutt, W.L. and Morse, J.W. 1985. "The Redox Chemistry of $Pu(V)O_2^+$ Interaction with Common Mineral Surfaces in Dilute Solutions and Seawater." *Geochimica et Cosmochimica Acta, 49*, 2577–2588. New York, New York: Pergamon Press. TIC: 237000.

Kelkar, S. and Travis, B. 1999. *Independent Test Case for TRACRN, Version 1.0*. Los Alamos, New Mexico: Los Alamos National Laboratory. ACC: MOL.19991221.0361.

Kerrisk, J.F. 1984. *Americium Thermodynamic Data for the EQ3/6 Database*. LA-10040-MS. Los Alamos, New Mexico: Los Alamos National Laboratory. TIC: 202354.

Knight, S.D. and Lawrence, F.O. 1988. *Sorption of Nickel and Neptunium in Tuff Using Groundwaters of Various Compositions*. Milestone R505. Los Alamos, New Mexico: Los Alamos National Laboratory. ACC: NN1.19881028.0004.

Knight, S.D. and Thomas, K.W. 1987. *Sorption of Radionuclides Using Different Groundwater Compositions*. Milestone M316. Los Alamos, New Mexico: Los Alamos National Laboratory. ACC: MOL.19980625.0236; NNA.19870902.0098.

Koeppenkastrop, D. and De Carlo, E.H. 1992. "Sorption of Rare-Earth Elements from Seawater onto Synthetic Mineral Particles: An Experimental Approach." *Chemical Geology, 95*, 251–263. Amsterdam, The Netherlands: Elsevier Science Publisher B.V. TIC: 237044.

Koeppenkastrop, D. and De Carlo, E.H. 1993. "Uptake of Rare-Earth Elements from Solution by Metal Oxides." *Environmental Science and Technology, 27*, (9), 1796–1802. Easton, Pennsylvania: American Chemical Society. TIC: 237057.

Krier, D.; Longmire, P.; Gilkeson, R.; and Turin, H.J. 1997. *Geologic, Geohydrologic, and Geochemical Data Summary of Material Disposal Area G, Technical Area 54, Los Alamos National Laboratory*. LAUR-95-2696. Los Alamos, New Mexico: Los Alamos National Laboratory. TIC: 247472.

Krishnaswami, S.; Graustein, W.C.; Turekian, K.K., and Dowd, J.F. 1982. "Radium, Thorium, and Radioactive Lead Isotopes in Groundwaters: Application to the In Situ Determination of

Adsorption-Desorption Rate Constants and Retardation Factors." *Water Resources Research, 18*, (6), 1633–1675. Washington, D.C.: American Geophysical Union. TIC: 224108.

La Flamme, B.D. and Murray, J.W. 1987. "Solid/Solution Interaction: The Effect of Carbonate Alkalinity on Adsorbed Thorium." *Geochimica et Cosmochimica Acta, 51*, 243–250. New York, New York: Pergamon Press. TIC: 237034.

LaBrecque, D.J.; Miletto, M.; Daily, W.; Ramirez, A.; and Owen, E. 1996. "The Effects of Noise on Occam's Inversion of Resistivity Tomography Data." *Geophysics, 61*, (2), 538–548. Tulsa, Oklahoma: Society of Exploration Geophysicists. TIC: 247174.

Langmuir, D. and Herman, J.S. 1980. "The Mobility of Thorium in Natural Waters at Low Temperatures." *Geochimica et Cosmochimica Acta, 44*, 1753–1766. New York, New York: Pergamon Press. TIC: 237029.

Langmuir, D. and Riese, A.C. 1985. "The Thermodynamic Properties of Radium." *Geochimica et Cosmochimica Acta, 49*, 1593–1601. New York, New York: Pergamon Press. TIC: 241035.

Lieser, K.H. and Hill, R. 1992. "Chemistry of Thorium in the Hydrosphere and in the Geosphere." *Radiochimica Acta, 56*, 141–151. Munchen, Germany: R. Oldenbourg Verlag. TIC: 237124.

Loeven, C. 1993. *A Summary and Discussion of Hydrologic Data from the Calico Hills Nonwelded Hydrologic Unit at Yucca Mountain, Nevada*. LA-12376-MS. Los Alamos, New Mexico: Los Alamos National Laboratory. ACC: NNA.19921116.0001.

Loubet, M. and Allegre, C.J. 1977. "Behavior of the Rare-Earth Elements in the Oklo Natural Reactor." *Geochimica et Cosmochimica Acta, 41*, 1539–1548. New York, New York: Pergamon Press. TIC: 237069.

Machesky, M.L. 1990. "Influence of Temperature on Ion Adsorption by Hydrous Metal Oxides." *Chemical Modeling of Aqueous Systems II, Los Angeles, California, September 25–30, 1988*. Melchior, D.C., and Bassett, R.L., eds., *ACS Symposium Series 416*, 282–292. Washington, D.C.: American Chemical Society. TIC: 241139.

Mackie, R.L. and Madden, T.R. 1993. "Three-Dimensional Magnetotelluric Inversion Using Conjugate Gradients." *Geophysical Journal International, 115*, (1) 215–229. Oxford, England: Blackwell Scientific. TIC: 247175.

Mantoglou, A. and Gelhar, L.W. 1987. "Stochastic Modeling of Large-Scale Transient Unsaturated Flow Systems." *Water Resources Research, 23*, (1), 37–46. Washington, D.C.: American Geophysical Union. TIC: 223510.

Mariano, A.N. 1989. "Economic Geology of Rare-Earth Elements." *Geochemistry and Mineralogy of Rare Earth Elements*, Lipin, B.R. and McKay, G.A., eds. *Reviews in Mineralogy,*

21, 309–337. Washington, D.C.: Mineralogical Society of America. On Order Library Tracking Number-1684.

Maya, L. 1982. "Sorbed Uranium(VI) Species on Hydrous Titania, Zirconia, and Silica Gel." *Radiochimica Acta, 31*, 147–151. München, Germany: R. Oldenbourg Verlag. TIC: 236887.

Means, J.L.; Crerar, D.A.; and Borcsik, M.P. 1978. "Adsorption of Co and Selected Actinides by Mn and Fe Oxides in Soils and Sediments." *Geochimica et Cosmochimica Acta, 42*, 1763–1773. New York, New York: Pergamon Press. TIC: 218336.

Meijer, A. 1990. *Yucca Mountain Project Far-Field Sorption Studies and Data Needs.* LA-11671-MS. Los Alamos, New Mexico: Los Alamos National Laboratory. ACC: NNA.19920131.0363.

Meijer, A. 1992. "A Strategy for the Derivation and Use of Sorption Coefficients in Performance Assessment Calculations for the Yucca Mountain Site." *Proceedings of the DOE/Yucca Mountain Site Characterization Project Radionuclide Adsorption Workshop at Los Alamos National Laboratory, September 11–12, 1990.* Canepa, J.A., ed. LA-12325-C. Los Alamos, New Mexico: Los Alamos National Laboratory. ACC: NNA.19920421.0117.

Meijer, A. 1993. "Far-Field Transport of Carbon Dioxide: Retardation Mechanisms and Possible Validation Experiments." *Proceedings of the Topical Meeting on Site Characterization and Model Validation, Focus '93, September 26–29, 1993, Las Vegas, Nevada*, 110–114. La Grange Park, Illinois: American Nuclear Society. TIC: 102245.

Meijer, A.; Triay, I.; Knight, S.; and Cisneros, M. 1989. "Sorption of Radionuclides on Yucca Mountain Tuffs." *Proceedings, Nuclear Waste in the Unsaturated Zone, Focus '89, September 17–21, 1989, Las Vegas, Nevada*, 113–117. La Grange Park, Illinois: American Nuclear Society. TIC: 222552.

Montazer, P. and Wilson, W.E. 1984. *Conceptual Hydrologic Model of Flow in the Unsaturated Zone, Yucca Mountain, Nevada.* Water-Resource Investigations Report 84-4345. Lakewood, Colorado: U.S. Geological Survey. ACC: NNA.19890327.0051.

Moore, R.M. and Hunter, K.A. 1985. "Thorium Adsorption in the Ocean: Reversibility and Distribution Amongst Particle Size." *Geochimica et Cosmochimica Acta, 49*, 2253–2257. New York, New York: Pergamon Press. TIC: 237520.

Murphy, J.B. and Hynes, A.J. 1986. "Contrasting Secondary Mobility of Ti, P, Zr, Nb, and Y in Two Metabasaltic Suites in the Appalachians." *Canadian Journal of Earth Sciences, 23*, (8), 1138–1144. Ottawa, Canada: National Research Council. TIC: 237341.

Murphy, W.M. 1992. "Natural Analog Studies for Geologic Disposal of Nuclear Waste." *Technology Today*, 16–21. San Antonio, Texas: Southwest Research Institute. TIC: 238853.

Neal, R.H.; Sposito, G.; Holtzclaw, K.M.; and Traina, S.J. 1987. "Selenite Adsorption on Alluvial Soils: I. Soil Composition and pH Effects." *Soil Science Society of America Journal, 51*, 1161–1165. Madison, Wisconsin: Soil Science Society of America. TIC: 237059.

Neretnieks, I. 1990. *Solute Transport in Fractured Rock—Applications to Radionuclide Waste Repositories*. SKB Technical Report 90-38. Stockholm, Sweden: Swedish Nuclear Fuel and Waste Management Company. TIC: 208618.

Neuman, S. P. 1990. "Universal Scaling of Hydraulic Conductivities and Dispersivities in Geologic Media." *Water Resources Research, 26,* (8), 1749–1758. Washington, D.C.: American Geophysical Union. TIC: 237977.

Neuman, S.P.; Winter, C.L.; and Newman, C.M. 1987. "Stochastic Theory of Field-Scale Fickian Dispersion in Anisotropic Porous Media." *Water Resources Research, 23,* (3), 453–466. Washington, D.C.: American Geophysical Union. TIC: 225294.

Newman, J. 1973. *Electrochemical Systems*. Englewood Cliffs, New Jersey: Prentice-Hall. TIC: 210201.

Nimmo, J.R. and Akstin, K.C. 1988. "Hydraulic Conductivity of a Sandy Soil at Low Water Content after Compaction by Various Methods." *Soil Science Society of America Journal, 52,* (2), 303–310. Madison, Wisconsin: Soil Science Society of America. TIC: 224083.

Nimmo, J.R. and Mello, K.A. 1991. "Centrifugal Techniques for Measuring Saturated Hydraulic Conductivity." *Water Resources Research, 27*, (6), 1263–1269. Washington, D.C.: American Geophysical Union. TIC: 224084.

Nimmo, J.R.; Rubin, J.; and Hammermeister, D. P. 1987. "Unsaturated Flow in a Centrifugal Field: Measurement of Hydraulic Conductivity and Testing of Darcy's Law." *Water Resources Research, 23*, (1), 124–134. Washington, D.C.: American Geophysical Union. TIC: 216671.

Nitsche, H.; Gatti, R.C.; Standifer, E.M.; Lee, S.C.; Müller, A.; Prussin, T.; Deinhammer, R.S.; Maurer, H.; Becraft, K.; Leung, S.; and Carpenter, S.A. 1993. *Measured Solubilities and Speciations of Neptunium, Plutonium, and Americium in a Typical Groundwater (J-13) from the Yucca Mountain Region*. LA-12562-MS. Los Alamos, New Mexico: Los Alamos National Laboratory. ACC: MOL.19950621.0265.

Nitsche, H.; Roberts, K.; Prussin, T.; Muller, A.; Becraft, K.; Keeny, D.; Carpenter, S.A.; and Gatti, R.C. 1995. *Measured Solubilities and Speciations from Oversaturation Experiments of Neptunium, Plutonium, and Americium in UE-25 p#1 Well Water from the Yucca Mountain Region*. LA-12563-MS. Los Alamos, New Mexico: Los Alamos National Laboratory. ACC: MOL.19951006.0171.

Noell, A.L.; Thompson, J.L.; Corapcioglu, M.Y.; and Triay, I.R. 1998. "The Role of Silica Colloids on Facilitated Cesium Transport Through Glass Bead Columns and Modeling."

Journal of Contaminant Hydrology, 31 (1-2), 23–56. Amsterdam, the Netherlands: Elsevier Science B.V. TIC: 245510.

O'Melia, C. and Tiller, C. 1993. "Physicochemical Aggregation and Deposition in Aquatic Environment." Chapter 8 of *Environmental Particles*. Buffle, J. and van Leeuwen, H.P., eds. Volume 2. New York, New York: Lewis Publishers. TIC: 238504.

Obeng, L.A.; Carrondo, M.J.T.; Perry, R.; and Lester, J.N. 1981. "The Influence of Zeolite Type A on Metal Concentrations in Water and Waste Water." *Journal of the American Oil Chemists' Society, 58*, (1), 81–85. Champaign, Illinois: American Oil Chemists' Society. TIC: 237902.

Ogard, A.E. and Kerrisk, J.F. 1984. *Groundwater Chemistry Along Flow Paths Between a Proposed Repository Site and the Accessible Environment*. LA-10188-MS. Los Alamos, New Mexico: Los Alamos National Laboratory. ACC: HQS.19880517.2031.

Ogard, A.E. and Vaniman, D.T., editors. 1985. *Research and Development Related to the Nevada Nuclear Waste Storage Investigations: July 1–September 30, 1984*. LA-10299-PR. Los Alamos, New Mexico: Los Alamos National Laboratory. ACC: NNA.19920922.0014.

Ortiz, T.S.; Williams, R.L.; Nimick, F.B.; Whittet, B.C.; and South, D.L. 1985. *A Three-Dimensional Model of Reference Thermal/Mechanical and Hydrological Stratigraphy at Yucca Mountain, Southern Nevada*. SAND84-1076. Albuquerque, New Mexico: Sandia National Laboratories. ACC: MOL.19980602.0331.

Payne, T.E.; Davis, J.A.; and Waite, T.D. 1990. "Modeling of Uranium Sorption to Substrates from the Weathered Zone in the Vicinity of the Koongarra Ore Body." *Alligators Rivers Analogue Project, First Annual Report 1988–89*. Duerden, P., ed. Menai, New South Wales, Australia: Australian Nuclear Science and Technology Organization. TIC: 244780.

Penrose, W.R.; Polzer, W.L.; Essington, E.H.; Nelson, D.M.; and Orlandini, K.A. 1990. "Mobility of Plutonium and Americium Through a Shallow Aquifer in a Semiarid Region." *Environmental Science and Technology, 24*, 228–234. Washington, D.C.: American Chemical Society. TIC: 224113.

Philip, J.R.; Knight, J.H.; and Waechter, R.T. 1989. "Unsaturated Seepage and Subterranean Holes: Conspectus, and Exclusion Problem for Circular Cylindrical Cavities." *Water Resources Research, 25*, (1), 16–28. Washington, D.C.: American Geophysical Union. TIC: 239117.

Polzer, W.L. and Fuentes, H R. 1988. "The Use of a Heterogeneity-Based Isotherm to Interpret the Transport of Reactive Radionuclides in Volcanic Tuff Media." *Radiochimica Acta, 44/45*, 361–365. München, Germany: R. Oldenbourg Verlag. TIC: 240183.

Prout, W.E. 1959. "Adsorption of Radioactive Waste by Savannah River Plant Soil." *Soil Science, 86*, 13–17. Baltimore, Maryland: Williams and Wilkins. TIC: 237056.

Rai, D. and Zachara, J.M. 1984. *A Critical Review.* Volume 1 of *Chemical Attenuation Rates, Coefficients, and Constants in Leachate Migration.* EPRI EA-3356. Palo Alto, California: Electric Power Research Institute. TIC: 237846.

Rancon, D. 1973. "Comportement Dans Les Milieux Souterrians De L'Uranium et Du Thorium Rejetes Par L'Industrie Nucleaire." *Environmental Behavior of Radionuclides Released in the Nuclear Industry, Proceedings of a Symposium Organized by the International Atomic Energy Agency, the OECD Nuclear Energy Agency, and the World Health Organization, Held in Aix-en-Provence, 14–18 May 1973.* IAEA-SM-172/55, 333–346. Vienna, Austria: International Atomic Energy Agency. TIC: 237674.

Reimus, P.W. and Dash, Z.V. 1999. *Models and Methods for the Reactive Transport Application, STN: 10032-MMS-1.1-00.* Los Alamos, New Mexico: Los Alamos National Laboratory. ACC: MOL.19990810.0051.

Reimus, P.W.; Adams, A.; Haga, M.J.; Humphrey, A.; Callahan, T.; Anghel, I.; and Counce, D. 1999. *Results and Interpretation of Hydraulic and Tracer Testing in the Prow Pass Tuff at the C-Holes.* Milestone SP32E7M4. Los Alamos, New Mexico: Los Alamos National Laboratory. TIC: 246377.

Rhodes, D.W. 1957. "Adsorption of Plutonium by Soil." *Soil Science, 84,* 465–469. Baltimore, Maryland: Williams and Wilkins. TIC: 237905.

Robinson, B.A.; Wolfsberg, A.V.; Zyvoloski, G.A.; and Gable, C.W. 1995. *An Unsaturated Zone Flow and Transport Model of Yucca Mountain.* Milestone 3468. Draft. Los Alamos, New Mexico: Los Alamos National Laboratory. ACC: MOL.19960415.0218

Rodi, W.L. 1976. "A Technique for Improving the Accuracy of Finite Element Solutions for Magnetotelluric Data." *Geophysics Journal of the Royal Astronomical Society, 44,* (2), 483–506. Oxford, England: Blackwell Science. TIC: 247178.

Rogers, P.S.Z. and Meijer, A. 1993. "Dependence of Radionuclide Sorption on Sample Grinding Surface Area and Water Composition." *High-Level Radioactive Waste Management, Proceedings of the Fourth Annual International Conference, Las Vegas, Nevada, April 26-30, 1993, 2,* 1509–1516. LaGrange Park, Illinois: American Nuclear Society. TIC: 208542.

Rose, A.W.; Hawkes, H.E.; and Webb, J.S. 1979. *Geochemistry in Mineral Exploration,* 2nd Edition. New York, New York: Academic Press. TIC: 247731.

Rosholt, J.N.; Prijana; and Noble, D.C. 1971. "Mobility of Uranium and Thorium in Glassy and Crystallized Silicic Volcanic Rocks." *Economic Geology, 66,* 1061–1069. El Paso, Texas: Economic Geology Publishing Company. TIC: 219186.

Rundberg, R.S. 1987. *Assessment Report on the Kinetics of Radionuclide Adsorption on Yucca Mountain Tuff.* LA-11026-MS. Los Alamos, New Mexico: Los Alamos National Laboratory. ACC: NNA.19930405.0075.

Rundberg, R.S.; Ogard, A.E.; and Vaniman, D.T. 1985. *Research and Development Related to the Nevada Nuclear Waste Storage Investigations, April 1–June 30, 1984*. LA-10297-PR. Los Alamos, New Mexico: Los Alamos National Laboratory. ACC: NNA.19920922.0018.

Rundberg, R.S.; Partom, I.; Ott, M.A.; Mitchell, A.J.; and Birdsell, K. 1987. *Diffusion of Nonsorbing Tracers in Yucca Mountain Tuff*. Milestone R524. Los Alamos, New Mexico: Los Alamos National Laboratory. ACC: NNA.19930405.0074.

Runde, W.; Meinrath, G.; and Kim, J.I. 1992. "A Study of Solid-Liquid Phase Equilibria of Trivalent Lanthanide and Actinide Ions in Carbonate Systems." *Radiochimica Acta, 58/59*, 93–100. München, Germany: R. Oldenbourg Verlag. TIC: 237409.

Russell, J.D.; Paterson, E.; Fraser, A.R.; and Farmer, V.C. 1975. "Adsorption of Carbon Dioxide on Goethite (α-FeOOH) Surfaces, and its Implications for Anion Adsorption." *Journal of the Chemical Society of London, Faraday Transactions I, 71*, 1623–1630. London, England: Royal Society of Chemistry. TIC: 224557.

Russo, D. 1988. "Determining Soil Hydraulic Properties by Parameter Estimation: On the Selection of a Model for the Hydraulic Properties." *Water Resources Research, 24*, (3), 453–459. Washington, D.C.: American Geophysical Union. TIC: 247182.

Russo, D. 1995. "Stochastic Analysis of the Velocity Covariance and the Displacement Covariance Tensors in Partially Saturated Heterogeneous Anisotropic Porous Formations." *Water Resources Research, 31*, (7), 1647–1658. Washington, D.C.: American Geophysical Union. TIC: 247180.

Sanchez, A.L.; Murray, J.W.; and Sibley, T.H. 1985. "The Adsorption of Plutonium IV and V on Goethite." *Geochimica et Cosmochimica Acta, 49*, (11), 2297–2307. New York, New York: Pergamon Press. TIC: 224091.

Schenker, A.R.; Guerin, D.C.; Robey, T.H.; Rautman, C.A.; and Barnard, R.W. 1995. *Stochastic Hydrogeologic Units and Hydrogeologic Properties Development for Total-System Performance Assessments*. SAND94-0244. Albuquerque, New Mexico: Sandia National Laboratories. ACC: MOL.19960318.0528.

SEA (Science and Engineering Associates). 1992. *The Use of Absorbent Materials to Collect In Situ Vadose Zone Liquids*. Topical Report No. SEATR-92-01. Santa Fe, New Mexico: Science and Engineering Associates, Inc. TIC: 247944.

Serne, R.J. and Relyea, J.F. 1982. *The Status of Radionuclide Sorption-Desorption Studies Performed by the WRIT Program*. PNL-3997. Richland, Washington: Pacific Northwest Laboratory. ACC: NNA.19900416.0121.

Siegel, M.D.; Hopkins, P.L.; Glass, R.J.; and Ward, D.B. 1992. "Design of an Intermediate-Scale Experiment to Validate Unsaturated-Zone Transport Models." *High Level Radioactive Waste Management: Proceedings of the Third International Conference, Las Vegas, Nevada,*

April 12–16, 1992, 2, 1972–1984. La Grange Park, Illinois: American Nuclear Society. TIC: 4447

Siegel, M.D.; Ward, D.B.; Cheng, W.C.; Bryant, C.; Chocas, C.S.; and Reynolds, C.G. 1993. "Preliminary Characterization of Materials for a Reactive Transport Model Validation Experiment." *High Level Radioactive Waste Management, Proceeding of the Fourth Annual International Conference, Las Vegas, Nevada, April 26–30, 1993, 1*, 348–358. La Grange Park, Illinois: American Nuclear Society. TIC: 208542.

Sillen, L.G. and Martell, A.E. 1964. *Stability Constants of Metal-ion Complexes.* Second edition. Special Publication No. 17. London, England: The Chemical Society. TIC: 247801.

Snelling, A.A. 1980. "Uraninite and its Alteration Products: Koongarra Uranium Deposit." *Proceedings of International Uranium Symposium on the Pine Creek Geosyncline, 1980.* Ferguson, J., and Goleby, A. B., eds. 487–498. Vienna, Austria: International Atomic Energy Agency. TIC: 236806.

Snelling, A.A. and Dickson, B.L. 1979. "Uranium-Daughter Disequilibrium in the Koongarra Uranium Deposit, Australia." *Mineralium Deposita, 14*, 109–118. New York, New York: Springer-Verlag. TIC: 237067.

Snodgrass, W.J. 1980. "Distribution and Behavior of Nickel in the Aquatic Environment." Chapter 9 of *Nickel in the Environment.* 203–274. New York, New York: John Wiley and Sons. TIC: 237686.

Soll, W.E. 1997. *Busted Butte Modeling, UZ Transport Modeling Notebook #1* (LA-EES-5-NBK-98-018). SN-LANL-SCI-048-V1. ACC: MOL.19991221.0369.

Spitsyn, V.I.; Balukova, V.D.; Naumova, A.F.; Gromov, V.V.; Spiridonov, F.M.; Vetrov, E.M.; and Grafov, G.I. 1958. "A Study of the Migration of Radioelements in Soils." *Proceedings of the International Conference on the Peaceful Uses of Atomic Energy, Geneva, September 1–13, 1958: Waste Treatment and Environmental Aspects of Atomic Energy, 18*, 439–448. Geneva, Switzerland: United Nations. TIC: 247777.

Stammose, D. and Dolo, J-M. 1990. "Sorption of Americium at Trace Levels on a Clay Mineral." *Radiochimica Acta, 51*, 189–193. München, Germany: R. Oldenbourg Verlag. TIC: 237004.

Stephens, D.B. and Rehfeldt, K.R. 1985. "Evaluation of Closed-Form Analytical Models to Calculate Conductivity in a Fine Sand." *Soil Science Society of America Journal, 49*, 12–19. Madison, Wisconsin: Soil Science Society of America. TIC: 224082.

SubTerra. 1998. *Final Report, TRW Environmental Safety Systems, Inc., Busted Butte Test Facility.* Project: 97-35. Preston, Washington: Sub Terra. TIC: 247628.

Taylor, S.R. and McLennan, S.M. 1988. "The Significance of the Rare Earths in Geochemistry and Cosmochemistry." Chapter 79 of *Handbook on the Physics and Chemistry of Rare Earths, Volume 11—Two-Hundred-Year Impact of Rare Earths on Science.* Gschneidner, K.A., Jr., and Eyring, L., eds. 485–580. New York, New York: North Holland Physics. TIC: 247238

Theis, T.L. and Richter, R.O. 1980. "Adsorption Reactions of Nickel Species at Oxide Surfaces." Chapter 4 of *Advances in Chemistry Series.* Washington, D.C.: American Chemical Society. TIC: 236944.

Thomas, K.W. 1987. *Summary of Sorption Measurements Performed with Yucca Mountain, Nevada, Tuff Samples and Water from Well J-13.* LA-10960-MS. Los Alamos, New Mexico: Los Alamos National Laboratory. ACC: NNA.19900604.0045.

Thomas, K.W. 1988. *Research and Development Related to the Nevada Nuclear Waste Storage Investigations, October 1–December 31, 1984.* LA-11443-PR. Los Alamos, New Mexico: Los Alamos National Laboratory. ACC: NNA.19920131.0372.

Torstenfelt, B.; Rundberg, R.S.; and Mitchell, A.J. 1988. "Actinide Sorption on Granites and Minerals as a Function of pH and Colloids/Pseudocolloids." *Radiochimica Acta, 44/45,* 111–117. München, Germany: R. Oldenbourg Verlag. TIC: 237496.

Travis, B.J. and Birdsell, K. *TRACRN 1.0: A Model of Flow and Transport in Porous Media for the Yucca Mountain Project, Model Description and User's Manual.* YMP Milestone Report T421. Los Alamos, New Mexico: Los Alamos National Laboratory. ACC: NNA.19891017.0060.

Triay, I.R.; Birdsell, K.H.; Mitchell, A.J.; and Ott, M.A. 1993. "Diffusion of Sorbing and Nonsorbing Radionuclides in Tuff." *High Level Radioactive Waste Management, Proceedings of the Fourth Annual International Conference, Las Vegas, Nevada, April 26–30, 1993, 2,* 1527–1532. La Grange Park, Illinois: American Nuclear Society. TIC: 208542.

Triay, I.R.; Cotter, C.R.; Huddleston, M.H.; Leonard, D.E.; Weaver, S.C.; Chipera, S.J.; Bish, D.L.; Meijer, A.; and Canepa, J.A. 1996. *Batch Sorption Results for Neptunium Transport through Yucca Mountain Tuffs.* LA-12961-MS. Los Alamos, New Mexico: Los Alamos National Laboratory. ACC: MOL.19980924.0050.

Triay, I.R.; Cotter, C.R.; Kraus, S.M.; Huddleston, M.H.; Chipera, S.J.; and Bish, D.L. 1996. *Radionuclide Sorption in Yucca Mountain Tuffs with J-13 Well Water: Neptunium, Uranium, and Plutonium.* LA-12956-MS. Los Alamos, New Mexico: Los Alamos National Laboratory. TIC: 226117.

Triay, I.R.; Furlano, A.C; Weaver, S.C.; Chipera, S.J.; and Bish, D.L. 1996. *Comparison of Neptunium Sorption Results Using Batch and Column Techniques.* LA-12958-MS. Los Alamos, New Mexico: Los Alamos National Laboratory. ACC: MOL.19980924.0049.

Triay, I.R.; Meijer, A.; Cisneros, M.R.; Miller, G.G.; Mitchell, A.J.; Ott, M.A.; Hobart, D.E.; Palmer, P.D.; Perrin, R.E.; and Aguilar, R.D. 1991. "Sorption of Americium in Tuff and Pure Minerals Using Synthetic and Natural Groundwaters." *Radiochimica Acta, 52/53*, 141–145. München, Germany: R. Oldenbourg Verlag. TIC: 222704.

Triay, I.R.; Meijer, A.; Conca, J.L.; Kung, K.S.; Rundberg, R.S.; Strietelmeier, B.A.; Tait, C.D.; Clark, D.L.; Neu, M.P.; and Hobart, D.E. 1997. *Summary and Synthesis Report on Radionuclide Retardation for the Yucca Mountain Site Characterization Project.* LA-13262-MS. Los Alamos, New Mexico: Los Alamos National Laboratory. ACC: MOL.19971210.0177.

Triay, I.R.; Robinson, B.A.; Lopez, R.M.; Mitchell, A.J.; and Overly, C.M. 1993. "Neptunium Retardation with Tuffs and Groundwaters from Yucca Mountain." *High Level Radioactive Waste Management, Proceedings of the Fourth Annual International Conference, Las Vegas, Nevada, April 26-30, 1993, 2*, 1504–1508. LaGrange Park, Illinois: American Nuclear Society. TIC: 208542.

Tsunashima, A.; Brindley, G.W.; and Bastovanov, M. 1981. "Adsorption of Uranium from Solutions by Montmorillonite: Compositions and Properties of Uranyl Montmorillonites." *Clays and Clay Minerals, 29*, (1), 10–16. Boulder, Colorado: Clay Minerals Society. TIC: 236914.

van Genuchten, M.T. 1980. "A Closed-Form Equation for Predicting the Hydraulic Conductivity of Unsaturated Soils." *Soil Science Society of America Journal, 44*, (5), 892–898. Madison, Wisconsin: Soil Science Society of America. TIC: 217327.

Weaver, S.C.; Triay, I.R.; and Clevenger, M.C. 1996. *Saturated Diffusion Cell Experiment.* LANL-CST-DP-66, R3. Los Alamos, New Mexico: Los Alamos National Laboratory. ACC: MOL.19971021.0345.

Wemheuer, R.F. 1999. "First Issue of FY00 NEPO QAP-2-0 Activity Evaluations." Interoffice correspondence from R.F. Wemheuer (CRWMS M&O) to R.A. Morgan, October 1, 1999, LV.NEPO.RTPS.TAG.10/99-155, with enclosures. ACC: MOL.19991028.0162.

White, A.F.; Benson, S.M.; Yee, A.W.; Wollenberg, H.A., Jr.; and Flexser, S. 1991. "Groundwater Contamination at the Kesterson Reservoir, California: 2. Geochemical Parameters Influencing Selenium Mobility." *Water Resources Research, 27*, (6), 1085–1098. Washington, D.C.: American Geophysical Union. TIC: 237455.

Wilson, M.L.; Gauthier, J.G.; Barnard, R.W.; Barr, G.E.; Dockery, H.A.; Dunn, E.; Eaton, R.R.; Guerin, D.C.; Lu, N; Martinez, M.J.; Nilson, R.; Rautman, C.A.; Robey, T.H.; Ross, B.; Ryder, E.E.; Schenker, A.R.; Shannon, S.A.; Skinner, L.H.; Halsey, W.G.; Gansemer, J.D.; Lewis, L.C.; Lamont, A.D.; Triay, I.R.; Meijer, A.; and Morris, D.E. 1994. *Total-System Performance Assessment for Yucca Mountain—SNL Second Iteration (TSPA-1993).* SAND93-2675. Executive Summary and two volumes. Albuquerque, New Mexico: Sandia National Laboratories. ACC: NNA.19940112.0123.

Wolfsberg, K. 1978. *Sorption-Desorption Studies of Nevada Test Site Alluvium and Leaching Studies of Nuclear Test Debris*. LA-7216-MS. Los Alamos, New Mexico: Los Alamos Scientific Laboratory. TIC: 201575.

Wolfsberg, K.; Bayhurst, B.P.; Levy, S.S.; Lawrence, F.O.; Knight, S.D.; Mitchell, A.J.; Ogard, A.E.; and Wanek, P.L. 1983. *Research and Development Related to Sorption of Radionuclides on Soils*. LA-UR-83-800. Los Alamos, New Mexico: Los Alamos Scientific Laboratory. TIC: 228735.

Wood, S.A. 1990. "The Aqueous Geochemistry of the Rare-Earth Elements and Yttrium: 1. Review of Available Low-Temperature Data for Inorganic Complexes and the Inorganic REE Speciation of Natural Waters." *Chemical Geology, 82*, 159–186. Amsterdam, The Netherlands: Elsevier Science Publishers B.V. TIC: 237051.

Yeh, T.-C.; Gelhar, L.W.; and Gutjahr, A.L. 1985. "Stochastic Analysis of Unsaturated Flow in Heterogeneous Soils: 2. Statistically Anisotropic Media with Variable α." *Water Resources Research, 21*, (4), 457–464. Washington, D.C.: American Geophysical Union. TIC: 239649.

YMP-LBNL-TIP/GP 5.0, Rev 0, Mod 0. *Ground Penetrating Radar Data Acquisition*. Berkeley, California: Lawrence Berkeley National Laboratory. ACC: MOL.19990205.0129.

Zhang, D. 1998. *Stochastic Model Notebook #1* (LA-EES-5-NBK-98-017). SN-LANL-SCI-047-V1. ACC: MOL.19991214.0179.

Zhang, D. 1999. "Nonstationary Stochastic Analysis of Transient Unsaturated Flow in Randomly Heterogeneous Media." *Water Resources Research, 35* (4), 1127–1141. Washington, D.C.: American Geophysical Union. TIC: 247193.

Zhang, D. and Neuman, S.P. 1995. "Eulerian-Lagrangian Analysis of Transport Conditioned on Hydraulic Data: 1. Analytical-Numerical Approach." *Water Resources Research, 31* (1), 39–51. Washington, D.C.: American Geophysical Union. TIC: 247195.

Zhang, D. and Winter, C.L. 1998. "Nonstationary Stochastic Analysis of Steady State Flow through Variably Saturated, Heterogeneous Media." *Water Resources Research, 34* (5), 1091–1100. Washington, D.C.: American Geophysical Union. TIC: 247192.

Zhang, D.; Wallstrom, T.C.; and Winter, C.L. 1998. "Stochastic Analysis of Steady-State Unsaturated Flow in Heterogeneous Media: Comparison of the Brooks-Corey and Gardner-Russo Models." *Water Resources Research, 34* (6), 1437–1449. Washington, D.C.: American Geophysical Union. TIC: 247194.

Zielinski, R.A. 1980. "Uranium in Secondary Silica: A Possible Exploration Guide." *Economic Geology, 75*, 592–602. El Paso, Texas: Economic Geology Publishing Company. TIC: 237418.

Zielinski, R.A.; Bush, R.W.; Spengler, R.W.; and Szabo, B.J. 1986. "Rock-Water Interaction in Ash Flow Tuffs (Yucca Mountain, Nevada, U.S.A.) – The Record from Uranium Studies."

Uranium, 2, 361–386. Amsterdam, The Netherlands: Elsevier Science Publishers B.V. TIC: 222472.

Zyvoloski, G.A.; Robinson, B.A.; Dash, Z.V.; and Trease, L.L. 1995. *Models and Methods Summary for the FEHM Application.* LA-UR-94-3787, Revision 1. Los Alamos, New Mexico: Los Alamos National Laboratory. TIC: 222337.

8.2 CODES, STANDARDS, REGULATIONS, AND PROCEDURES

AP-3.10Q, Rev. 2, ICN 2. *Analysis and Models.* Washington, D.C.: U.S. Department of Energy, Office of Civilian Radioactive Waste Management. ACC: MOL.20000619.0576.

AP-3.15Q, Rev. 1, ICN 1. *Managing Technical Product Inputs.* Washington, D.C.: U.S. Department of Energy, Office of Civilian Radioactive Waste Management. ACC: MOL.20000218.0069.

AP-SIII.2Q, Rev. 0, ICN 2. *Qualification of Unqualified Data and the Documentation of Rationale Accepted Data.* Washington, D.C.: U.S. Department of Energy, Office of Civilian Radioactive Waste Management. ACC: MOL.19991214.0625.

AP-SI.1Q, Rev. 2, ICN 4. *Software Management.* Washington, D.C.: U.S. Department of Energy, Office of Civilian Radioactive Waste Management. ACC: MOL.20000223.0508.

AP-SV.1Q, Rev. 0, ICN 1. *Control of Electronic Management of Data.* Washington, D.C.: U.S. Department of Energy, Office of Civilian Radioactive Waste Management. ACC: MOL.20000512.0068.

LANL-CST-DP-66, R3, Appendix 1. 1996. *Saturated Diffusion Cell Experiment.* Los Alamos, New Mexico: Los Alamos National Laboratory. ACC: MOL.19971021.0345.

LANL-YMP-QP-S5.01, Rev 0. 2000. *Electronic Data Management.* Los Alamos, New Mexico: Los Alamos National Laboratory. ACC: MOL.20000621.0094.

QAP-2-0, Rev. 5. *Conduct of Activities.* Las Vegas, Nevada: CRWMS M&O. ACC: MOL.19980826.0209.

QAP-2-3, Rev. 12. *Classification of Permanent Items.* Las Vegas, Nevada: CRWMS M&O. ACC: MOL.20000112.0155.

8.3 SOFTWARE

DeltaGraph, V4.0.1, Macintosh.

LBNL 1999. *Software Code: CART V1.0.* 10046-1.0-00. SUN, UNIX. URN-0384.

LLNL 2000. *Software Code: ZOMBIE V3.0.* 10298-3.0-00. URN-0385.

Los Alamos National Laboratory 1999. *Software Code: FEHM V2.00.* V2.00. SUN Ultra Sparc. 10031-2.00-00.

LANL (Los Alamos National Laboratory) 1999. *Software Code: RTA V1.1.* V1.1. SUN. 10032-1.1-00.

LANL (Los Alamos National Laboratory) 1999. *Software Code: TRACRN V1.0.* V1.0. SUN Ultra 2. 10106-1.0-00.

LANL 2000. *Software Code: LAGRIT V1.0.* 10212-1.0-00. URN-0351.

LANL 2000. *Software Code: STO-UNSAT V1.0.* 10292-1.0LV-00. URN-0387.

Microsoft Excel, V5, Macintosh.

Microsoft Excel 97 SR-1.

8.4 SOURCE DATA, LISTED BY DATA TRACKING NUMBER

GS000408312231.003. Relative Humidity Calculated Porosity Measurements on Samples from Borehole USW SD-9 Used for Saturated Hydraulic Conductivity. Submittal date: 04/10/2000.

GS920408312321.001. Chemical Composition Data and Laboratory Analyses for Ground Water from Test Wells in the Yucca Mountain Area. Submittal date: 04/24/1987.

GS920408312321.003. Chemical Composition of Groundwater in the Yucca Mountain Area, Nevada 1971-1984. Submittal date: 04/24/1987.

GS930308312323.001. Chemical Composition of Groundwater and the Locations of Permeable Zones in the Yucca Mountain Area. Submittal date: 03/05/1993.

GS930908312323.003. Hydrochemical Data from Field Tests and Lab Analyses of Water Samples Collected at Field Stations USW VH-1, JF3, UE-29 UZN#91, Virgin Spring, Nevares Spring, UE-25 J#12, UE-25 J#13, UE-22 Army#1, and USW UZ-14. Submittal date: 09/30/1993.

GS940508312231.006. Core Analysis of Bulk Density, Porosity, Particle Density, and In Situ Saturation for Borehole UE-25 UZ#16. Submittal date: 05/04/1994.

GS950408312231.004. Physical Properties and Water Potentials of Core from Borehole USW SD-9. Submittal date: 03/01/1995.

GS950608312231.008. Moisture Retention Data from Boreholes USW UZ-N27 and UE-25 UZ#16. Submittal date: 06/06/1995.

GS950808312322.001. Field, Chemical, and Isotopic Data Describing Water Samples Collected in Death Valley National Monument and at Various Boreholes and around Yucca Mountain, Nevada, between 1992 and 1995. Submittal date: 08/16/1995.

GS951108312231.009. Physical Properties, Water Content, and Water Potential for Borehole USW SD-7. Submittal date: 09/26/1995.

GS960808312231.001. Water Permeability and Relative Humidity Calculated Porosity for Boreholes UE-25 UZ#16 and USW UZ-N27. Submittal date: 08/28/1996.

GS960808312231.003. Moisture Retention Data for Samples from Boreholes USW SD-7, USW SD-9, USW SD-12, and UE-25 UZ#16. Submittal date: 08/30/1996.

GS960808312231.005. Water Permeability and Relative Humidity Calculated Porosity for Samples from Boreholes USW SD-7, USW SD-9, USW SD-12, and USW UZ-14. Submittal date: 08/30/1996.

GS970708312314.007. Results of Hydraulic Conservative Tracer Tests in Miocene Tuffaceous Rocks at the C-Hole Complex, 1995-1997, Yucca Mountain, Nevada. (Submitted Input Request Tracking Number 00067.R). Submittal date: 07/31/1997.

GS970708312315.001. Concentrations of 2,6 DFBA and Pyridone from Tracer Tests Conducted at the C-well complex, 1/8/97–7/11/97. Submittal date: 07/18/97.

GS980908312322.008. Field, Chemical, and Isotopic Data from Precipitation Sample Collected behind the Service Station in Area 25 and Ground Water Samples Collected at Boreholes UE-25 C#2, UE-25 C#3, USW UZ-14, UE-25 WT#3, UE-25 WT#17 And USW WT-24, 10/06/97 to 07/01/98. Submittal date: 09/15/1998.

GS981008312314.002. Pump Test Data Collected at the C-wells Complex, 1/8/97–3/31/97. (Submitted Input Request Tracking Number 00067.R) Submittal date: 10/28/1998.

GS981008312314.003. Pumping Test Data Collected at the C-wells Complex, 5/7/96–12/31/96. Submittal date: 10/28/1998.

GS990308312242.007. Laboratory and Centrifuge Measurements of Physical and Hydraulic Properties of Core Samples from Busted Butte Boreholes UZTT-BB-INJ-1, UZTT-BB-INJ-3, UZTT-BB-INJ-4, UZTT-BB-INJ-6, UZTT-BB-COL-5, AND UZTT-BB-COL-8. Submittal date: 03/22/1999.

GS990408312231.001. Saturated Hydraulic Conductivity of Core from SD-9, 2/27–3/27/95. Submittal date: 04/27/1999.

GS990408312315.002. Transducer, Barometric Pressure, and Discharge Data Collected from 4/18/98 through 11/24/98 in Support of the Ongoing Hydraulic and Tracer Tests Being Conducted at the UE-25 C-Well Complex, Nevada. Submittal date: 04/06/1999.

GS990608312133.001. Ground-Water Quality Data. Submittal date: 06/09/1999.

GS990708312242.008. Physical and Hydraulic Properties of Core Samples from Busted Butte Boreholes. Submittal date: 07/01/1999.

GS990808312322.001. Field and Isotopic Data from Ground Water Samples from Wells in the Amargosa Valley and NTS. Submittal date: 08/23/1999.

LA000000000034.001. Diffusion of Sorbing and Non-Sorbing Radionuclides. Submittal date: 01/22/1993.

LA000000000034.002. Diffusion of Sorbing and Non-Sorbing Radionuclides. Submittal date: 06/22/1993.

LA000000000106.001. Report on the Study of Kinetic Effects Using Crushed Tuff Columns: Neptunium in Sodium Bicarbonate Waters. Submittal date: 11/01/1994.

LA0001JC831361.001. Radionuclide Transport through Saturated Fractures. Submittal date: 01/14/2000.

LA0001JC831361.002. Radionuclide Transport through Saturated Fractures. Submittal date: 01/14/2000.

LA0002JC831341.001. Depth Intervals and Bulk Densities of Alluviums. Submittal date: 03/08/2000.

LA0002JC831341.002. Quantitative X-ray Diffraction (QXRD) Results of Three Alluviums. Submittal date: 03/08/2000.

LA0002JC831341.003. Selenium Batch Adsorption on Nonwelded Zeolitic Tuff. Submittal date: 03/08/2000.

LA0002JC831361.001. Column Studies Using G4-268 Devitrified Tuff with J-13 Well Water and Radionuclides (H-3 and Pu-239). Submittal date: 03/16/2000.

LA0002JC831361.002. Column Studies Using G4-268 Devitrified Tuff with Synthetic UE-25 p#1 Water and Radionuclides (H-3 and Pu-239). Submittal date: 03/16/2000.

LA0002JC831361.003. Column Studies Using G4-268 Devitrified Tuff with J-13 Well Water and Radionuclides (H-3 and Tc-95m). Submittal date: 03/16/2000.

LA0002JC831361.004. Column Studies Using GU3-1414 Vitric Tuff with J-13 Well Water and Radionuclides (H-3 and Tc-95m). Submittal date: 03/16/2000.

LA0002JC831361.005. Column Studies Using G4-1533 Zeolitic Tuff with J-13 Well Water and Radionuclides (H-3 and Tc-95m). Submittal date: 03/16/2000.

LA0002PR831231.001. Bullfrog Reactive Tracer Test Data. Submittal date: 02/04/2000.

LA0002SK831352.001. Total Colloidal Particles Concentration and Size Distribution in Groundwaters from the Nye County Early Warning Drilling Program. Submittal date: 02/24/2000.

LA0002SK831352.002. Total Colloidal Particles Concentration and Size Distribution in Groundwaters around Yucca Mountain. Submittal date: 02/25/2000.

LA0003JC831341.001. Adsorption of Np-237 in Three Types of Alluvium as a Function of Time and Stratigraphic Position. Submittal date: 03/09/2000.

LA0003JC831341.002. Adsorption of Tc-99 in Three Types of Alluvium as a Function of Time and Stratigraphic Position. Submittal date: 03/09/2000.

LA0003JC831341.003. Adsorption of I-129 in Three Types of Alluvium as a Function of Time and Stratigraphic Position. Submittal date: 03/09/2000.

LA0003NL831352.002. The K_d Values of ^{239}Pu on Colloids of Hematite, Ca-Montmorillonite, and Silica in Natural and Synthetic Groundwater. Submittal date: 03/29/2000.

LA0004AM831234.001. Flow-through Cell Measurements for NC-EWDP-01S, 22-Feb-99 and 23-Feb-99. Submittal date: 04/17/2000

LA0004AM831234.002. Downhole Probe Measurements for NC-EWDP-03S, 23-Feb-99. Submittal date: 04/17/2000.

LA0004AM831341.001. Uranium Sorption Coefficients for Minerals and Tuff under Oxidizing Conditions in J-13 Water. Submittal date: 05/01/2000.

LA0004AM831341.002. Np Sorption onto Clinoptilolite-rich Tuff in J-13 Water under Atmospheric Conditions with Ka, Kd, and SA. Submittal date: 05/03/2000.

LA0004JC831224.001. Preliminary Unsaturated Hydraulic Conductivities of Tuffs from Yucca Mountain Boreholes, Tunnel Bed 5 (G-Tunnel) and Bandelier Tuff (Los Alamos). Submittal date: 05/01/2000.

LA0004JC831361.001. Preliminary Retardation Data for Selenium Transport through Unsaturated Tuffs. Submittal date: 04/19/2000.

LA0004WS831372.002. Sorption of Np, Pu, and Am on Rock Samples From Busted Butte, NV. Submittal date: 04/19/2000.

LA0005NL831352.001. The K_d Values of ^{243}Am on Colloids of Hematite, Montmorillonite, and Silica in Natural and Synthetic Groundwater. Submittal date: 05/03/2000.

LA9907AM831234.003. Downhole Eh and pH Measurements for NC-EWDP-01S, 11-Jan-99. Submittal date: 01/27/2000.

LA9907AM831234.009. Flow-through Cell Measurements for NC-EWDP-01S, NC-EWDP-03S, NC-EWDP-09SX, 5/17/99, 5/18/99, 5/20/99. Submittal date: 01/27/2000.

LA9907AM831234.010. Flow-through Cell Measurements for SD6-ST1, 02-Jun-99 and 08-Jun-99. Submittal date: 01/27/2000.

LA9907AM831234.011. Flow-through Cell Measurements for AD-2, 10-Jun-99. Submittal date: 01/27/2000.

LA9909PR831231.003. Interpretations of Bullfrog Reactive Tracer Test Data—Modeling Data. Submittal date: 09/02/1999.

LA9909PR831231.004. Laboratory Data from C-Wells Core. Submittal date: 09/02/1999.

LA9909PR831231.005. Interpretations of Tracer Data–Modeling Data. Submittal date: 09/02/1999.

LA9909WS831372.001. Busted Butte UZ Transport Test: Phase I Collection Pad Extract Concentrations. Submittal date: 09/29/1999.

LA9909WS831372.002. Busted Butte UZ Transport Test: Phase I Collection Pad Tracer Loading and Tracer Concentrations. Submittal date: 09/30/1999.

LA9909WS831372.005. QXRD Results for Samples from Lower Tpt Section. Submittal date: 10/04/1999.

LA9909WS831372.006. Mineral Abundances (weight %) in Calico Hills Formation. Submittal date: 10/01/1999.

LA9909WS831372.007. Quantitative XRD Results for USW H-5 Core and Drill Cuttings. Submittal date: 10/04/1999.

LA9909WS831372.010. Mineral Abundances (weight %) in Calico Hills Formation. Submittal date: 10/01/1999.

LA9909WS831372.011. Preliminary Measured Sorption Coefficients. Submittal date: 10/13/1999.

LA9909WS831372.014. Microsphere Suspension Preparation for the Busted Butte UZ Transport Test. Submittal date: 09/30/1999.

LA9909WS831372.015. ICPAES Porewater Analysis for Rock Samples from Busted Butte, NV. Submittal date: 10/01/1999.

LA9909WS831372.016. Ion Chromatography Porewater Analysis for Rock Samples from Busted Butte, NV. Submittal date: 09/30/1999.

LA9909WS831372.017. pH of Porewater of Rock Samples from Busted Butte, NV. Submittal date: 09/30/1999.

LA9909WS831372.018. Gravimetric Moisture Content of Rock Samples from Busted Butte, NV. Submittal date: 09/30/1999.

LA9909WS831372.022. Fracture and Matrix Property Sets Used in Simulations for the Phase-2 Test. Submittal date: 04/11/2000.

LA9910SK831341.005. Total Colloidal Particles Concentration and Size Distribution in NTS-ER-20-5-1, NTS-ER-20-5-3, and J-13 Groundwater. Submittal date: 12/07/1999.

LA9910WS831372.008. Busted Butte UZ Transport Test: Gravimetric Moisture Content and Bromide Concentration in Selected Phase 1A Rock Samples. Submittal date: 11/03/1999.

LA9910WS831372.009. QXRD Data for UZTT Busted Butte Samples. Submittal date: 11/03/1999.

LAAM831311AQ98.005. Geochemical Field Measurements for UE-25 WT#17, 27-Jan-98. Submittal date: 09/14/1998.

LAAM831311AQ98.007. Flow-through Cell and Static Measurements at UE-25 WT#3, 22-Jun-98. Submittal date: 09/14/1998.

LAAM831311AQ98.008. Analysis of Bailed Sample for UE-25 WT#17, 04-Jun-98. Submittal date: 09/14/1998.

LAAM831311AQ98.010. Static Measurements for US-25 WT#17, 01-Jul-98. Submittal date: 09/14/1998.

LAIT831341AQ96.001. Radionuclide Retardation Measurements of Batch-Sorption Distribution Coefficients for Barium, Cesium, Selenium, Strontium, Uranium, Plutonium, and Neptunium. Submittal date: 11/12/1996.

LAIT831341AQ97.002. Reversibility of Radionuclide Sorption. Submittal date: 06/09/1997.

LAIT831361AQ95.001. Crushed Rock Column Data to Obtain Sorption Coefficients for Pu(IV), Np, Tc-95m, Using J-13 and UE-25 p#1 Waters, Yucca Mountain, Nevada. Submittal date: 09/29/1995.

LAIT831361AQ95.003. Transport Data of H-3, Np, and Tc-95m Collected to Calculate Retardation Coefficients Using J-13 and UE-25 p#1 Waters. Submittal date: 08/20/1997.

LAIT831362AQ95.001. Solid Rock Diffusion Data Collected to Determine Rate of Movement for Np, U, and HTO through an Unsaturated Tuff. Submittal date: 09/29/1995.

LAPR831231AQ99.001. Prow Pass Reactive Tracer Test Field Data. Submittal date: 02/10/1999.

LASC831321AQ98.003. Results of Real Time Analysis for Erionite in Drill Hole USW SD-6, Yucca Mountain, Nevada. Submittal date: 06/11/1998.

LB00032412213U.001. Busted Butte Ground Penetrating Radar Data Collected June 1998 through February 2000 at the Unsaturated Zone Transport Test (UZTT): GPR Velocity Data. Submittal date: 03/24/2000.

LB970601233129.001. The Site-Scale Unsaturated Zone Model of Yucca Mountain, Nevada for the Viability Assessment. Submittal date: 06/09/1997.

LL990612704244.098. ERT Data for Busted Butte. Submittal date: 06/21/1999.

MO0004GSC00167.000. As-built Coordinate of Boreholes in the Test Alcove and Running Drift, Busted Butte Test Facility. Submittal date: 04/20/2000.

MO9907YMP99025.001 YMP-99-025.01, List of Boreholes. Submittal date: 07/19/1999.

8.5 OUTPUT DATA, LISTED BY DATA TRACKING NUMBER

LA0003AM831341.001. Preliminary Revision of Probability Distributions for Sorption Coefficients (K_ds). Submittal date: 03/29/2000.

LA0003JC831362.001. Preliminary Matrix Diffusion Coefficients for Yucca Mountain Tuffs. Submittal date: 04/10/2000.

LA9909WS831372.019. Busted Butte Simulation Results 3-D Model. Submittal date: 04/11/2000.

LA9909WS831372.020. Summary of Monte Carlo Cases Including Correlation Length of Heterogeneities. Submittal date: 04/12/2000.

LA9909WS831372.021. Busted Butte Phase 1-A Modeling Results for Stochastic Model. Submittal date: 04/11/2000.